Ionospheric Corrections for SHF Satellite Radar Altimetry

Richard Peter Leigh

being a thesis submitted to the Faculty of Science of the University of Leicester

in candidature for the degree of Philosophiae Doctor

Department of Physics

University of Leicester

1989

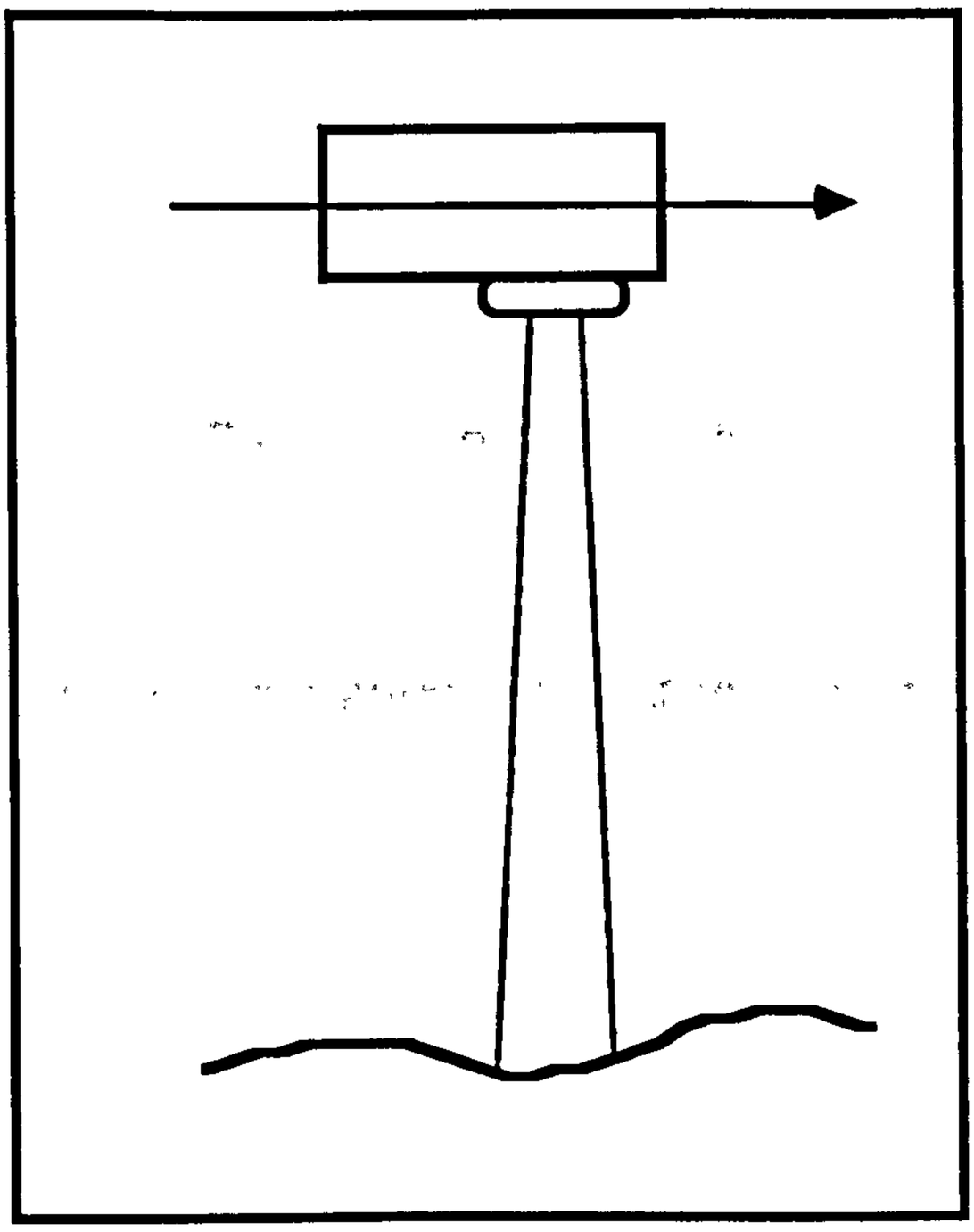

Dedicated to my parents

numquam iterum faciam dum iterum

Fac. 100

IONOSPHERIC CORRECTIONS FOR SHF SATELLITE RADAR ALTIMETRY

Richard Peter Leigh

To measure the satellite-ocean altitude, a radar altimeter transmits a nadir–directed microwave pulse and times the return of the surface reflection. The intervening free electrons of the ionosphere cause group delay of the pulse resulting in an overestimate of the platform altitude by an amount directly proportional to the sub–satellite electron content. In effect the figure of the ocean surface detected by the altimeter is modulated by the spatial and temporal variation of the ionospheric electron content.

A two stage technique has been developed to remove the bias imposed by the ionosphere on altimetric measurements. The first stage generates a prediction of electron content based on ionospheric climatology. The second stage is an adaptive modelling procedure which makes use of data from satellite–ranging radar systems.

The first chapter of this thesis gives an introduction to the Earth's ionosphere, describes its effect on radar altimetry and suggests a technique to correct for this influence. Chapter Two reviews previous work in related areas before Chapter Three embarks on a description of the spatial and temporal behaviour of electron content. Chapter Four describes the mathematical sub–models which form the basis of the empirical model and Chapter Five is devoted to the calibration and validation of this model. Chapter Six covers the calculation of the coherence functions of electron content which are crucial for the operation of the adaptive procedure. Chapter Seven compares the new model with one employed for a previous altimeter mission and Chapter Eight summarizes what has gone before and suggests topics for future research.

Acknowledgements

My thanks are due to the following :

Professors E. A. Davis and K. A. Pounds, heads of the Department of Physics during the course of this research, for the opportunity of working at the University.

Professor Tudor Jones, Dr Terry Robinson and Dr Mark Lester of the Ionospheric Physics Group at the University of Leicester for their guidance throughout the course of my research and who also undertook the arduous task of proof–reading the manuscript; the errors which remain, however, are mine alone.

The Marconi Research Centre, Great Baddow and the Science and Engineering Research Council for a CASE postgraduate studentship.

My supervisors at MRC, John Milsom for many helpful discussions on the coherence of the ionosphere and Nick Riley for his time and assistance, but most of all for his hospitality. The magnetometer data utilized in Chapter Six was supplied by MRC.

The World Data Centre C1 at the Rutherford Appleton Laboratory, Chilton and Dr M. A. Hapgood for the provision of the Faraday rotation electron content data and vertical–incidence ionosonde data employed in this research.

The Algorithm Development Facility at the Royal Aircraft Establishment National Remote Sensing Centre and Dr M. D. Elkington for the provision of the Seasat ionospheric correction data employed in Chapter Seven.

The University Library for its services, particularly Mr Stephen Rawlinson for his assistance with several literature searches which formed the basis of Chapter Two.

The University Computer Centre for access to the VAX Cluster mainframe (VAX Dei) and its peripheral devices. Particularly to Dr R. J. Mobbs for his assistance with the retrieval of the Faraday

rotation data from its original source and to Nick Mattin of the Ionospheric Group for much programming advice.

My particular thanks go to Mr Roy Buckley for his help and encouragement with the mathematical aspects of my research. Coherence theory was explained by Terry Robinson.

The frontispiece of this book was freely adapted from the cover of Rapley et al (1985).

Finally, to everyone I have had the pleasure of meeting over the last four years without whom the long days would have been very different.

Per ardua ad ionosphere.

written between October 1987 and June 1989

on a Macintosh™ Plus PC with the WriteNow™ and MacDraw™ applications

printed on an Apple Laserwriter Plus

set in 10 point Helvetica

Contents

Chapter 1 : Introduction

What follows is an account of the research and development of an ionospheric group delay correction procedure for SHF satellite radar altimetry.

1.1 The Atmosphere

Parameters which characterize the physical properties of the Earth's atmosphere are illustrated as a function of altitude in Figure 1.1. The monotonic decrease of atmospheric pressure with increasing altitude is governed by the atmospheric scale height which is defined in Equation 1.1. There is a factor e^{-1} drop in pressure over an altitude increase of one scale height. The corresponding rapid decrease of density leaves only one millionth of the total mass of the atmosphere above 100 km. The scale height itself varies with altitude, being typically 7 km for altitudes below 100 km and approximately 70 km at an altitude of 350 km.

$$H = \frac{kT}{\mu g} \tag{1.1}$$

H = atmospheric pressure scale height

T = absolute temperature $\quad$ k = Boltzmann's constant

μ = mean molecular mass $\quad$ g = acceleration due to gravity

The terminology of atmospheric regions is based upon the vertical distribution of temperature and composition, the parameters necessary to describe an atmosphere in hydrostatic equilibrium (Bauer 1973). The nomenclature of the temperature regions is given in Figure 1.2.

- The troposphere is the region from ground level to the tropopause, near 10 km, with a negative temperature gradient of approximately 10 K km^{-1} (the adiabatic lapse rate).
- The stratosphere extends to the stratopause at 50 km and is the region where the temperature increases due to the absorption of solar radiations by ozone.
- The mesosphere lacks this heating mechanism and the temperature again falls; at the mesopause, between 80 km and 90 km, the atmospheric temperature reaches its minimum.

- The thermosphere is the region above the mesopause where the temperature gradient again becomes positive. The gradient over the first 200 km of the region is very strong, but then the temperature becomes fairly constant at altitudes above 500 km. The diurnal maximum of thermospheric temperature depends on the activity of the Sun and typically lies between 800 K and 2 000 K.

The primary source of heat in the upper atmosphere is solar ultraviolet (uv) radiation. Photochemical reaction products are heated by the energy of the uv photons in excess of the activation energy. These products distribute their energy to the rest of the medium; below 100 km heat is transported to different levels by infrared radiation, above 100 km conduction is most important, though between these regimes is a transitional region where convection is the dominant process.

The vertical temperature profile controls the mixing of atmospheric gases. Below 100 km the overall negative gradient allows convection, or eddy diffusion, resulting in a nearly constant composition dominated by molecular nitrogen and molecular oxygen. The composition of the atmosphere at ground level is given in Table 1.1. Above 100 km the positive temperature gradient inhibits thermal convection. Each species then acquires an altitude distribution governed by molecular diffusion and determined by its individual scale height. The result is a composition which is altitude dependent with atomic oxygen, helium and hydrogen becoming prominent. The composition profiles for thermospheric temperatures of 600 K, 1 000 K and 1 800 K are shown in Figure 1.3.

1.2 The Ionosphere

The upper atmosphere above 70 km is weakly ionized by solar extreme–ultraviolet (euv) and X–ray radiation. The energies of photons in these wavebands are greater than the 10–25 ev ionization potentials of the principal atmospheric constituents. A quasi-equilibrium is established between production, recombination and transport processes governed by Equation 1.2, the Equation of Continuity.

$$\frac{\partial N}{\partial t} = q - r - \nabla . N \underline{u} \qquad (1.2)$$

N = electron density $\underline{u}$ = electron drift velocity

q = production rate r = total loss rate

In 1901 the long–distance radio propagation experiments of Marconi succeeded in receiving a signal transmitted from across the Atlantic (Marconi 1902) and a year later Heaviside and Kennelly independently suggested this phenomenon to be due to an electrically conducting layer of the upper atmosphere. The presence of what was originally known as the Kennelly–Heaviside layer was determined experimentally in 1925 by Appleton and Barnet and Breit and Tuve. A contemporary review of the early history of ionospheric research covering the above events in more detail is given by Kenrick and Pickard (1930). The component of the upper atmosphere which is sufficiently ionized to influence the propagation of radio waves is known as the ionosphere (after Watson–Watt 1933).

The efficiency of plasma production by radiation of a given frequency is determined by the power of the solar radiation of that frequency, the density of the atmosphere and the ionization cross-sections of the individual species present. The Chapman theory (Chapman 1931) predicts a maximum of electron production at the altitude corresponding to unit optical depth. The complex interaction between the ionizing solar radiation and the atmosphere, and the consequent photochemical reactions and plasma transport processes, causes stratification of the ionosphere into several distinct layers, the nomenclature used being that of Appleton (1932). The altitude ranges of the layers are illustrated in Figure 1.4 and the electron density ranges are listed in Table 1.2. Figure 1.5 illustrates the solar radiations responsible for the production of each layer.

- The D–region occurs at altitudes between 60 and 90 km, is present only in the daytime, has low electron densities, is generated by hard X–rays and has no maximum of electron density.
- The E–region is the most regular of the ionospheric layers (except at high latitudes) with a production maximum around 105 km due to soft X–ray and euv radiation.
- The F1–region is a daytime feature with a production maximum between 160 km and 180 km caused by the most heavily absorbed part of the euv spectrum.
- The F2–region has the highest electron densities of the ionosphere with a peak anywhere between 200 km and 600 km, though usually near 250 km in the daytime. Unlike the E– and F1–regions there is no production maximum to account for the F2–region peak. The increase of electron density in the bottomside of the layer is a consequence of the recombination dominated loss rate falling off more quickly than the production rate as the altitude increases. This is halted and reversed when the loss rate becomes dominated by vertical diffusion which becomes more efficient at greater altitudes. The F2–region encompasses the vast majority of the atmospheric plasma. Through the action of thermospheric winds the F2–region persists through the night, though at a greater altitude and with lower electron densities.

The ionosphere is a weakly ionized plasma, even in the F–region no more than 1% of the neutral atmosphere is in the thermal plasma state. A comprehensive review of the basic physics of the F–region was given by Rishbeth (1967) which, apart from a brief historical discourse, detailed the processes which are believed to control the free electron density of the atmosphere.

The ionosphere is under solar control and is, therefore, subject to diurnal, seasonal and solar cycle variations. The power of solar radiations fluctuates with a period of approximately eleven years, known as the solar activity cycle, and is quantified by the number of sunspots seen on the disk of the Sun (the sunspot number). For a particular situation the atmospheric plasma density is greatest at times of high solar activity (high sunspot number). The seasonal variation of electron density is plagued by anomalies (Rishbeth 1967). The electron density is unusually high during the equinoxes (the semi–annual anomaly), is greater at noon during winter than summer (the seasonal anomaly) and, when averaged over both hemispheres, is approximately 20% greater in December than June (the annual anomaly). In the northern hemisphere the annual and seasonal anomalies are in phase resulting in a predominantly seasonal variation, whereas in the southern hemisphere they oppose each other allowing the semi–annual variation to dominate.

A representation of mid–latitude ionospheric temporal variations from Georges (1968) is depicted in Figure 1.6, where the ratio of maximum to minimum electron density is plotted for a seven decade range of periods. The larger amplitude fluctuations at the solar, seasonal and diurnal periods underline the solar control of the ionosphere. Also evident are the less powerful irregular variations of the ionosphere due to geomagnetic storms and wave motions.

A synoptic overview of the spatial fluctuations of electron density from Szuszczewicz et al (1983) is presented in Figure 1.7. This shows a noon–midnight meridian scan of electron density at a height of 350 km in the geomagnetic northern hemisphere. The general increase of electron density with decreasing latitude seen in this figure is another consequence of the solar control of the ionosphere. Also shown in the figure are two large scale ionospheric features; the Main Trough (a region of depleted electron density) and the Equatorial Anomaly (at ±15° magnetic latitude where the electron density is greater than at the Equator). On a plot similar to Figure 1.7 the variation with latitude would have a $\log_{10}$ power of approximately 0.7. Smaller scale fluctuations in the polar, auroral and nightside equatorial zones are also evident.

Height integration of the vertical electron density profile yields the ionospheric electron content (Equation 1.3). The electron content can be physically interpreted as the number of free electrons in a column of one square metre cross–section.

$$E = \int_{h=0}^{h_u} N(h)\, dh \qquad (1.3)$$

h = altitude h_u = upper altitude limit

E = electron content below h_u N(h) = electron density profile

Electron content is also subject to diurnal, seasonal and solar cycle variations and is of wide interest due to its influence on the trans–ionospheric propagation of radio waves. The fluctuations of electron density, both regular and irregular, are impressed on electron content. Vertical electron transport processes change the electron density at a given height but do not influence the height integrated electron density.

1.3 Translonospheric Radio Propagation

The presence of highly mobile free electrons influences the propagation of radio waves through the ionosphere. A characteristic plasma frequency can be associated with a given electron density through the relationship of Equation 1.4. For the terrestrial ionosphere the plasma frequency can range from below 1 MHz to above 20 MHz.

$$N = 1.24\, F^2 \qquad (1.4)$$

N = electron density (10^{10} electrons m^{-3})

F = plasma frequency (MHz)

The greatest plasma frequency in each ionospheric region is termed the critical frequency of that region and is denoted, for example, as foF2 for the F2–region. A contour map is presented in Figure 1.8 of the global distribution of foF2 calculated from the numerical maps of the Comité Consultatif International des Radiocommunications (CCIR) for 12 UT during March at a sunspot number of 150. To operate through the ionosphere satellite–borne radio systems must work at frequencies well above the highest plasma frequency along the propagation path, in other words well above the critical frequency of the F2–region. Frequencies lower than this are strongly retarded and eventually reflected at the altitude where the plasma frequency equals the transmitted frequency. Consequently satellite radio systems operate in the VHF, UHF and SHF bands where the propagation can be described with ray theory; the radio frequency bands are defined in Table 1.3.

Of fundamental importance in wave propagation studies is the phase refractive index of the dispersive ionosphere. This is described by the Appleton Equation in terms of wave frequency and characteristic frequencies of the atmospheric plasma (Appleton 1932). Consideration of the magnitude of each term in the Appleton Equation allows simplified versions of the equation to be applied for certain frequencies. For transmissions in the VHF band the electron collision frequency is much less than the wave frequency and the corresponding absorption term can be neglected. The electron gyrofrequency is also relatively small, but not so much so that it can be similarly ignored. If in addition the quasi–longitudinal approximation can be made, which assumes the transmission to be more than 5° from normal to the geomagnetic field, the VHF approximation of the Appleton Equation can be given as in Equations 1.5 to 1.8.

$$n^2 = 1 + \frac{\omega_N^2}{\omega \ (\omega \pm \omega_L)} \tag{1.5}$$

$$\omega_N^2 = \frac{N e^2}{\varepsilon_0 m} \tag{1.6}$$

$$\omega_B = \frac{e B}{m} \tag{1.7}$$

$$\omega_L = \omega_B \cos\theta \tag{1.8}$$

n	=	phase refractive index	ε_0	=	free space permittivity
ω_N	=	angular plasma frequency	ω_B	=	electron gyrofrequency
ω_L	=	longitudinal component of electron gyrofrequency			
ω	=	angular frequency of electromagnetic wave			
θ	=	angle between propagation direction and geomagnetic field			
N	=	electron density	B	=	geomagnetic flux density
e	=	electronic charge	m	=	electronic mass

The geomagnetic field makes the ionosphere birefringent at radio frequencies. An electromagnetic wave of arbitrary polarization entering the ionosphere is decomposed into two characteristic waves termed the ordinary, or o–mode and the extraordinary, or x–mode. The o–mode refractive index is given by the positive sign in Equation 1.5 and that of the x–mode by the negative sign. Both are circularly polarized, though in the opposite sense with respect to the geomagnetic field. For propagation in the direction of the field the o–mode has right–hand polarization and the x–mode left–hand polarization. The resultant wave is produced by the superposition of the two characteristics (Davies 1968). Since the phase velocity of the o–mode

is greater than that of the x–mode then, as the resultant propagates, its angle of polarization rotates in the same sense as the o–mode. This property of magnetized media is known as Faraday rotation after its discovery by Michael Faraday (Faraday 1846). The rotation angle of the plane of polarization of signals with frequencies above 100 MHz is given to a good approximation by Equation 1.9.

$$\Omega = \frac{23\,650}{f^2} \int_{h=0}^{h_s} B(h) \cos\theta \, \mathrm{SEC}\chi \, N(h) \, dh \qquad (1.9)$$

Ω = Faraday rotation angle (radians)

f = electromagnetic wave frequency (Hz)

χ = ground station – satellite zenith angle

h = altitude $\qquad$ h_s = altitude of satellite

N(h) = electron density profile $\qquad$ B(h) = geomagnetic flux density profile

The various symbols of Equation 1.9 are illustrated in Figure 1.9. Line–of–sight electron content data can be deduced from measurements of the Faraday rotation on signals transmitted by satellite beacons. The amount of polarization rotation is determined by the electron content along the ray path, though weighted by the altitude profile of the pervading geomagnetic field. Figure 1.10 shows the ray path of transmissions from a geostationary satellite in the meridian of Sagamore Hill (41°N,281°E) and the relative orientations of the ray path and the geomagnetic field. Since the geomagnetic flux density falls off as the inverse cube of geocentric distance and the electron density maximizes at altitudes of a few hundred kilometres, the integral is heavily biased towards low altitudes. Consequently the polarization of transmissions from geostationary satellites can be considered to be only appreciably rotated below an altitude of 2 000 km (Titheridge 1972).

The geomagnetic field profile is a weak function of altitude hence, the weighting term (B $\cos\theta$ $\mathrm{SEC}\chi$) can be replaced by the field–factor, its value at a mean field height (Yeh and Gonzales 1960). The mean field height is usually taken to be at 420 km (Titheridge 1972). This allows all terms of Equation 1.9, except the electron density profile, to be taken outside the integral. The Faraday rotation is then given by Equation 1.10.

$$\Omega = \frac{23\,650}{f^2} M E \qquad (1.10)$$

M = the field–factor (T)

E = equivalent vertical electron content (electrons m^{-2})

By measuring the rotation on two spaced frequencies 2π rotation ambiguities can be removed and the equivalent vertical electron content below the 2 000 km limit can be measured to an accuracy of approximately 5% (Titheridge 1973). Access to numerous VHF beacons mounted on geostationary satellites has made Faraday rotation the most widespread technique for measuring the ionospheric electron content.

For frequencies in the SHF band the phase refractive index can be approximated to the even simpler form of Equation 1.11 since, in this case, $\omega \gg \omega_B$.

$$n^2 = 1 - \frac{\omega_N^2}{\omega^2} \qquad (1.11)$$

At these frequencies the ionosphere is no longer significantly birefringent, the refractive index becomes a simple function of electron density and wave frequency. The group refractive index is defined by Equation 1.12.

$$r = \frac{c}{v} = c\frac{\partial \kappa}{\partial \omega} = \frac{\partial}{\partial \omega}(n\omega) \qquad (1.12)$$

r = group refractive index
n = phase refractive index
v = group velocity
c = speed of light in free space
κ = electromagnetic wave number

Substituting Equation 1.11 into 1.12 gives the group refractive index as Equation 1.13.

$$r^2 = \left(1 - \frac{\omega_N^2}{\omega^2}\right)^{-1} \qquad (1.13)$$

The transit time of an electromagnetic signal through the ionosphere is greater than the free–space propagation time for the same distance. The time difference is known as ionospheric group delay and this property can be employed to study electron content. The one–way group delay on a slant path, as illustrated in Figure 1.9, is defined by Equations 1.14 and 1.15.

$$\tau = \int_s \frac{r}{c}\, ds - \int_s \frac{1}{c}\, ds \qquad (1.14)$$

$$\tau = \frac{40.3}{cf^2} E \,\mathrm{SEC}\chi \qquad (1.15)$$

s = slant path distance
τ = group delay

The dispersive property of group delay allows electron content to be calculated from

measurements of transit time on two frequencies. The group delay method of measuring electron content is more accurate than Faraday rotation because no magnetic weighting term is involved and all the electrons along the ray path contribute equally to the delay. Satellite beacons in the SHF band, though, are not as common as those operating at VHF, hence the Faraday rotation technique still remains the principal method for investigating ionospheric electron content. The electron content found above 2 000 km and not measured by the Faraday method is known as the plasmaspheric electron content and constitutes approximately 45% of the total electron content at night and approximately 10% by day (Soicher 1977). The total electron content comprises the ionospheric (or Faraday) electron content plus the plasmaspheric contribution.

Single frequency radar altimetry is a trans–ionospheric radio technique which is critically dependent on knowledge of the ionospheric electron content. The radar altimeter is a remote sensing instrument operating in the microwave band with special applications in the areas of oceanography and climatology.

1.4 Satellite Radar Altimetry

A radar altimeter is a satellite–borne active sounder designed to study the topography of the seas and oceans. Unlike Earth surveillance with optical instruments, microwave sensors provide an all–weather, all–illumination capability. These properties allow observation of regions which are normally obscured by cloud and of polar oceans which are often in darkness for months at a time. More importantly the altimeter can operate during the whole orbit over both the dayside and nightside of the Earth. Reviews of the operational capabilities of radar altimeters are given by Griffiths (1986) and Chase et al (1987) and scientific uses of radar altimeter data are described by Rapley et al (1985).

The foundations of radar altimetry were laid during the NASA Earth and Ocean Physics Applications Program which developed radar altimeters as ocean surveillance instruments with the eventual aim of 100 mm precision for mean ocean height measurements. Instruments were flown on Skylab in 1973, on GEOS3 in 1975 and on Seasat in 1978, the Seasat instrument eventually satisfying the precision requirement. An evaluation of the successes of the Seasat altimeter system was given by Lame and Born (1982).

The Seasat instrument operated for one hundred days and demonstrated the quality and quantity of geophysical data to be gleaned through satellite radar altimetry. As an example of the sort of

data acquired through altimetry, the mean sea surface topography acquired from 18 days of Seasat altimeter data is presented in Figure 1.11. A more detailed plot of the sea surface height measured along Seasat revolution number 521 is presented in Figure 1.12 which shows the western North Atlantic region across the Gulf Stream. The high quality of data already gleaned from radar altimetry has sustained interest in the technique and the first of the next generation of altimeters is scheduled to fly in 1990 on the ESA Earth Resources Satellite, ERS1.

The ERS1 platform will have a circular retrograde orbit of 98° inclination at an altitude, depending on the repeat cycle, of between 745 km and 825 km. The platform will carry a package of active microwave instrumentation including a single frequency radar altimeter. An artist's impression of the satellite is given in Figure 1.13. The ERS1 radar altimeter will operate in the Ku microwave band from a one metre diameter parabolic dish antenna directed towards the satellite nadir. The altimeter will be required to measure the satellite–surface distance to an overall precision of 100 mm.

The fundamental equation of satellite altimetry is Equation 1.16 the elements of which are illustrated in Figure 1.14.

$$a(p,t) = r(p,t) - D(p) - h(p,t) \qquad (1.16)$$

p = spatial co–ordinate t = temporal co–ordinate

a(p,t) = dynamic ocean topography (fluctuation of the ocean about the geoid)

r(p,t) = radial component of the satellites ephemeris

D(p) = time–invariant figure of the geoid

h(p,t) = altimeter height measurement

Given the satellite's ephemeris and the altimeter height measurements the ocean elevation (D(p)+a(p,t)) can be calculated. The geoid is a reference figure of the Earth defined as the iso–geopotential surface that the oceans would assume in the absence of tidal forces. Given an accurate geoid model the dynamic fluctuations about the geoid, that is the ocean topography a(p,t), can be calculated. Geoid models however have uncertainties of the order of several metres, whereas the ocean topography has vertical scales of the order of a metre. This problem can be overcome by using a repeat track crossing technique which eliminates the time invariant geoid (Fu 1983). The NASA Geophysical Research Mission (Pisacane 1984), though, should reduce geoid uncertainties to the 0.1 m level and such model geoids could be employed for the ERS1 mission.

The ocean elevation is a fundamental variable of oceanography because of its direct relation to current velocity. The ocean currents distribute heat and so moderate extremes in the Earth's climate (the reason for the temperate weather of the British Isles). Over half the heat transported from the Equator to the Poles is carried by the oceans. Accurate altimetric measurements of the ocean elevation, therefore, allows calculation of the ocean circulation patterns which in turn allows an insight into the Earth's climatology. The magnitude of the ocean topography resulting from mesoscale current flows, which have horizontal scales of between 10 and 1 000 km, is several hundreds of millimetres. Figure 1.15 shows the seasonal variation of the ocean topography across the Gulf Stream to be of this order.

An altimeter transmits a nadir–directed microwave pulse and measures the return time of the surface reflection. With the assumption of free–space propagation the return time (approximately 5 ms for an altimeter at 800 km) is converted to the satellite–surface altitude. In conjunction with an accurate determination of the satellite's geocentric position, a satellite altimeter in a near–polar orbit can provide global scale and long term measurements of the dynamic ocean topography. This extensive coverage would be impractical with ground based techniques.

The calculation of altitude with the assumption of free space propagation leads to its overestimation because group delay of the sounding pulse occurs due to the troposphere and ionosphere. Table 1.4 compares typical values of the subtractive atmospheric corrections with the orbit accuracy and the accuracy goal. The tropospheric correction is independent of the wave frequency and has a component proportional to the surface atmospheric density and a component proportional to the water vapour content of the sounding path. The problem of atmospheric group delay in altimeter systems has been reviewed by Dodson (1986).

The ionosphere introduces group delay to otherwise accurate radar measurements because the electron content controls the electromagnetic path length through the ionosphere. The ionospheric correction is frequency dependent and directly proportional to the electron content of the sounding path.

For a vertical path the one–way subtractive ionospheric correction is given from Equation 1.15 by $c\tau$, which is ε in Equation 1.17.

$$\varepsilon = 40.3 \frac{E}{f^2} \qquad (1.17)$$

ε = the subtractive ionospheric correction f = radar altimeter frequency

Figure 1.16 shows the variation of the ionospheric correction with typical values of ionospheric electron content for the ERS1 altimeter frequency of 13.8 GHz. Other ionospheric propagation effects are insignificant at the SHF frequencies employed for altimetry. For the mid–latitude ionosphere a ray propagating from a zenith angle of 60° would undergo Faraday rotation of less than 1.1°, be refracted by less than 0.4" and be absorbed by less than 10^{-3} dB (Flock 1987).

The stringent precision requirements of radar altimetry mean that ionospheric corrections and their associated uncertainties would comprise a significant percentage of the error budget if allowed to go uncorrected. The constraints of the ionosphere on altimeter performance have greatest impact by day during times of high solar activity. It is important to remove the effects of ionospheric morphology (of order 0.1 m) from the data in order to fully reveal the pattern of the ocean fluctuations arising from currents and steric effects (of order several 0.1 m). Particularly problematical are steep horizontal gradients in the ionospheric electron content which, if unaccounted for, might be wrongly interpreted as features of the ocean topography. In effect the figure of the ocean surface detected by the altimeter is modulated by the spatial and temporal variation of the electron content.

1.5 The Present Investigation

There are five principal research objectives :

1. To investigate the spatial and temporal behaviour of electron content and its variability.
2. To develop, calibrate and validate an empirical model to predict the monthly mean behaviour of electron content on a global scale and for a wide range of solar activity.
3. To investigate the spatial and temporal coherence of electron content variability and to study the variation of coherence with latitude, Local Time, season and solar activity.
4. To develop an adaptive procedure to admit direct measurements of electron content into the empirical model to improve its accuracy in the space–time vicinity of the data.
5. To incorporate the above research into a procedure capable of providing predictive and adaptive ionospheric corrections for the ERS1 altimeter mission.

The fundamental difficulty in making the ionospheric correction for SHF radar altimetry is the provision of an accurate value of the sub–satellite electron content. A two stage approach to this problem has been developed which comprises an empirical predictive model to estimate the monthly mean electron content and an adaptive model to adjust the mean model with available data to account for the prevailing local conditions.

The Predictive Model estimates, on a monthly mean basis, the sub–altimeter electron content and so provides the first level of ionospheric correction. The predictive modelling technique employs a theoretical profile of electron density, which is scaled by CCIR numerical maps of ionospheric parameters. The scaled profile is height integrated up to the nominal 800 km orbit altitude to calculate the electron content. The limitation of predictive modelling lies in the day–to–day variability of electron content about the mean level, typically 20% by day and 50% at night. During the conditions of high solar activity expected for the ERS1 mission this variability could produce unacceptably large errors in the predictions. Therefore an adaptive model option was developed to improve the prediction accuracy.

The Adaptive Model employs a least–squares linear regression technique to include local and recent electron content measurements to adjust the mean value. The adjustment depends on the deviation of the measurement from its corresponding mean level and the space–time coherence of electron content between the measurement point and the prediction point. The coherence functions determine the suitability of data for the Adaptive Model. The limitations of the Adaptive Model stem from the necessity that the electron content variations at the measurement and prediction points must be strongly correlated to produce significant (greater than 30%) improvements. In practice this means that, for a solar activity level given by a twelve–month running mean sunspot number of 170, the altimeter sounding and the data must be separated by less than 1 500 km East–West or 1 300 km North–South or, if co–located, by less than 90 minutes. To consistently invoke the Adaptive Model would require a global network of monitoring sites separated by no more than twice the correlation distance. A network of this density would be prohibitively expensive and impossible to extend to the ocean regions. Hence the Adaptive Model can only be expected to be implemented under special circumstances, and this fact stresses the need for an accurate Predictive Model.

The foundation of the research reported here was provided by electron content data measured by the Faraday rotation technique at ten northern hemisphere sites during the declining phase of solar cycle 21, comprising a total of 664 station months of data.

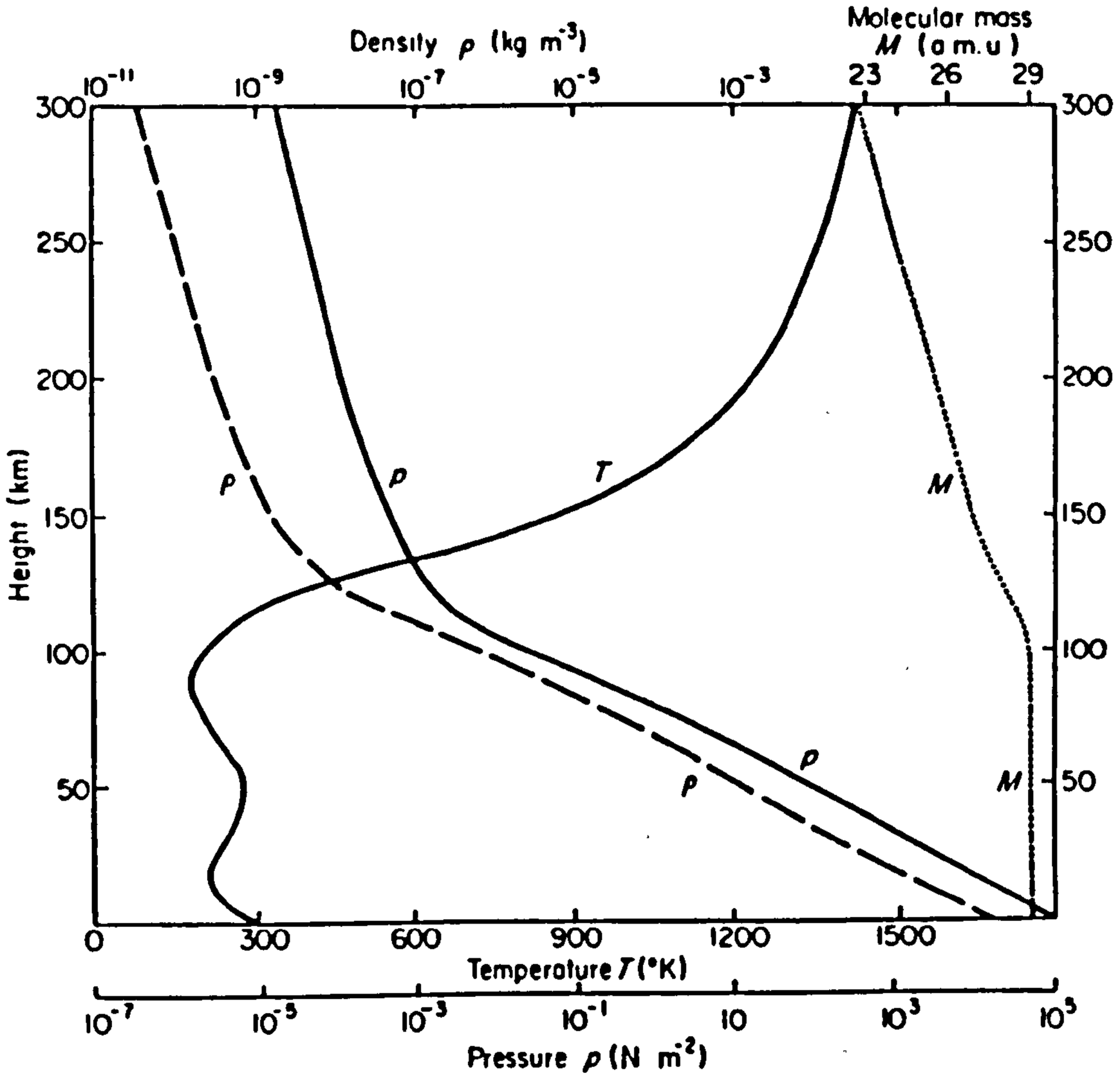

Figure 1.1 : Altitude profile to 300 km of the fundamental atmospheric parameters (after Rishbeth and Garriott 1969).

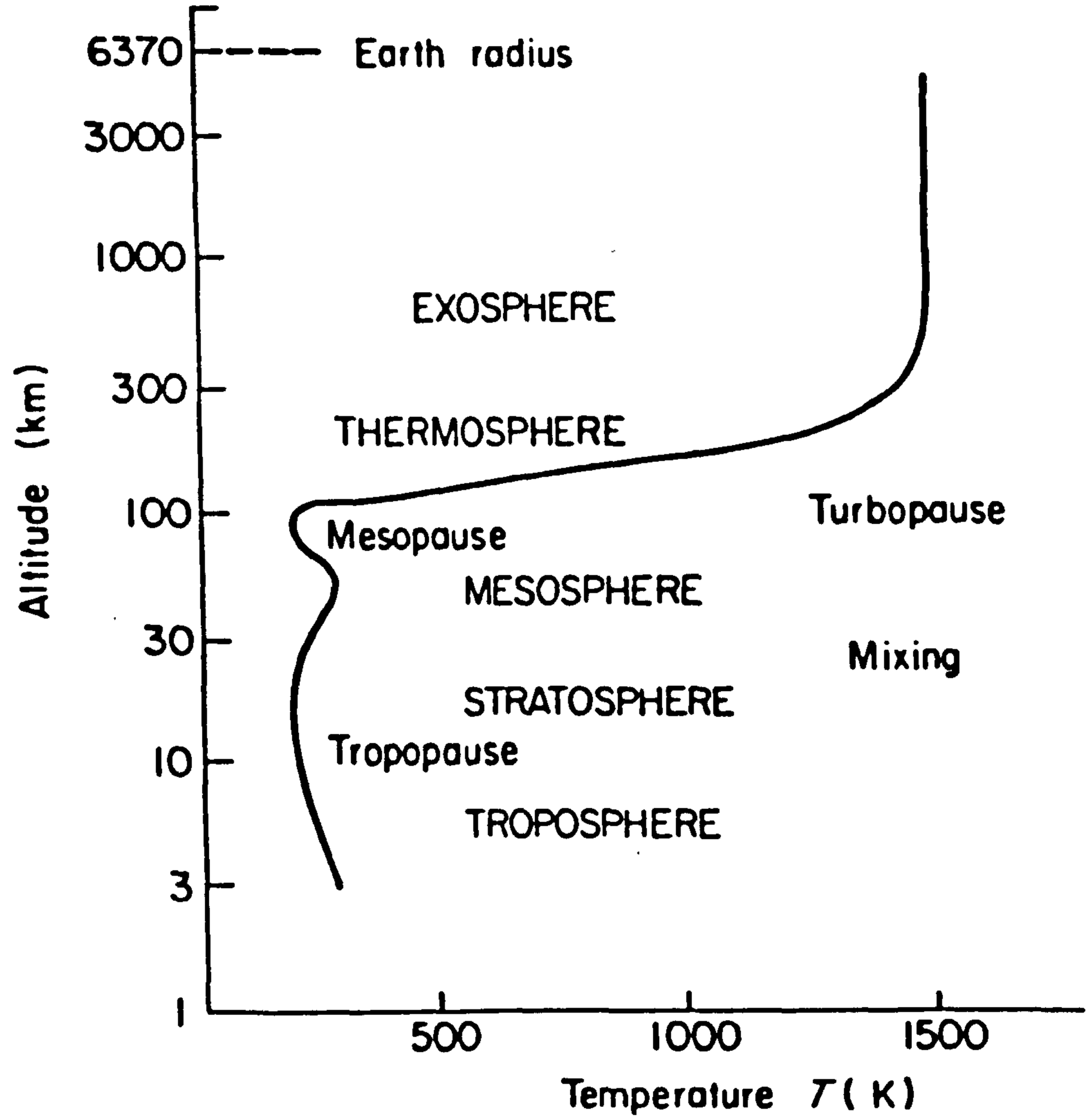

Figure 1.2 : Altitude profile of the atmospheric temperature depicting the various spheres and pauses (after Rishbeth and Garriott 1969).

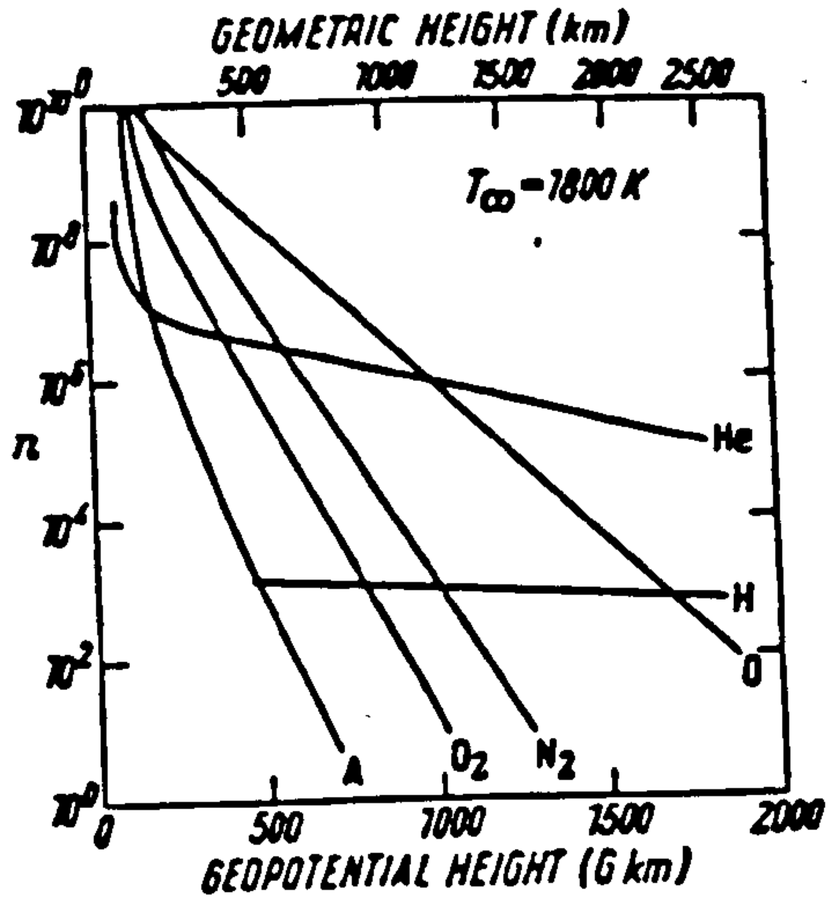

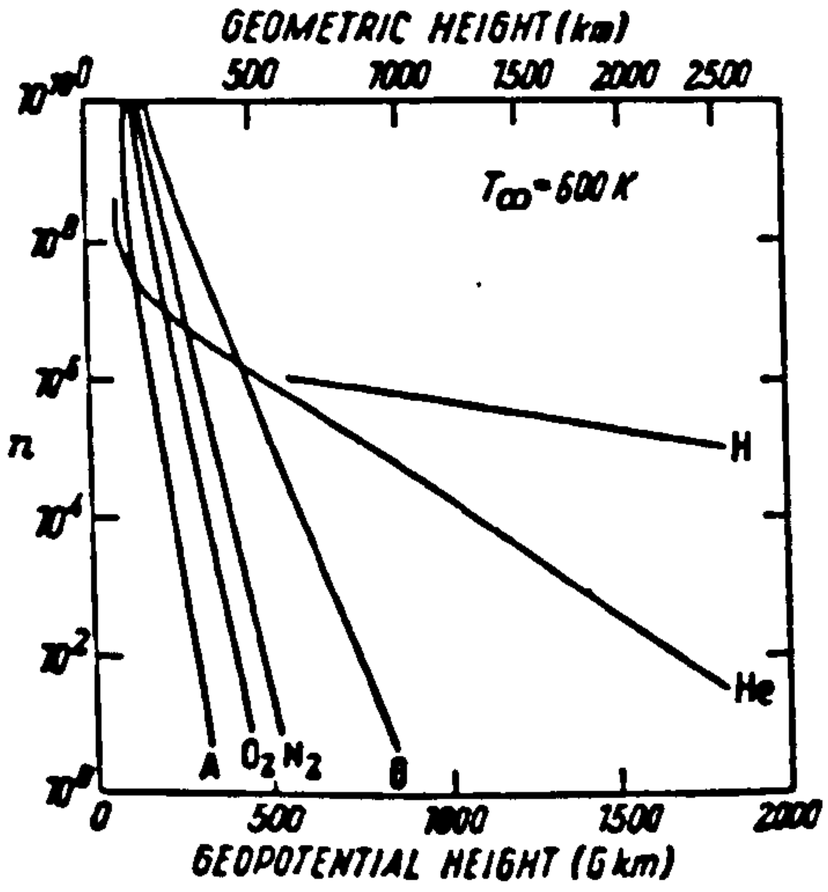

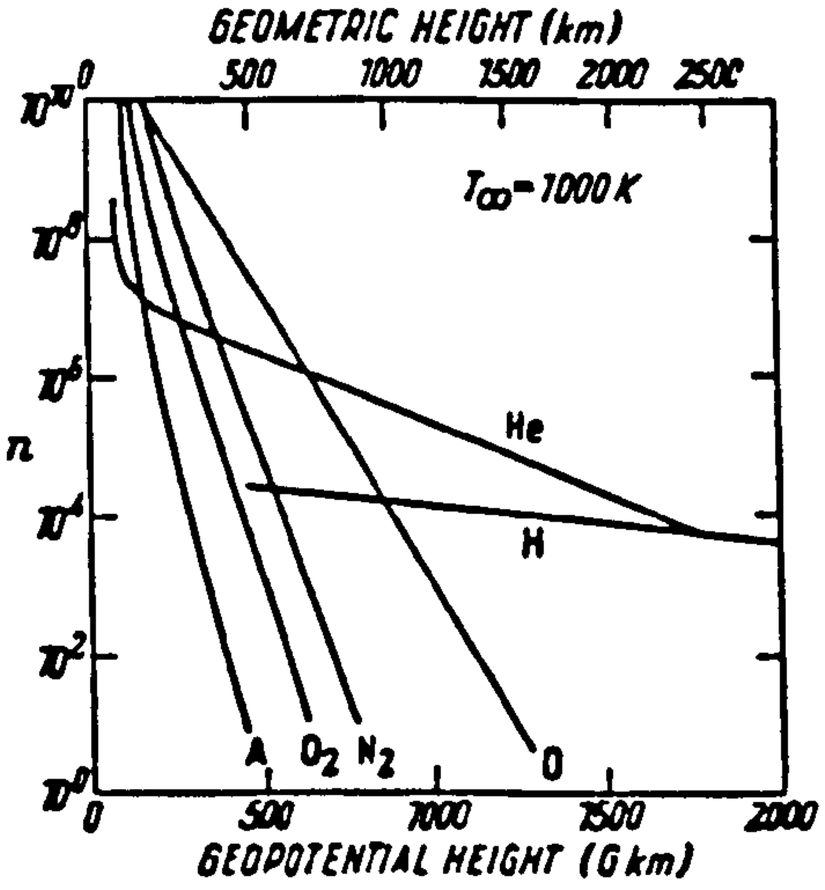

Figure 1.3 : Composition altitude profiles for thermospheric temperatures of 600 K, 1 000 K and 1 800 K (after CIRA 1972).

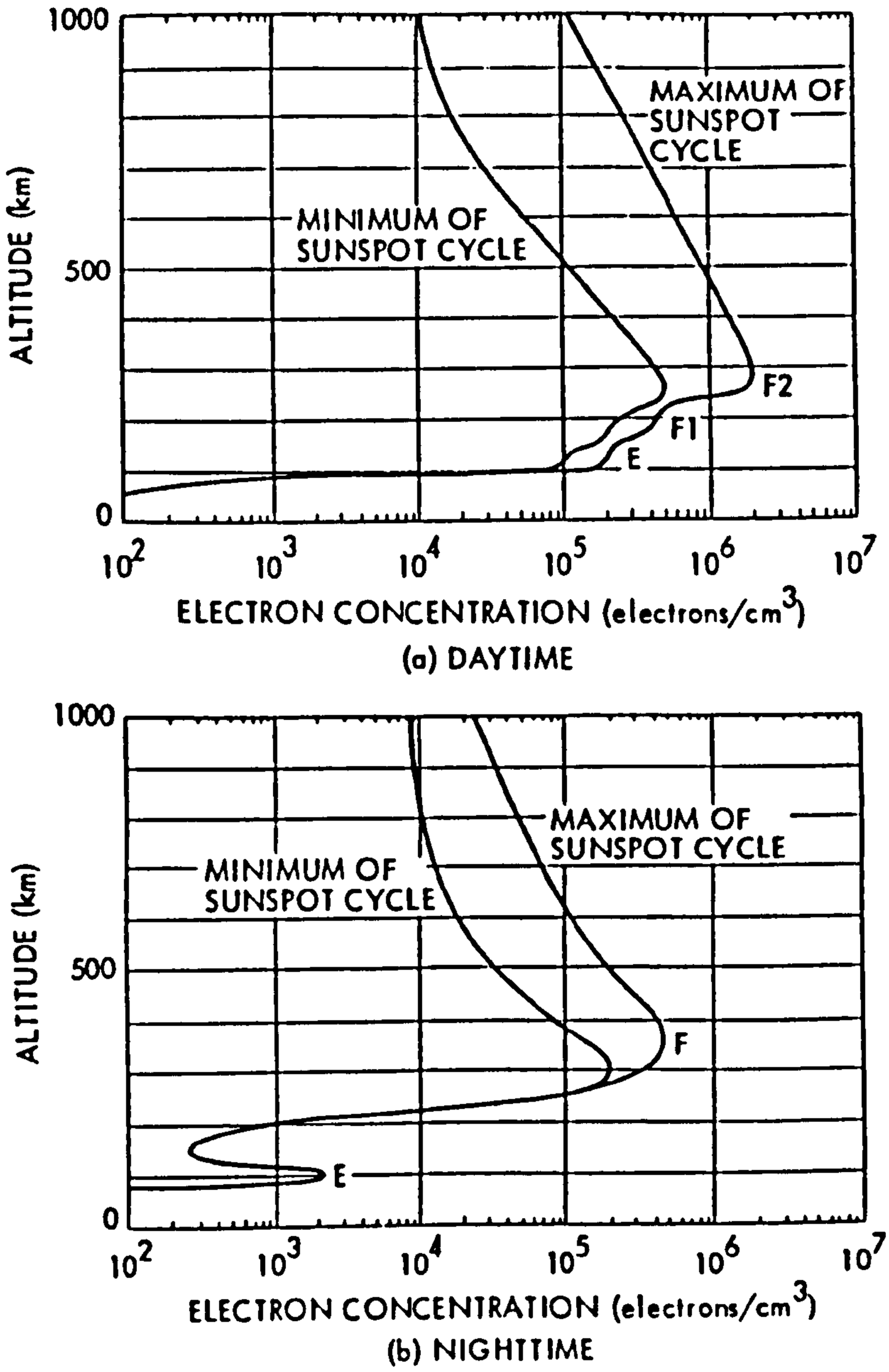

Figure 1.4 : Typical daytime and nighttime altitude profiles of electron density (after Hanson 1965). The nomenclature of the different altitude regions of electron density is also depicted.

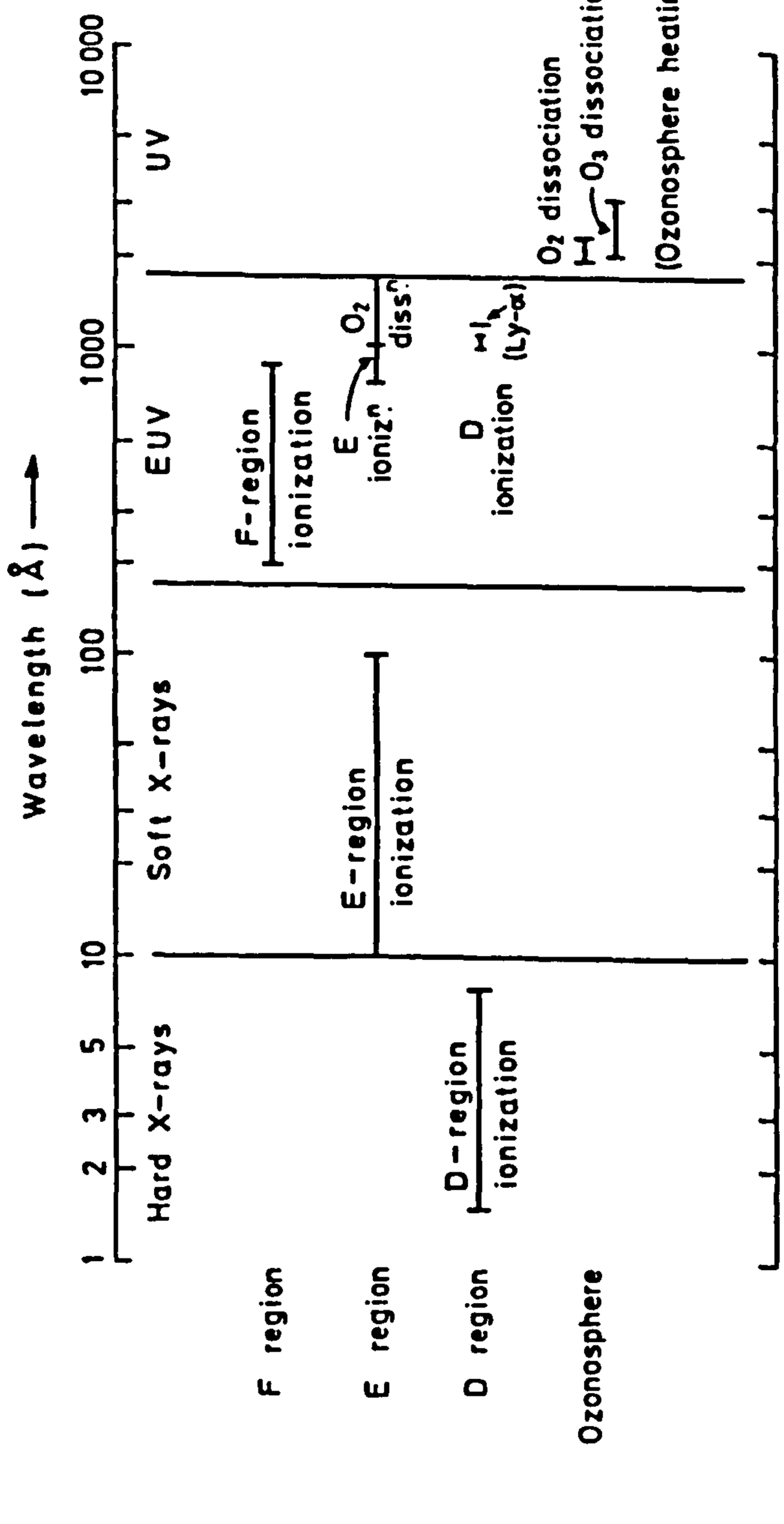

Figure 1.5 : The frequencies of solar radiation responsible for production of the different ionospheric regions (after Hargreaves 1979).

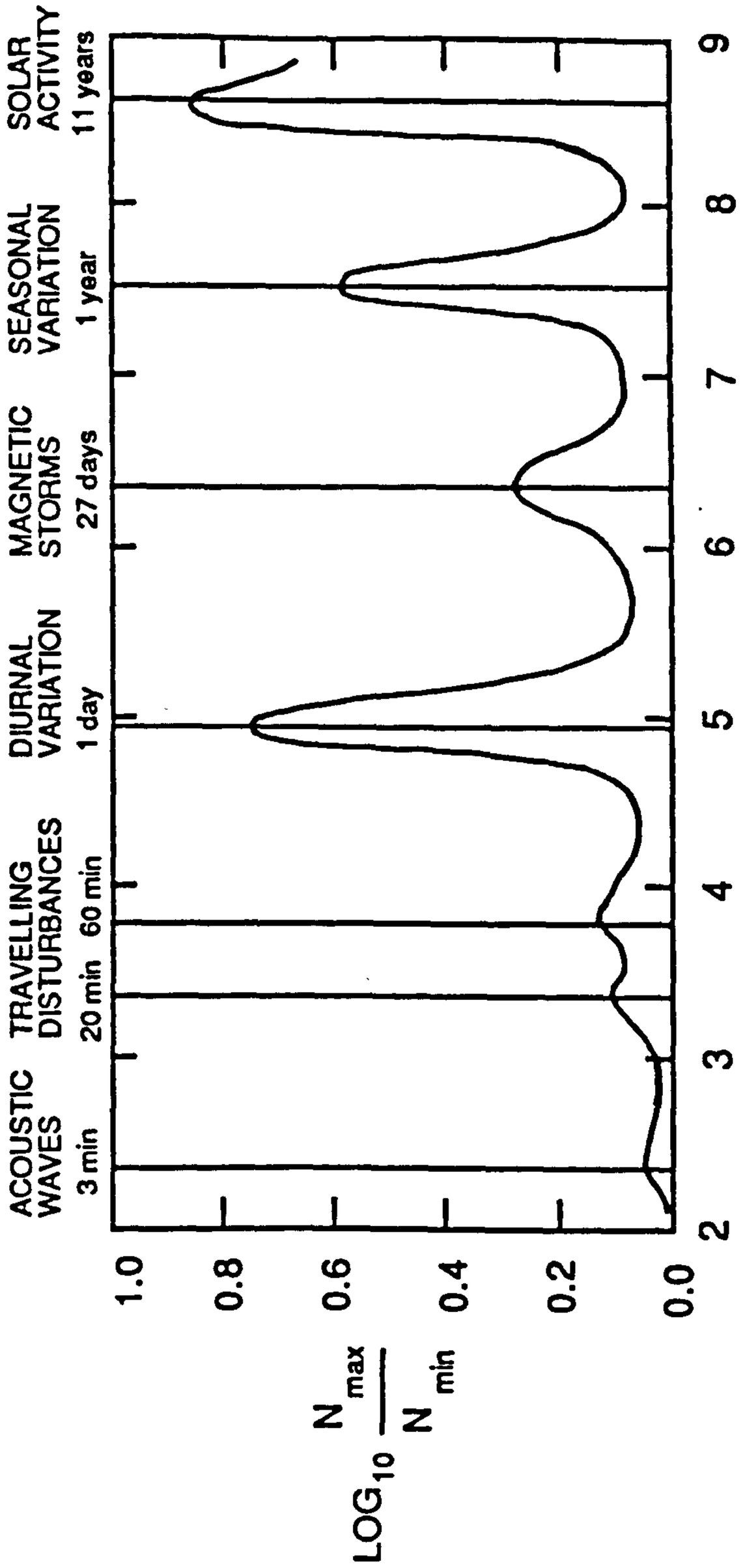

Figure 1.6 : A schematic illustration of the temporal power spectrum of electron density (after Georges 1968).

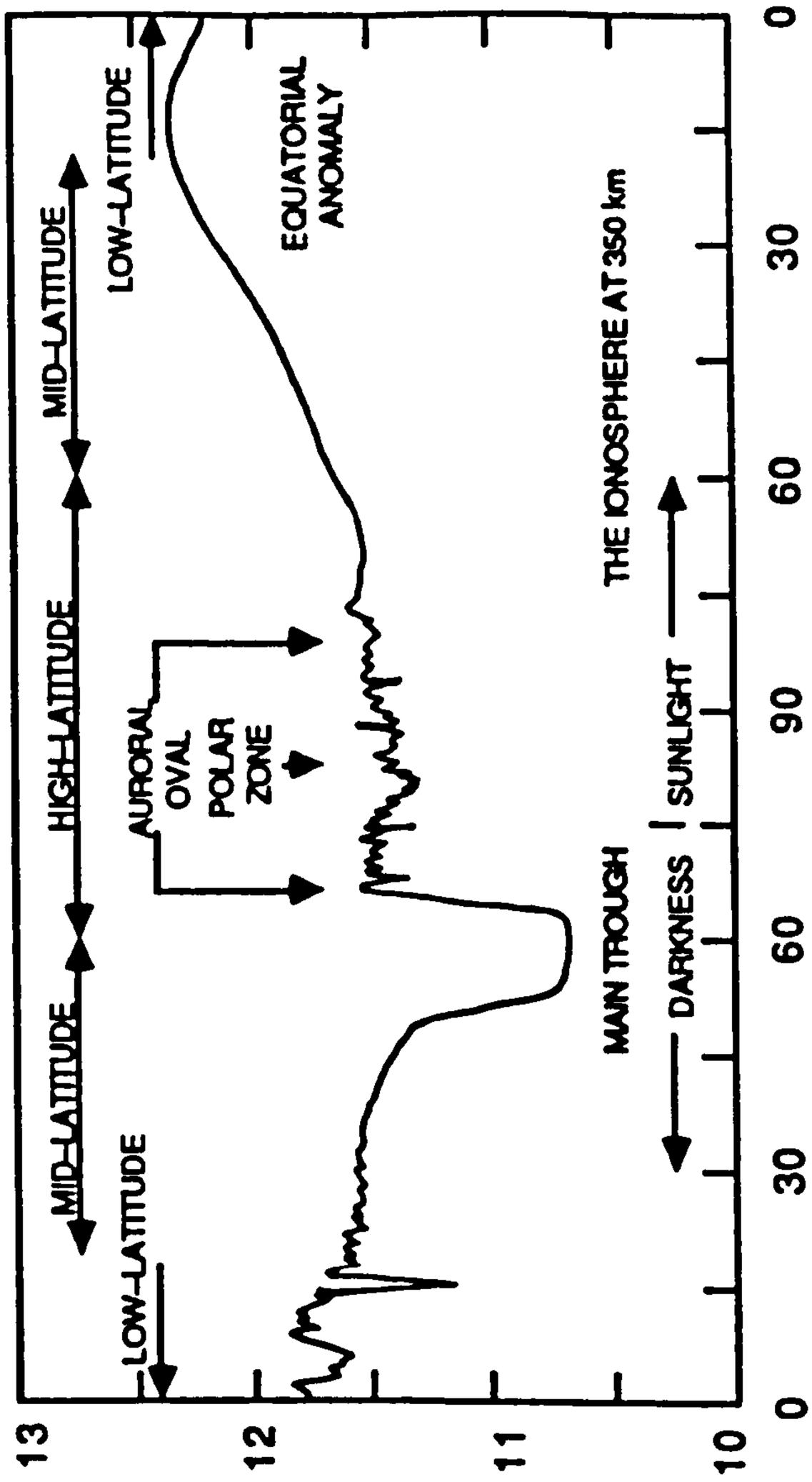

Figure 1.7 : A schematic illustration of the ionospheric electron density at an altitude of 350 km in the geomagnetic northern hemisphere (after Szuszczewicz et al 1983).

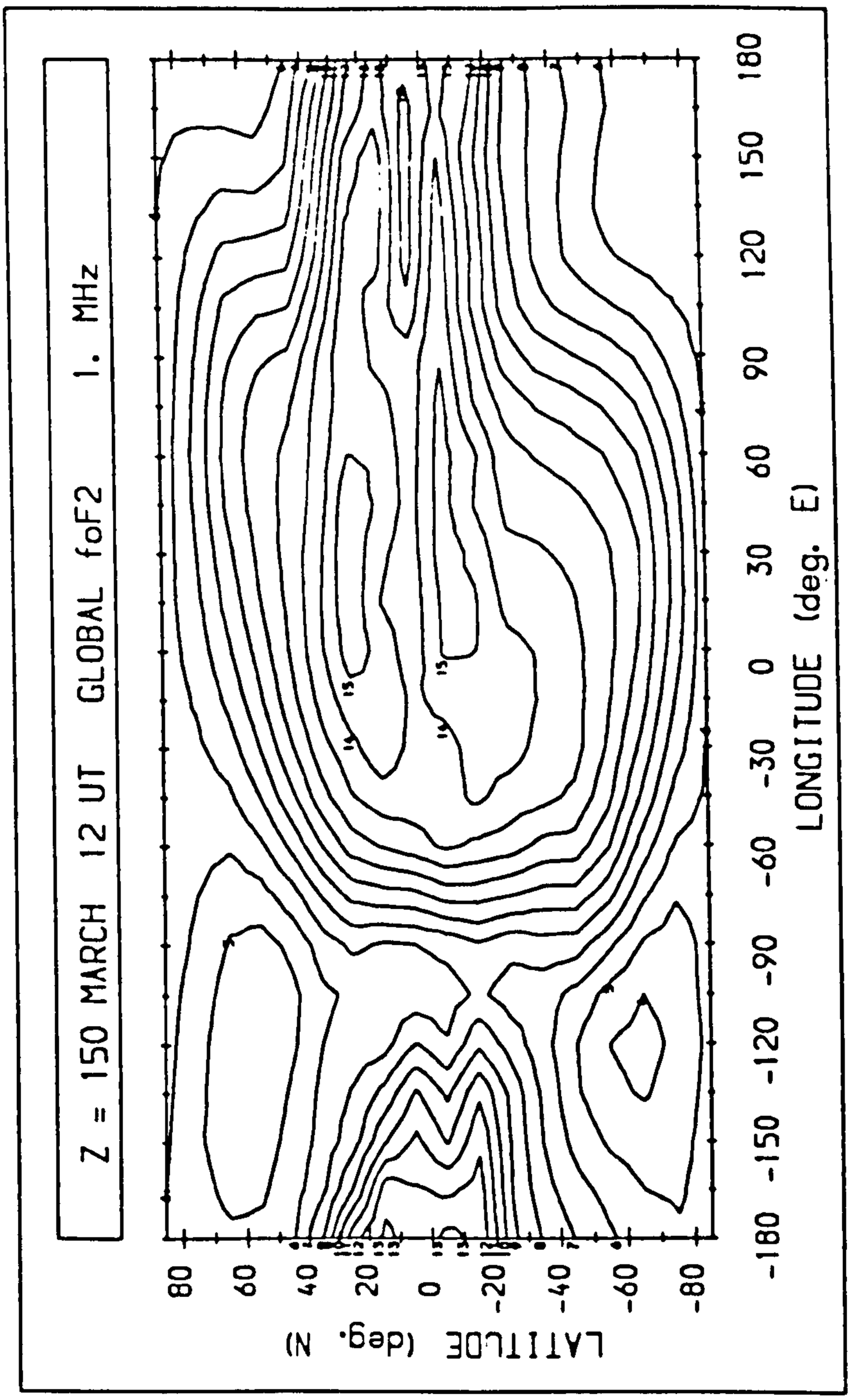

Figure 1.8 : A contour map of the monthly mean F2-region critical frequency as predicted from the CCIR Model at 12 UT during March for a sunspot number of 150. The contour interval is 1 MHz.

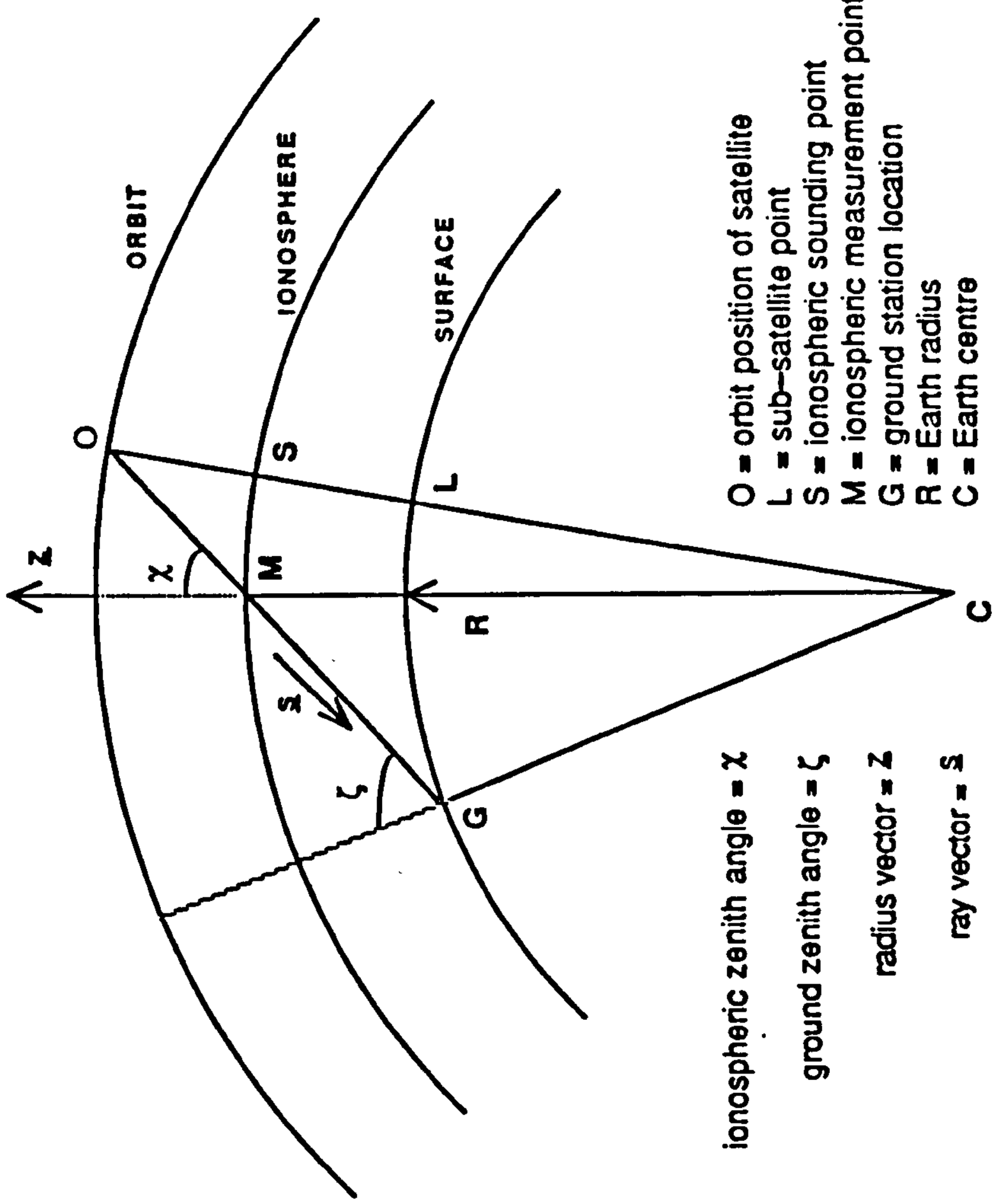

Figure 1.9 : An illustration of the terms and parameters associated with the reception of satellite transmissions along slant ray paths.

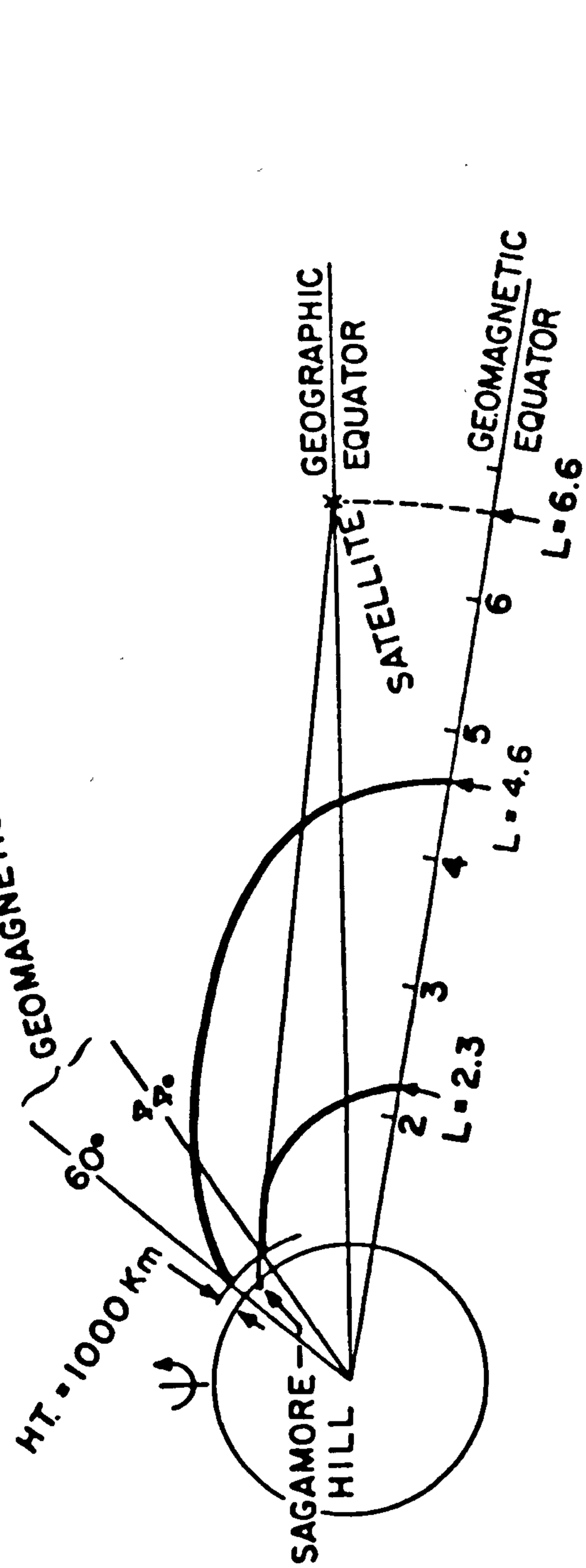

Figure 1.10 : The ray path of transmissions from a synchronous satellite in the meridian of Sagamore Hill (41°N,281°E) (after Klobuchar 1973).

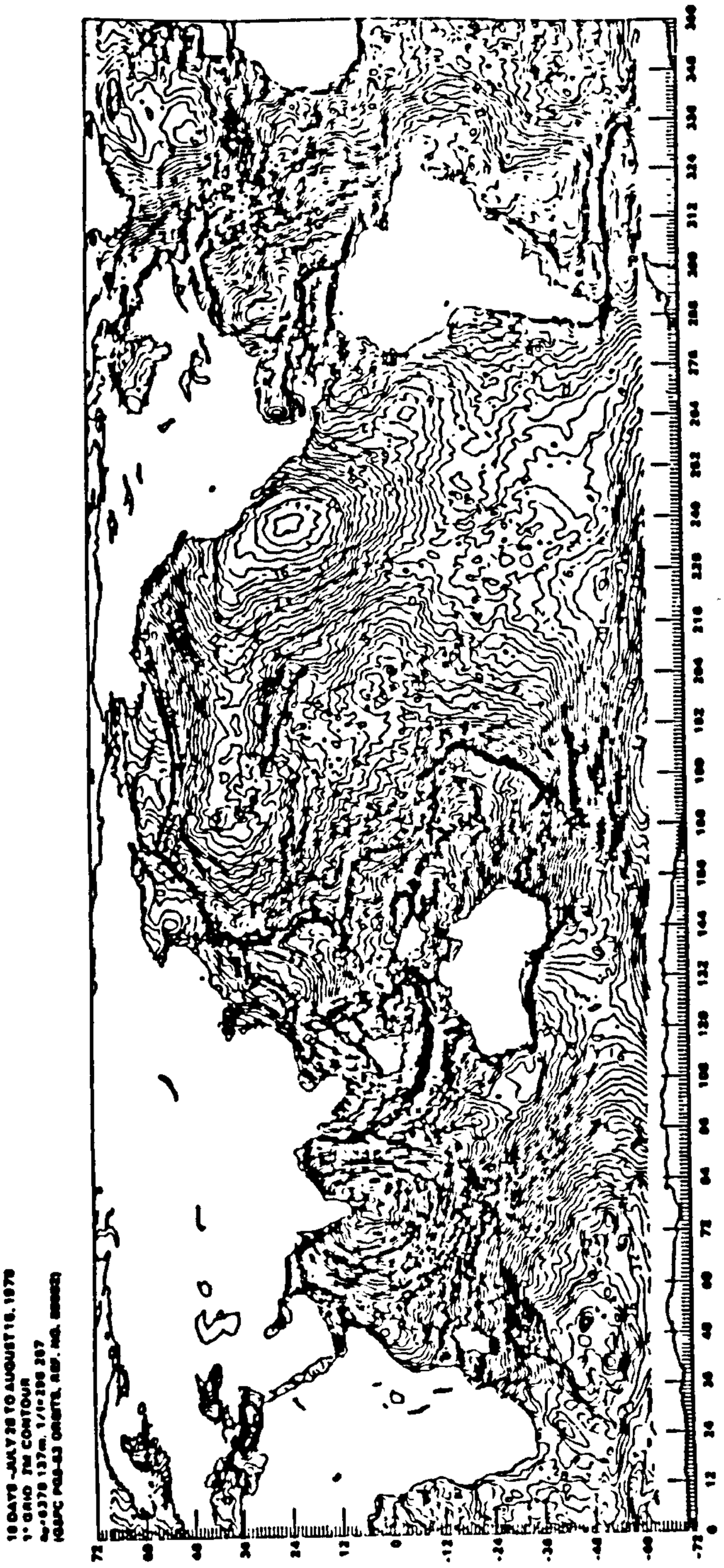

Figure 1.11 : The mean sea surface topography as measured from eighteen days of Seasat data (after Marsh and Martin 1982).

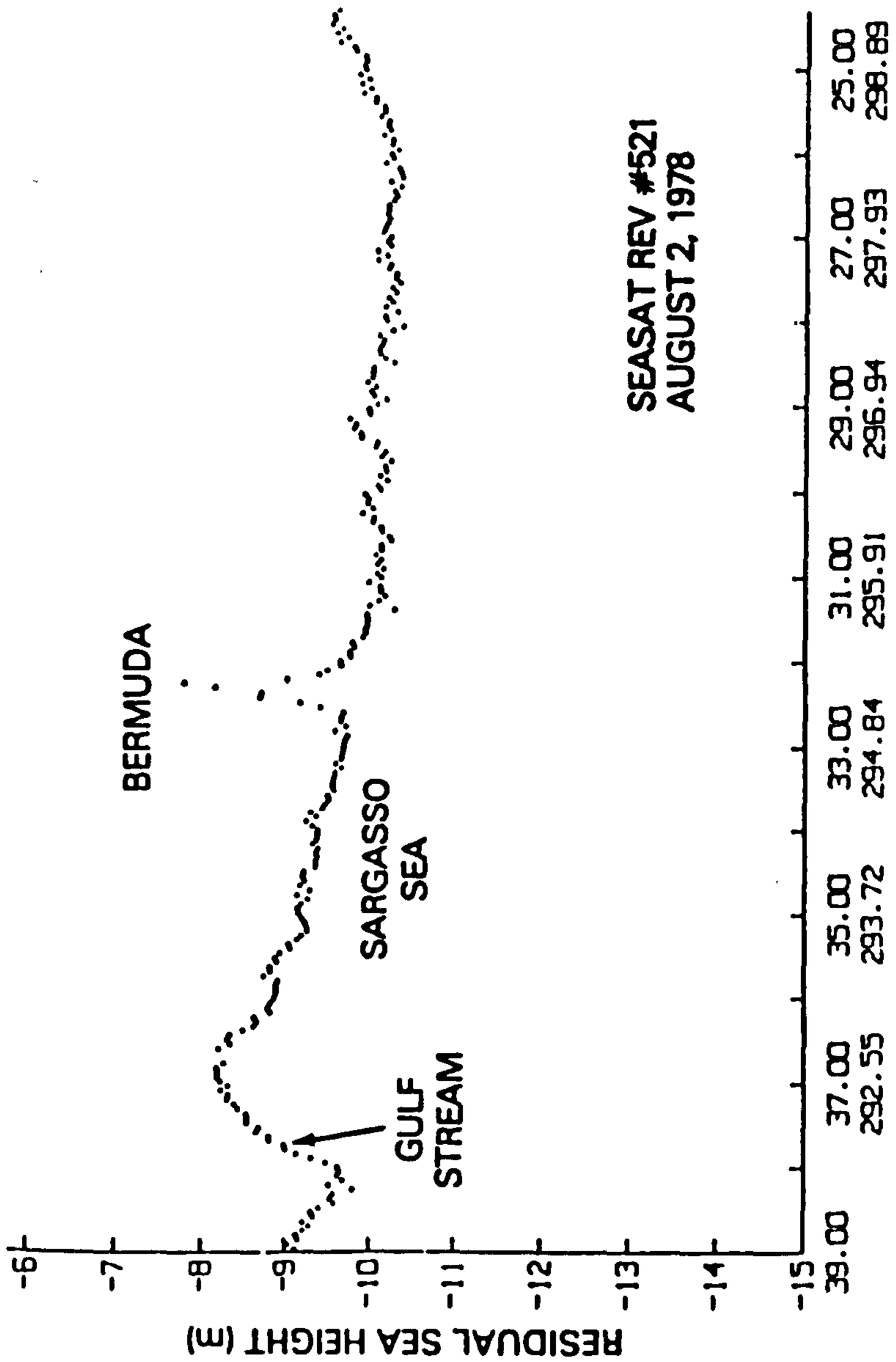

Figure 1.12 : The mean sea surface topography measured along revolution 521 of the Seasat mission (after Cheney 1982). The Gulf Stream is evident at 38°N.

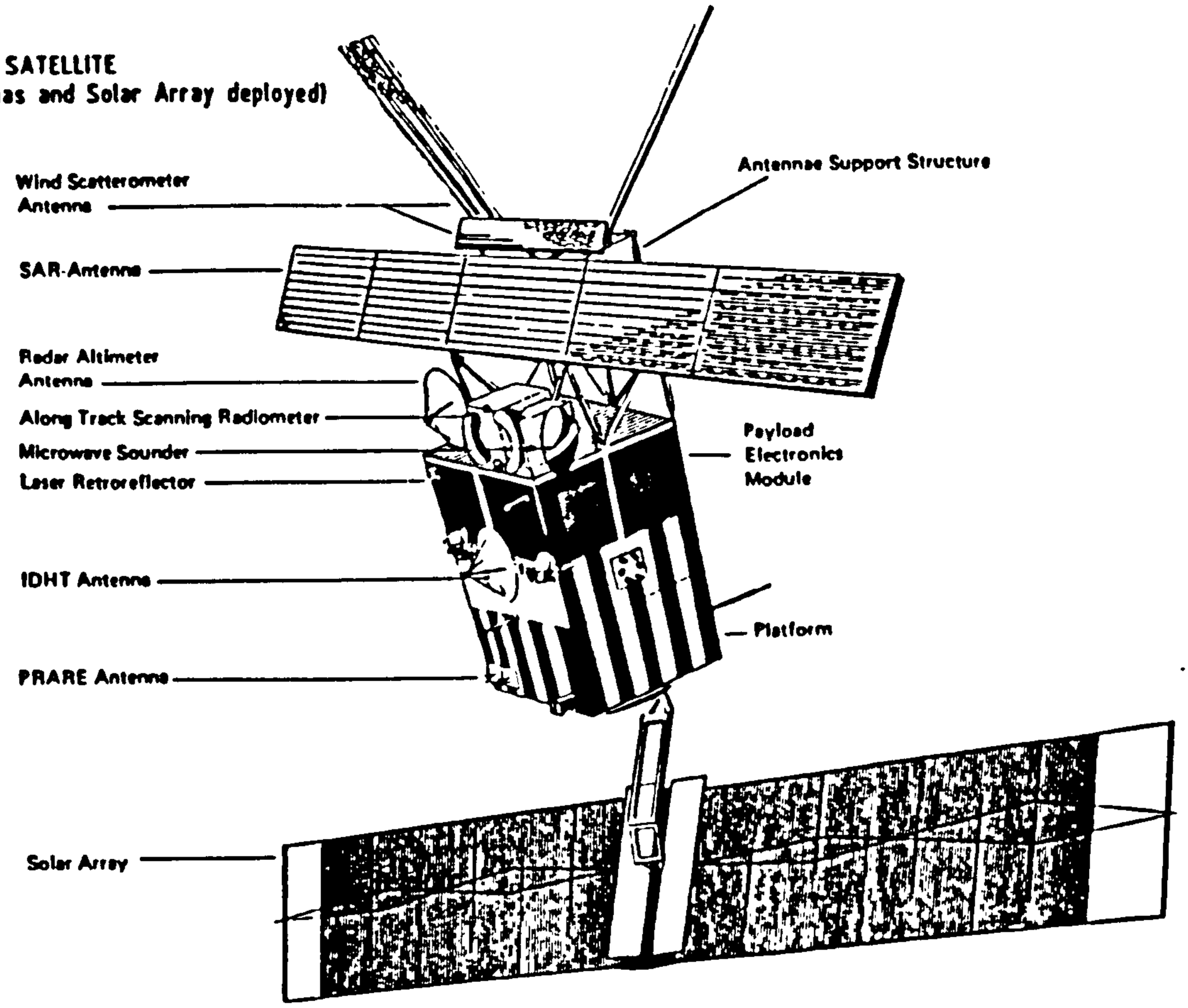

Figure 1.13 : An artist's impression of the ERS1 satellite and instrumentation package (after Velten 1984).

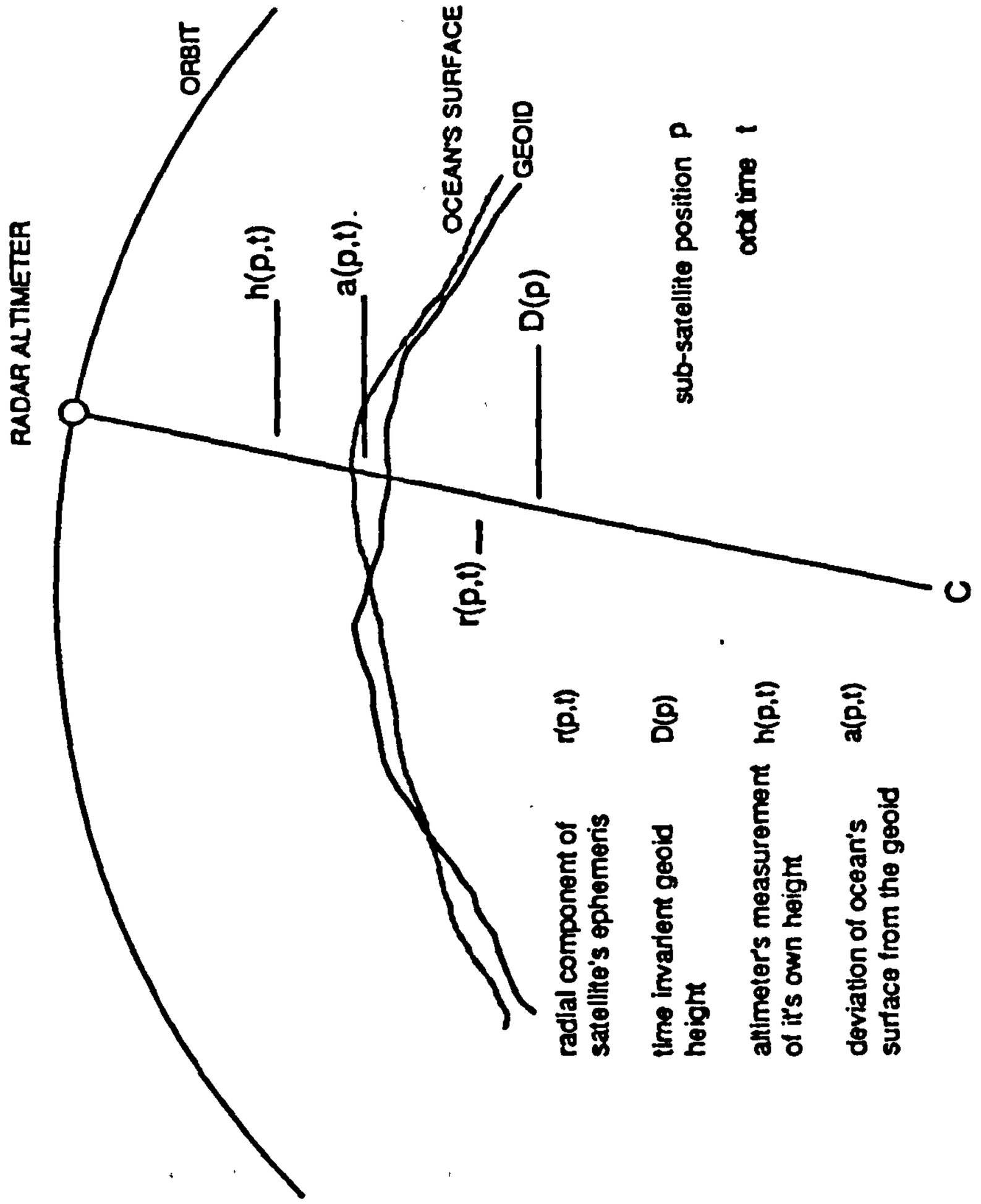

Figure 1.14 : An illustration of the terms and parameters associated with the remote sensing technique of satellite radar altimetry.

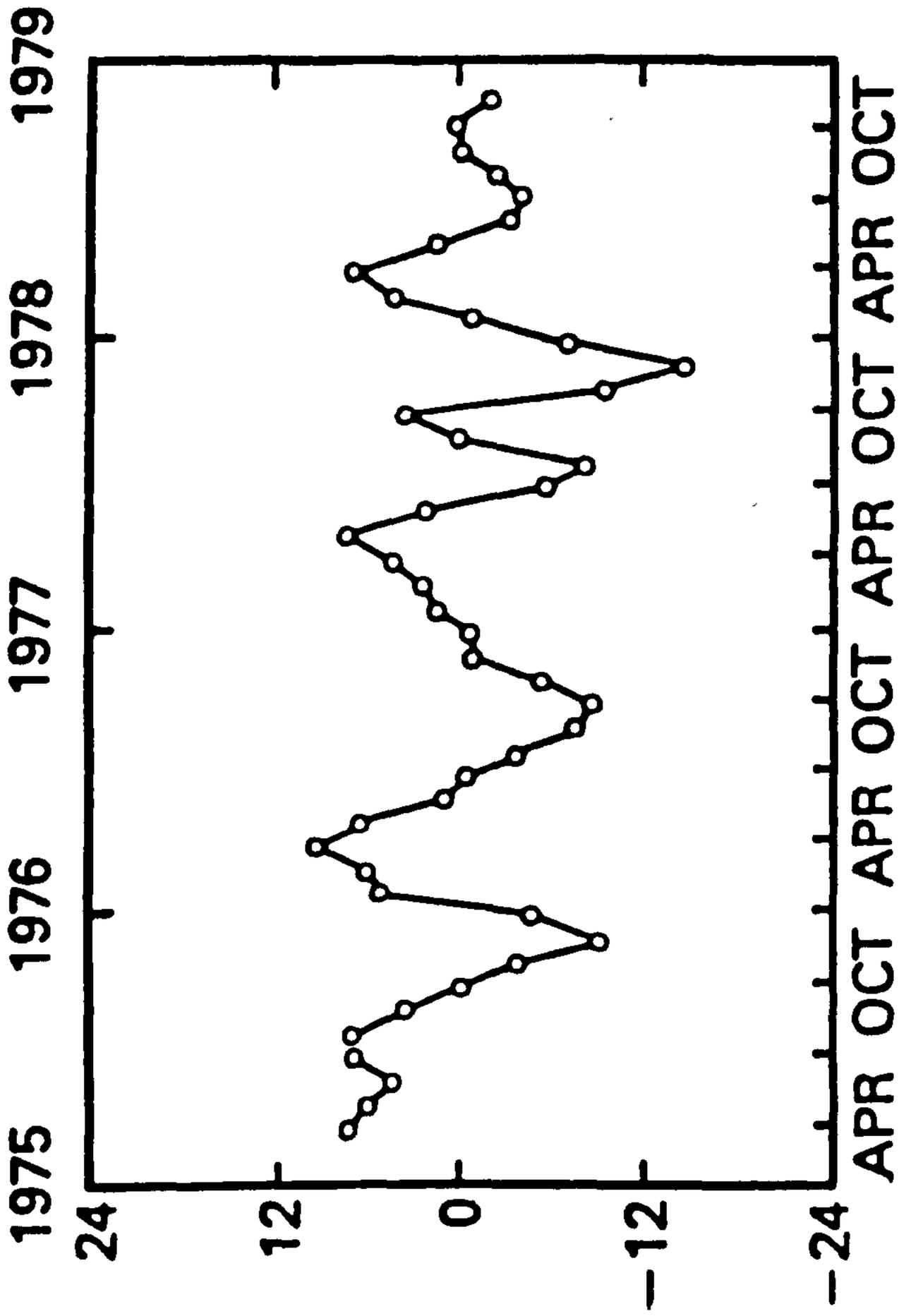

Figure 1.15 : The seasonal variation of the sea level difference between the southern and northern edges of the Gulf Stream (after Fu et al 1986).

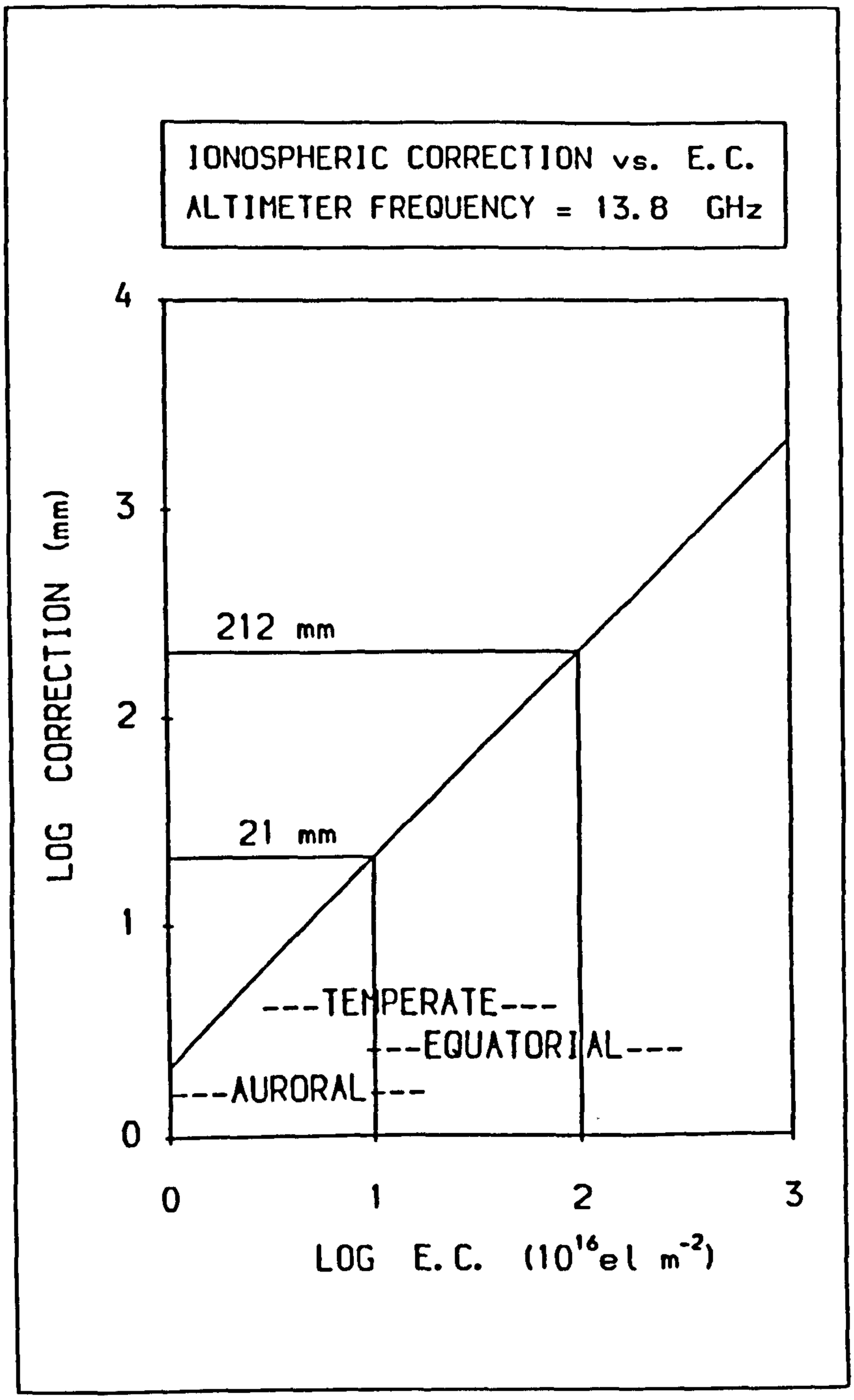

Figure 1.16 : The ionospheric corrections for the range of electron content likely to be encountered during the ERS1 mission (altimeter frequency 13.8 GHz).

SUBSTANCE		PERCENTAGE BY VOLUME
NITROGEN	N_2	78.09
OXYGEN	O_2	20.95
ARGON	Ar	0.93
CARBON DIOXIDE	CO_2	0.03
NEON	Ne	0.002
HELIUM	He	0.0005
METHANE	CH_4	0.0002
KRYPTON	Kr	0.0001
HYDROGEN	H_2	0.00005

Table 1.1 : The composition of the terrestrial atmosphere at ground level (Tennent 1971).

LAYER DESIGNATION	APPROXIMATE ALTITUDE RANGE (km)	APPROXIMATE DAYTIME ELECTRON DENSITY (m^{-3})
D–REGION	60 – 90	10^9
E–REGION	90 – 140	10^{11}
F1–REGION	140 – 200	5.10^{11}
F2–REGION	200 and above	10^{12}

Table 1.2 : The regions of the ionosphere with their altitude ranges and typical electron densities.

FREQUENCY BAND	RANGE	NORMAL PROPAGATION MODE
High Frequency (HF)	3 - 30 MHz	Reflection from E– and F–regions.
Very High Frequency (VHF)	30 - 300 MHz	Line of sight. Group delay. Ionospheric scintillation.
Ultra High Frequency (UHF)	300 - 3 000 MHz	Line of sight. Weaker scintillation and group delay.
Super High Frequency (SHF)	3 - 30 GHz	Line of sight. Weak scintillation and group delay.

Table 1.3 : The radio spectrum bands for frequencies between 3 MHz and 30 GHz.

COMPONENT	STATE	UNCERTAINTY OR CORRECTION (mm)
ORBIT	LAUNCH	2 000
	LAUNCH + 3 MONTHS	500
	BEST	100
TROPOSPHERE	DRY ATMOSPHERE COMPONENT	2 300
	WATER VAPOUR COMPONENT	0 – 380
IONOSPHERE	DAYTIME maximum	10 – 1100
	NIGHTTIME minimum	1 – 220

Table 1.4 : A comparison of the orbital uncertainties and atmospheric corrections involved in satellite radar altimetry.

Chapter 2 : Review of Previous Work

The foundation of the research reported in this thesis comprised 664 station months of electron content measurements taken over six years at ten northern hemisphere sites. These data allowed :

1. An investigation of electron content behaviour.
2. Calibration of a predictive and adaptive electron content model.
3. Calculation of the spatial and temporal coherence functions of electron content variability.

Before embarking on a description of these studies it is necessary to summarize the previous work which has been carried out in the above areas by other researchers. The sections below cover each of the above three areas in turn, although there is often some overlap due to their interdependence.

2.1 Electron Content Behaviour

2.1.1 Measurement Campaigns

The calculation of ionospheric electron content from measurements of the Faraday rotation on signals from the radio beacons of artificial satellites dates from the early days of the space age. The earliest studies were carried out with the USSR Sputnik series and the USA Explorer series of low-orbiting satellites (Garriott 1960). These satellites had some severe disadvantages for the observation of electron content; only two or three measurements a day could be made at a particular site and their rapid motion past the measuring equipment made data interpretation difficult and confused spatial and temporal effects.

Garriott and Little (1960) proposed that the radio beacons mounted on geostationary satellites, which orbit in the equatorial plane of the Earth at an altitude of approximately 35 800 km, should be employed for ionospheric research. Since synchronous satellites hold station over a particular point on the Earth's surface they have the capability to monitor continuously the ionosphere at an

invariant point and they therefore avoid the problems associated with low–orbiting radio beacons. Early experiments were recorded by Garriott et al (1963) with the Syncom III satellite and by Klobuchar and Whitney (1965) with the Early Bird satellite. A fuller account of the early history of satellite beacon studies of the ionosphere is given by Rawer (1983).

A review of the Faraday rotation technique was presented by Titheridge (1972). Under most conditions Faraday rotation was demonstrated to allow calculation of electron content below an altitude of 2 000 km to an accuracy of ±5%. It was also demonstrated that a fixed value of the geomagnetic field–factor, as described in Equation 1.9, could be employed for geostationary satellite measurements. This simplifies greatly the calculation of electron content data from polarization measurements. Previous researchers found values of electron content could be described more conveniently by defining an electron content unit (ecu) equal to 10^{16} electrons per square metre and this convention will be adopted here.

The relative simplicity of the Faraday rotation technique for measuring electron content from geostationary satellite transmissions has ensured its popularity right up to the present day. A review of the technique and the scope of possible research was given by da Rosa (1974). The technique is suitable for all locations except those at polar latitudes and so has been employed at many sites by many different researchers to study the electron content of the ionosphere. Investigations have been made of diurnal and seasonal variations and of solar and geomagnetic influences. Some of the more recent publications on electron content behaviour are summarized below.

In North America electron content has been monitored at Goldstone, California by Green et al (1980), at Sagamore Hill, Massachusetts by Hawkins and Klobuchar (1975), at Boulder, Colorado by Davies et al (1976), at Fort Monmouth, New Jersey by Soicher and Gorman (1985), at Lorman, Mississippi by Paul (1982), at Anchorage, Alaska by Soicher (1985) and at Thule, Greenland by Mendillo and Klobuchar (1973). In the European sector data taken in the United Kingdom have been analyzed by Huang (1983) and long term measurements taken at Neustrelitz between 1976 and 1980 have been discussed by Jakowski and Paasch (1984). In the Middle East, at Haifa, Israel, the structure of electron content has been discussed by Soicher et al (1982) and at Athens, Greece by Soicher et al (1984). On the Indian sub–continent measurements of electron content spanning half a solar cycle taken at Delhi have been analyzed by Bhuyan et al (1983) and by Bhuyan and Tyagi (1983). In the Far East three years of measurements have been collected at Lunping, Taiwan by Huang (1981). Minakoshi and Sinno (1985) have described the characteristic variations of electron content with the use of

seven years of data collected during solar cycle 21 at Tokyo, Japan. In the southern hemisphere fewer measurement campaigns have been undertaken. McNamara and Smith (1982) measured the electron content at Sydney, Australia for seven years of solar cycle 20, Essex (1978) monitored the electron content from Melbourne between 1971 and 1974 and Tyagi et al (1982) reported observations of electron content made over twelve months at Natal, Brazil.

2.1.2 Mean Behaviour

A succinct representation of the diurnal and seasonal variation of the electron content at Goldstone, California (35°N,243°E) through a year of high solar activity was given by Green et al (1980) and is reproduced as Figure 2.1. The illustration deserves close analysis since it summarizes concisely the behaviour of electron content on both diurnal and seasonal time scales. The diurnal variation shows low nighttime electron contents below 10 ecu. At sunrise the electron content starts to increase and continues to do so until just after midday. An almost constant level is maintained for approximately two hours and a decline begins in the late afternoon with the nighttime value being reached at about 22 hours Local Time (LT). A similar behaviour is found for every month, though the amplitude of the diurnal variation is distinctly dependent on the season. The amplitude is greatest for the equinoctial months (the semi–annual anomaly), the maximum electron content being approximately 80 ecu. The amplitude is least for the summer months (the seasonal anomaly) giving a maximum electron content less than half that of the equinoctial value of approximately 30 ecu. The amplitude in December is greater than that in June (the annual anomaly) with monthly average maxima of around 60 ecu.

The monthly mean diurnal variations of electron content measured by Soicher et al (1984) during 1980 at Haifa, Israel (33°N,35°E) are reproduced as Figure 2.2. The Local Time behaviour of electron content is broadly similar to that found at Goldstone with maximum daytime values occurring at the equinoxes and minimum daytime values during the summer.

Observations made between 1967 and 1973 at Sagamore Hill, Massachusetts (41°N,281°E) by Hawkins and Klobuchar (1975) found electron content to have a close correlation with solar activity. Again the seasonal variation of the daytime electron content exhibited maxima in the equinoctial seasons and a minimum in summer. The seasonal variation of the nighttime minimum was also found to have a maximum in the summer months. Similar conclusions were reached by Minakoshi and Sinno (1985) from observations made at Tokyo between 1977 and 1984.

The behaviour of electron content with regard to the solar cycle has also been investigated by Huang (1978) with data from the mid–latitude site at Sagamore Hill. The monthly mean values of electron content for eight Local Times were plotted for each month in the period from November 1967 to the end of 1976 which covered sunspot numbers from above 100 to below 20. The variations of the monthly mean and twelve–month running mean electron content at the chosen Local Times are reproduced as Figure 2.3, which also shows the sunspot numbers prevailing during the measurement period. The increase in electron content with solar activity is evident from the twelve–month running mean representation and is more pronounced for daytime values. For all Local Times a correlation coefficient of greater than 0.94 was found between the twelve–month running mean electron content and the smoothed sunspot number. The correlation coefficient between the monthly average electron content and the smoothed sunspot number was between 0.7 and 0.85. The lower values in this range are due to the seasonal variation in the monthly average electron content which is not present in the smoothed sunspot number. As the solar activity declined so the seasonal variation in electron content became less distinct and the unsmoothed monthly data show an apparent, rather than a true, seasonal variation because of this. Nevertheless, some important conclusions for the seasonal variation can still be drawn, the principal ones being in agreement with the findings of Soicher et al (1984) and Green et al (1980).

The seasonal anomaly was found to be absent from observations made between 1971 and 1974 at Melbourne (37°S,145°E) by Essex (1978). It was suggested that the annual and seasonal anomalies in the southern hemisphere cancelled out at this location, leaving the semi–annual anomaly to dominate. In support of the observations of Minakoshi and Sinno (1985) a maximum of the midnight electron content was also found for the summer months. The solar cycle and Local Time variations were found to be similar to those at a northern hemisphere site.

Mendillo and Klobuchar (1975) employed a network of six Faraday rotation receiving stations near the 290°E meridian to monitor the electron content over 34°–73° invariant latitude. A similar attempt to describe the electron content over a wide range of latitudes was made by Soicher and Gorman (1982) who employed Faraday rotation measurements from six stations to deduce the latitudinal, seasonal and solar cycle dependence of electron content.

The latitudinal structure of electron content was described by Mendillo and Klobuchar (1975) via contour maps made up from electron content data collected at six sites and interpolated in latitude and Local Time. The representation of monthly mean electron content for December 1971 is reproduced as Figure 2.4. The solar control of ionospheric electron content can be seen in the

diurnal variation and the fall off of in magnitude towards higher latitudes. A North–South gradient in nighttime electron content can be seen at invariant latitude 50°N running into the Main Trough which separates the mid– from the high–latitude ionosphere. The electron content reaches a minimum between 03 LT and 06 LT around the latitude of Goose Bay; this is the Main Trough revealed through its depleted electron content.

Wolff (1985), employing data from Boulder, Colorado (40°N,255°E) and Urbana, Illinois (40°N,272°E), correlated the maximum electron content with the difference between that maximum and the minimum value of each day over two solar maximum months and two solar minimum months. In all cases correlation coefficients of greater than 0.93 were found implying that the solar activity level exerted a strong influence on the magnitude of daytime electron content. This compares well with the 0.94 correlation coefficient of the twelve–month running mean maximum electron content with the twelve–month running mean sunspot number found by Huang (1978).

2.1.3 Disturbed Behaviour

The variability of electron content about its mean level is important for models which attempt more accurate predictions than the monthly mean. An analysis by Johanson et al (1978) of the distribution of the differences from the monthly mean of the daily electron content at Hamilton, Massachusetts during June 1971 formed a well defined Normal distribution which is reproduced as Figure 2.5. The monthly mean diurnal variations of electron content for March under solar maximum and minimum conditions are plotted in Figure 2.6 with their associated standard deviations as error bars. The standard deviations are larger in absolute terms by day but are larger in relative terms at night.

Fluctuations of electron content resulting from short term increases of solar or magnetic activity are a major cause of error in model ionospheres. Ogawa and Ohbu (1986) linked bursts of euv and soft X–rays from solar flares with sudden increases in ionospheric electron content. Jakowski et al (1986) also concluded that sporadic solar activity was the dominant causal mechanism for irregular ionospheric behaviour. From studies of nighttime enhancements of electron content measured at Cuba during solar cycle 21 the occurrence probability of disturbed conditions was found to depend significantly on the prevailing level of solar activity.

Geomagnetic activity exerts a strong influence on the ionospheric F–region and is characterised by short term fluctuations of the geomagnetic field. Essex (1979) crosscorrelated electron

content data collected at Melbourne with the two geomagnetic indices ΣKp and AE which quantify the geomagnetic fluctuations (Hargreaves 1979). Plots of the time lag to maximum coherence against Local Time suggested a preferred Local Time for the onset of the manifestation of a geomagnetic storm in the ionosphere. This is supported by the findings of Mendillo (1973) who suggested that an enhancement of electron content would occur during the afternoon following the commencement of a storm.

Geomagnetic storms generally deplete the ionospheric plasma though often this is preceded by a short–lived enhancement. According to Mendillo and Klobuchar (1975) the positive phase of a storm is due to upward convection of the plasma during the noon–dusk period to regions where the loss rate is lower, thus increasing the electron density and, therefore, the electron content. After 18 LT the direction of the plasma drift reverses and there is a rapid return to nighttime values. The sustained negative phase which follows over the next few days is due to an increase of the concentration of molecular nitrogen in the F2–region which increases the rate of recombination loss. A latitudinal chain of receiving sites was employed to investigate the influence of a geomagnetic storm on electron content morphology. The measurements taken on the 17th and 18th December 1971 are plotted in Figure 2.7 and illustrate the differences in response to the storm at four stations located near the 290°E meridian. The Hamilton site monitored a rapid enhancement over the six hours following the storm commencement of over 300% of the monthly average. An increase of 50% was recorded at the Goose Bay site, though only small increases were seen at Narssarssuaq (61°N,315°E) and Thule (77°N,291°E). The spatial and temporal irregularity over the two days can be easily discerned from Figure 2.7.

Particularly variable regions of the ionosphere are the auroral zones where geomagnetic field lines extend out into the magnetosphere allowing energetic particles from the solar wind to become a significant source of ionization. During 1984 Lambert and Cohen (1986) observed the electron content from Macquarie Island (55°S,159°E) using the Faraday rotation of geostationary satellite signals. A depression of nighttime electron content was observed when the ray path from the satellite to the ground passed through the Main Trough of the southern hemisphere. Large scale fluctuations of electron content were seen in the data as a result of auroral activity. A second station at Melbourne observed similar fluctuations, though delayed by such a time so as to attribute a speed of between 200 and 1 000 ms^{-1} to the disturbances. These speeds are wholly consistent with the theory that the disturbances are caused by travelling ionospheric disturbances (TIDs), the ionospheric manifestation of atmospheric gravity waves, propagating from the auroral zone to mid–latitudes. TIDs have also been observed in the northern auroral

zone by Hunsucker and Hargreaves (1988) who monitored the SMS1, ATS1 and ATS6 synchronous satellites from Fairbanks, Alaska (65°N,148°E) between 1978 and 1981. Quasi–periodic oscillations in the electron content were found to be present for more than 98% of daylight hours and were thought to be associated with geomagnetic activity.

2.1.4 Influence on Altimetry

The effect of ionospheric fluctuations on altimeter measurements has been summarized by Callahan (1984) who considered the effects of large and small scale variations and took the dividing line between such events as 500 km or 1 hour. The large scale features were those that a predictive model could hope to account for on a monthly mean basis. The Main Trough and Equatorial Anomaly were singled out as special large scale features which could disrupt radar altimetry. Small scale irregularities are often found in auroral and polar regions as evidenced in electron density by Figure 1.7. It was suggested that the day–to–day variability of large scale features and small scale fluctuations could be compensated for by an adaptive model of electron content.

The strong influence of solar activity on the behaviour of the electron content makes it important to have an idea of the conditions prevailing, or expected to prevail, for times when predictions are required. Since the ERS1 mission is due to fly during the peak of solar cycle 22 it is necessary to have a reliable prediction of the levels of solar activity which might be expected for that epoch. The sunspot number is a very difficult quantity to predict, though Schatten and Sofia (1987) suggested that the magnitude of cycle 22 will be similar to that of cycle 21. Using dynamo theory a twelve–month running mean sunspot number of 170±25 was predicted for the peak of cycle 22 which can be compared with 165 at the peak of cycle 21. The predictions are reproduced in Figure 2.8 which also shows the proposed duration of the ERS1 mission and also that calibration data was available from times with similar high levels of solar activity.

2.2 Electron Content Modelling

A general review of the potential problems involved with trans–ionospheric propagation as a result of the group delay of electromagnetic waves was given by Klobuchar (1976). Electron content models to compensate for these effects can be either theoretical or empirical in nature. Theoretical modelling involves the numerical solution of the Equation of Continuity, whereas empirical models are essentially succinct mathematical descriptions of experimental data.

Advantages of theoretical models, such as the Anderson Model (Anderson and Klobuchar 1983 and references therein), are that they are ideal for testing the response of output variables to changes in the input parameters such as sunspot number and are valid for all levels of solar and geomagnetic activity and in all ionospheric regions. Another advantage is that they can be employed to interpolate measurements to regions where further measurement is impossible, for instance Rush et al (1983 and 1984) extrapolated ionosonde data to the ionosphere above the oceans in an attempt to improve the CCIR maps of foF2. However, weighed against their flexibility, theoretical models require large amounts of supercomputer time and as such they are expensive and not commonly available to researchers. Empirical models are based on statistical ionospheric behaviour and, compared to theoretical models, are mathematically simpler and require far fewer input parameters. Consequently, empirical models are favoured when frequent values of ionospheric parameters are required on a worldwide basis. General summaries of the capabilities and limitations of ionospheric predictions have been given by Klobuchar (1980) and Davies (1981).

Although several models of electron content have been developed which could be employed to generate predictions of electron content (for example Ching and Chiu (1973), Klobuchar (1975), Köhnlein (1978)) only models which have a documented history of success in this field will be considered. In practice this restricts discussion to the International Reference Ionosphere, the Bent Model and the Jet Propulsion Laboratory Model.

The International Reference Ionosphere (IRI) was established by the Union Radio Scientifique International (URSI) and the Committee for Space Research (COSPAR) to produce a standard model of the fundamental ionospheric parameters (Rawer et al 1978). The aims of the model were to represent the mean spatial and temporal behaviour of the electron density, composition and temperature of the ionosphere. The model is a world standard and undergoes continual revision (for example Bilitza 1986). The IRI generates the electron density profile which, when height integrated, yields the electron content. So far only data from periods when the sunspot number has been below 130 has been included and the model has not been calibrated with data from auroral or polar regions which casts doubt on its efficacy during more active times and at high–latitudes, neither does the model admit an allowance for geomagnetic activity.

The Bent Model of electron content (Llewellyn and Bent 1973) was developed with the intention of providing the community of users who rely on trans–ionospheric radio propagation with a flexible model to compensate for the group delay effect of the ionosphere on various electromagnetic systems such as radio telescope interferometers and satellite–to–satellite

ranging systems. Over 400 000 bottomside and 60 000 topside soundings went into its construction. The formulation of the Bent Model is relatively simple; the bottomside is represented by a biparabolic curve and the topside by a series of regions where the electron density decays exponentially, the top and bottomside regions are linked, above the peak, by a fitting parabola which ensures continuity in the altitude gradient of electron density. Electron content is then given by analytical integration to the required altitude. The electron content of the E– and F1–regions is included in the single bottomside layer. Calibration was performed with ionosonde and satellite data whose coverage included the auroral zone, but only for times when the sunspot number was below 110. As with the IRI no allowance for magnetic activity is made.

The Jet Propulsion Laboratory (JPL) developed an electron content model to account for ionospheric effects on the Deep Space Tracking Network, the primary navigation system for interplanetary probes such as the Pioneer and Voyager spacecraft. Rather than scale and integrate an empirical profile the JPL Model calculated electron content directly (Lorell et al 1982). A predetermined global morphology of electron content was scaled with electron content data from at least one monitoring station which, in effect, extrapolated the measurements around the globe.

The three empirical models described above are less accurate than the Anderson theoretical model and neither can allow for short–term ionospheric fluctuations or magnetic disturbances. The IRI and Bent Models are keyed to an indicator of solar activity which must be provided before predictions can be generated. Equivalently, the JPL Model requires at least one source of electron content data in order to function. An interruption of these driving parameters would cause severe degradation of these models. However, compared to a theoretical model, the empirical models need fewer input parameters and require much less computing power and as such are more suitable to the task of developing an ionospheric correction algorithm for radar altimetry mission.

Most empirical models are based upon the CCIR maps of foF2 and the 3 000 km F2–region propagation factor M(3000)F2. The maps are derived from vast quantities of ionosonde data collected during solar cycle 19. The accuracy of the CCIR Model has been investigated by King and Slater (1973) who employed monthly mean ionosonde data from Port Stanley (52°S,302°E) and Lindau (52°N,10°E) covering a wide range of solar activity. The average error of foF2 predictions was 9%, the lowest values of 4% occurring during summer and the largest of 16% occurring during winter. The time of greatest uncertainty was around dawn. The quartile range of the monthly data was, on average, twice as great as the errors of the monthly mean prediction

which implied that more accurate predictions could be more easily obtained by the inclusion of local measurements than by an increase in the accuracy of the model.

Employing data from the ISS b topside sounder satellite Wakai and Matuura (1980) produced maps of foF2 for five periods between August 1978 and June 1979. The comparison with the CCIR Model was good in the northern hemisphere. In the southern hemisphere, though, there was a tendency for values of foF2 derived from the CCIR Model to differ from those measured by ISSb. Over South America and the southern Atlantic Ocean the CCIR values were greater than those of ISSb, with the reverse situation over the southern Pacific Ocean. Nonetheless, these differences were not sufficiently large to cast doubt on the usefulness of the CCIR maps to act as the basis of empirical electron content models.

As an international standard the International Reference Ionosphere has been investigated extensively. A particular strength of the IRI model is considered to be its realistic altitude profile of electron density. The comparison of electron content predicted from the model with measured values coupled with ionosonde data can provide a good test of the accuracy of the profile. This work has been undertaken by McNamara and Wilkinson (1983) who compared IRI electron content predictions with data from Sydney (34°S,151°E) and ionosonde data from Brisbane (27°S,153°E) from a year of high and a year of low solar activity. Discrepancies of 20–50% were noted and it was explained that, since these were not due to errors in the predictions of the model's peak parameters, the profile figure was, to some extent, incorrect.

The investigation was followed up by McNamara (1984) in a more general survey with data from fifteen widely dispersed stations, six of which were situated conveniently close to ionosonde sites. The IRI Model was found to give good predictions at mid– and high–latitudes during all seasons for both high and low solar activity. The predictions were of similar accuracy when the peak parameters were given from either monthly mean ionosonde data or predicted from the CCIR Model. At low–latitude sites, however, severe underestimations of daytime electron content were observed and comparison with ionosonde data again demonstrated this not to be due to prediction errors of the CCIR Model. A comparison with the Anderson theoretical model for a low–latitude station revealed the IRI Model profile to be too thin to reproduce the high electron content.

The Bent Model was validated by its developers (Llewellyn and Bent 1973) with 100 station months of electron content data which covered times with sunspot numbers of up to 110. The

model was able to reproduce monthly average electron content data with accuracies of 75–90%. A comparison of electron content predictions from the Bent Model with electron content data has also been undertaken by Mulkern (1976). Four stations from a wide range of northern latitudes supplied solar maximum electron content data to investigate the ability of the Bent Model to estimate the diurnal variation of the monthly mean. The prediction quality was generally good at all four stations except for the equinoctial seasons. A comparison with ionosonde data again led to the conclusion that the profile shape was in error.

Maps of electron content or ionospheric correction calculated from the Bent Model have been published for specific times by several researchers. Figure 2.9 shows the 00 UT 1.6 GHz ionospheric correction on a global scale calculated from the electron content predictions of the Bent Model (Klobuchar 1978) for the conditions pertaining to March 1968 (sunspot number of 105). The Equatorial Anomaly, Main Trough and strong dawn Terminator gradients are distinguished as large scale features. A similar map for March 1980 at 20 UT was also calculated by Klobuchar (1982) and for January at 12 UT by Nesterczuk (1981).

The JPL Model accuracy was tested by Fleury (1986) who employed data from four sites over more than five years of the declining phase of solar cycle 21. Data from one of the sites was required for the reference input to the model. As expected the accuracy was good near the reference site, slightly worse for a location 1 200 km distant and much worse for a location very remote from the reference site. The distance from the calibration site was considered crucial to the accuracy of the model. This finding emphasized the need for electron content measurements in the locality of the prediction point. For the JPL Model to return accurate estimates of electron content Nesterczuk (1981) suggested a distance of 800 km as an outer limit. An example of the use of the JPL Model to remove the influence of the Earth's ionosphere in a determination of the electron content of the plasma torus along the orbit of Jupiter's moon Io was given by Royden et al (1980).

With the same data Fleury (1986) also studied the efficacy of the Bent Model for electron content predictions. As for the JPL Model the accuracy was found to be good for low solar activity, defined as when the sunspot number was below 70, but serious errors were noted during high solar activity, especially for a low–latitude site. With the assumption of accurate values for peak parameters the calibration of the Bent profile thickness is the overriding concern. The Bent Model sub–model for the bottomside and topside semi–thicknesses employed a look–up table containing these values for a range of latitudes, seasons and solar activity levels; the value for a particular situation being calculated by linear interpolation.

With the intention of improving the Bent Model Rawer and Bilitza (1985) associated the bottomside predictions of electron content from the more detailed International Reference Ionosphere with an equivalent biparabolic thickness. The resulting description simplified the calculation of electron content by circumventing the look–up table procedure and is defined by Equations 2.1 to 2.5.

$$\bar{y}_m = 82.6 + 9.31\,\bar{F} \tag{2.1}$$

$$y_m = \bar{y}_m - (A + B\cos(15\,(LT+C))) \tag{2.2}$$

$$A = 22 - 52\,\mathrm{EXP}\left(-\left(\frac{d - 182.5}{68.9}\right)^2\right) \tag{2.3}$$

$$B = 30 - 7\cos\left(\frac{d - 15.2}{365}\,360\right) \tag{2.4}$$

$$C = 5.5 + 4.5\cos\left(\frac{d - 15.2}{365}\,360\right) \tag{2.5}$$

LT = Local Time (hours) d = day number of year

F = critical frequency of the F–region (MHz)

y_m = semi–thickness of bottomside biparabolic layer (km)

overbars indicate noon values

The influence of solar activity on the ionospheric thickness is included indirectly through the noontime value of foF2. The Bent Model definition (Llewellyn and Bent 1973) gave the topside parabolic thickness from that of the bottomside and the F–region critical frequency. If foF2 was greater than 10.5 MHz then the topside parabolic semi–thickness was given by Equation 2.6, otherwise it was simply set equal to the semi–thickness of the bottomside.

$$y_t = y_m\,(1 + 0.1333\,(\bar{F} - 10.5)) \tag{2.6}$$

y_t = semi–thickness of the fitting parabola (km)

Rawer and Bilitza (1985) developed a version of the Bent Model which incorporated these definitions of the biparabolic and parabolic thicknesses amongst other modifications. A comparison was made with the output of the resultant model and electron content data from four stations which demonstrated an improvement over the original version.

2.3 Coherence of Electron Content Variability

It is generally accepted that the inclusion of measurements of electron content taken sufficiently close to a prediction point can increase the accuracy of model estimates for that point by allowing for conditions in the local ionosphere. The accuracy of the JPL Model predictions for a location close to the reference station being a good example of this. The updating technique is known as adaptive modelling and has been investigated for situations when the data available for adjustment was to some extent either temporally or spatially separated from the point where a prediction was required.

Analyses of updated models prove that, unless data is taken within a restricted space–time cell, no significant improvement is gained over monthly average predictions. It is therefore necessary to determine the spatial and temporal extent of the cell in order to decide whether or not it is worthwhile incorporating the available data into the model. The space–time boundary of this cell is determined by the coherence of electron content.

The temporal coherence of electron content is a measure of the persistence of a deviation from its mean level, similarly the spatial coherence is a measure of how well a deviation at one point is mirrored at a remote point (Milsom, private communication). The Coherence Time shall be defined as the time delay after which the temporal correlation coefficient falls to 0.7 The Coherence Distance is defined similarly as the separation where the spatial correlation coefficient falls to 0.7. The spatial and temporal coherence functions therefore give a quantitative measure of the usefulness of a remote measurement for updating purposes. If the decorrelation can be assumed to be linear the Coherence Time and Coherence Distance define their respective coherence functions.

Feen et al (1975) found daytime variations of approximately 25% and nighttime variations of approximately 50% about monthly mean electron content predictions from an empirical model at solar maximum. For a daytime electron content of 100 ecu and a nighttime value of 10 ecu these figures give uncertainties in the range correction of 53 mm and 11 mm at 13.8 GHz. The daytime uncertainty is greater than that tolerable in high accuracy altimeter systems. Updating the model with data led to residuals of 20 to 40% after three hours. Similar values were found after updating with data 1 000 km remote from the target site.

da Rosa (1974) calculated the correlation coefficient between the electron contents measured at two mid–latitude sites separated by 700 km during a time of high solar activity. The diurnal

average correlation coefficient was approximately 0.8, implying a Coherence Distance of 1 050 km.

DuLong (1977) studied the effect of adjusting monthly mean variations with data to attempt an estimate of the electron content several hours in advance. Data collected at Hamilton, Massachusetts over the descending half of solar cycle 20 were employed. Adaptive adjustments made for more than three hours in advance gave estimates which were found to be no better than the monthly mean. However, the residual error decreased monotonically as the time lag decreased becoming acceptable for lags of less than 60 minutes.

Donatelli and Allen (1978) similarly investigated the efficacy of updating an electron content model by scaling its prediction of the mean diurnal signature with real measurements. From zero at the time of update, the error was seen to increase monotonically with time. During daytime at solar maximum most of the benefit of an update was lost after approximately three hours, though only updates less than one hour old were found to beneficial for daytime predictions at solar minimum. Longer period fluctuations which only appear during solar maximum conditions were postulated to explain this disparity. A warning was given regarding advance predictions to a time beyond the Terminator, especially across the Dawn Terminator. It was suggested that predictions should be limited to no more than thirty minutes ahead because of the steep and unpredictable gradients which exist there.

Klobuchar (1980) also warned that problems may be encountered when trying to update a prediction from data taken from the other side of the Terminator. Coherence Times of less than three hours at solar maximum and less than one hour at solar minimum were proposed for the dayside electron content to obtain a reduction of 50% in prediction error. These figures tally with those suggested by Donatelli and Allen (1978).

Further work by Donatelli and Allen (1981) considered the relative merits of multiplicative and additive adjustments to the monthly mean variation. The multiplicative method involves scaling the diurnal prediction by the ratio of the measurement to the corresponding estimate. The additive method involves a linear adjustment of the prediction dependent on the signed deviation of the measurement from the corresponding estimate. It was demonstrated that the multiplicative adjustment was dependent on the ratio of the standard deviation of electron content to its mean, whereas the additive adjustment was dependent on the standard deviation. The diurnal variations of the standard deviation and its ratio to the mean were such that for predictions more than a few hours ahead the multiplicative method has an advantage over the additive method. However, for

the short coherence times of electron content (less than three hours) neither method has an advantage.

Nisbet et al (1981) considered updates of a model with remote data were found to be most useful if taken within 1 000 km of the update point. Beyond 3 000 km the accuracy of the updated model was no better than the predictions from the model alone. It was concluded that to obtain more accurate predictions from models it would be necessary to include a measure of the day–to–day variability, a similar conclusion to that drawn by King and Slater (1973) for foF2.

Kane (1975) made observations of electron content at six mid– and low–latitude stations during the maximum of solar cycle and found the Coherence Distance of electron content to be approximately 1 800 km. A suggestion was made that convection cells in the neutral thermosphere produced ionospheric irregularities, the scale size of which determined the coherence distances in the ionosphere.

Bent et al (1975) investigated the weighting which should be applied to remote foF2 measurements before employing them to adjust a monthly mean prediction and found that data taken within 2 000 km was useful in updating monthly mean estimates. Rush (1976) found Coherence Distances of approximately 1 150 km North–South and 2 300 km East–West for foF2 with data from thirty two ionosonde stations collected during the high solar activity period known as the International Geophysical Year. The correlation coefficients were slightly higher for the midday period, lowest for winter nighttime and equinoctial values were slightly greater than those for summer and winter.

The principal study of the spatial coherence of daytime electron content was made by Klobuchar and Johanson (1977) for the daytime behaviour. Data taken between 10 LT and 16 LT from a network of nine northern hemisphere sites were employed to calculate the spatial decorrelation. Anisotropic Coherence Distances were found which were 1 800 km North–South and 2 900 km East–West, slightly longer than those found by Rush (1976) for foF2. This difference, as shall be demonstrated later, was accentuated by the longitudinal analysis being made with data from times of higher solar activity than the data employed for the latitudinal analysis. No consistent seasonal influence was found upon correlation coefficients in either direction. The spatial correlograms of Klobuchar and Johanson are reproduced in Figure 2.10.

Soicher (1978) examined the spatial decorrelation of electron content during a quiet phase of the solar cycle between the ionospheric points of Fort Monmouth, New Jersey (37°N,283°E)

and Richmond, Florida (24°N,278°E). The crosscorrelation coefficient was found to be approximately 0.7 during equinoctial times, though slightly greater during winter. The ionospheric points are separated by 1 750 km and this can be considered as the Coherence Distance in this case. The seasonal variation found in this instance was the reverse of that found by Rush (1976) for foF2, the equinoctial coherence being slightly worse than in other seasons. It was also noted that the coherence of electron content between the two stations was enhanced during a magnetic storm.

Huang (1983) investigated the latitudinal decorrelation of electron content between two sites in the UK at Aberystwyth and Hawick during the solar minimum conditions of 1975 and 1976. The 420 km ionospheric points had a North–South separation of approximately 900 km. The crosscorrelation coefficients between electron content measurements at the two sites were found to be approximately 0.9, equivalent to a Coherence Distance of 2 700 km.

Huang (1984) investigated the spatial decorrelation between two equatorial sites in the Far East. Due to the proximity of the sites (280 km approximately North–South) high correlation coefficients were found from nine months of data taken between December 1981 and November 1982. Again, a good comparison with the North–South results of Klobuchar and Johanson (1977).

Soicher et al (1984) investigated the spatial coherence of mid–latitude electron content during the solar maximum year 1980 and found a Local Time variation, but no seasonal variation. The electron content measured at the 420 km ionospheric points of Athens and Haifa were employed in the study. The data from the two sites was initially adjusted to the same Local Times. Crosscorrelation coefficients calculated from the adjusted data exhibited a Local Time variation where the coefficients for the early morning period were approximately half those prevailing during the remainder of the day, though no pronounced seasonal variation was found. An average of the daily correlations gave an equivalent Coherence Distance of 1 900 km.

Essex (1978) investigated the coherence of electron content measured at Melbourne from two synchronous satellites whose ionospheric points were separated by 1 400 km. For magnetically quiet days differences between the diurnal variations at the two points were quite small and ascribed to gravity waves, for more active days the differences were larger though still in the same sense relative to the monthly mean. This suggests the coherence of electron content is stronger for times of magnetic activity as, indeed, was found by Soicher (1978).

Bhuyan et al (1984) similarly observed two synchronous satellites from Delhi during March and April 1979 and hence monitored the electron content fluctuations at two ionospheric points separated by approximately 900 km. An indistinct diurnal variation of correlation coefficient was observed with the nighttime values being greater during March and the reverse situation holding for April. Diurnal average correlation coefficients were found to be slightly greater than 0.6 corresponding to a Coherence Distance of approximately 675 km. Bhuyan and Tyagi (1986) employed a chain of observatories in and around the Equatorial Anomaly crest to investigate the spatial variation of electron content there. It was observed that the decorrelation was stronger in both the East–West and North–South directions than was the case for mid–latitudes.

A summary of the Coherence Distances found by the above researchers is given by Table 2.1. The anisotropic coherence was only revealed by the studies of Rush (1976), the earlier studies did not distinguish between North–South and East–West separations. All the documented work since then has reinforced the view that the North–South Coherence Distance is shorter than that East–West for both electron content and foF2. Table 2.1 also summarizes the properties of Coherence Times found by other researchers. The increase of coherence time with solar activity is a feature of the investigations which covered extremes of solar activity. This ties in with the suggestion of Donatelli and Allen (1978) that coherence is enhanced during times of high solar activity.

2.4 Chapter Summary

The previous chapter has summarized the work on electron content published in open literature in the areas of mean and disturbed behaviour, spatial and temporal coherence and predictive and adaptive modelling. Although much work has been devoted to the analysis of electron content measurements there is scope for further work in all these areas especially towards the blending of these areas of knowledge into a dedicated correction algorithm for satellite radar altimetry. There is a need for improvement in the climatological models of electron content especially at low–latitudes. The data available for this study include low–latitude measurements and were collected relatively recently (from 1980 to 1985); as such they should provide a novel insight into the characteristics of ionospheric electron content.

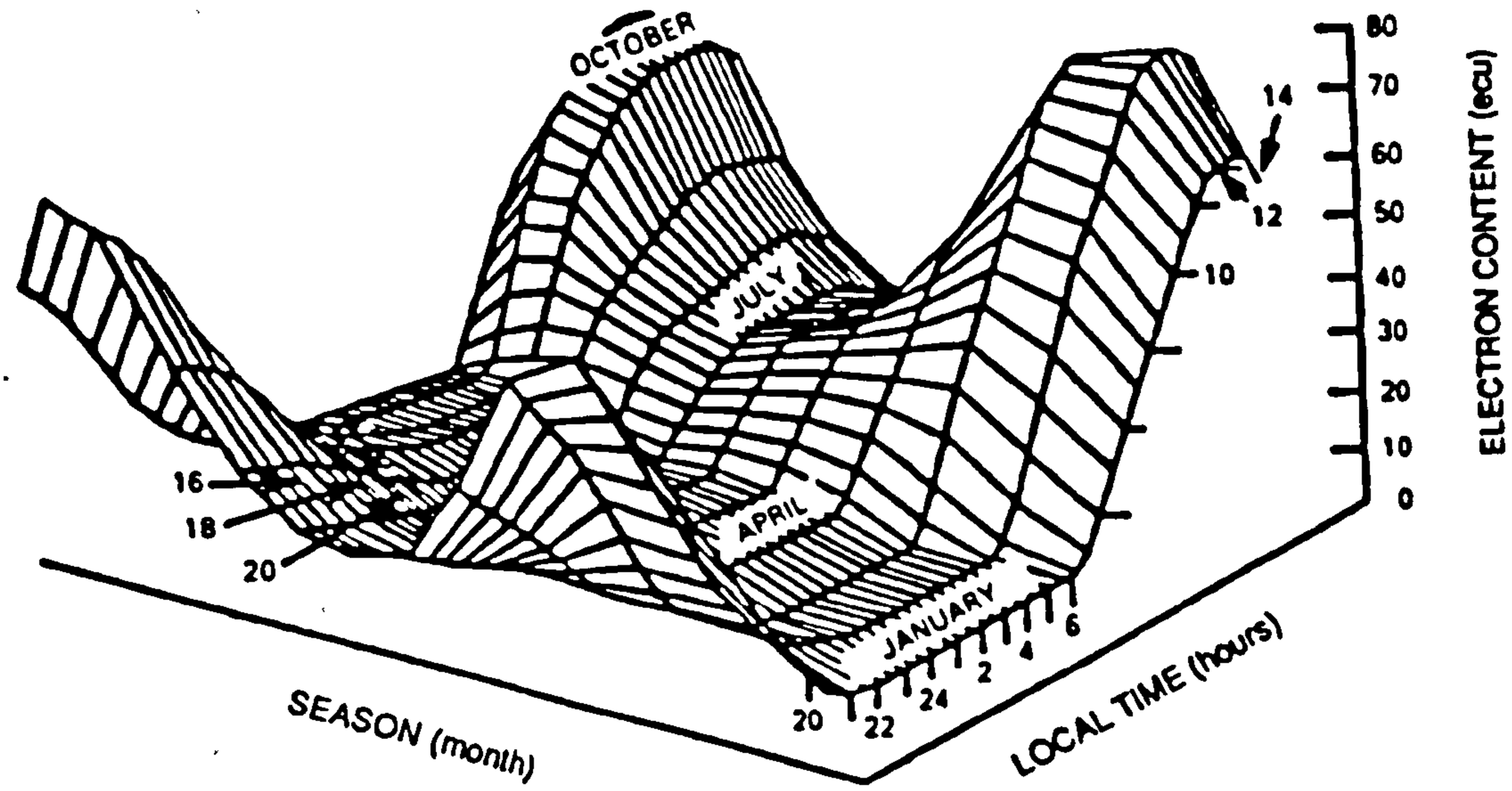

Figure 2.1 : The diurnal and seasonal variation of monthly average electron content measured from Goldstone, California (35°N,243°E) (after Green et al 1980).

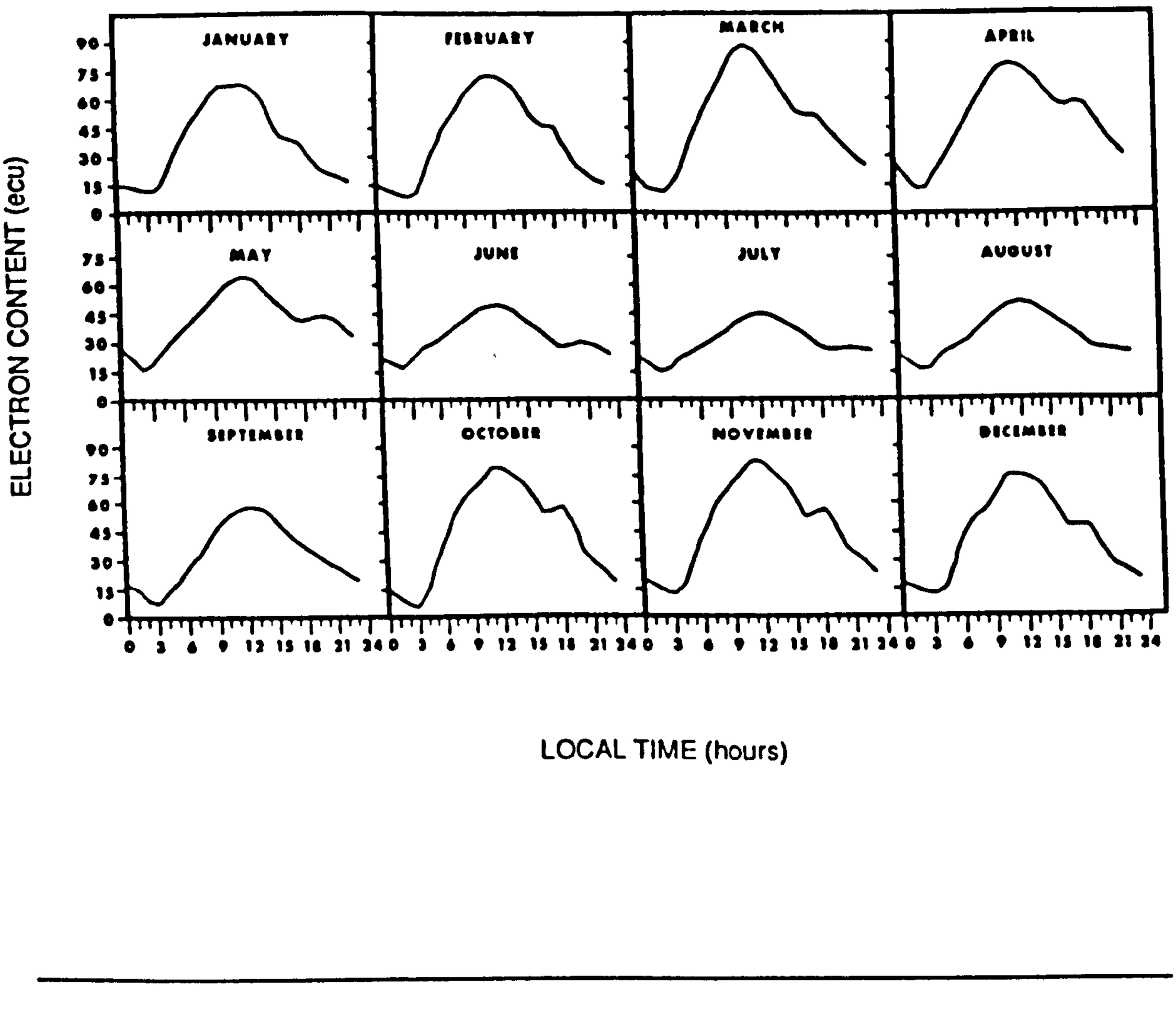

Figure 2.2 : The diurnal and seasonal variation of monthly average electron content measured from Haifa, Israel (33°N,35°E) (after Soicher et al 1984).

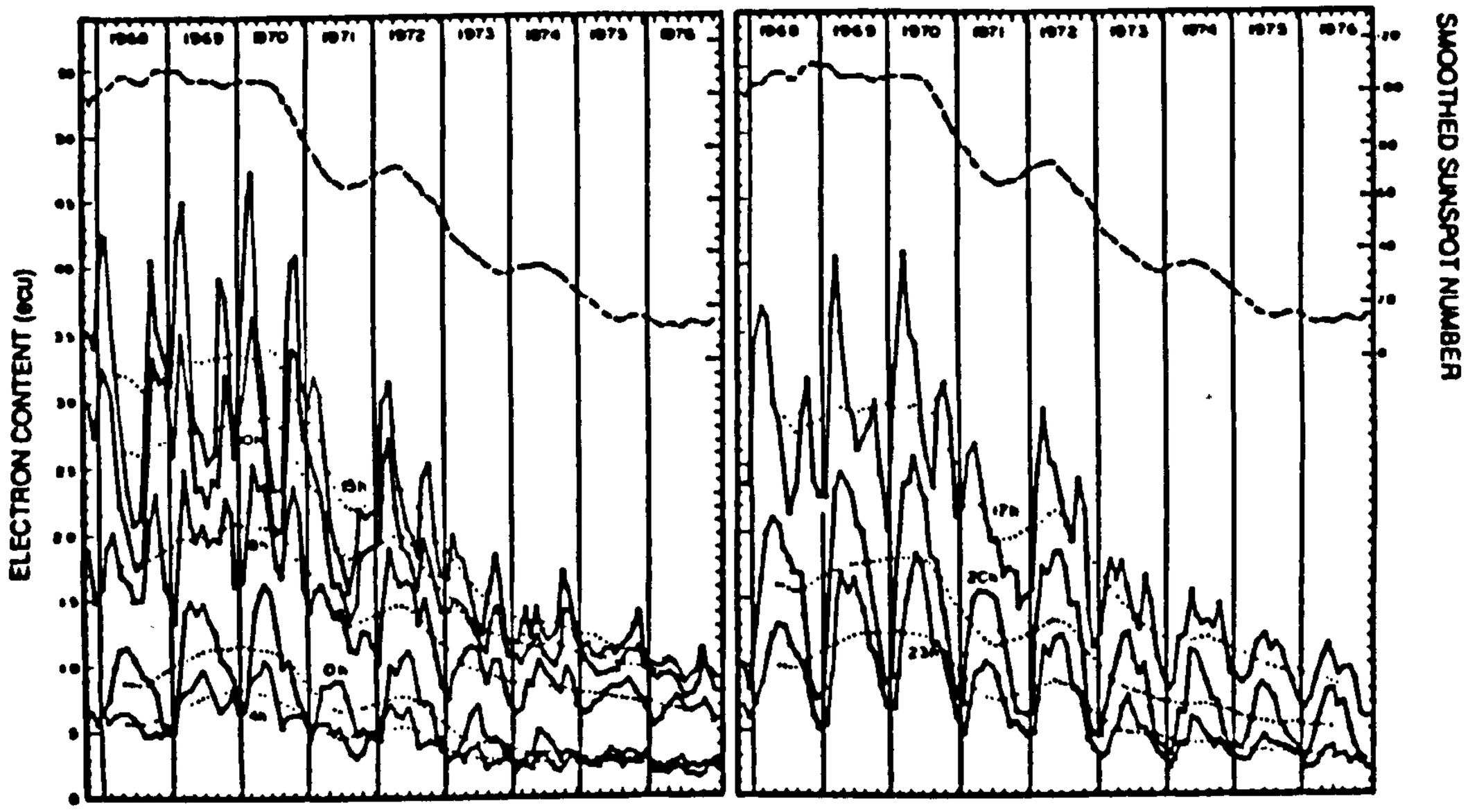

Figure 2.3 : The monthly average electron content at eight local times measured over nine years from Sagamore Hill, Massachusetts (41°N,281°E) (after Huang 1978). The twelve–month running mean values are shown with dotted lines. The prevailing twelve–month running mean sunspot number is shown at the top of the figure.

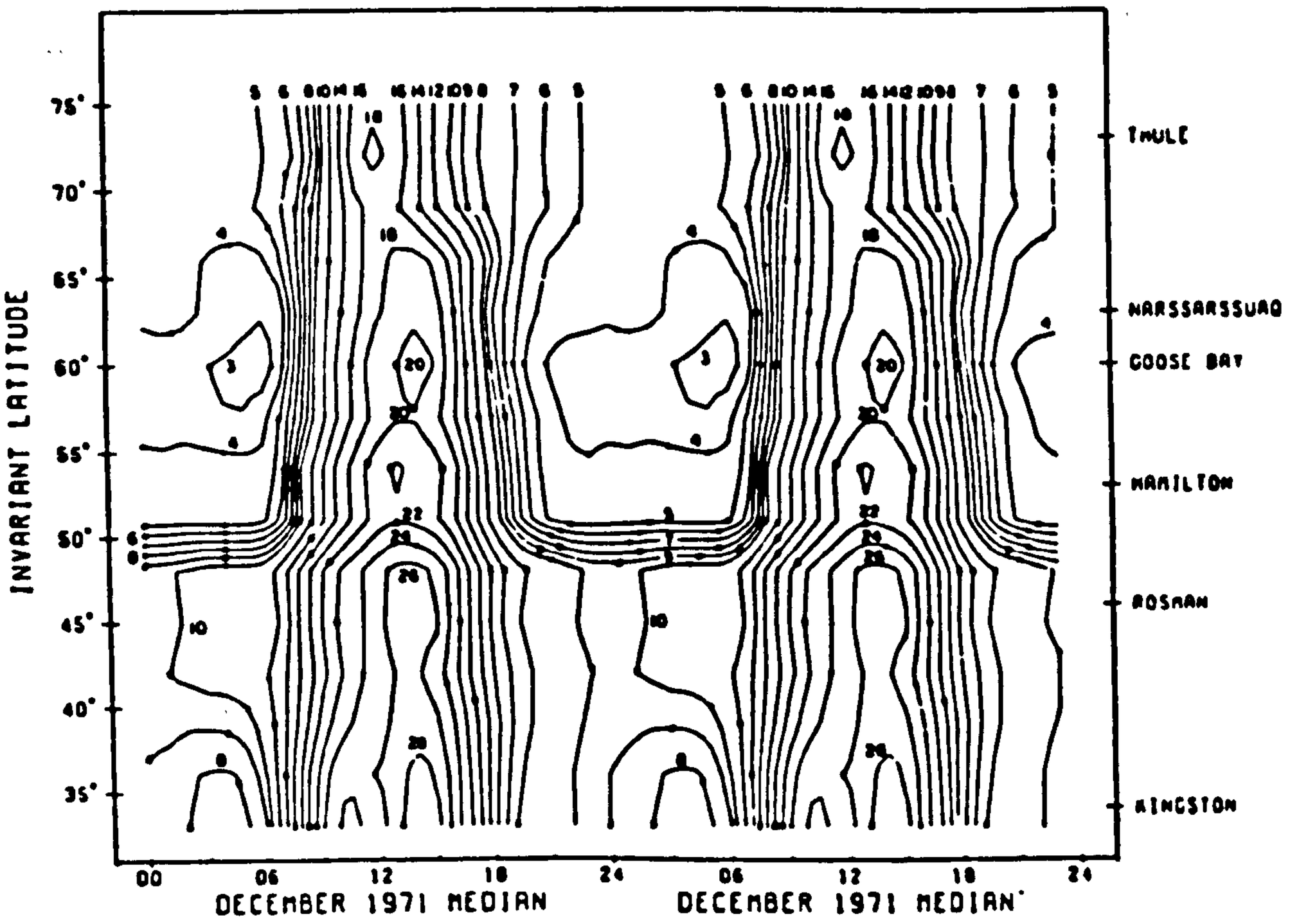

Figure 2.4 : The latitudinal variation of monthly average electron content for December 1971 measured from six northern hemisphere sites (after Mendillo and Klobuchar 1975). The contour interval is one ecu.

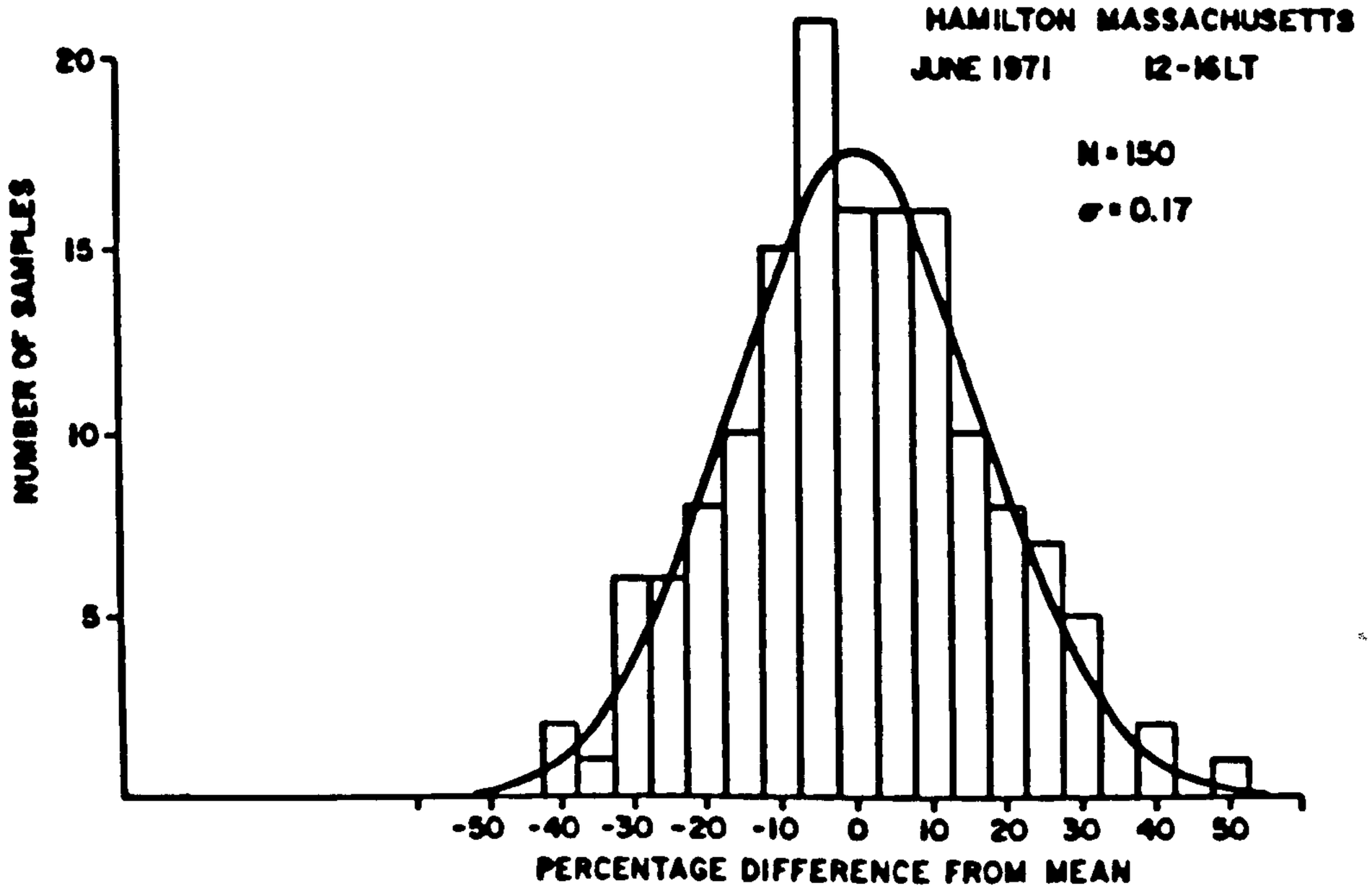

Figure 2.5 : The distribution of daytime deviations from the monthly mean electron content of December 1971 at Hamilton, Massachusetts (43°N,289°E) overlaid with the corresponding Normal distribution (after Johanson et al 1978).

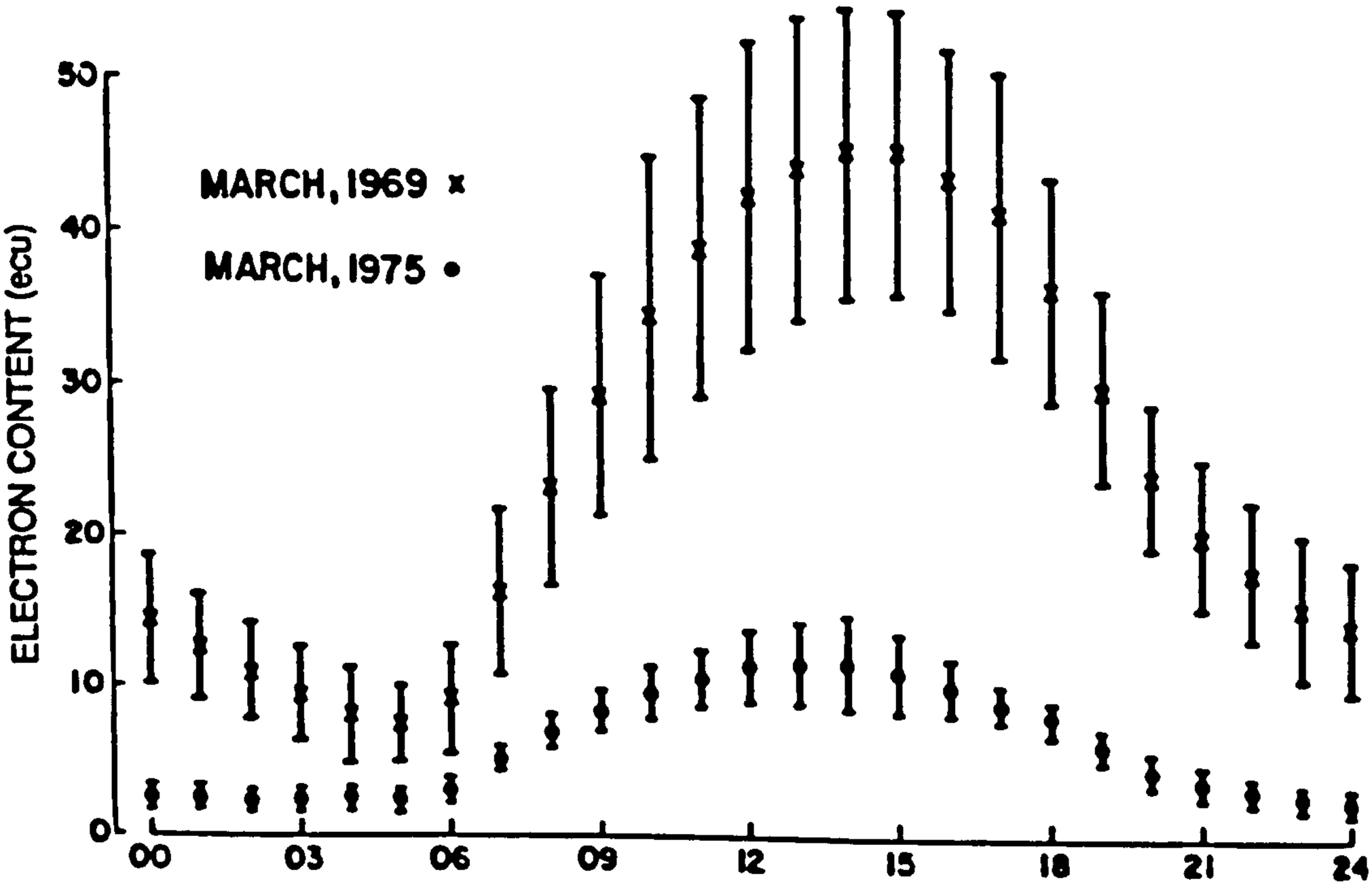

Figure 2.6 : The diurnal variation of the monthly mean electron content at Hamilton, Massachusetts (43°N,289°E) for a solar maximum and a solar minimum year (after Johanson et al 1978). The corresponding standard deviations are plotted as error bars.

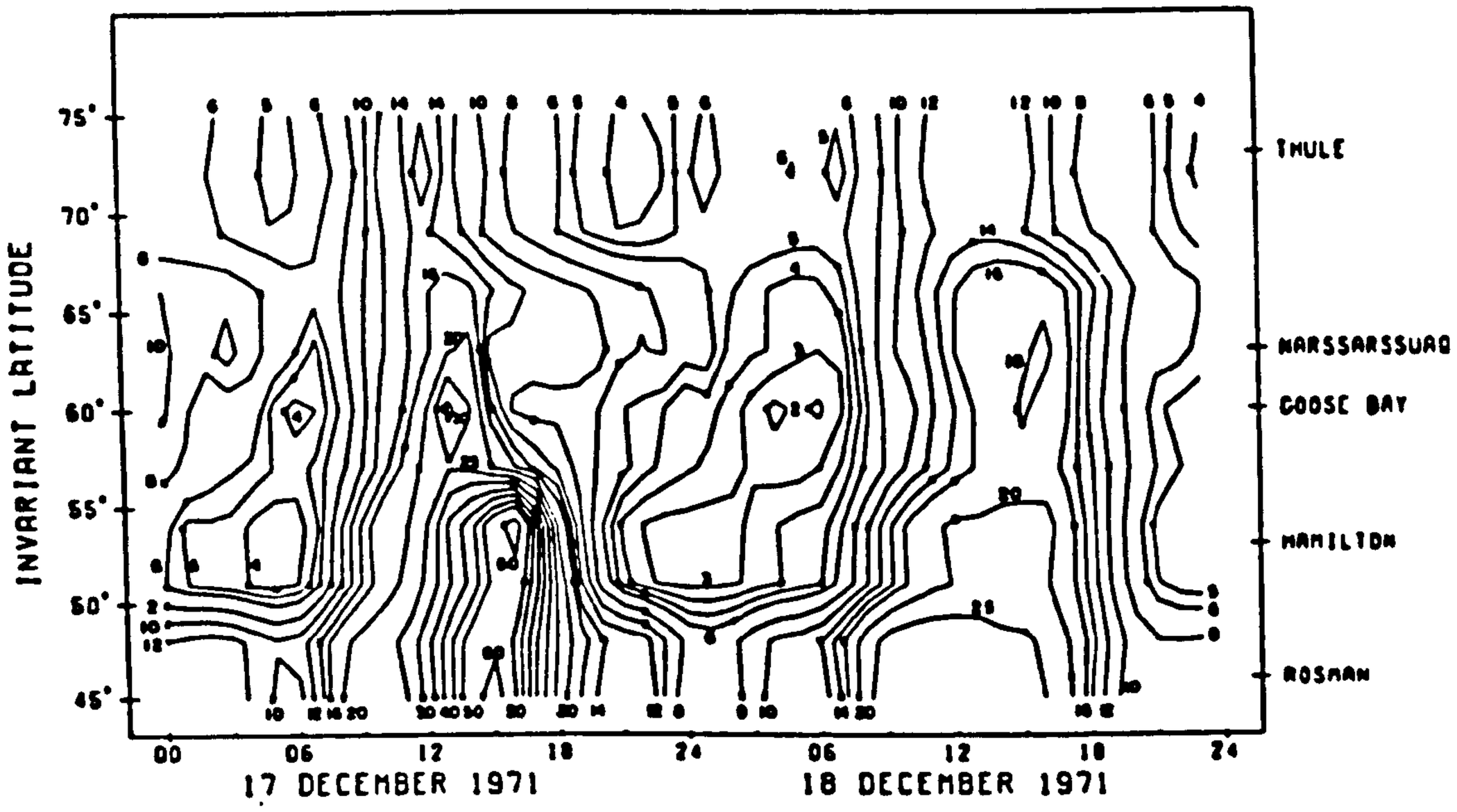

Figure 2.7 : The irregular latitudinal variation of electron content for 17th and 18th December 1971 measured from five northern hemisphere sites (after Mendillo and Klobuchar 1975). The contour interval is one ecu. (c.f. Figure 2.4.)

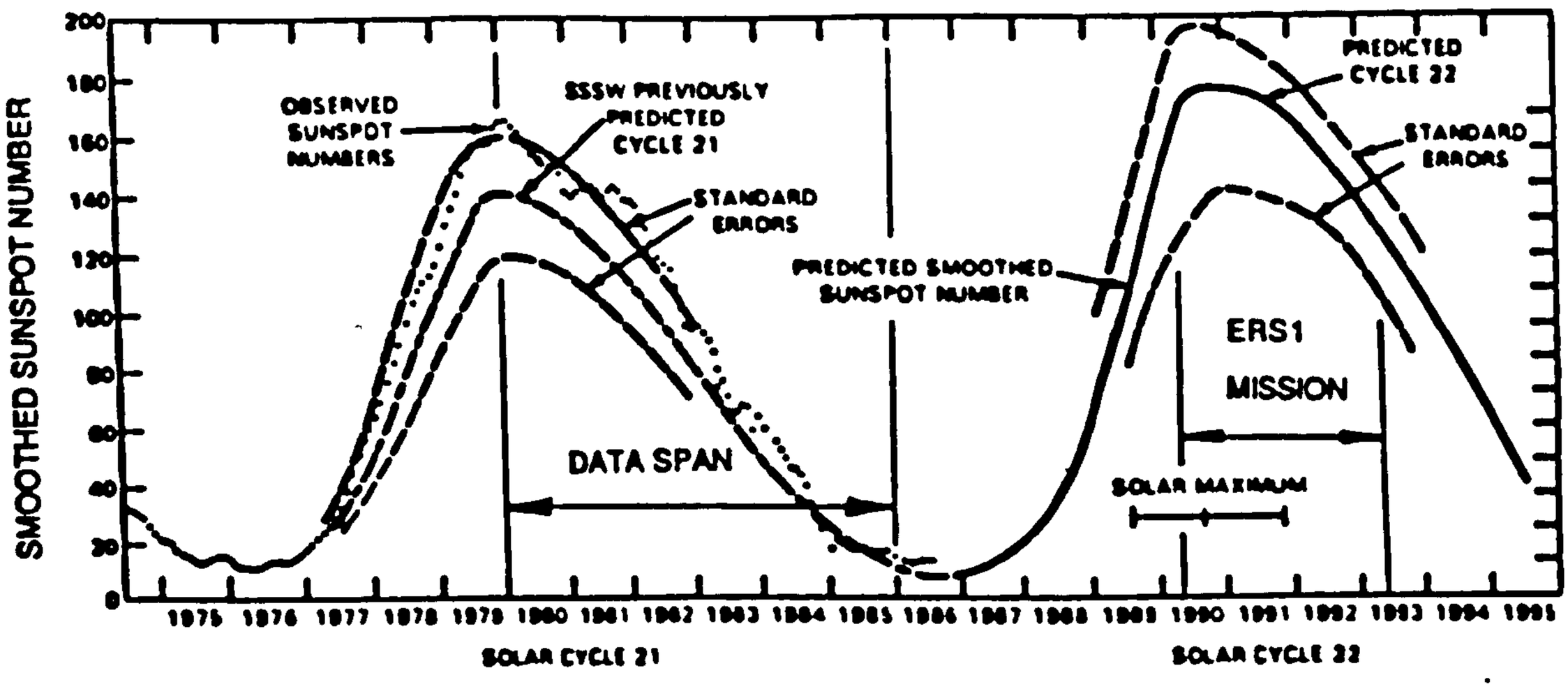

Figure 2.8 : The measured twelve–month running mean sunspot numbers for solar cycle 21 and the predicted values for solar cycle 22 (after Schatten and Sofia 1987). Also shown is the proposed duration of the ERS1 mission and the temporal extent of the data available for electron content investigations.

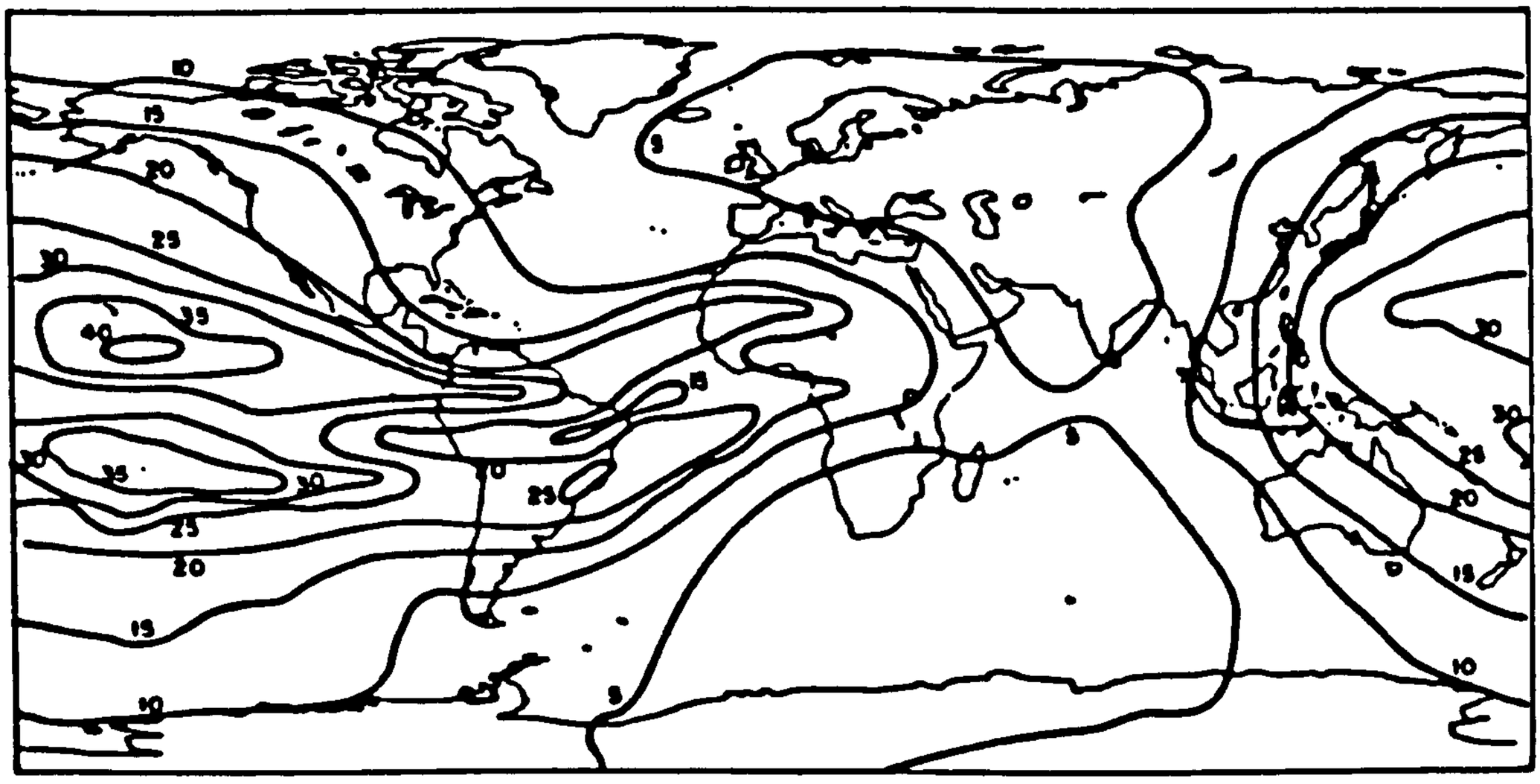

Figure 2.9 : The spatial variation of monthly average 1.6 GHz group delay predicted from the Bent Model for 00 UT during March 1968 (after Klobuchar 1978). The contour labels in nanoseconds can be converted to electron content units by multiplying by 1.9.

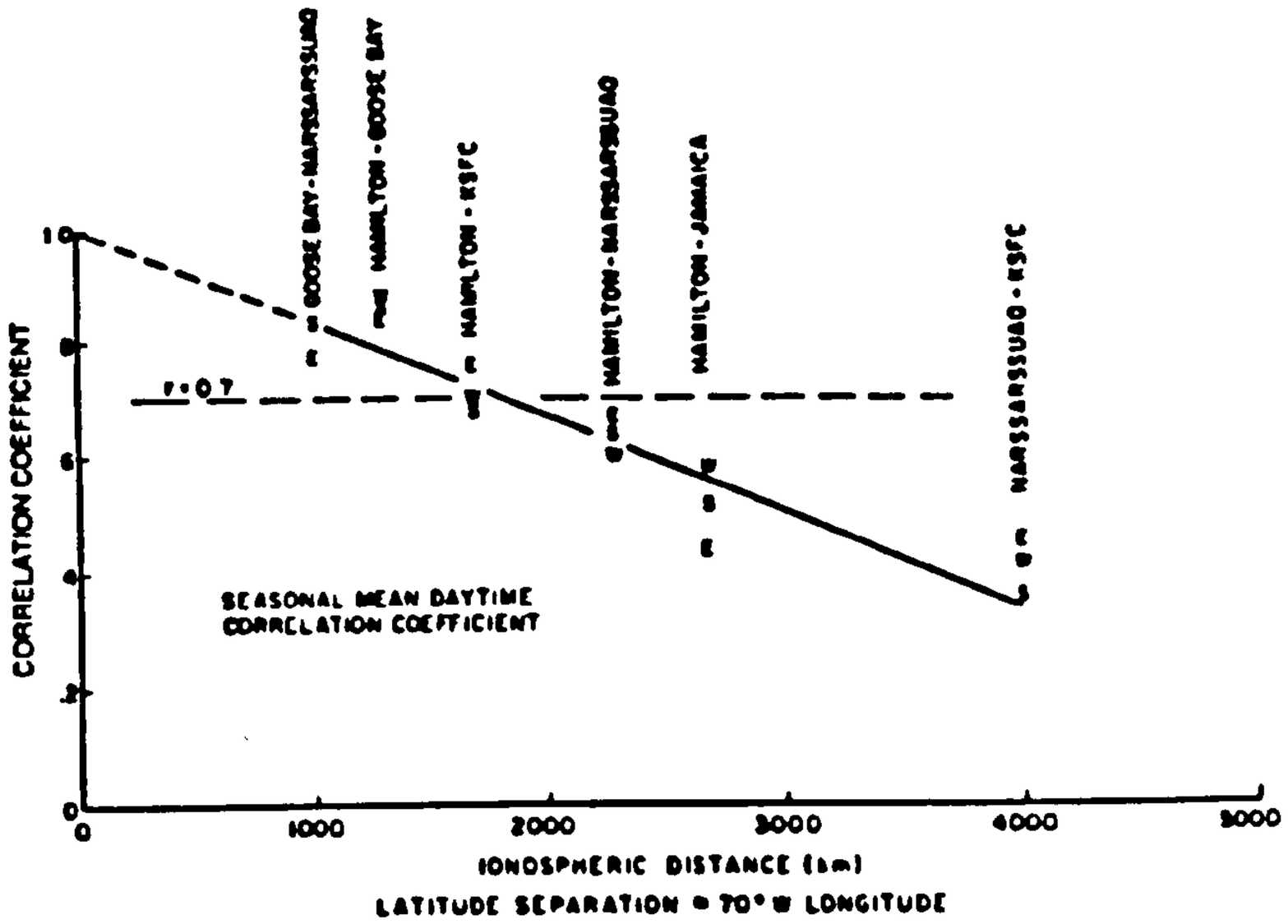

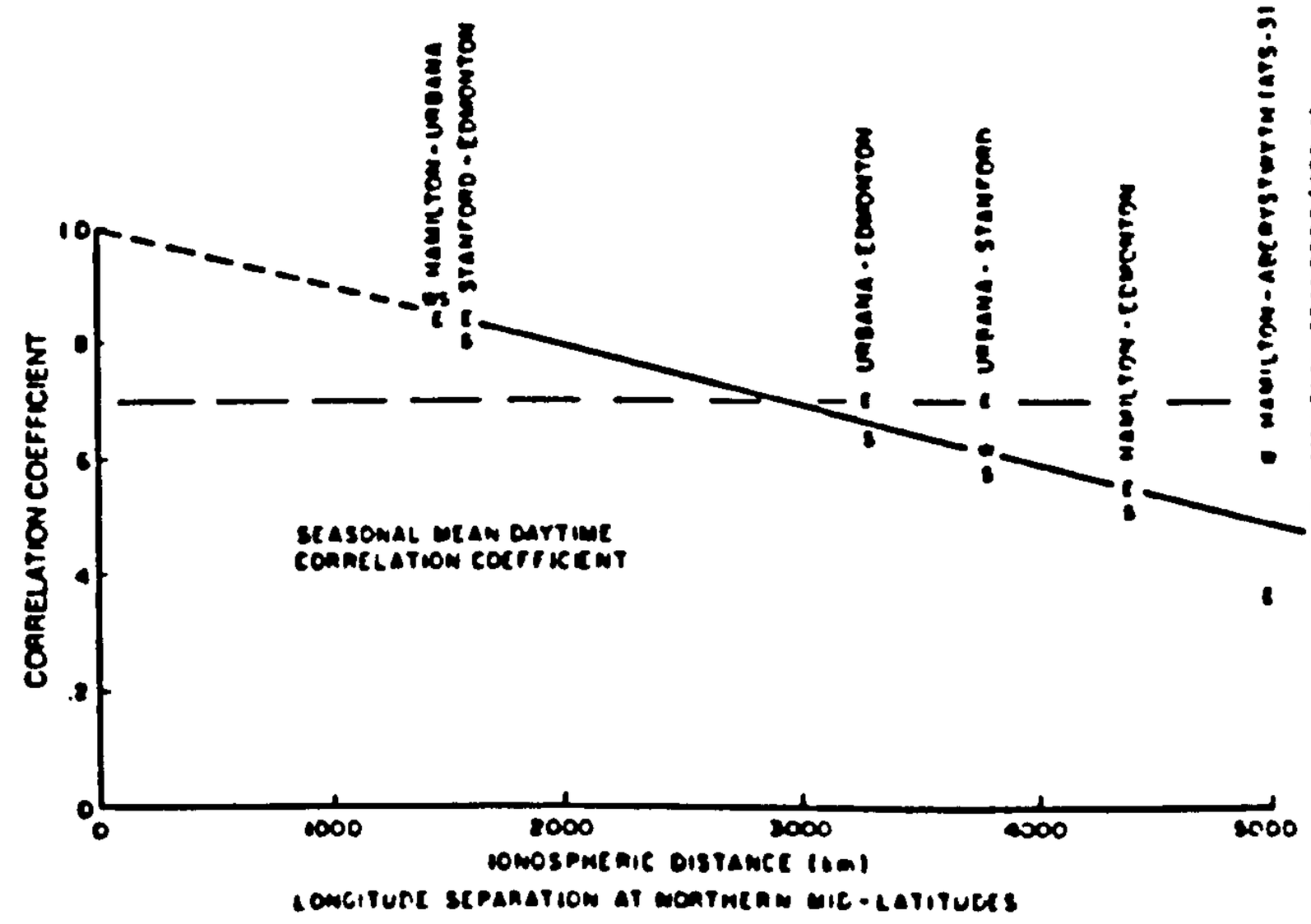

Figure 2.10 : The linear spatial decorrelation of electron content (after Klobuchar and Johanson 1975). The upper correlogram is for North–South separation and the lower for East–West, note the anisotropy. The letters denote the season; W–winter, E–equinoctial, S–summer.

RESEARCHER / S	DATE	DATA	COHERENCE DISTANCE (km)	
			UNRESOLVED	
DA ROSA	1974	H	1 050	
FEEN	1975	H	1 000	
KANE	1975	H	1 800	
			NORTH–SOUTH	EAST–WEST
KLOBUCHAR et al	1977	H	1 800	2 900
SOICHER	1978	L	1 750	–
NISBET et al	1981	L	1 000	1 000
HUANG	1983	L	900	–
BHUYAN et al	1984	H	–	675
HUANG	1984	H	1 800	–
SOICHER et al	1984	H	–	1 900

RESEARCHER / S	DATE	DATA	APPROXIMATE COHERENCE TIME (minutes)	
			SOLAR MAXIMUM	SOLAR MINIMUM
FEEN	1975	H	180	–
DULONG	1977	W	180	180
DONATELLI et al	1978	W	180	60
KLOBUCHAR et al	1980	W	180	60

Table 2.1 : Summary of Coherence Distances and Coherence Times of electron content found by previous researchers. Calculations have been made with data from times of high (H), low (L) and a wide range (W) of solar activity.

Chapter 3 : Spatial and Temporal Structure of Electron Content

This chapter presents a phenomenological perspective of the spatial and temporal behaviour of ionospheric electron content. The purpose is to recognize the fundamental properties of electron content which an empirical model must represent. The data employed in the survey were collected over six years at ten sites by the Faraday rotation technique. Monthly mean data will be employed to illustrate the quiet time variations on diurnal, seasonal and solar cycle time scales and the variation with latitude and longitude. The response of electron content to a particular magnetic storm will be discussed to illustrate the short term variability of the ionosphere.

3.1 Data Preparation

The map in Figure 3.1 shows the location of the ten receiving stations at which Faraday rotation data were collected. Table 3.1 lists the locations of these stations and the satellite beacon observed. Table 3.2 lists the corresponding geographical and geomagnetic co–ordinates of the ten stations. The latter table also gives the co–ordinates of the ionospheric point where the satellite to ground station ray path intersects the 420 km mean–field altitude. Each station monitored the electron content at its ionospheric point rather than its zenith point.

The full data base of electron content measurements was collected at ten northern hemisphere sites over six years giving good temporal and spatial resolution, though only in the northern hemisphere. Tranches of the full data set from four stations (Goose Bay, Boulder, Patrick Air Force Base and Palehua), which cover a range of northern latitudes, were employed to provide examples of typical electron content behaviour. These four receiving sites will be referred to as the calibration stations. Attention was focussed on data from the three years 1980, 1982 and 1985 since the twelve–month running mean sunspot numbers during these years spanned, respectively, 150, 100 and 20 – conditions representative of high, medium and low solar activity. Henceforth the term sunspot number will be taken to mean to the twelve–month running mean sunspot number. The data from March, June, September and December were taken to represent the state of the ionosphere during the four seasons of the northern hemisphere. These years and months will be referred to as calibration times. The sunspot numbers during the calibration

times are listed in Table 3.3. This subset of the data, comprising forty eight station months of measurements, will be referred to as the calibration data set.

The uncertainties introduced by the reduction of polarization measurements to electron content data were discussed by Titheridge (1972). Because the data provided were already converted to electron content no assessment could be made of errors arising from this reduction process. It should be recorded, however, that some data were corrupted, principally as a result of the incorrect use of descriptive letters in the original data. In the original data file the field reserved for each electron content measurement would only allow values of up to 99.9 ecu to be recorded; 'hundreds' of ecu were represented by a descriptive letter e.g. a letter 'M' associated with a measurement implied that one hundred should be added to the recorded number. Graphical inspection of the data revealed this letter had been erroneously inserted on several occasions in six station months of data. This problem was also noted for this data set by Fleury (1986).

Station months where data were corrupted by incorrect scaling were excluded from the investigations. Twenty station months of data were missing because of equipment failure. No data were available from Anchorage during 1980. A further eighteen months of data from various stations were not employed because more than half the measurements were missing. Therefore, a total of 664 station months of data were available for the investigations.

To investigate the behaviour of electron content, the line–of–sight measurements must first be corrected to equivalent vertical values. The correction factor depends upon the ionospheric zenith angle, which is defined as the angle made by the receiving site–satellite ray path to the local vertical at an altitude of 420 km and is the angle χ in Figure 1.9. It has been demonstrated that for ionospheric zenith angles of less than 70° a simple correction factor, equal to the cosine of the ionospheric zenith angle, is sufficiently accurate to deal with the obliquity of the observations (McNamara 1983). Furthermore since all the data analyzed here were collected from radio beacons mounted on geostationary satellites, the zenith angle at each station remained constant. The zenith angles calculated for each site are also listed in Table 3.2 and Figure 3.2 depicts the obliquity correction factors for each of the ten sites. Occasionally a different satellite beacon than the one given in Table 3.1 was monitored, in this case the new zenith angle was used for the slant correction.

3.2 Temporal Structure of Electron Content

The temporal power spectrum of electron content depicted in Figure 3.3 is analogous to that of electron density fluctuations shown in Figure 1.6. This power spectrum was estimated from the mean data of the calibration set along with short term fluctuation data from Hunsucker and Hargreaves (1988) and Mendillo and Klobuchar (1975). With one exception the electron content is variable on the same time scales as the electron density, though the fluctuation range at each of the characteristic periods is slightly less. This may be explained by the fact that electron content is a height–integrated parameter and so one dimension of possible fluctuation is suppressed. The $\log_{10}$ power of 0.7 estimated for the solar cycle time scale agrees with the value estimated by Rajaram and Rastogi (1977). The following sections describe the variations of electron content with these characteristic periods.

Solar cycle and diurnal variations of electron content measured from the Boulder station during March of the three calibration years are illustrated by Figure 3.4, along with the corresponding ionospheric correction values for an altimeter frequency of 13.8 GHz. The systematic variations in Local Time and with solar activity are evident. At sunrise the electron content begins to increase, the rate of increase being greater for times of higher solar activity. The electron content continues to build up through the morning as the local solar zenith angle decreases, finally reaching a maximum one or two hours after local noon. This maximum value exhibits a solar cycle dependence. The highest values are obtained at times of high solar activity when the power of the Sun's radiation in the ionizing frequency bands is greatest. This relationship, though, is certainly not linear there being a substantial increase between the 1985 data and the 1982 data but virtually no increase between the 1982 and the 1980 data. During the late afternoon and early evening the electron content decreases until the electron content reaches its nighttime value at around 22 LT. Plasma transport processes enable the F–region ionosphere to persist throughout the night with an almost constant electron content. At Boulder this has a monthly mean value for March of below 10 ecu.

The noon and midnight values of the monthly mean electron content measured at Boulder for all 71 months of available data are plotted in Figure 3.5 along with their twelve–month running means. The midday electron content varied from 45 ecu at solar maximum down to approximately 10 ecu at solar minimum, the corresponding midnight values being 10 ecu and 5 ecu. The twelve–month running means – which eliminate the seasonal variation – confirm the non–linear increase of electron content as the sunspot number increases, there being an apparent saturation condition for sunspot numbers above 140.

An apparent seasonal dependence of midday electron content can be seen from Figure 3.5 which becomes less pronounced for low solar activity. This is not the true seasonal variation because the magnitude of electron content is modulated by the level of solar activity. Some useful comparisons, though, can still be drawn from an analysis of the modulated seasonal variation. At least on a monthly mean basis, large values at noon are to be found during the equinoctial seasons. This is referred to as the semi–annual anomaly and can be explained by a seasonal variation of the composition of the neutral atmosphere. The noon values of electron content are generally greater during spring than autumn though this is due to the monotonic decrease of the sunspot number during the year. The noon values during winter are similar to or slightly less than the equinoctial values but those during summer are distinctly less. This phenomenon when seen in electron density is known as the seasonal anomaly and can be explained by a lower electron loss rate in the colder winter hemisphere. The seasonal variation of the midnight values can also be seen in Figure 3.5. The midnight values during summer are slightly higher than for the other seasons though, apart from this, there appears to be minimal seasonal variation of the nighttime electron content.

A perspective of both the mean Local Time and seasonal structure of electron content measured from Boulder is given by the isometric projection of Figure 3.6. The diurnal variation exhibited is consistent with the solar control of electron content. The daytime electron content can, again, be seen to be greatest for the equinoctial seasons and least for the summer months.

Throughout the month the electron content does not simply follow the pattern of the monthly mean, but fluctuates about this level due to the dynamic nature of the ionosphere. Shown in Figure 3.7 is the Local Time variation of electron content at Patrick Air Force Base during the four calibration months of 1982. The form of the variation is, on the whole, similar on successive days but details of the daily variations demonstrate the short term instability of the ionosphere. Figure 3.8 concentrates on the variation of the noon electron content of the same months about the mean value and illustrates more clearly the day–to–day variability. The diurnal variation of mean electron content at Patrick during the calibration months of 1982 is shown in Figure 3.9, the error bars delineate the standard deviation of the data from the mean for each hour of Local Time. Compared to nighttime values the daytime standard deviations are larger in absolute terms though smaller in relative terms.

The distribution of daily electron content deviations from the mean also demonstrates the day–to–day variability. The distributions of Patrick data for the four calibration months of 1982 are shown in Figure 3.10 overlaid with the equivalent Normal distribution. A considerable proportion

of the deviations were found to fall into the three central bins implying that for most of the time electron content fluctuates close to its mean level. The representation of the difference distribution by a Gaussian function is very good with only a small proportion of the data falling outside the figure. Large differences from the mean occur rather infrequently and are one of the ionospheric manifestations of magnetic storms.

Standard deviation values calculated from the Boulder calibration data set are listed in Table 3.4 along with the number of measurements involved in their calculation. The standard deviations of 1985 data are 1–2 ecu, but for 1980 and 1982 data are 3–6 ecu. The standard deviations of all three years have no obvious seasonal variation.

A diurnal variation of the difference distribution of the data taken from Patrick during March 1982 is illustrated by the four panels of Figure 3.11, each panel covering one six hour period of Local Time. The sectors of Local Time were centred on midnight, 06 LT, noon and 18 LT so as to represent periods of darkness, sunrise, daylight and sunset, respectively. A Normal distribution still gave a good representation of the distribution for all four Local Time sectors. Local Time patterns of standard deviation are evident, with the similar values during the noon and dusk periods being approximately 50% larger than those for the midnight and dawn periods.

The standard deviations calculated over all Local Times of the electron content measured at Boulder for the 71 months of available data are plotted in Figure 3.12 along with their twelve–month running mean. In all cases the standard deviation was found to be less than 8 ecu. The trend reveals a general fall off in the standard deviation as the sunspot number decreases which, again, is far from being linear. No seasonal variation of the standard deviations is evident from the figure.

The principal cause of high levels of variability in the ionosphere is magnetic activity. Strong magnetic storms occur in the ionosphere approximately 30 hours after a solar flare when the solar plasma emitted during the event collides with the geomagnetic field. The recurrence of weaker magnetic storms on the mean solar rotation period of approximately 27 days is a result of active regions in the solar chromosphere, so called M–regions, persisting over several rotations (Hultqvist 1973). The exact response to a magnetic storm is dependent on many factors including the location of the site and the Local Time and the state of the geomagnetic field at the onset of the storm.

The response of high–latitude electron content to a magnetic storm is shown in Figure 3.13 which illustrates the behaviour of the electron content measured at Goose Bay from between the 12th and 14th February 1982. During the storm time the daily sum of the Kp index was greater than 34 and the Ap index was above 40, which satisfied the definition of a storm according to Mendillo (1973). On day one of the storm the daytime content was enhanced by up to 10 ecu for six hours, fell below the mean at dusk and remained depleted over the next two days by between 5 ecu and 10 ecu. The behaviour of electron content during this storm matches the findings of Mendillo and Klobuchar (1975) described earlier and follows the same pattern as a storm described by da Rosa (1974).

Smaller magnitude fluctuations in electron content are caused by Travelling Ionospheric Disturbances (TIDs) which are a class of plasma fluctuations associated with atmospheric gravity waves. Two types are recognized: large scale TIDs which occur after magnetic storms with periods of approximately 60 minutes travelling between 400 and 700 ms^{-1} and medium scale TIDs which occur after severe tropospheric weather conditions with periods of approximately 20 minutes travelling between 100 and 200 ms^{-1}. The passage of TIDs, which are observed over 98% of the time at high latitudes, cause fluctuations in electron content of between 1 and 4% (Hunsucker and Hargreaves 1988). TIDs reveal themselves through power spectrum analysis of electron content fluctuations (Iyer and Nagpal 1983), though it was not possible to detect them in the available Faraday rotation data since the time resolution of the data was only one hour.

The preceding section has discussed the behaviour of electron content over a six decade range of time scales, what follows will extend the consideration of this behaviour to include the influence of location and hence describe the spatial structure of electron content.

3.3 Spatial Structure of Electron Content

To investigate the morphology of electron content and the influence of latitude on the scale of ionospheric variations the electron content is depicted by Figures 3.14 to 3.16 which illustrate the monthly mean noon and midnight values and their twelve–month running means at, respectively, the Goose Bay, Patrick and Palehua sites between January 1980 and December 1985. The midday electron content at Palehua varied from approximately 70 ecu at solar maximum down to approximately 25 ecu at solar minimum, the corresponding midnight values being 30 ecu and 10 ecu. For Goose Bay the decrease of the magnitude of electron content with latitude results in equivalent values of 25 to 5 ecu and 10 to 3 ecu, respectively.

The values measured from Patrick are intermediate to these. The twelve–month running means all confirm the fall off in the electron content, and the non–linearity of that fall, as the sunspot number decreases. The saturation of the noon electron content for sunspot numbers above 140 is, again, evident in the data. Apart from the influence of latitude on the magnitude of the variations, similar behaviour to that at Boulder (Figure 3.5) was observed at all three stations.

Seasonal variations of the noon and midnight electron content at the above three sites can also be seen from Figures 3.14 to 3.16. Again, apart from a question of scale, the seasonal variation is similar to that found at Boulder with the noon values greatest during the equinoctial months, least during the summer and between these extremes during the winter. A similar variation to that at Boulder of the midnight data is also evident with greatest values occurring during the summer months.

Perspectives of both the Local Time and seasonal variations of mean electron content measured during 1980 at Goose Bay, Patrick and Palehua are afforded by Figures 3.17 to 3.19, respectively. The seasonal variation described previously for Boulder (Figure 3.6) is repeated at the other three calibration stations. The low values of nighttime electron content measured from Goose Bay is due to the ionospheric point of the site lying inside the Main Trough of the northern hemisphere.

The standard deviations of electron content at Goose Bay, Patrick AFB and Palehua for the full data set are plotted on the graphs of Figures 3.20 to 3.22 along with their twelve–month running means. These figures should be compared in conjunction with Figure 3.12 for Boulder. Relative to the Boulder standard deviations, the Goose Bay values are smaller and those for Patrick slightly greater, though the trend with solar activity at both stations is the same. The Palehua statistics, on the other hand are quite different, being a factor of four greater than even the Patrick values and with almost no decline with sunspot number. This behaviour can be assigned to the high variability of the ionosphere in the Equatorial Anomaly region which seems to remain high during the quiescent phase of the solar cycle.

3.4 Chapter Summary

From the above discussion of the monthly mean variation of electron content it is clear that, at least in the long term and on large spatial scales, synoptic descriptions of electron content can give a good representation of its behaviour. To a first order approximation the electron content

follows the behavioural patterns of electron density in that daytime values are greater than nighttime, the seasonal variation is anomalous, there is a strong positive correlation with solar activity and equatorial features of electron density are mirrored in electron content. It is this mean behaviour which reliable predictive models of electron content aim to reproduce.

What is equally evident, though, is that on shorter time scales descriptions of electron content based on ionospheric climatology are inadequate. Models can only overcome the problem of variability with the inclusion of an adaptive facility which incorporates suitable measurements of electron content to update and scale the climatological prediction.

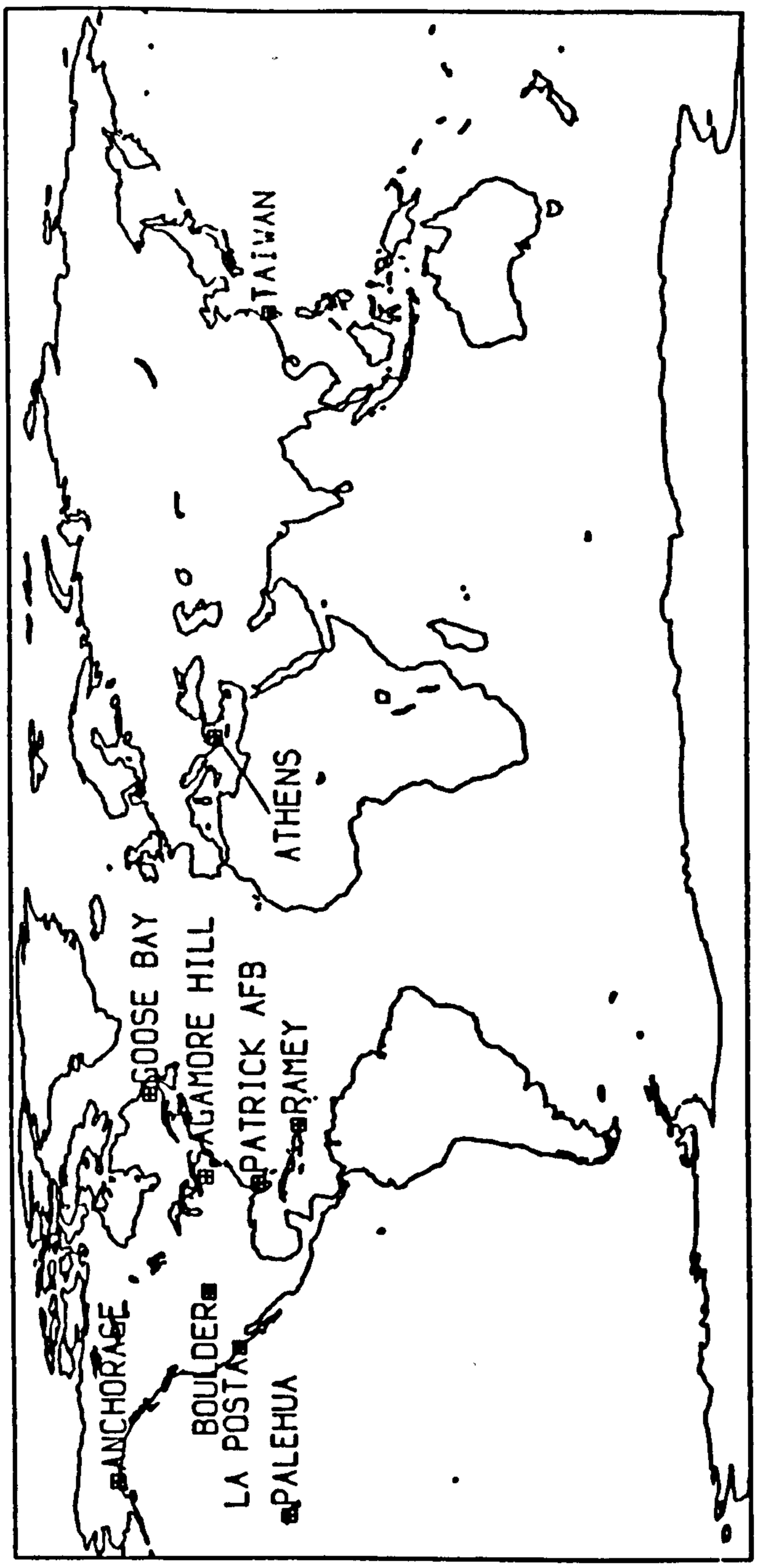

Figure 3.1 : A map showing the location of the ten Faraday rotation receiving sites which provided research data.

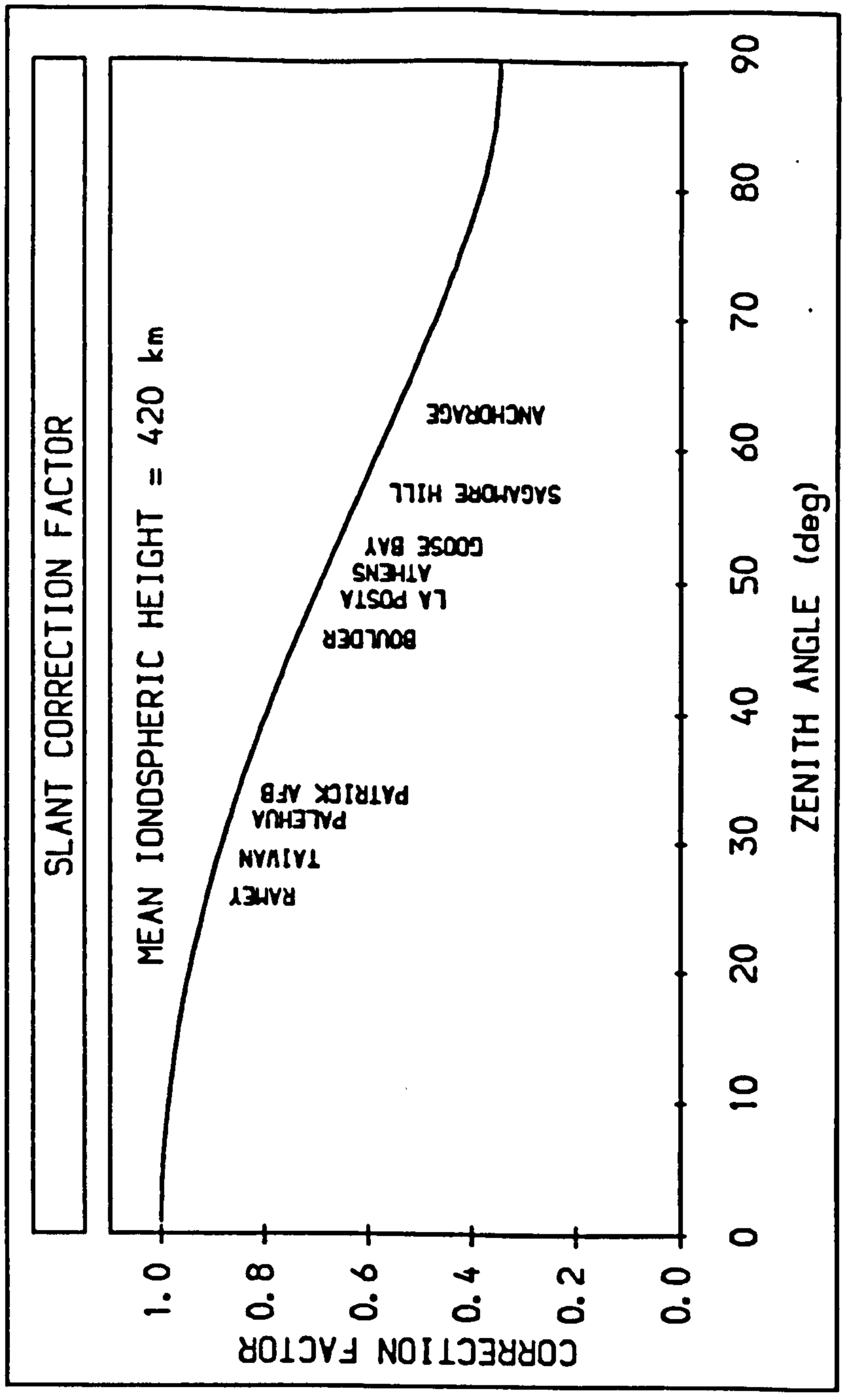

Figure 3.2 : The ionospheric zenith angles and corresponding obliquity correction factors for the ten Faraday rotation monitoring sites.

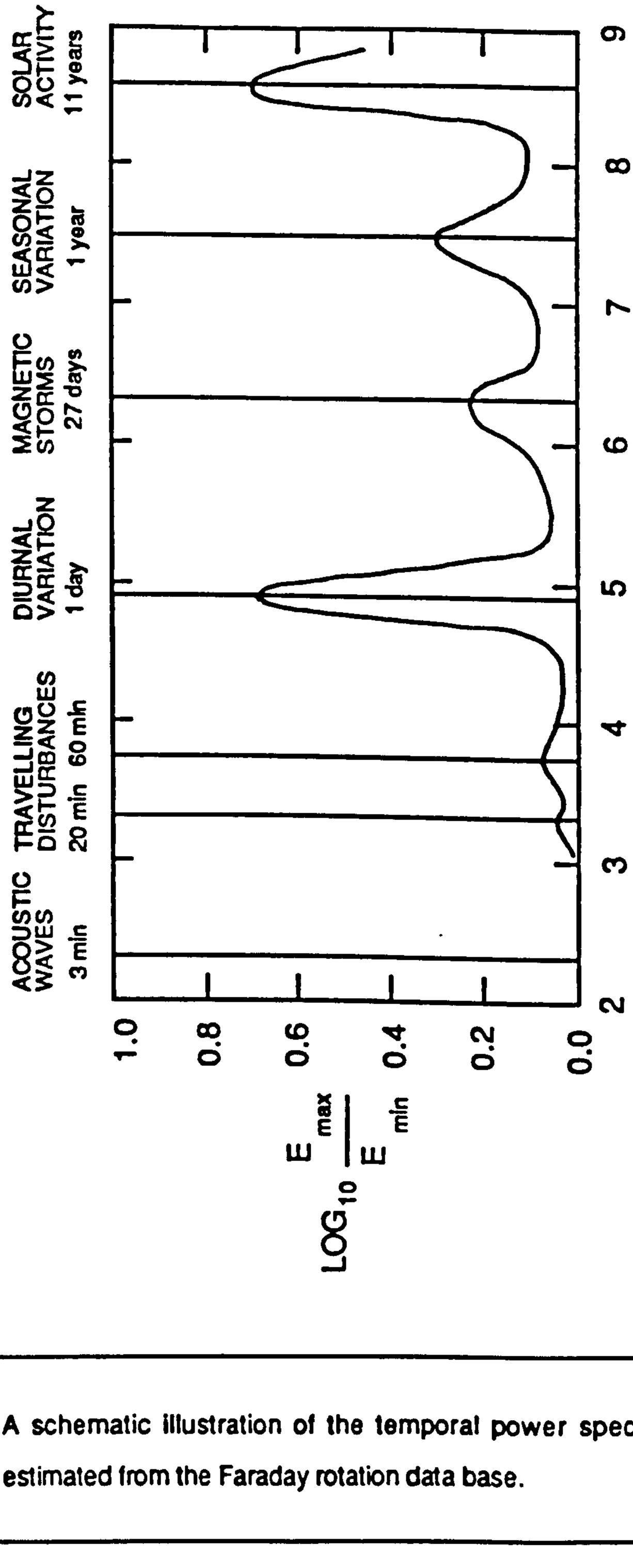

Figure 3.3 : A schematic illustration of the temporal power spectrum of electron content estimated from the Faraday rotation data base.

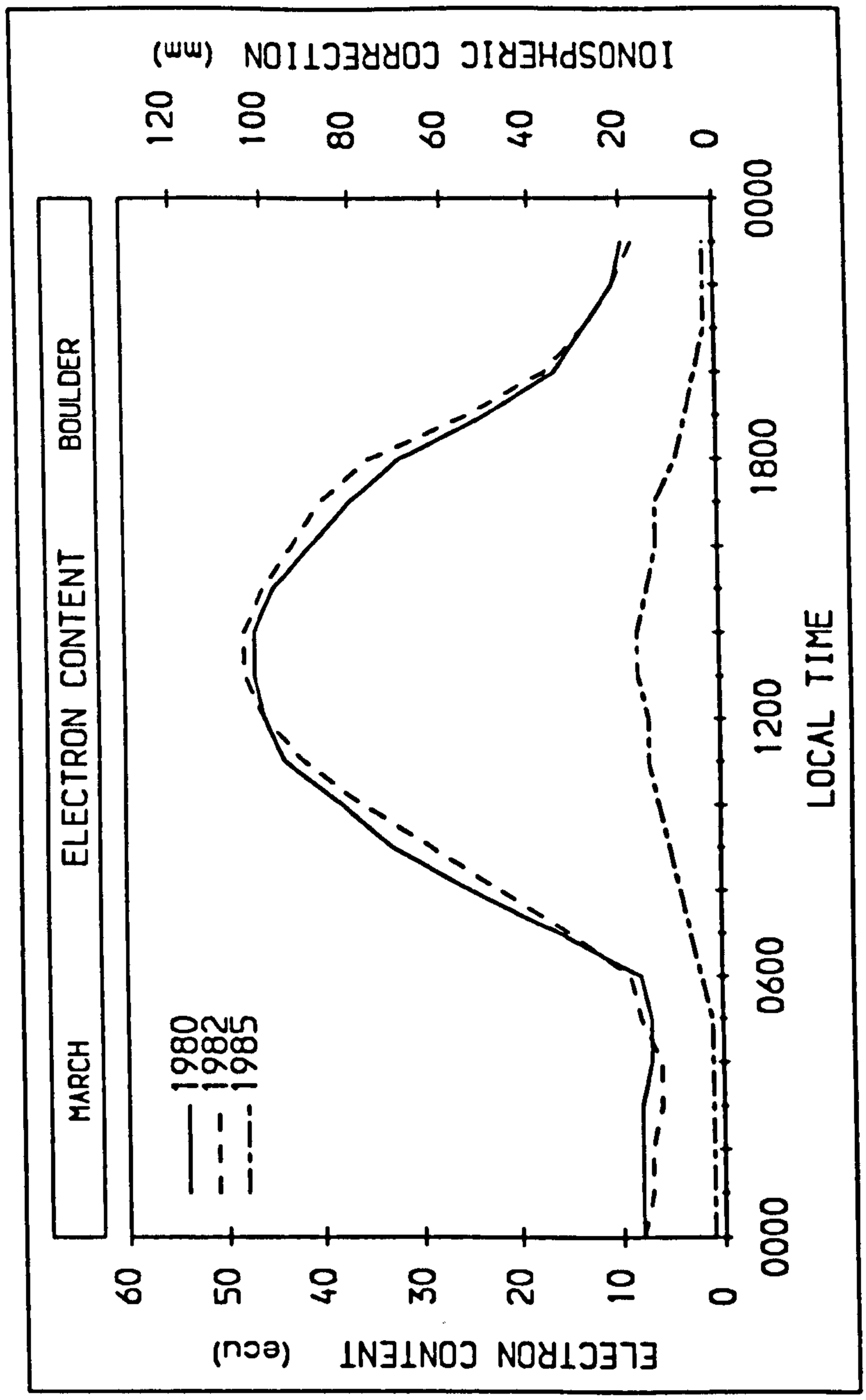

Figure 3.4 : The diurnal variation of monthly average electron content measured at Boulder during March of the three calibration years. Also shown is the corresponding ionospheric correction for an altimeter frequency of 13.8 GHz.

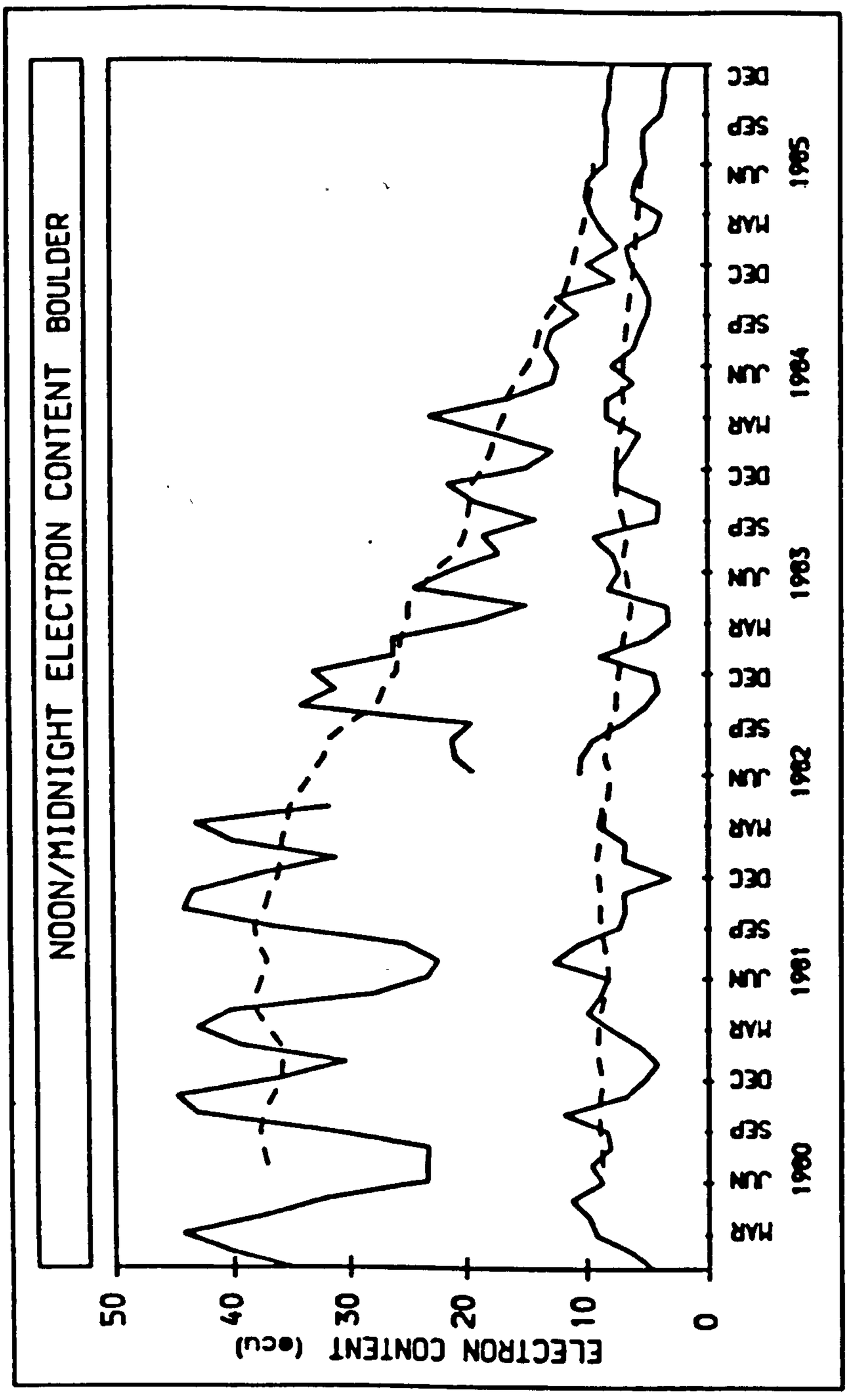

Figure 3.5 : The variation of monthly average noon and midnight electron content and their twelve–month running means measured from Boulder over the seventy two months between 1980 and 1985 inclusive (sunspot numbers 164 to 15).

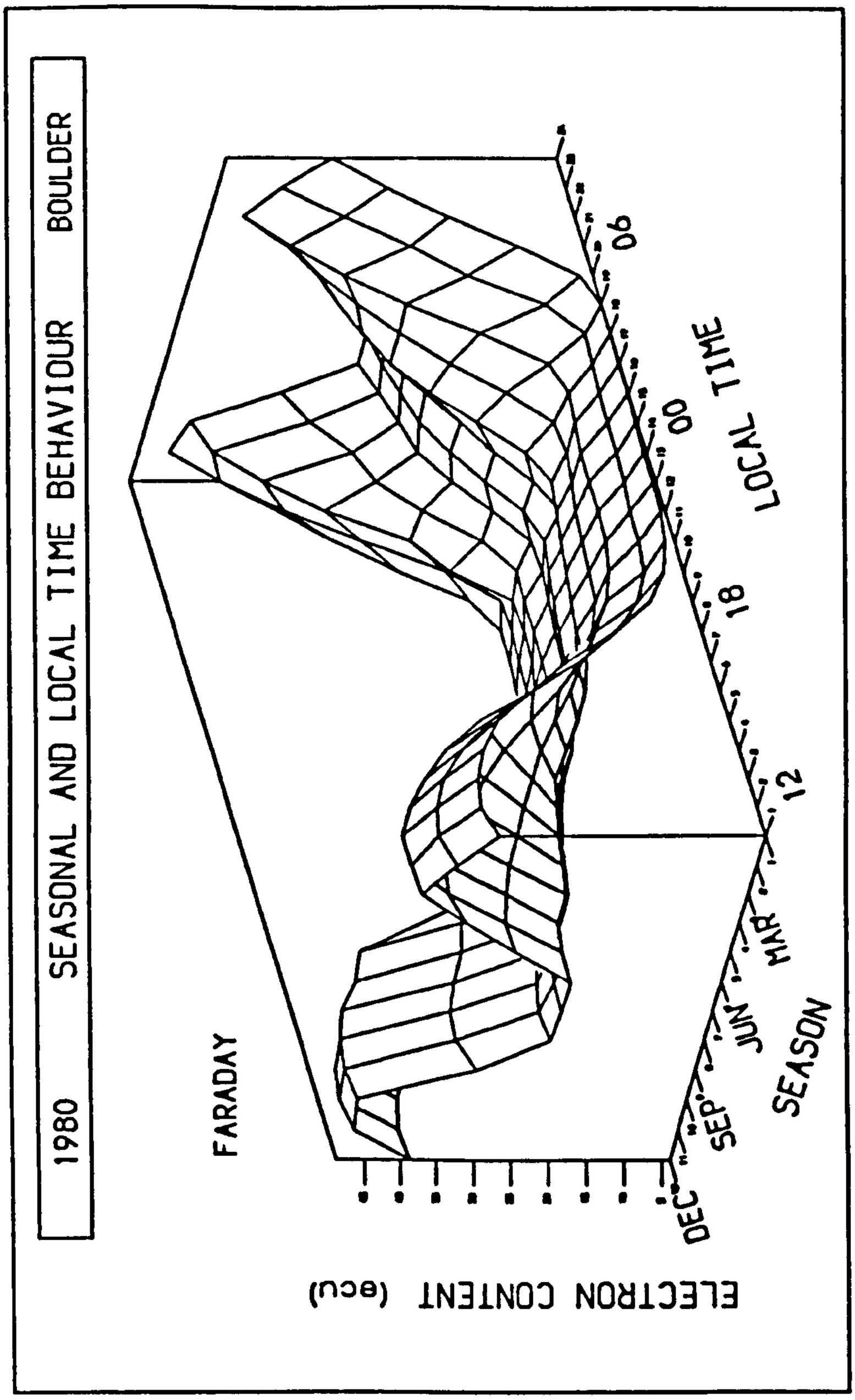

Figure 3.6 : An isometric projection showing the diurnal and seasonal variation of electron content measured from Boulder during 1980.

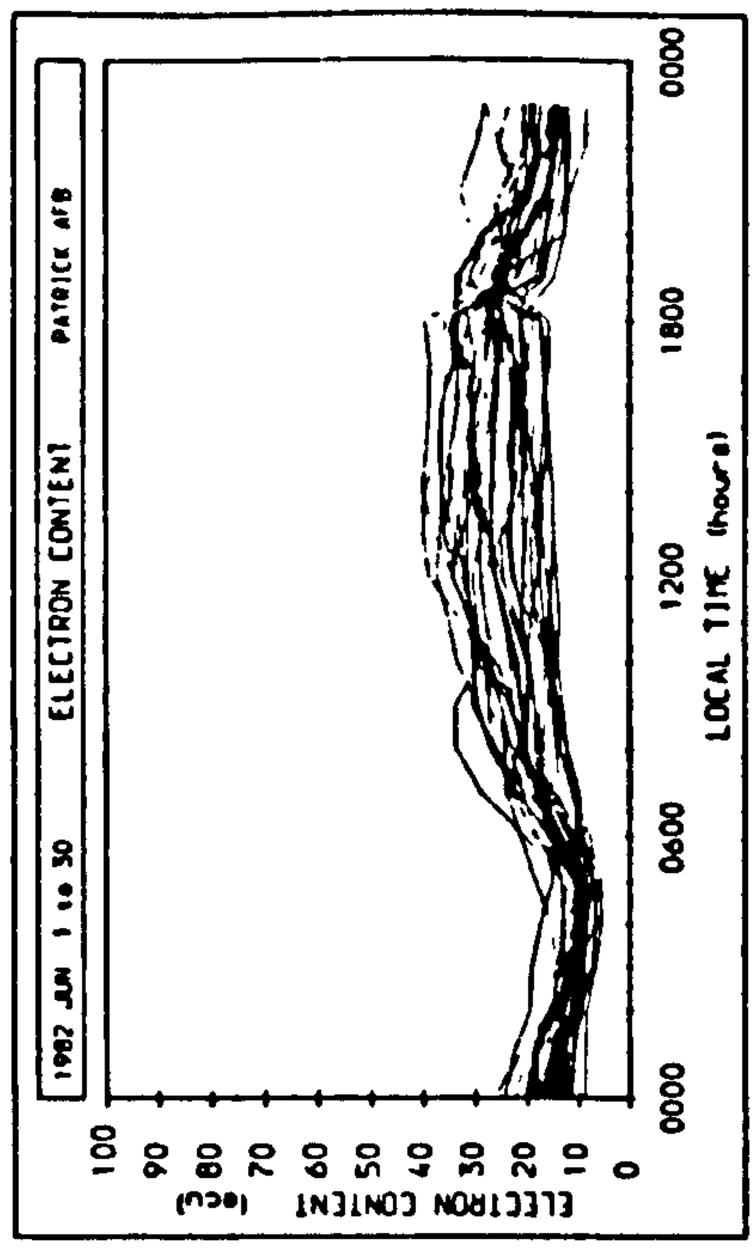

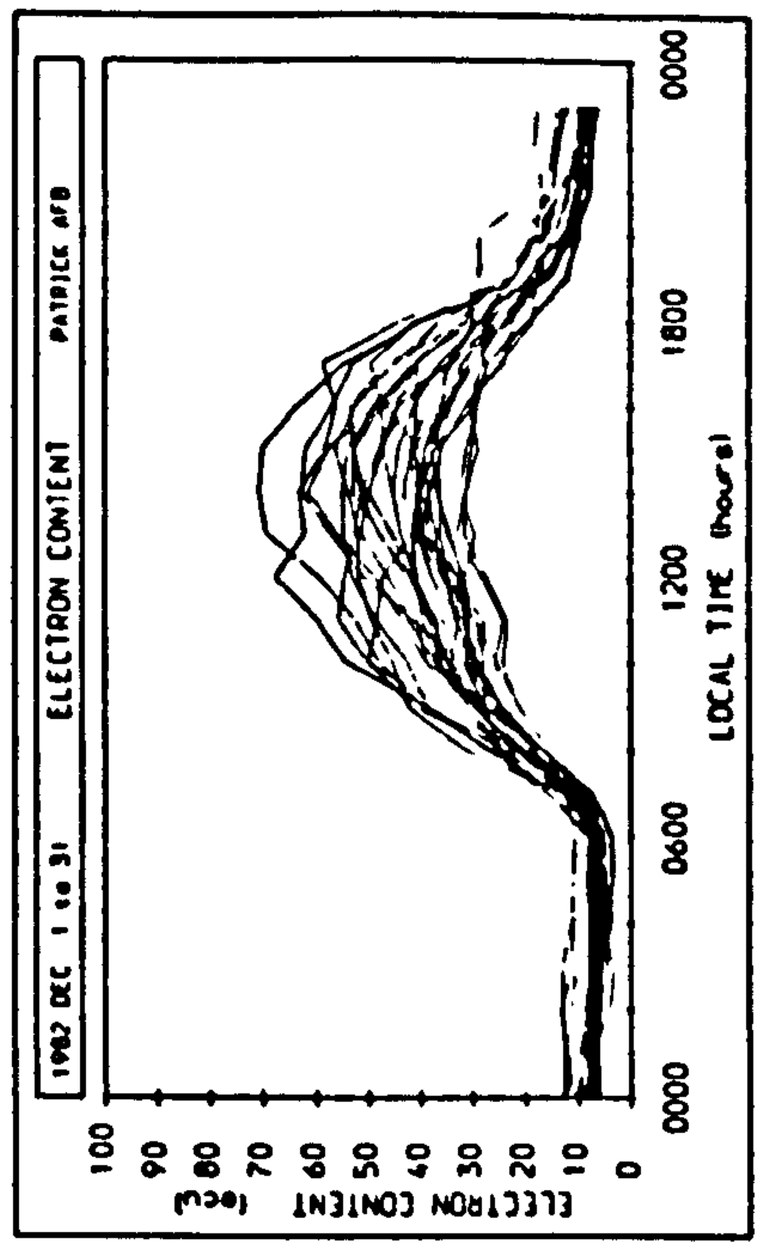

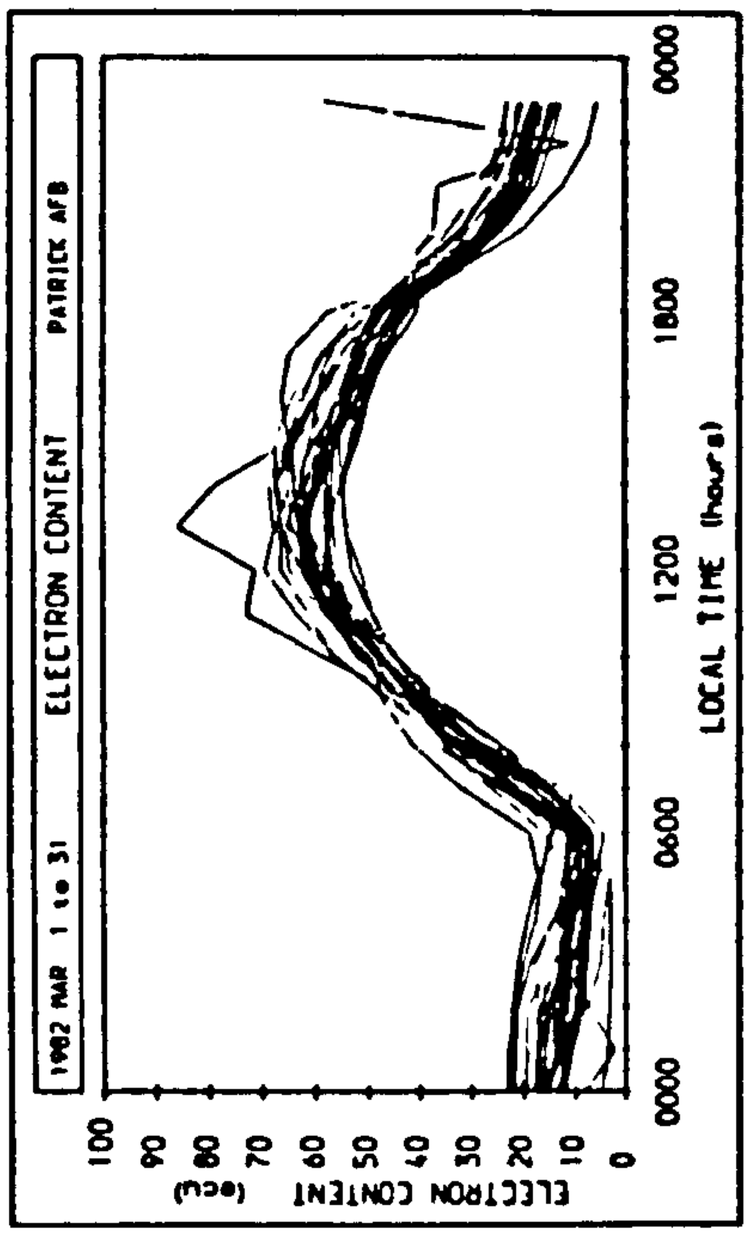

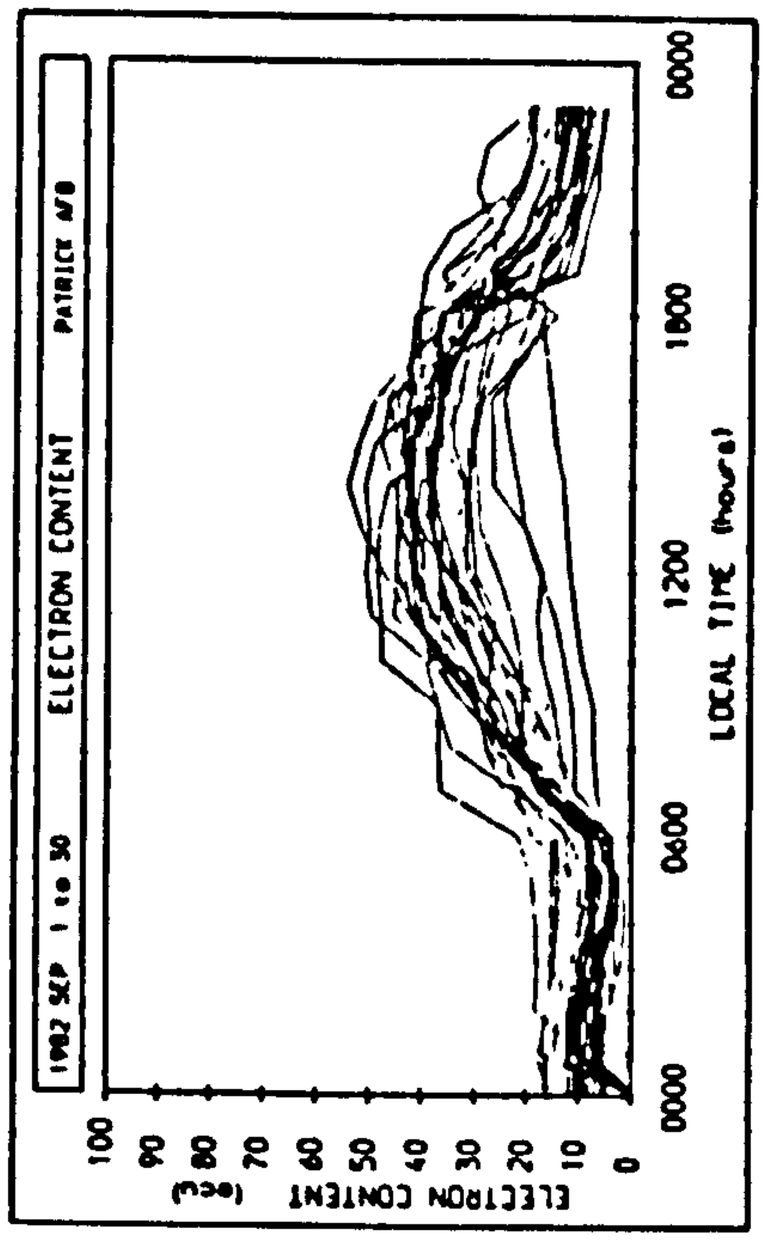

Figure 3.7 : The daily measurements of electron content taken from Patrick AFB during the calibration months of 1982.

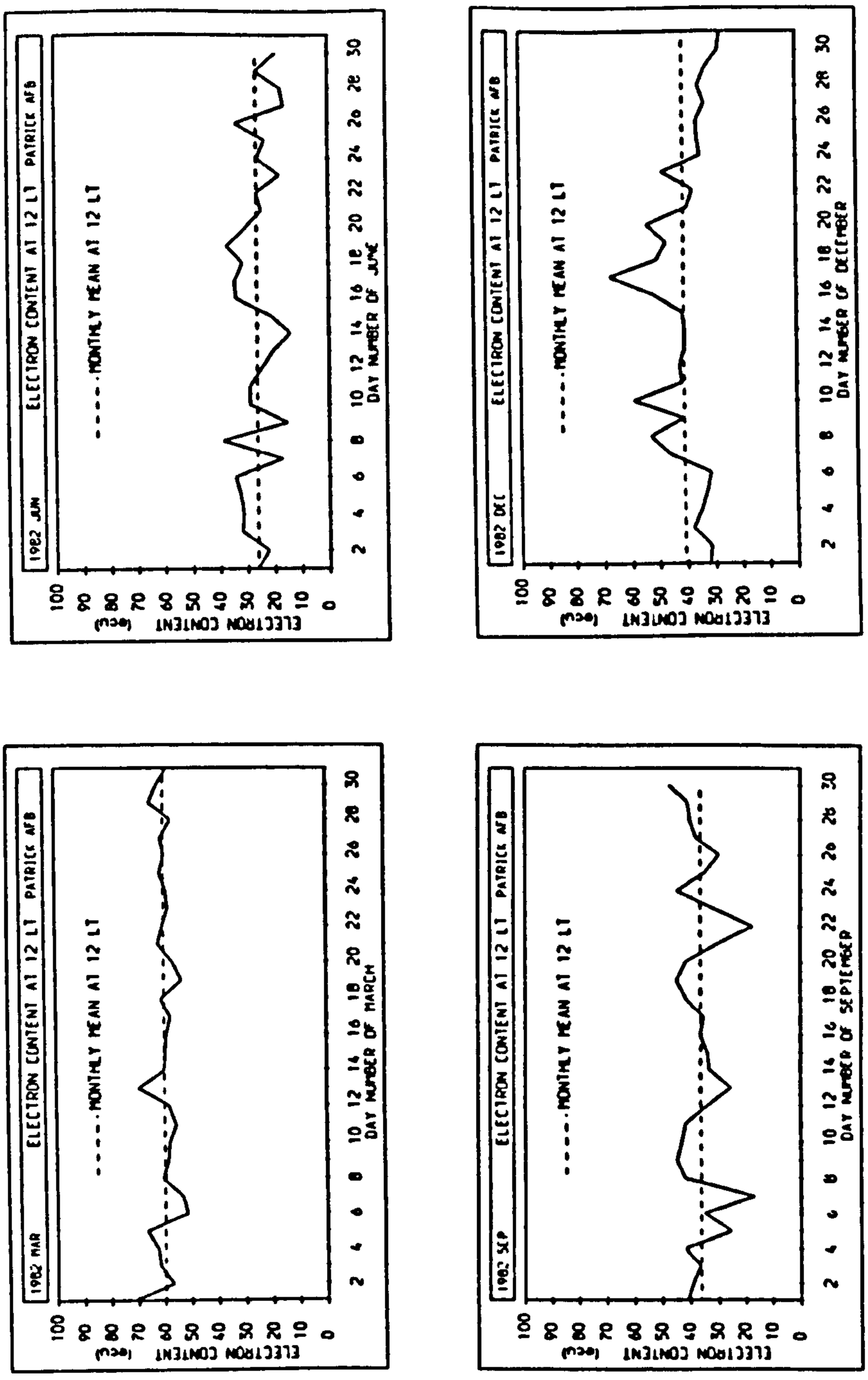

Figure 3.8 : The fluctuation of the noontime electron content about its monthly mean value as measured during the calibration months of 1982 from Patrick AFB.

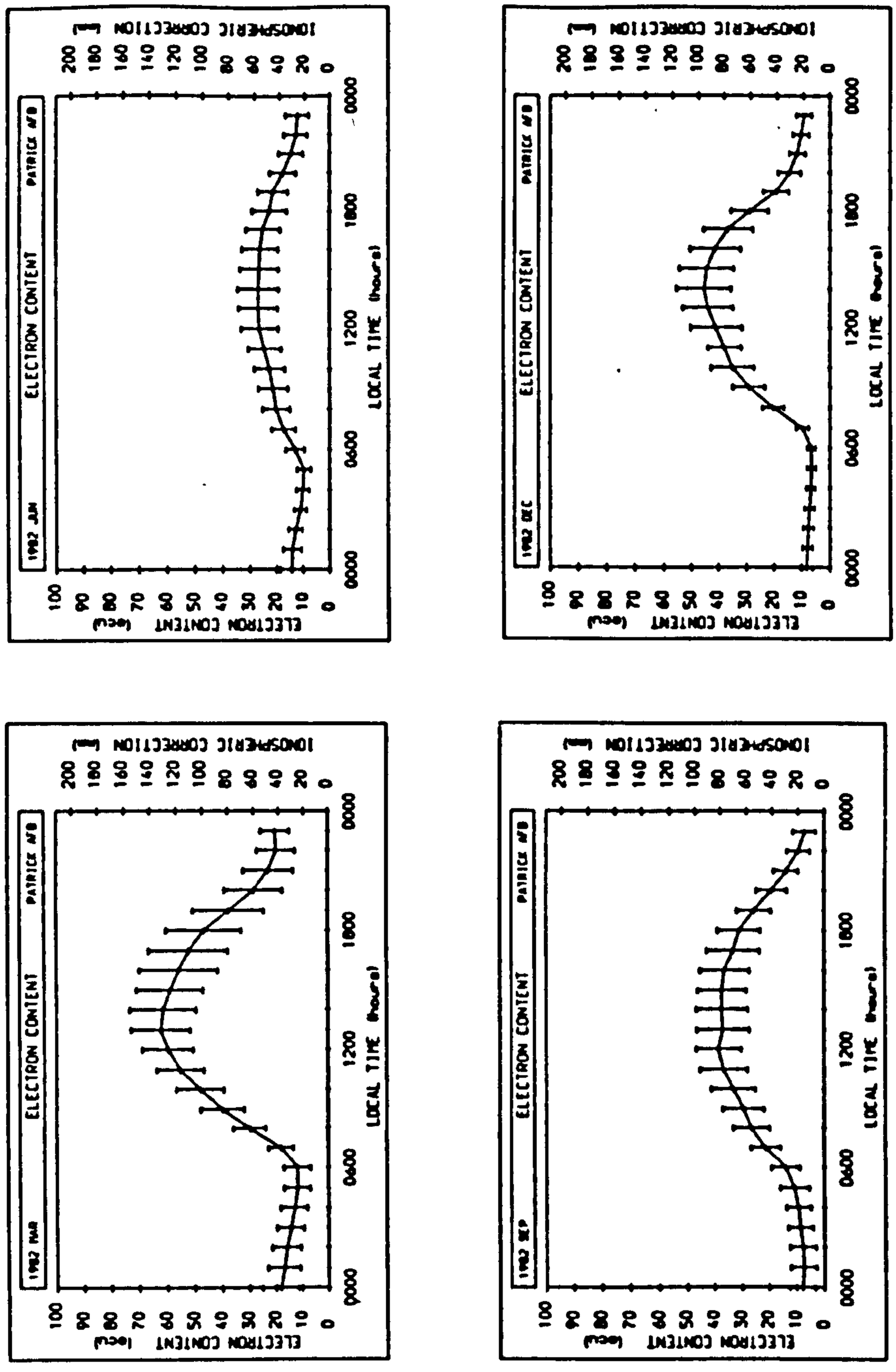

Figure 3.9 : The diurnal variation of the monthly mean electron content measured during the calibration months of 1982 from Patrick AFB. The standard deviations about the monthly mean level are depicted as error bars. The equivalent 13.8 GHz ionospheric corrections are also shown.

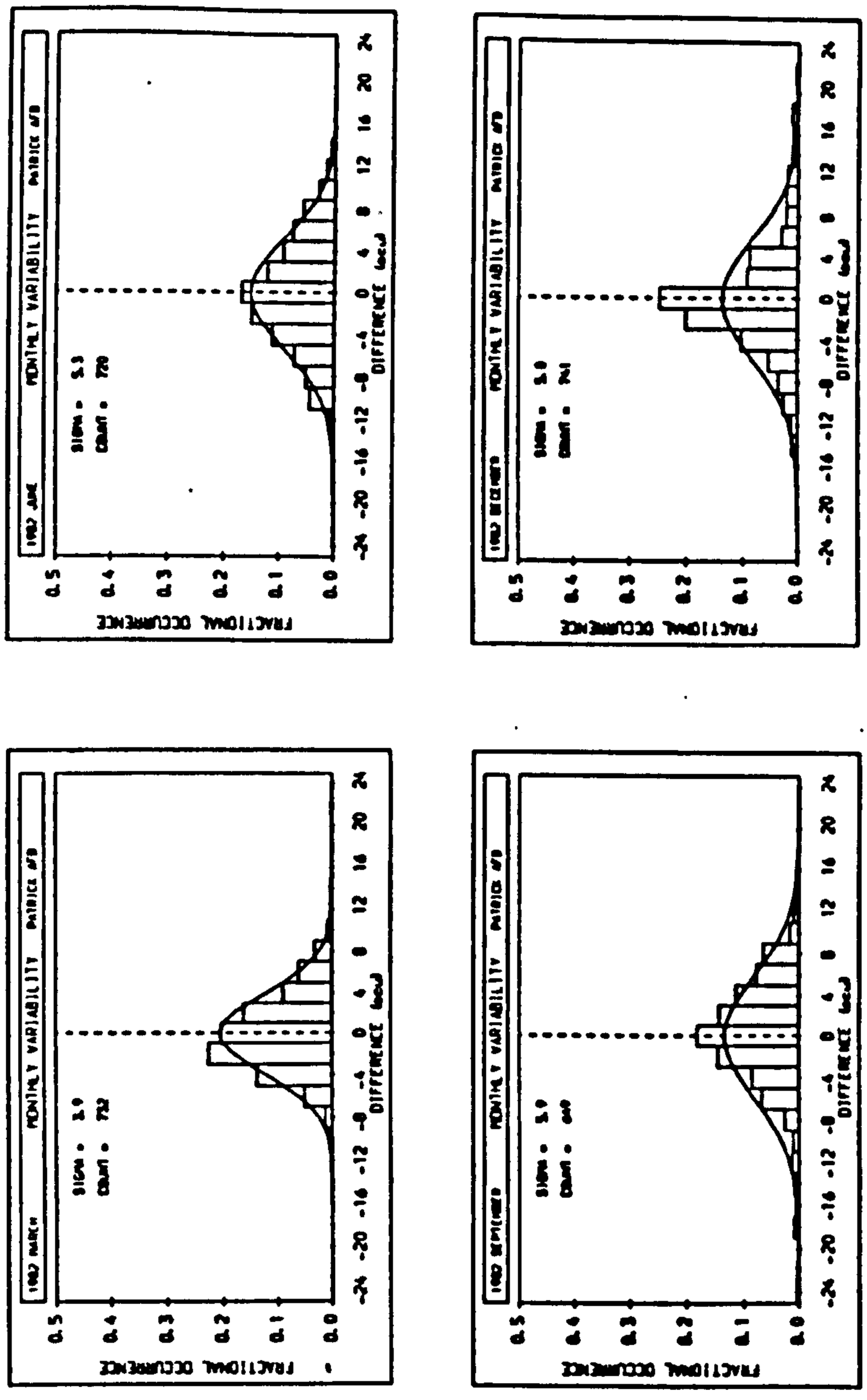

Figure 3.10 : The distribution of differences from the monthly mean of the electron content measured from Patrick during the calibration months of 1982. The histograms are overlaid with the equivalent Normal distribution. The number of hours of data available for the calculations is given as the count and the standard deviation is displayed as sigma.

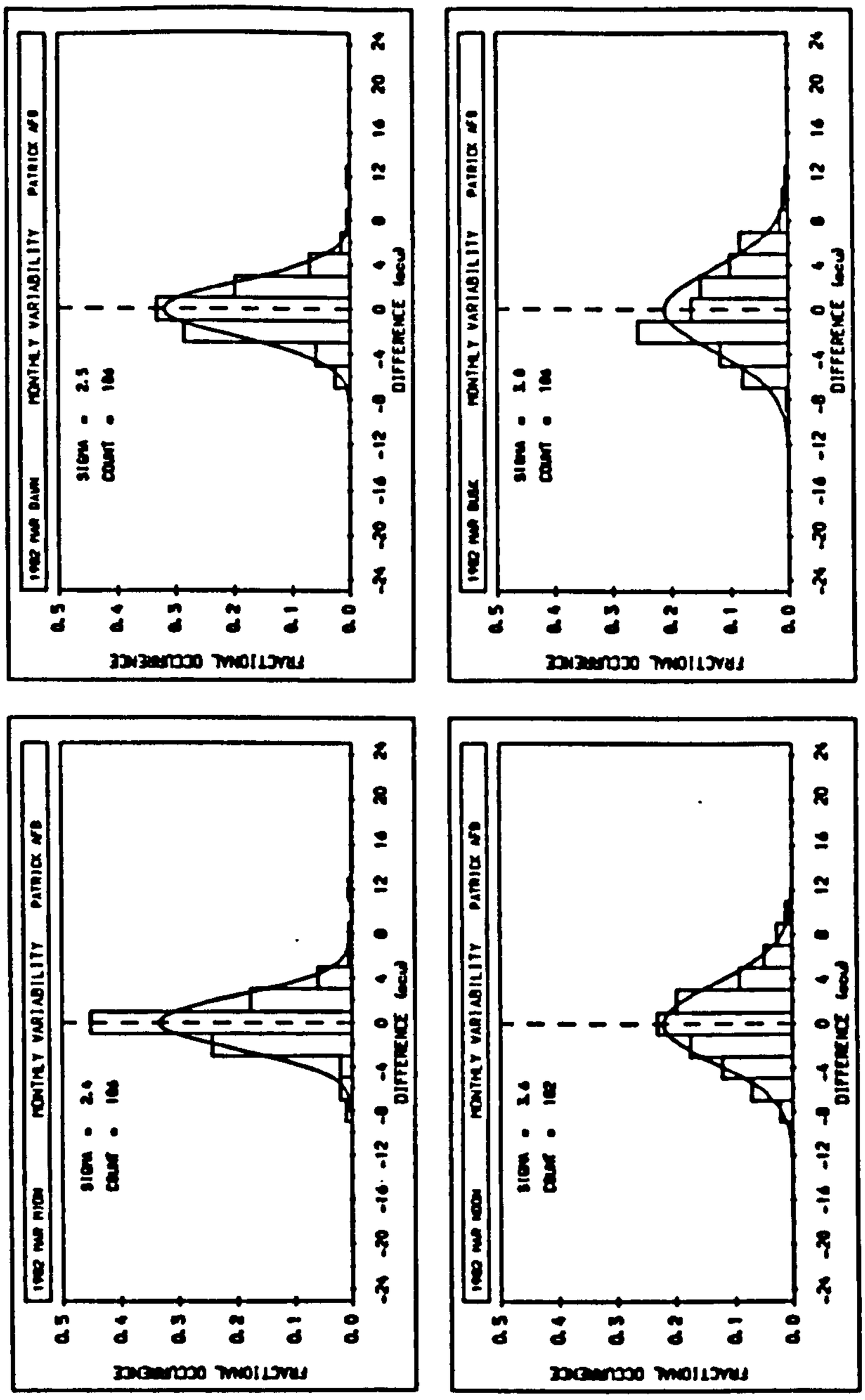

Figure 3.11 : The distribution of differences from the monthly mean of the electron content measured from Patrick during March 1982. The data is binned into four local time sectors and each panel represents one sector. The histograms are overlaid with the equivalent Normal distribution and standard deviation and counts are given as before.

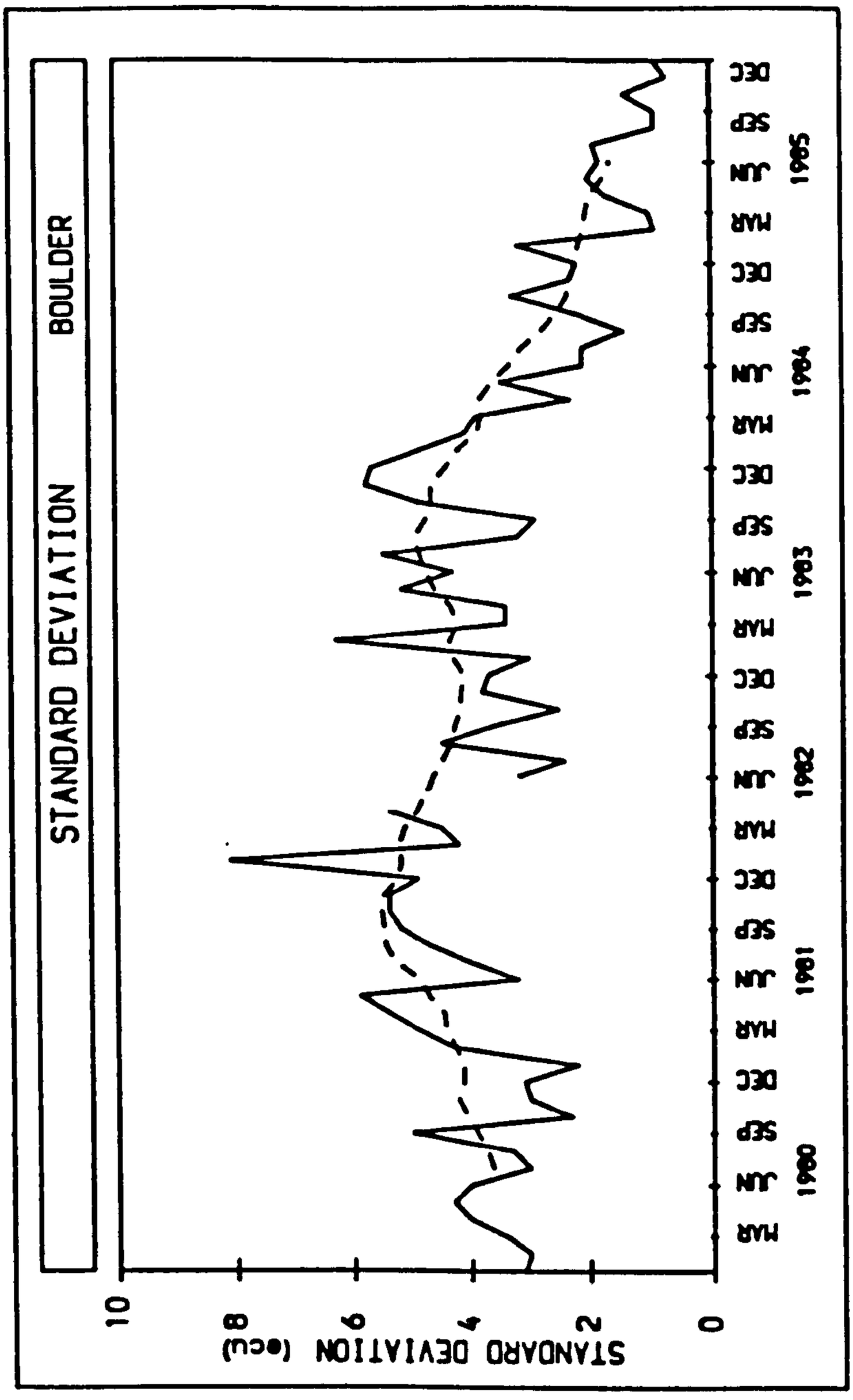

Figure 3.12 : The variation of the standard deviation of electron content and its twelve–month running mean measured from Boulder between 1980 and 1985 inclusive (sunspot numbers 164 to 15). The calculations were made over all hours of Local Time.

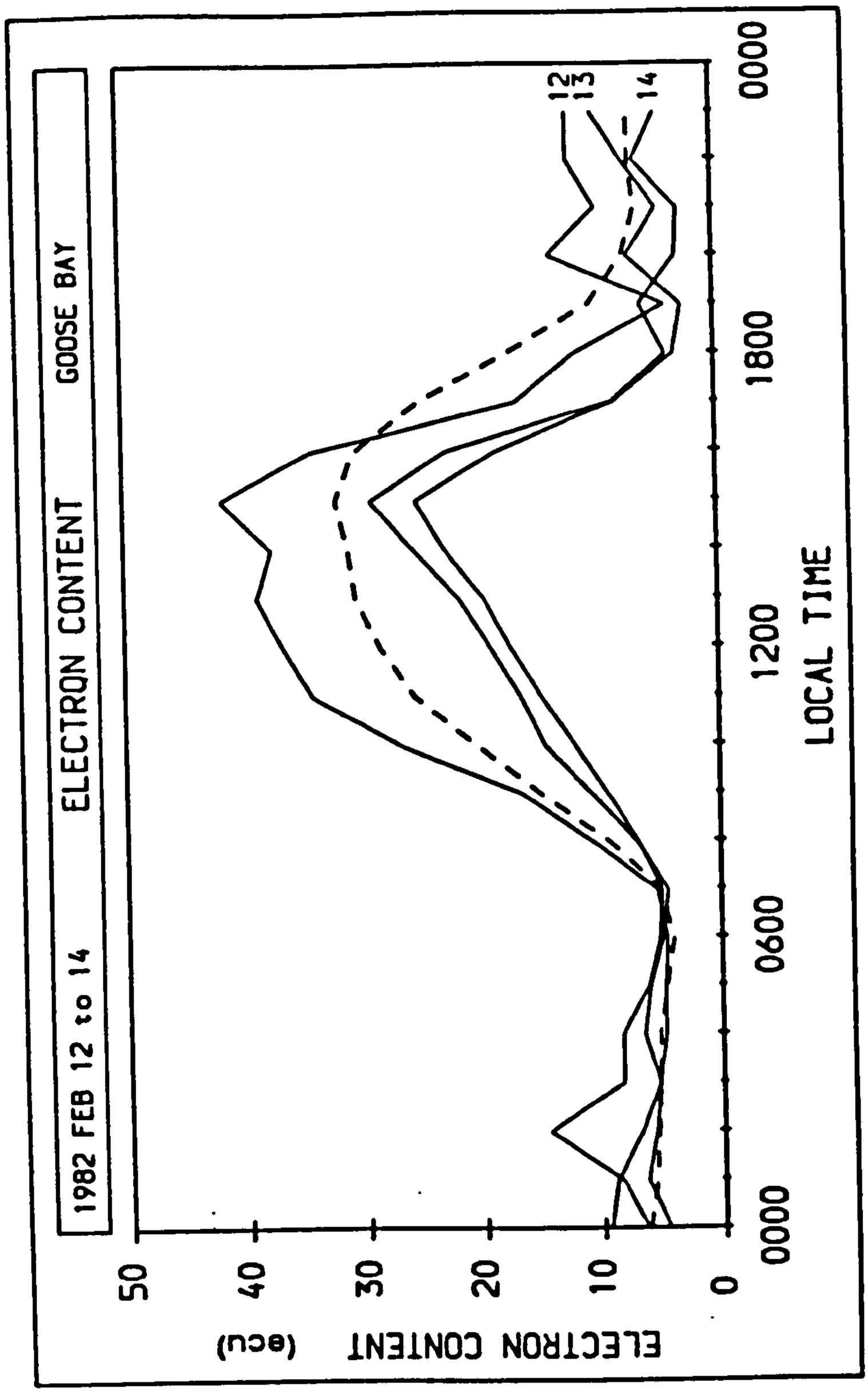

Figure 3.13 : The behaviour of electron content measured from Goose Bay during the magnetic storm 12th–14th February 1982 compared to its monthly mean (shown dotted). The trace for each day is labelled with its date.

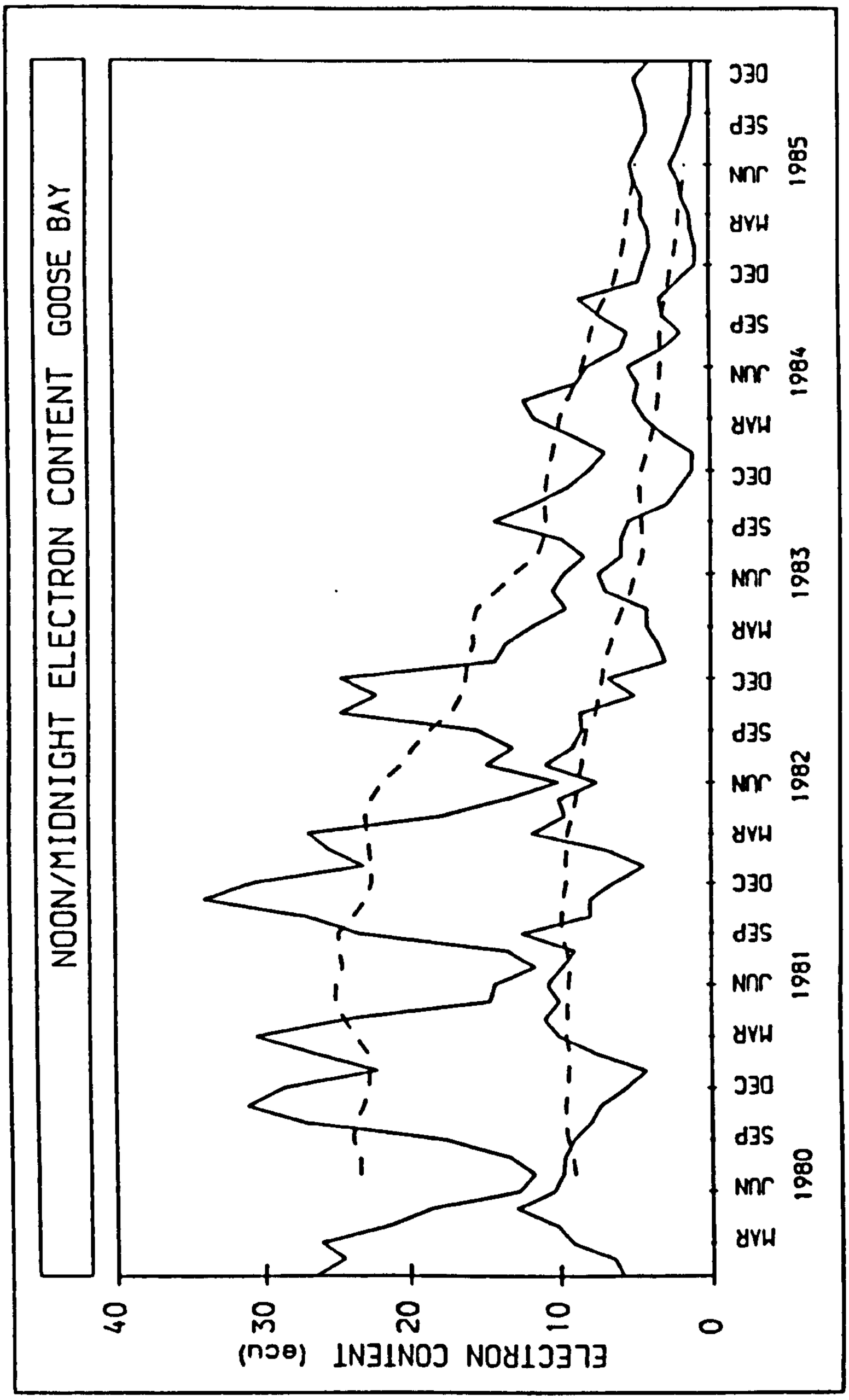

Figure 3.14 : The variation of monthly average noon and midnight electron content and their twelve-month running means measured from Goose Bay between 1980 and 1985 inclusive (sunspot numbers 164 to 15).

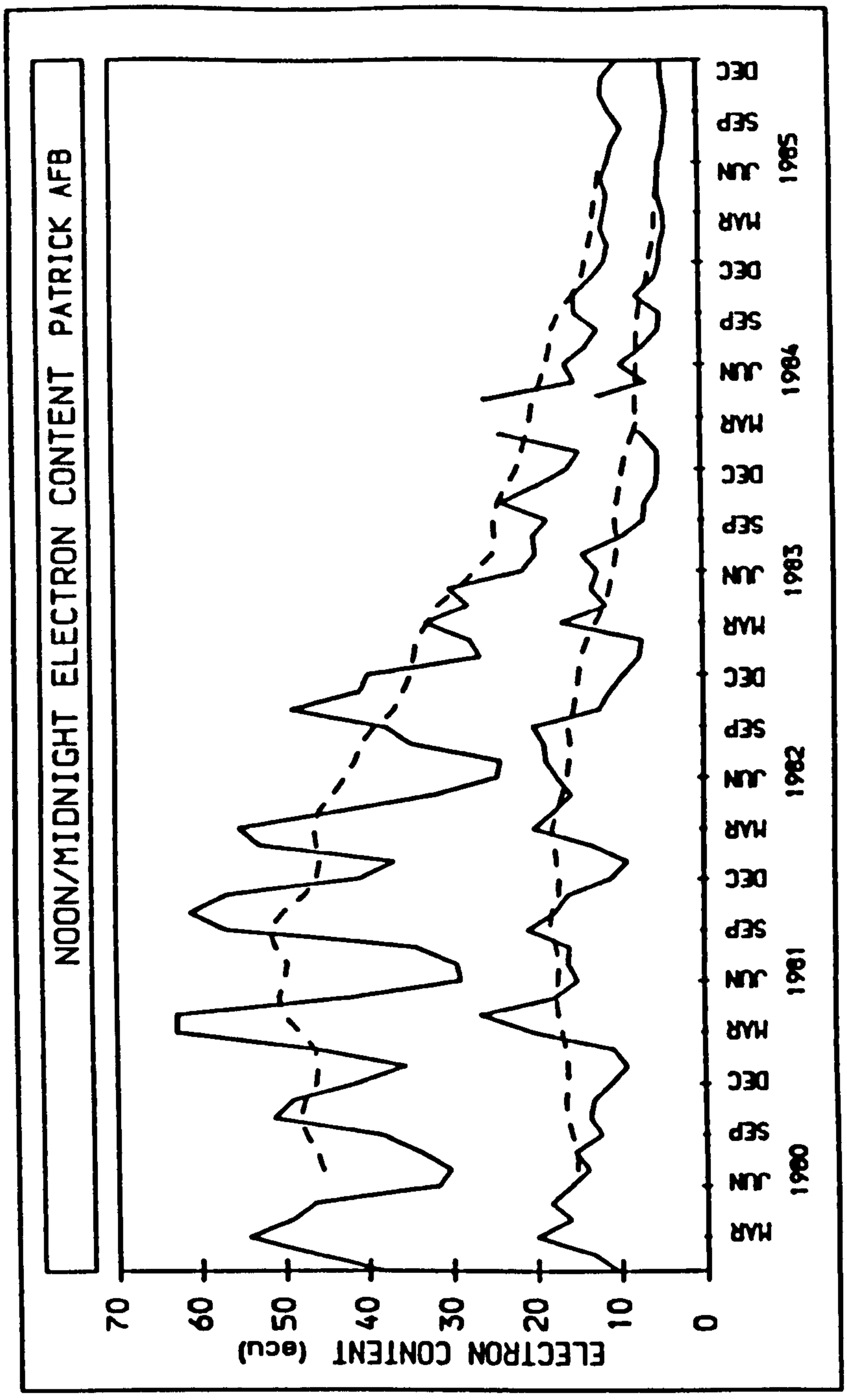

Figure 3.15 : The variation of monthly average noon and midnight electron content and their twelve–month running means measured from Patrick AFB between 1980 and 1985 inclusive (sunspot numbers 164 to 15).

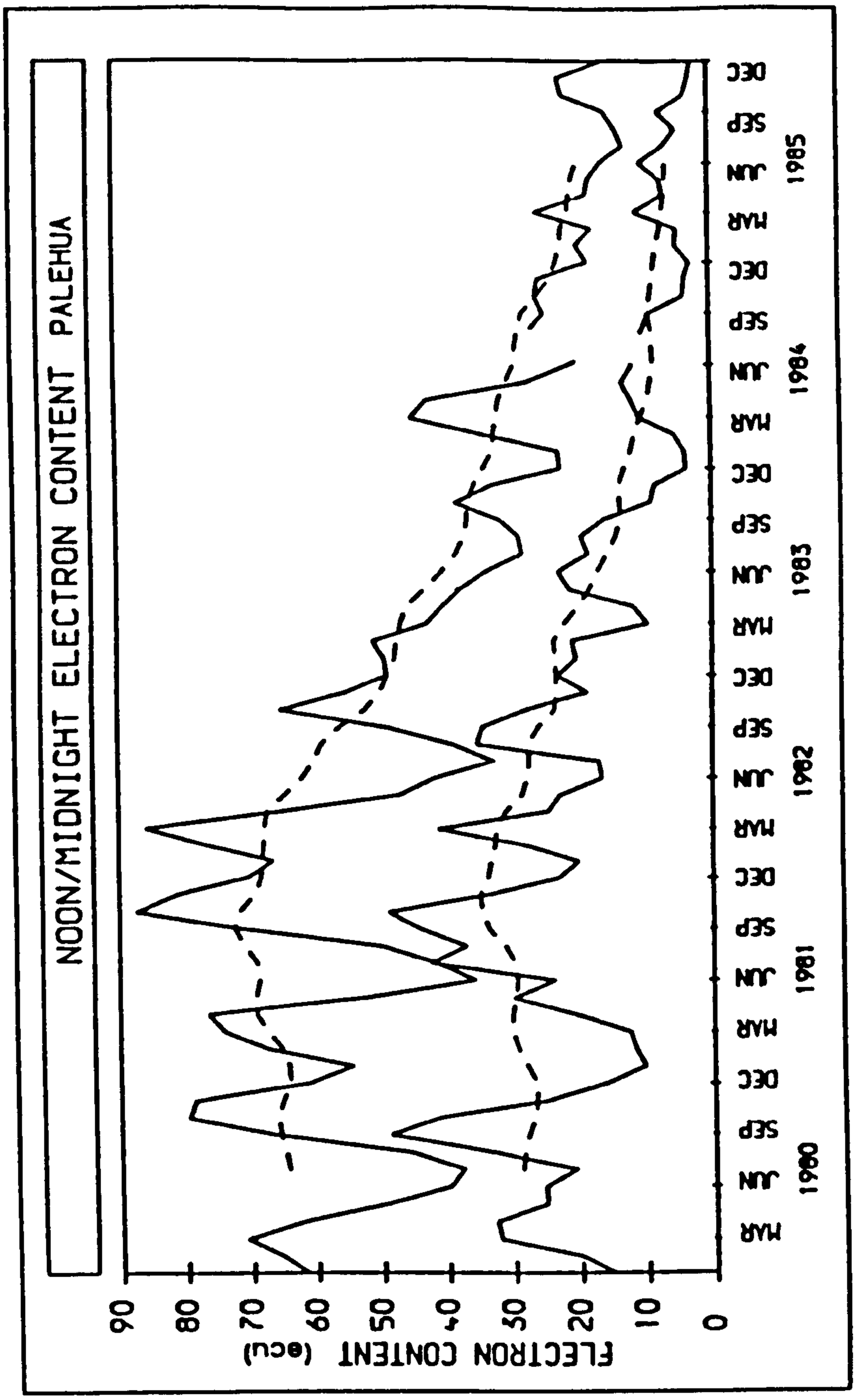

Figure 3.16 : The variation of monthly average noon and midnight electron content and their twelve–month running means measured from Palehua between 1980 and 1985 inclusive (sunspot numbers 164 to 15).

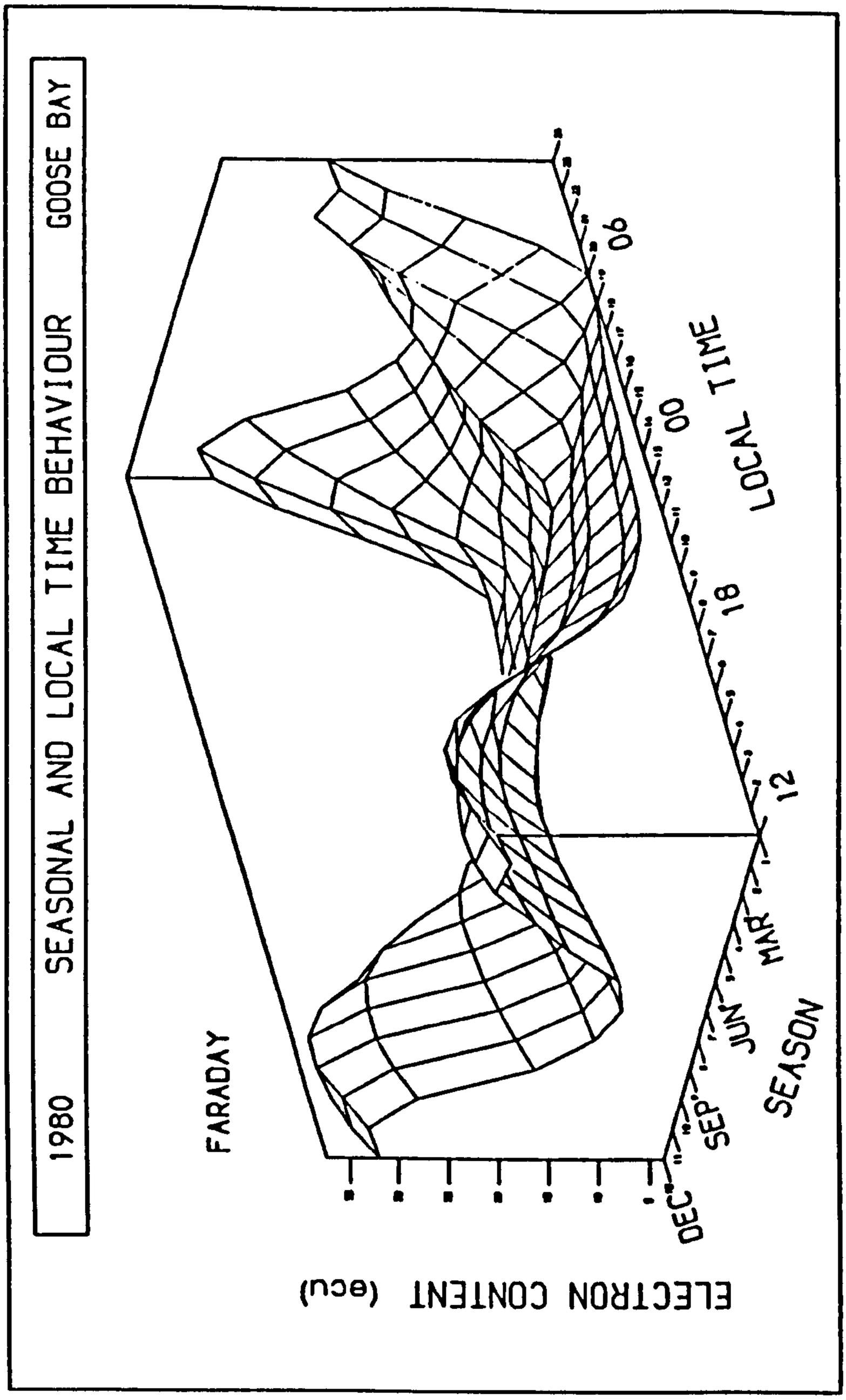

Figure 3.17 : An isometric projection showing the diurnal and seasonal variation of electron content measured from Goose Bay during 1980.

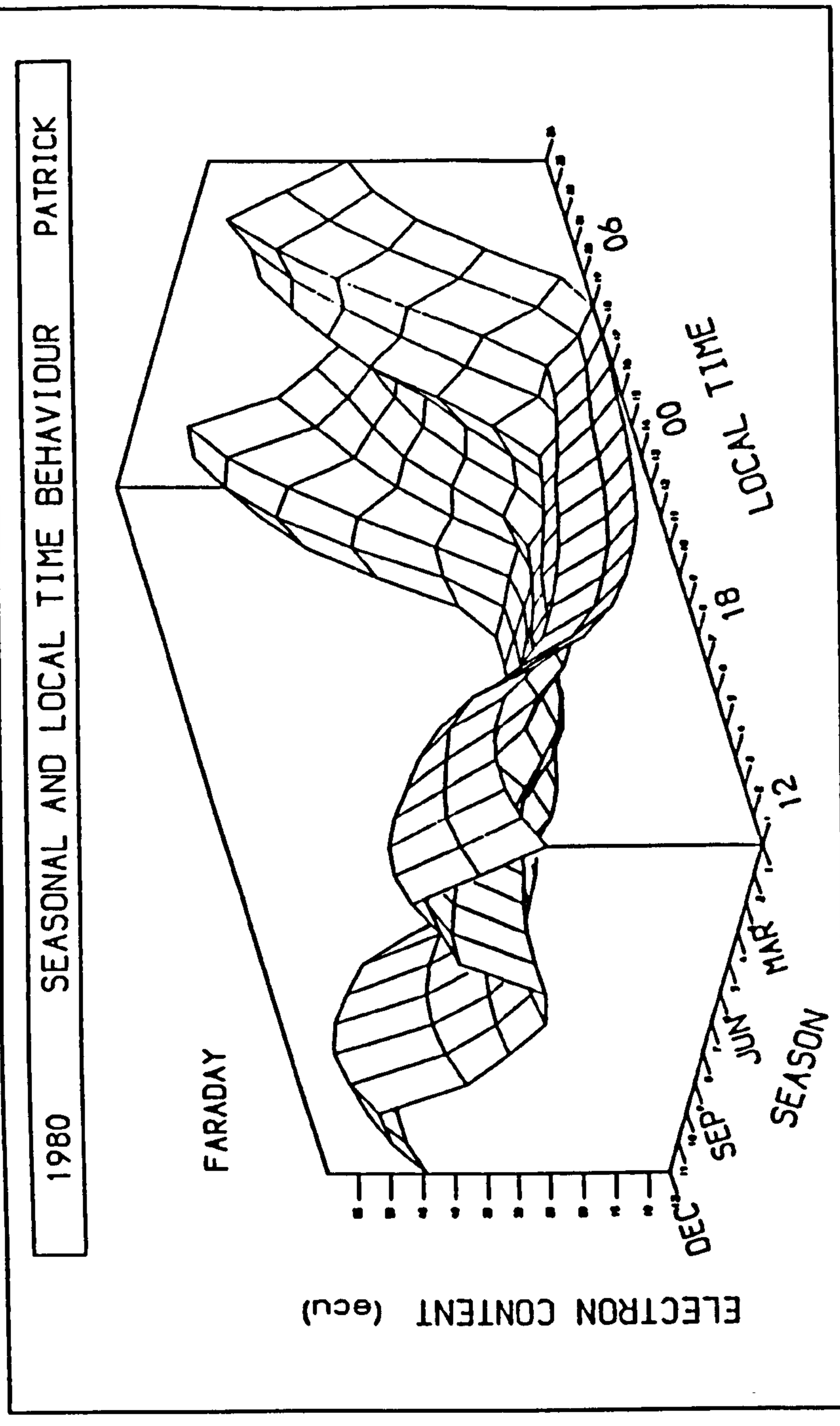

Figure 3.18 : An isometric projection showing the diurnal and seasonal variation of electron content measured from Patrick AFB during 1980.

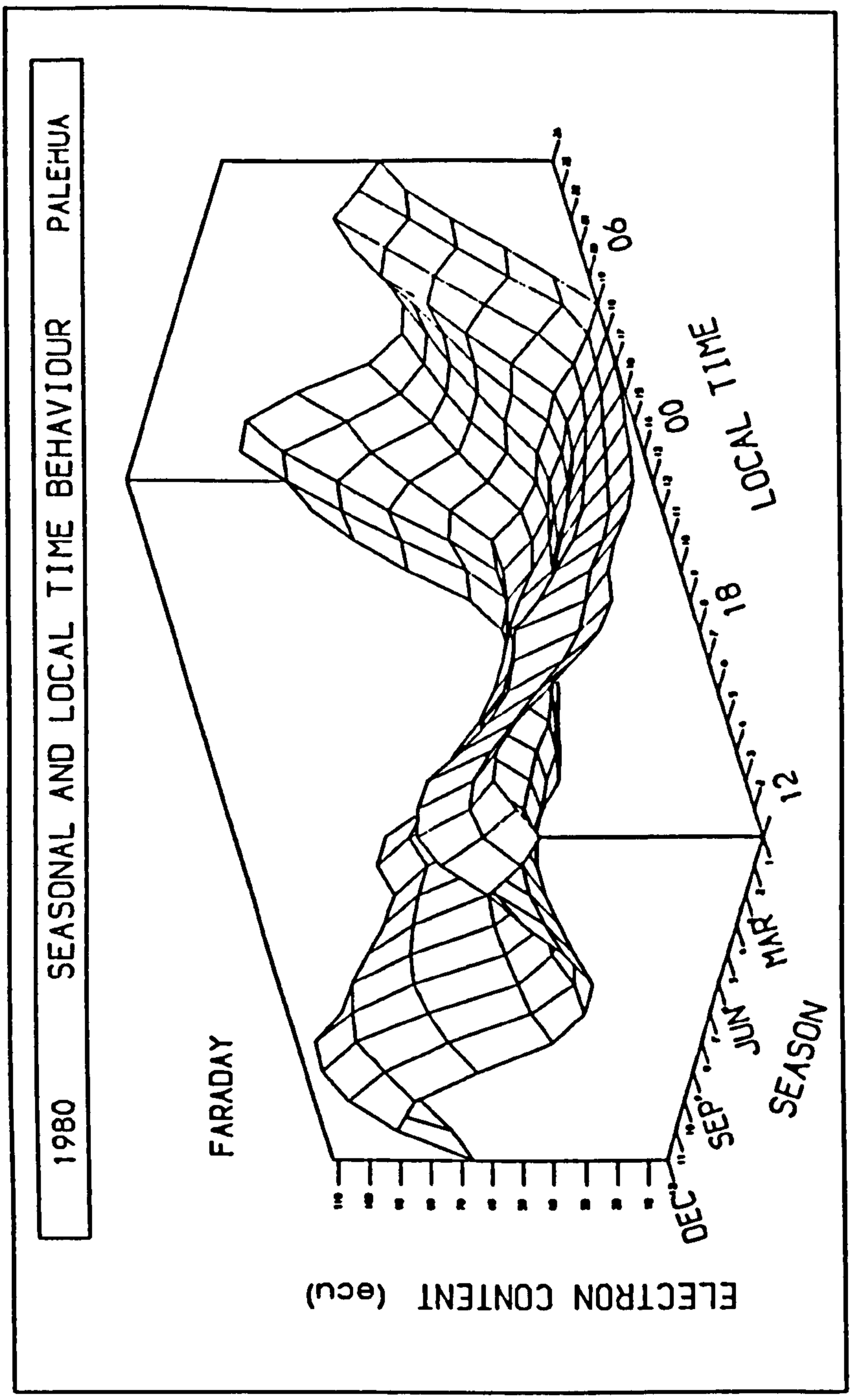

Figure 3.19 : An isometric projection showing the diurnal and seasonal variation of electron content measured from Palehua during 1980.

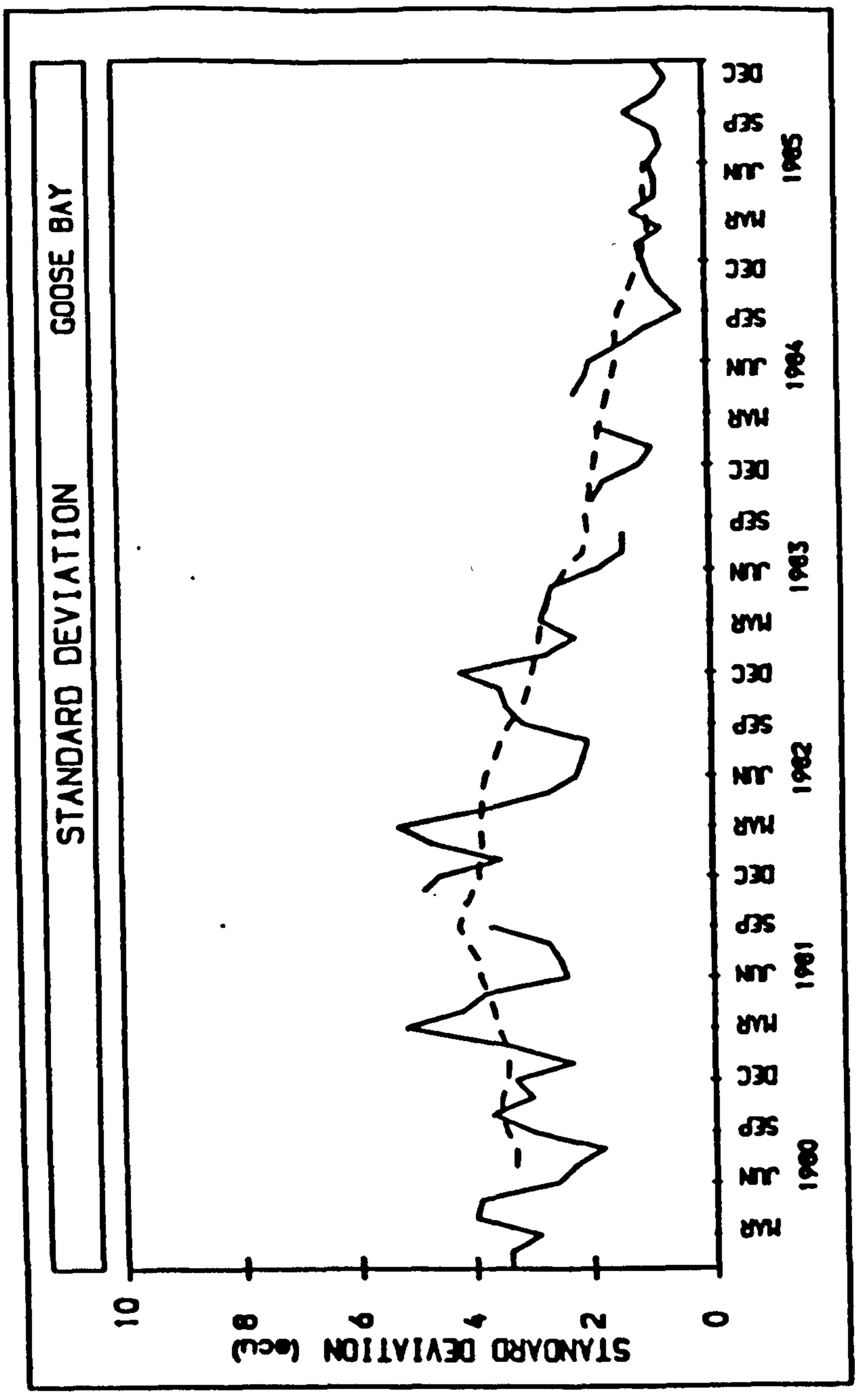

Figure 3.20 : The variation of the standard deviation of electron content and its twelve–month running mean measured from Goose Bay over the seventy two months between 1980 and 1985 inclusive (sunspot numbers 164 to 15). The calculations were made over all hours of Local Time.

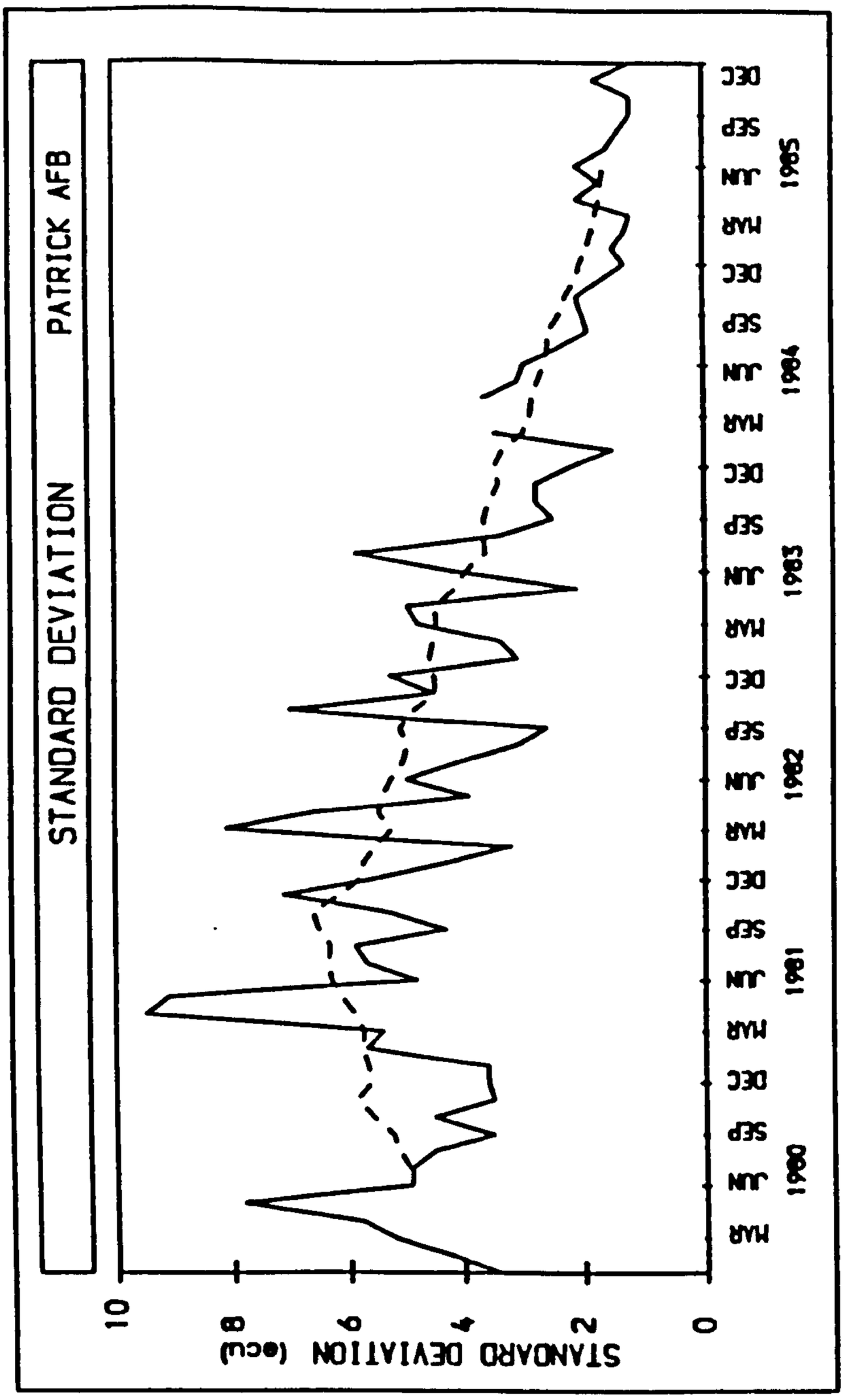

Figure 3.21 : The variation of the standard deviation of electron content and its twelve–month running mean measured from Patrick AFB over the seventy two months between 1980 and 1985 inclusive (sunspot numbers 164 to 15). The calculations were made over all hours of Local Time.

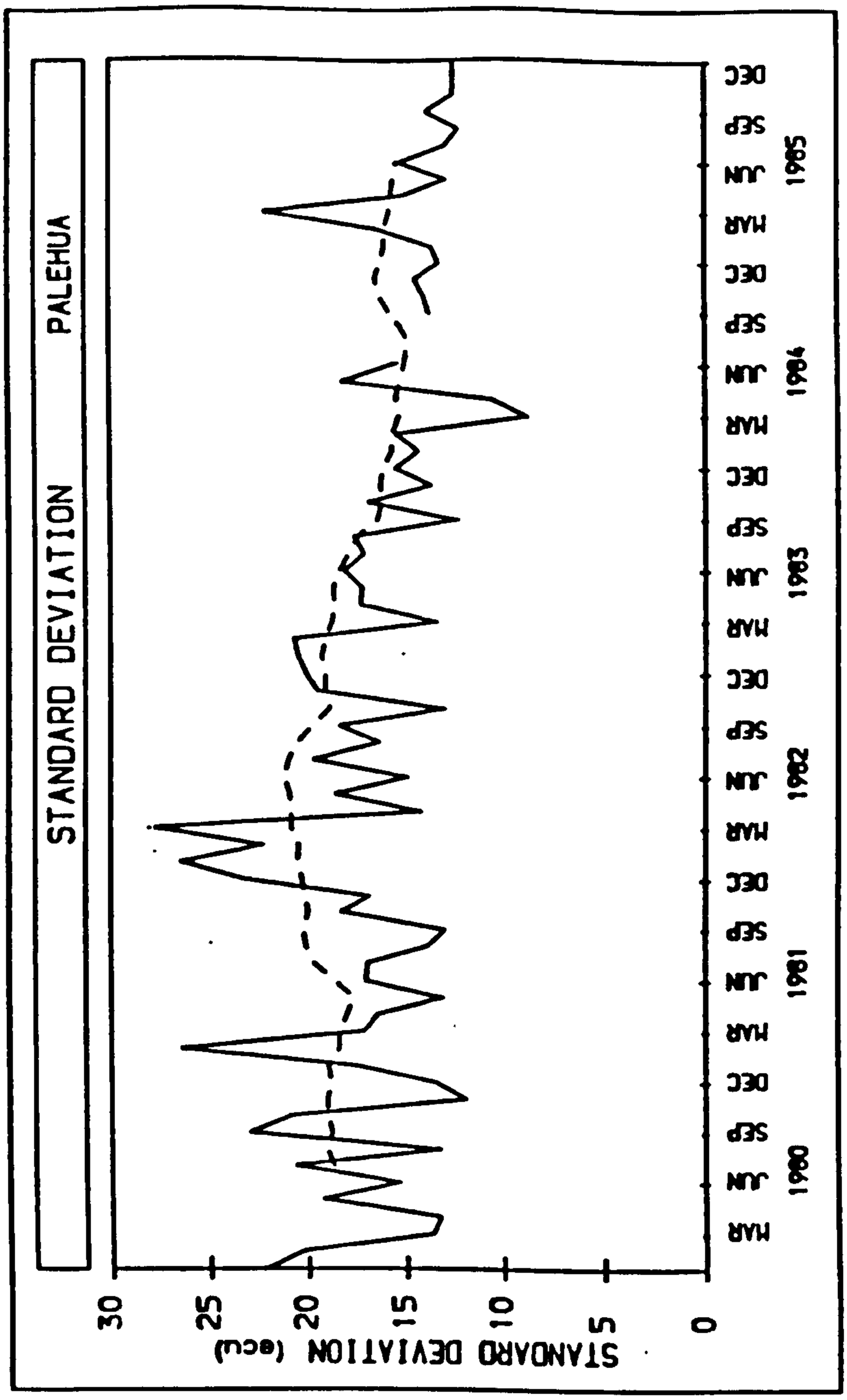

Figure 3.22 : The variation of the standard deviation of electron content and its twelve–month running mean measured from Palehua over the seventy two months between 1980 and 1985 inclusive (sunspot numbers 164 to 15). The calculations were made over all hours of Local Time.

	STATION NAME	SATELLITE (1980)
1	ANCHORAGE, ALASKA	GOES2
2	ATHENS, GREECE	SIRIO
3	BOULDER, COLORADO	GOES2
4	GOOSE BAY, LABRADOR	ATS5
5	LA POSTA , CALIFORNIA	GOES1
6	PALEHUA, HAWAII	ATS1
7	PATRICK AIR FORCE BASE, FLORIDA	ATS5
8	RAMEY, PUERTO RICO	ATS5
9	SAGAMORE HILL, MASSACHUSETTS	ATS5
10	LUNPING, TAIWAN	ETS2

Table 3.1 : The ten Faraday rotation receiving sites where, between 1980 and 1985, the electron content data employed in this study were collected.

RECEIVING SITE	GEOG. POINT (°N, °E)	IONOS. POINT (°N, °E)	L–SHELL OF IONOS. POINT	ZENITH ANGLE (degrees)
ANCHORAGE	61 210	53 216	3.0	63
GOOSE BAY	53 300	48 298	3.8	53
SAGAMORE HILL	41 281	39 289	2.4	57
BOULDER	40 255	36 255	2.0	46
ATHENS	38 24	35 18	1.5	53
LA POSTA	33 242	30 247	1.6	52
PATRICK A.F.B.	28 279	26 280	1.6	32
LUNPING	25 121	23 122	1.1	29
PALEHUA	21 202	20 204	1.1	32
RAMEY	19 293	17 294	1.5	26

Table 3.2 : Geographical co–ordinates of the Faraday rotation receiving sites and the geographical and geomagnetic co–ordinates of their ionospheric points.

	1980	1982	1985
MARCH	161	129	19
JUNE	155	117	18
SEPTEMBER	150	101	17
DECEMBER	143	95	15

Table 3.3 : The 12 month running mean sunspot number prevailing during the twelve calibration months.

YEAR	MONTH	STANDARD DEVIATION	STATION HOURS	POSSIBLE
1980	MAR	3.7	665	744
	JUN	4.2	579	720
	SEP	5.5	681	720
	DEC	3.0	743	744
1982	MAR	4.9	682	744
	JUN	3.2	461	720
	SEP	4.1	688	720
	DEC	4.2	704	744
1985	MAR	1.0	738	744
	JUN	1.9	660	720
	SEP	1.0	634	720
	DEC	1.0	737	744

Table 3.4 : The standard deviations of electron content as measured at the Boulder site during the calibration months along with the number of station hours of data available from Boulder for each of the twelve months.

Chapter 4 : Definition of the Predictive and Adaptive Models

This chapter aims to describe the various mathematical sub–models which, when assembled, produce climatological models of electron content. In addition it reviews the adaptive technique by which estimates of the mean so generated can be adjusted for day–to–day ionospheric variability. The function of the Predictive Model is the reproduction of monthly average variations of electron content as closely as possible for a restricted set of input conditions. The purpose of the Adaptive Model is the incorporation of electron content measurements to adjust predictions for the conditions prevailing in the ionosphere local to the prediction point.

4.1 Electron Density Profiles

The first stage of the prediction of monthly mean electron content requires the definition of an altitude profile of electron density. In the context of electron content prediction, the detail of the profile is unimportant as long as the electron content is predicted accurately. Two profiles often employed for ionospheric work were assessed, the Chapman profile (Chapman 1931) shown in Figure 4.1 and the Bent profile (Llewellyn and Bent 1973) shown in Figure 4.2. The Chapman profile is described continuously in altitude by Equations 4.1 and 4.2, whereas the Bent profile is described discontinuously by Equations 4.3 to 4.7. Both profiles essentially describe the ionosphere as a single layer. The Chapman profile is the result of one of the earliest physical models of ionospheric production whereas the Bent profile is a purely descriptive model derived from hundreds of thousands of topside and bottomside ionosonde profiles.

Two types of Chapman profile are defined according to the dominant electron loss process. If electrons are lost through attachment to neutral molecules then the resulting layer is known as a β–Chapman profile. If the principal loss process is direct recombination with positive ions then a thicker α–Chapman profile is the result. Preliminary tests on the prediction of noon electron content values revealed that the thinner β–profile underestimated the electron content quite severely and hence only the α–Chapman layer was considered further and henceforth the α–prefix will be dropped.

The α–Chapman profile is given by Equations 4.1 and 4.2.

$$Ch(z) = N_0 \, EXP(0.5 \, (1 - z - e^{-z})) \tag{4.1}$$

$$z = \frac{h - h_0}{H_0} \tag{4.2}$$

N_0 = maximum electron density z = reduced altitude (dimensionless)

h_0 = altitude of the peak of the layer h = altitude

H_0 = atmospheric pressure scale height at the peak altitude

The bottomside region of the Bent profile, extending from the base of the ionosphere to the peak, is described as a semi–biparabola by Equation 4.3.

$$Be1(y) = N_0 \, (1 - \frac{y^2}{y_m^2})^2 \tag{4.3}$$

$$y = h - h_0 \tag{4.4}$$

y_m = bottomside biparabolic semi–thickness

The decaying electron density of the topside region is broken into two sections at an altitude which will be referred to as the fitting point. The section immediately above the peak is described by a semi–parabola (Equation 4.5) and the upper region by an exponential form (Equation 4.6). The topside shape was determined from sounder data collected by the Alouette satellites.

$$Be2(y) = N_0 \, (1 - \frac{y^2}{y_t^2}) \tag{4.5}$$

y_t = topside parabolic semi–thickness

Above the peak of the F–region the electron density distribution has a scale height twice that of the neutral atmosphere as a consequence of its control by vertical diffusion (Hargreaves 1979). The electron density profile of this region is taken as exponential, where the rate of decay is controlled by the scale height of the neutral atmosphere.

$$Be3(x) = N_1 \, EXP(- \frac{x}{2H_1}) \tag{4.6}$$

$$x = h - h_1 \tag{4.7}$$

h_1 = altitude of the fitting point $1/2H_1$ = topside decay coefficient

N_1 = electron density at the fitting point H_1 = scale height at the fitting point altitude

The parabolic and exponential topside sections are joined at the altitude where their gradients match, the altitude of the fitting point being given by Equation 4.8. Bent et al (1975) found statistically that $h_1 \approx h_0 + y_m/4$ and $N_1 \approx 0.86\, N_0$.

$$h_1 = h_0 + (y_t^2 + H_1^2)^{\frac{1}{2}} - H_1 \qquad (4.8)$$

The definition of the Bent topside profile included three equal–interval exponential sections, each with its own decay coefficient, to represent the electron density at the altitudes between the fitting point and 1 000 km. Above 1 000 km two further exponential sections each covering an altitude range of 500 km were postulated. Since the predictive electron content model was designed to reproduce the content below 800 km, it was proposed to simplify the calculations and clarify the model by taking just one exponential section from the fitting point up to this altitude. In order to compare predictions by the model with monthly mean electron content data measured by the Faraday rotation method the profile was required to cover the altitude range up to 2 000 km. This was achieved by the addition of three further exponential sections to the profile, the first from 800 km to 1 000 km, the next to 1 500 km and the final one to 2 000 km. Each section was scaled by its own decay coefficient (i.e. estimate of scale height).

To increase the efficiency of the computer programs the electron contents of each of the six Bent profile altitude sections were calculated from analytic integration formulae. The formulae for the biparabolic, parabolic and exponential sections are given below in Equations 4.9 to 4.11, respectively.

$$EC1 = N_0 \frac{8}{15} y_m \qquad (4.9)$$

$$EC2 = N_0 \left((h_1 - h_0) - \frac{(h_1 - h_0)^3}{3y_t^2} \right) \qquad (4.10)$$

$$EC3 = N_1 H_1 \left(1 - EXP\left(-\frac{(h_1 - h_0)}{H_1} \right)\right) \qquad (4.11)$$

EC1 = bottomside region electron content

EC2 = fitting region electron content

EC3 = exponential region electron content

The integration of the Chapman profile was performed in three sections with the NAG Library routine D01BDF. The section boundaries were from zero altitude to the peak, from the peak to 800 km and from 800 km to 2 000 km. For a Chapman profile the ratio of the topside electron content to the total electron content is constant at approximately 0.68:1 regardless of the prevailing scale height. The total electron content (TEC) of a Chapman profile (i.e. the electron content from zero to infinite altitude) is given by Equation 4.12.

$$E = (2\pi e)^{\frac{1}{2}} N_0 H_0 \qquad (4.12)$$

4.2 Scaling of the Profile Peak

The magnitude and altitude of the maximum electron density (N_0 and h_0) are vitally important to the accuracy of the representation of electron content. This is because the peak electron density scales the electron density of the rest of the model profile and the height of this peak controls the scale height of the profile topside. The monthly mean values of the two peak parameters can be calculated from numerical maps of the F2–region critical frequency (foF2) and the propagation factor (M(3000)F2) recommended by the Comité Consultatif International des Radiocommunications (CCIR) and described in the CCIR Report 340 (1967) and a later supplement CCIR Report 340–2 (1975).

The foundations of the CCIR numerical maps are foF2 and M(3000)F2 data collected by a global network of ionosonde sites between 1954 and 1958 during which time the sunspot number ranged from 3 to 201). For each of the five years these measurements were reduced on a month–to–month basis to tables of Fourier series and Chebychev polynomial coefficients (Jones and Gallet 1962). A straight line was fitted to the harmonic coefficients of each of the sixty months which allowed the coefficients for two levels of solar activity given by sunspot numbers of 0 and 100 to be calculated. The coefficients required to reconstruct values of foF2 or M(3000)F2 at other levels of solar activity are found by linear interpolation of the two reference values.

The CCIR Model provides good estimates of the peak parameters in regions with a high density of ionosonde sites which provided data for the original calibration, for example the European sector. The accuracy, though, is thought to be less good in regions which did not provide calibration data, for example over the oceans. This is somewhat unfortunate in this case since the altimeter is principally an ocean sensing instrument. At high–latitudes, again because of a lack of calibration data, the prediction of the peak parameters must be considered only approximate. Despite these caveats the CCIR Model is the best currently available and so was adopted for the Predictive Model.

The CCIR Model estimates of the monthly mean peak parameters are generated by the WOMAP Fortran computer program with the coefficient look–up tables, Universal Time (UT), day number, geographic location and sunspot number as inputs. The WOMAP program also provided an estimate of the critical frequency of the E–region (foE) calculated by the Muggleton method (Muggleton 1975). By repeatedly running the WOMAP program for locations spaced evenly over a global grid it is possible to generate maps of monthly mean foF2, M(3000)F2 and foE for a given Universal Time. Equation 1.4 relates foF2 and peak electron density (N_0); a map of monthly mean N_0 for March at 12 UT with a twelve–month running mean sunspot number of 150 is shown in Figure 4.3. The Equatorial Anomaly, Main Trough and strong gradients across the Terminator are prominent features of this map. In order to allow fair and consistent comparisons other maps will be produced for these conditions which will, henceforth, be referred to as standard conditions.

The propagation factor and altitude of the maximum electron density are strongly correlated and various empirical formulae have been proposed which give the altitude of the peak as a function of M(3000)F2 (Bilitza et al 1979). A second order formula for the peak altitude was developed for the Bent Model (Llewellyn and Bent 1973) from the work of Appleton and Beynon (1940 and 1947) on HF propagation. The quadratic formula, referred to as the AAB Model, is given in Equation 4.13. A global map of peak altitude calculated from the AAB Model for standard conditions is shown in Figure 4.4.

$$h_0 = 1346.92 - 526.4\,M + 59.825\,M^2 \qquad (4.13)$$

h_0 = altitude of the peak (km) M = propagation factor

Another formula for the peak altitude is that of Bilitza, Sheikh and Eyfrig (1979), the BSE Model, given in Equations 4.14 to 4.19. This peak model was calibrated with data from incoherent

scatter radars which, unlike the ionosonde data employed for the AAB Model, measures the peak altitude unambiguously. The noontime calibration data was collected by the Millstone Hill, Arecibo and Jicamarca incoherent scatter radars between 1964 and 1970, the ascending phase of solar cycle 20. The formulation of the BSE Model is essentially a development of that proposed by Shimazaki (1955) which introduced the correction term ΔM defined in Equations 4.15 to 4.19. The correction term accounts for the variation with solar activity and geomagnetic latitude and the ratio term foF2/foE allows for the important effect of the ionization below the peak. The diurnal variation of the propagation factor was presumed to give the diurnal variation of the peak altitude.

$$h_0 = \frac{1490}{M + \Delta M} - 176 \qquad (4.14)$$

$$\Delta M = \frac{F_1(Z)\ F_4(Z,\beta)}{foF2/foE - F_2(Z)} - F_3(Z) \qquad (4.15)$$

$$F_4(Z,\beta) = 1 - \frac{Z}{150}\ \mathrm{EXP}\left(-\frac{\beta^2}{1600}\right) \qquad (4.16)$$

$$F_3(Z) = 0.096\ \frac{(Z - 25)}{150} \qquad (4.17)$$

$$F_2(Z) = 1.2 - 0.0116\ \mathrm{EXP}(0.0239\ Z) \qquad (4.18)$$

$$F_1(Z) = 0.222 + 0.00323\ Z \qquad (4.19)$$

h_0 = altitude of the peak (km) β = geomagnetic latitude

Z = twelve–month running mean sunspot number

The geomagnetic latitude was calculated by spherical trigonometry with an Earth–centred dipole approximation taking the northern geomagnetic pole at 79°N, 290°E. To ensure physically realistic results a lower saturation level of 1.5 was set for the foF2 to foE ratio. A global map of peak altitude calculated from the BSE Model under the standard conditions is drawn in Figure 4.5. For high levels of solar activity the BSE Model predicts lower peak altitudes than the AAB Model, though the values are similar for low activity. The morphology of the peak altitude predicted by the two models is broadly similar. Rawer and Bilitza (1985) tested the BSE Model against Jicamarca incoherent scatter measurements of the monthly mean peak altitude for hours other than noon and found the majority of the differences between the modelled and measured values were within 10 km.

4.3 Comparison of Candidate Predictive Models

From the above sub–models five predictive models of electron content were assembled which will be referred to below by their development code letters A1, A2, B, C and D. The one sub–model common to all five models was the CCIR Model for calculating foF2 and M(3000)F2. Chapman profiles formed the basis of two of the models with the other three being based on the Bent profile. For the Chapman profile the scale height model and the sub–model for calculating the peak altitude are critical. For the Bent profile the critical parameters are the parabolic semi–thicknesses (y_m and y_t) and the topside decay coefficients.

- **Model A1** Based on a Bent profile with the peak altitude given by the BSE Model. Investigations with Faraday rotation data produced a new relationship between y_m and noontime foF2. The topside decay coefficients were determined from look–up tables of scale height calculated with the Jacchia Thermospheric Model (Jacchia 1965) which is described in Appendix A.
- **Model A2** Defined as Model A1 except that a new relationship found between y_m and noontime peak altitude was employed. In both versions of Model A the value of the y_t parameter was set equal to y_m.
- **Model B** Based on a Bent profile with the peak altitude given by the AAB Model. Of the two y_m formulations suggested by Rawer and Bilitza (1985) the mathematically simpler sub–model in terms of noontime foF2 was implemented (Equations 2.1 to 2.5). The topside semi–thickness was calculated with the rule given in Equation 2.6 by Llewellyn and Bent (1973). The topside decay coefficients were calculated at the base of each exponential section with scale heights calculated from an empirical formula given by Bent et al (1975) which will be referred to as the NASA Model.
- **Model C** Based on a Chapman profile and as for Model B the peak altitude was given by the AAB Model. The scale height at the peak was given by the NASA Model.
- **Model D** Based on a Chapman profile with the peak altitude given by the BSE Model. The scale height at the peak was determined from the Jacchia Model.

These five empirical models were proposed as candidates for an electron content model to provide group delay corrections for an altimeter system. Their predictive capabilities were tested against monthly mean electron content data to determine which model should be adopted for the ionospheric correction algorithm.

The second element of the ionospheric correction routine allows the introduction of electron content measurements into the prediction procedure with the aim of reducing the residual ionospheric correction still further.

4.4 The Adaptive Procedure

Much of the difficulty in the representation of the ionosphere with monthly mean models arises from the intrinsic variability of the ionosphere on a wide range of time scales other than the diurnal, seasonal and solar cycle periods. To overcome the problem of ionospheric variability an electron content model requires a facility for incorporating data to adjust the monthly mean estimate from the Predictive Model to account for the conditions prevailing in the local ionosphere. This facility will be referred to as the Adaptive Model and is based on least mean square estimation. King and Slater (1973) and Nisbet et al (1981) concluded that prediction accuracy could be improved to a greater extent by including day–to–day variations than by enhancing the accuracy of modelled mean values. The outline below is based on the method of Gautier and Zacharisen (1965) which was initially described for the adaptive correction of foF2.

The first step in the Adaptive Model adjustment is the estimation by the Predictive Model of the mean electron content at the measurement point. The deviation of the measurement from the estimated mean (which can be either positive or negative) is then weighted by the electron content correlation coefficient between the position and time of the altimeter sounding and the position and time of the measurement. This quantity is finally added to the estimate for the sub–altimeter point. The adaptive procedure is summarized by Equation 4.20. The correlation coefficient acts as a weighting term which accounts for the spatial and temporal separation of the altimeter sounding and the electron content measurement. The reduction in the uncertainty of the prediction afforded by the Adaptive Model is determined by the correlation coefficient as in Equation 4.21.

$$E_p - \bar{E}_0 = P \frac{s_0}{s_1} (E_1 - \bar{E}_1) \qquad (4.20)$$

$$s_p^2 = s_0^2 (1 - P^2) \qquad (4.21)$$

E_1 = electron content at the time and position of the measurement

E_0 = electron content at the time and position of the altimeter sounding

E_p = prediction for the time and position of the altimeter sounding

(overbars indicate mean values)

s_1 = standard deviation of electron content at the measurement point

s_0 = standard deviation of electron content at the altimeter sounding point

s_p = standard deviation of the adjusted electron content

P = combined correlation coefficient between the two times and positions

The standard deviations of the electron content measurements made at the four calibration stations are plotted in Figure 3.12 and Figures 3.20 to 3.22. The adaptive procedure assumes the Predictive Model gives an accurate value of the monthly mean electron content at both points. This is unlikely to be realized in practice, hence, Equation 4.21 should be written as Equation 4.22. The deviation of the modelled electron content about the true monthly average will be covered later.

$$s_p^2 = (s_0^2 + t_0^2)(1 - P^2) \tag{4.22}$$

t_0 = standard deviation of the Predictive Model about the true mean

A quality factor (Q) can be defined as in Equation 4.23 which quantifies the improvement gained from application of the Adaptive Model. A quality factor of unity implies that the electron content can be predicted exactly; this situation could arise if a measurement of electron content was made coincident with an altimeter sounding. A quality factor of zero implies that a measurement affords no improvement over the predicted monthly mean.

$$Q = 1 - (1 - P^2)^{\frac{1}{2}} \tag{4.23}$$

As depicted in Figure 4.6 the percentage improvement increases with the correlation coefficient. It is therefore prudent to define a lower limit to the correlation coefficient below which the Adaptive Model is not activated because the improvement gained would not be commensurate with the effort involved. For the adaptive correction procedure the lower limit is taken as 0.7, equivalent to a quality factor of approximately 0.3. In physical terms this implies that a 30% improvement in prediction accuracy is possible with the available measurement.

To clarify the adaptive adjustment technique, consider the situation where a measurement of electron content has been made at a point in the ionosphere where, one hour later, the electron content is required to correct an altimeter sounding. The first level correction is provided by the

Predictive Model which estimates the monthly mean electron content. The Adaptive Model first calculates the deviation of the electron content, measured one hour previously, from the mean at that time. The temporal correlation coefficient is then calculated for a time lag of one hour. If the correlation coefficient is less than 0.7 then the adaptive procedure is abandoned and only the predictive correction is applied. However, as will be shown later, for a sunspot number of 170 the temporal decorrelation over one hour results in a correlation coefficient of approximately 0.80 (i.e. a 40% reduction in uncertainty is possible). Since the measurement and sounding are co–located then the standard deviation ratio term of Equation 4.20 is unity. The adaptive adjustment to the predictive correction is then the deviation found one hour earlier weighted by the 0.80 correlation coefficient.

In practice the above situation must be considered as a special case since the measurement and sounding point would normally be separated in both time and space. This raises the question of how to combine the spatial and temporal correlation correlation coefficients which before now have only been considered in isolation. The combination of the two anisotropic spatial correlation coefficients was especially important since the formulation had to reduce to the individual components for the special cases of the two points separated East–West or North–South.

The resolution to the problem of combining the spatial coherence functions can be explained by reference to Figure 4.7 which shows the measurement point at a general azimuth angle from the sub–altimeter point. Successive applications of the Adaptive Model calculate the adjustment at the intermediate point (Equation 4.24) and then map the intermediate adjustment to the sub–altimeter point (Equations 4.25 and 4.26). Since the measurement must be close to the sounding to invoke the Adaptive Model, the statistics of the ionosphere are unlikely to vary over such relatively short distances and the ratio s_0/s_1 can be taken as unity.

$$E_i - \bar{E}_i = R_N \ (E_1 - \bar{E}_1) \tag{4.24}$$

$$E_0 - \bar{E}_0 = R_E \ (E_i - \bar{E}_i) \tag{4.25}$$

$$E_0 - \bar{E}_0 = R_N \ R_E \ (E_1 - \bar{E}_1) \tag{4.26}$$

R_N = NS spatial correlation coefficient R_E = EW spatial correlation coefficient

R_T = temporal correlation coefficient

subscript 1 corresponds to the measurement point

subscript i corresponds to the intermediate point

subscript 0 corresponds to the sub–altimeter point

Consequently the general spatial correlation coefficient is given by the product of the North–South and East–West coefficients. Extension of this argument to the time domain suggests that a combined correlation coefficient product (P) can be defined as in Equation 4.27. The combined correlation coefficient is that referred to by Equations 4.20 and 4.23.

$$P = R_N R_E R_T \tag{4.27}$$

The Adaptive Model is dependent upon the magnitude of the time difference between the measurement and prediction and, hence, can be employed for backcasting as well as forecasting as long as the temporal separation is within the coherence time limit. Only the most recent and/or closest of the available measurements is employed in the Adaptive Model since little is gained by the use of more than one measurement.

4.5 Chapter Summary

This chapter has defined the components and described the construction of five predictive models which can provide estimates of monthly mean electron content. An adaptive facility to update the electron content estimates from these models with actual measurements was also described.

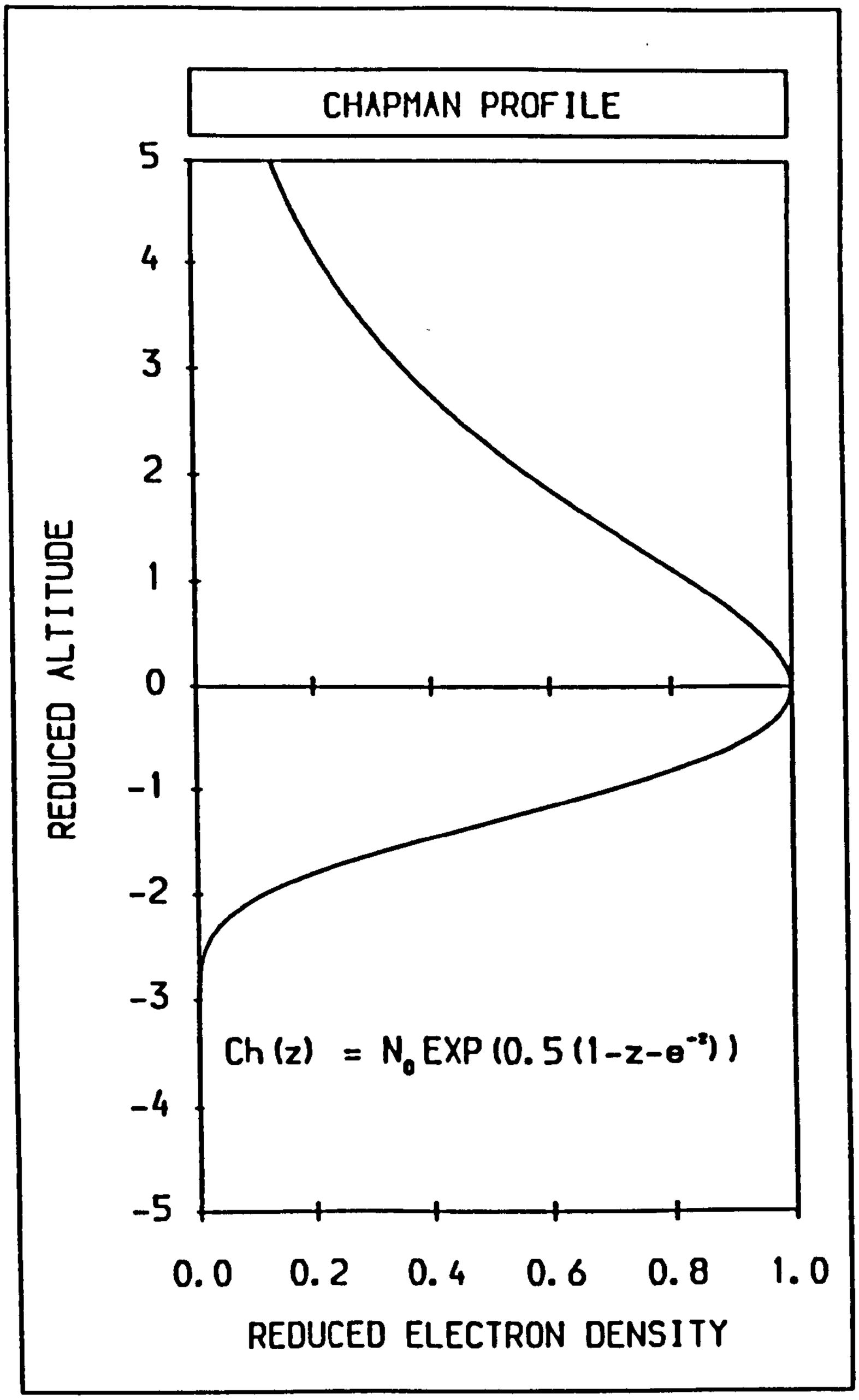

Figure 4.1 : The Chapman altitude profile of electron density.

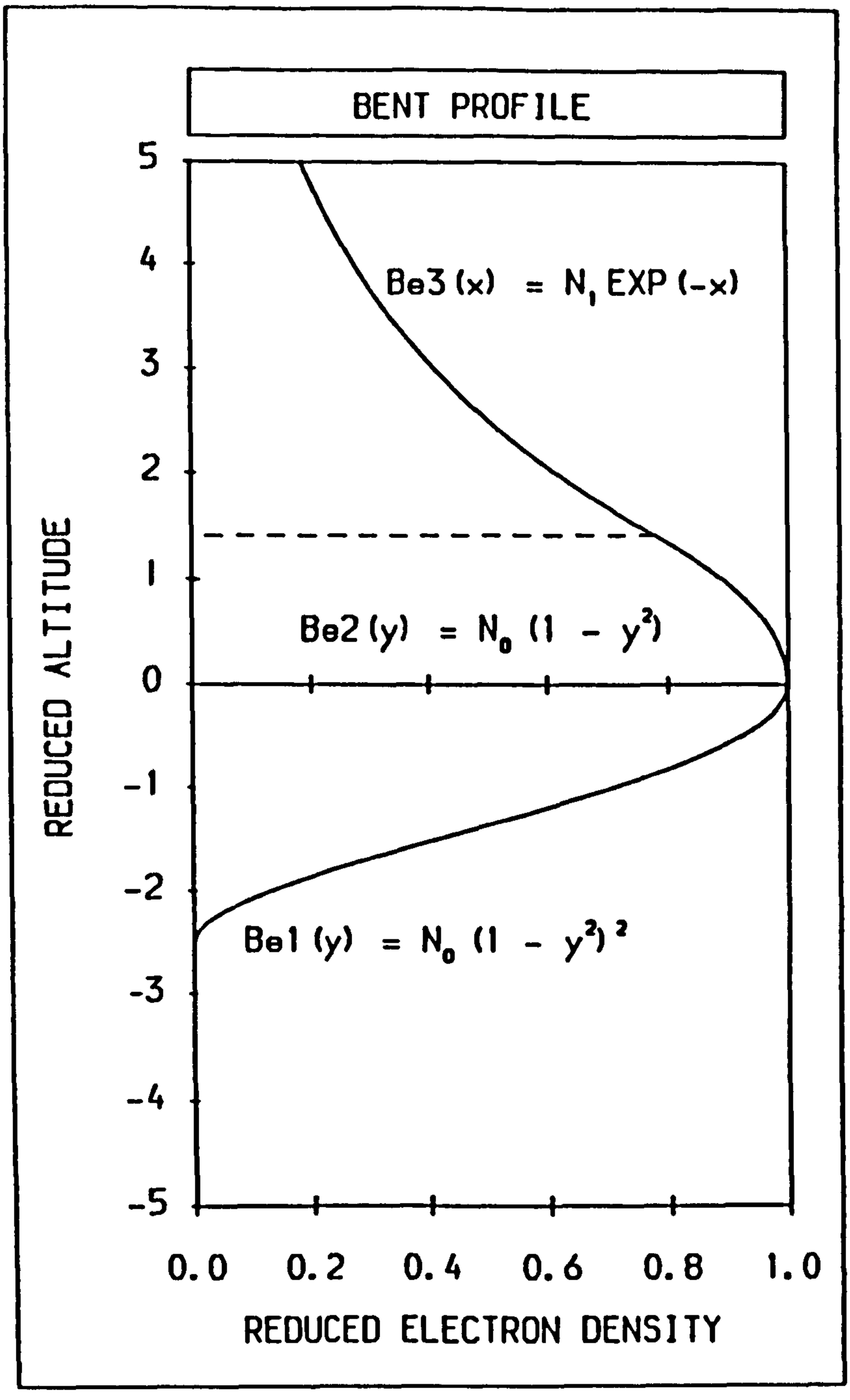

Figure 4.2 : The Bent altitude profile of electron density.

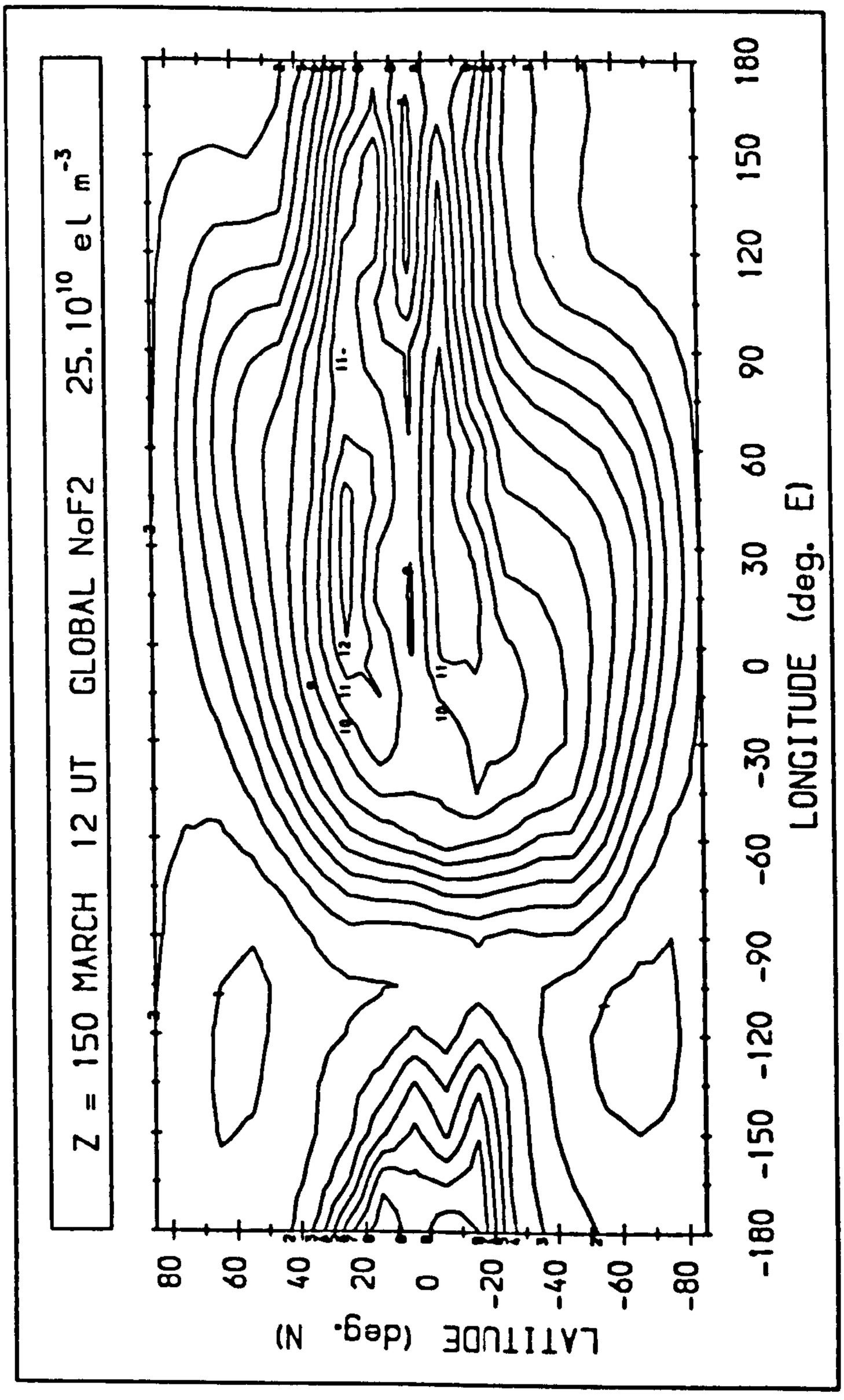

Figure 4.3 : A global map of F2–region peak electron density for standard conditions (March, 12 UT, sunspot number of 150) calculated from the CCIR Model (CCIR 1967). The contour interval is 25.10^{10} m^{-3}.

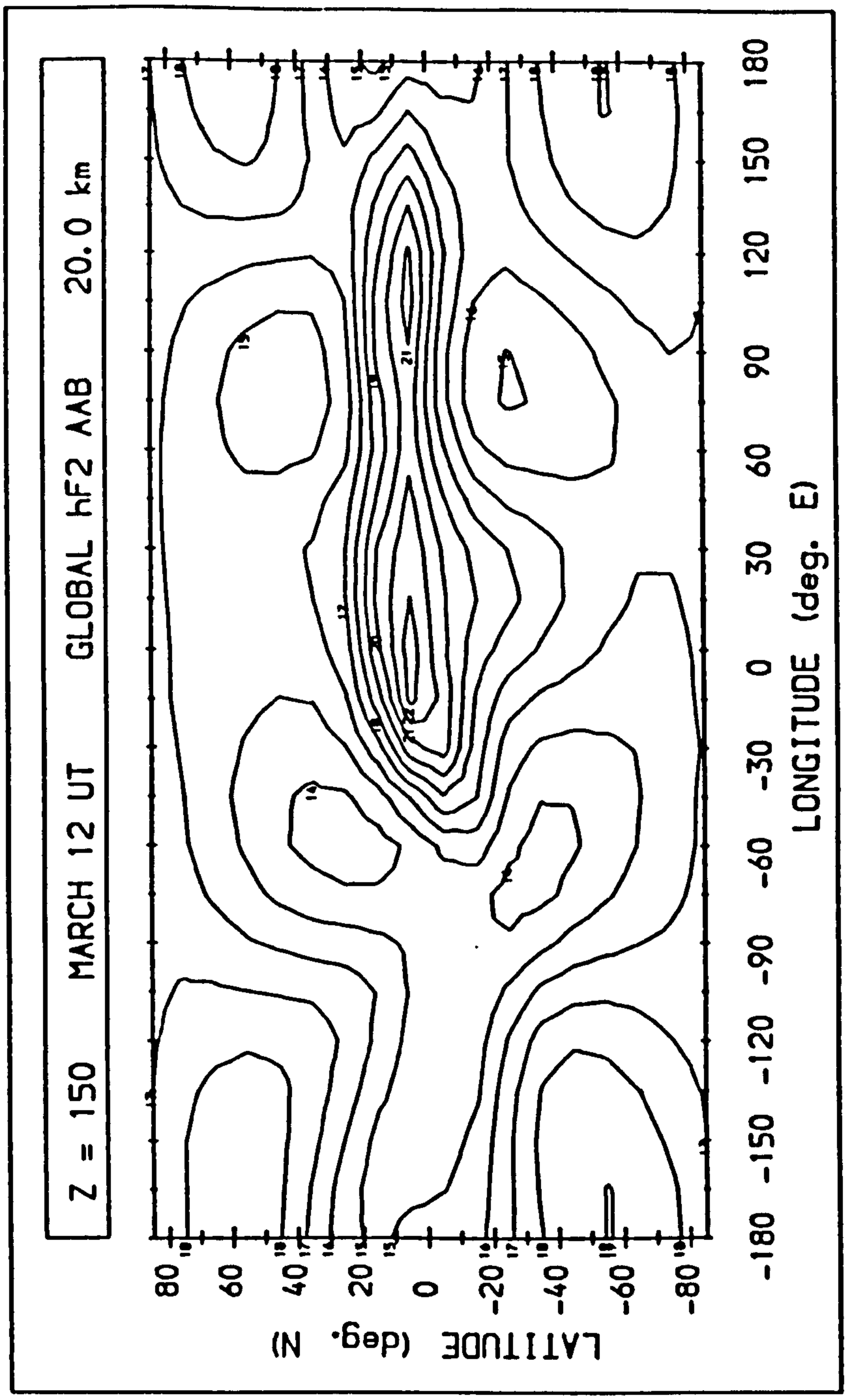

Figure 4.4 : A global map of F2–region peak altitude calculated for standard conditions from the AAB Model given by Llewellyn and Bent (1973). The contour interval is 20 km.

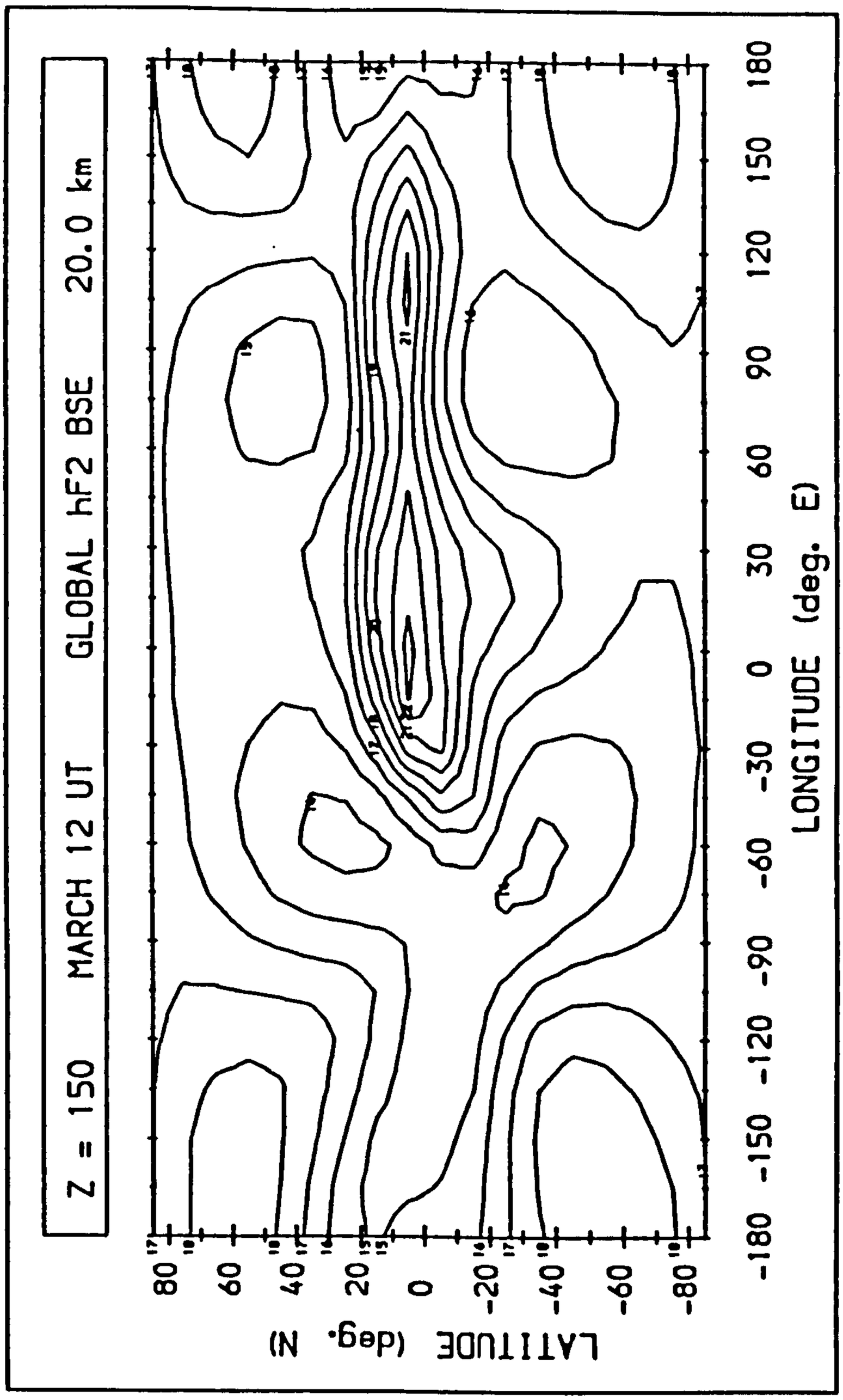

Figure 4.5 : A global map of F2–region peak altitude calculated for standard conditions from the BSE Model given by Bilitza et al (1979). The contour interval is 20 km.

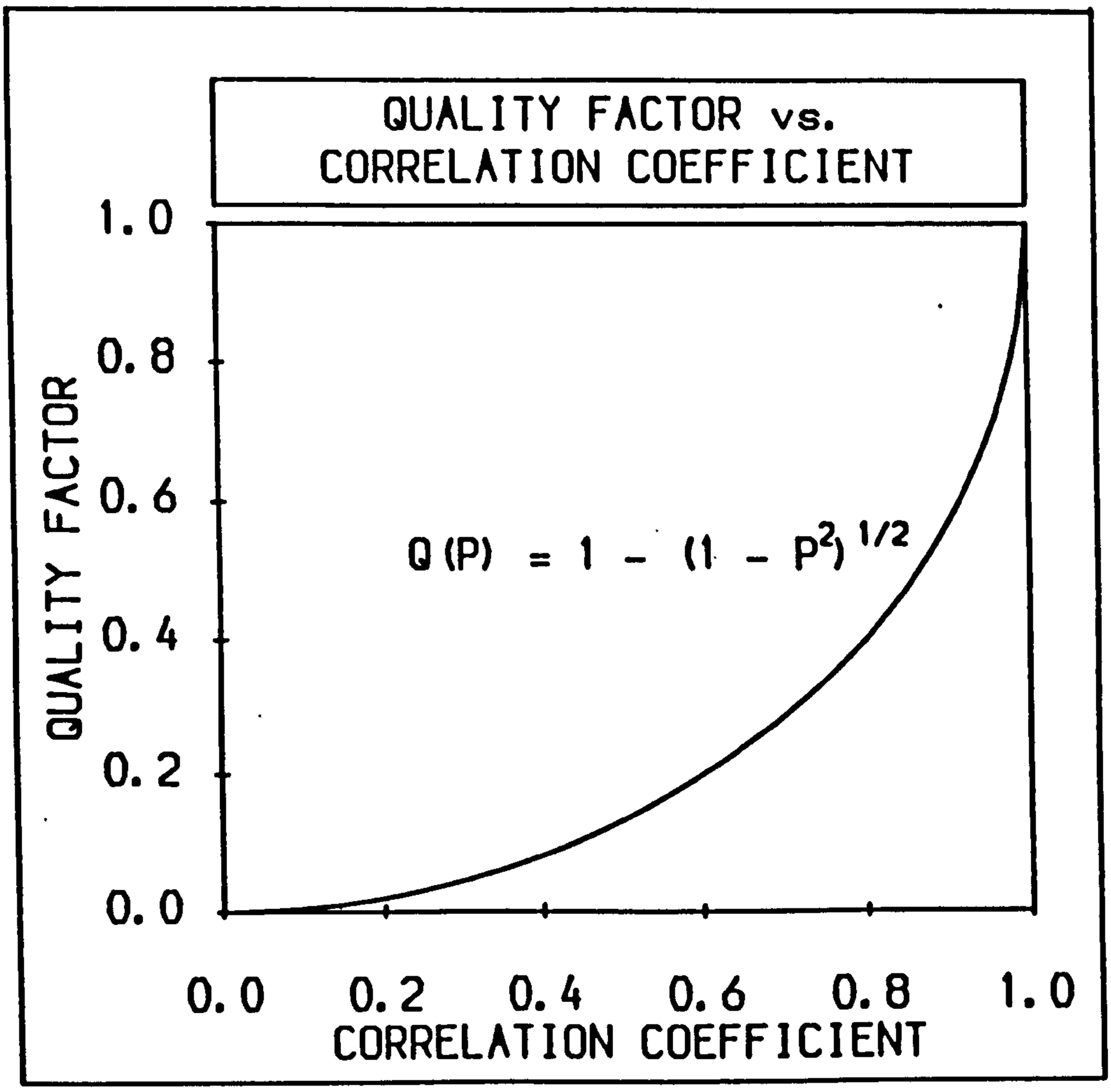

Figure 4.6 : A plot depicting the non–linear relationship between the quality factor (Q) and the correlation coefficient (P).

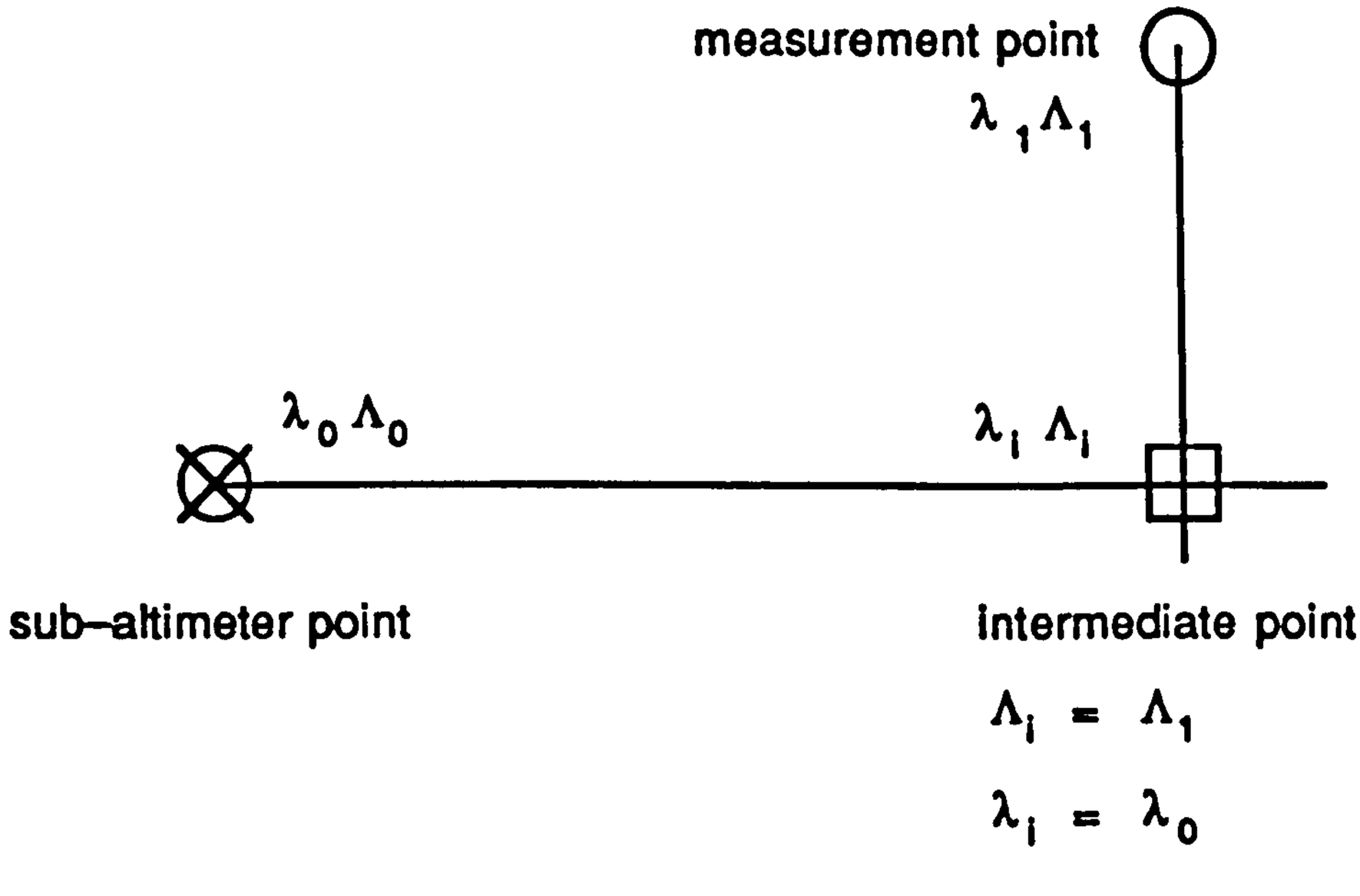

Figure 4.7 : A sketch illustrating the multiplicative combination of the North–South and East–West spatial correlation coefficients.

Chapter 5 : Calibration and Validation of the Predictive Model

This chapter begins with a report of tests made with monthly mean ionosonde data on the sub–models for the magnitude and altitude of the monthly mean F2–region peak electron density. The predictive models of electron content defined in the previous chapter are then calibrated. The third part describes the validation tests of the five predictive models against benchmarks of 531 station months of independent electron content data. The tests were made in several stages and the performance of each model was judged on how accurately it reproduced the diurnal variation of monthly mean electron content data. Initially the two versions of Model A were tested to determine which was most realistic, the most successful version being retained for the rest of the study. A comparison of the precision afforded by each of the four remaining predictive models was then made in a similar manner. The two least successful models were then eliminated and the two most successful models were tested again. The best of this third comparison was adopted as the Predictive Model for the ionospheric correction algorithm. The fourth section presents the results of an investigation into the benefit to the Predictive Model precision arising from the use of monthly mean ionosonde data in place of the CCIR Model. Finally the spatial and temporal behaviour of the electron content generated by the Predictive Model is described.

5.1 Validation of the Peak Sub–models

All the Predictive Models had as their foundation the CCIR numerical maps of foF2 and M(3000)F2 which allowed the maximum electron density and the peak altitude to be calculated. Although tested and found to be accurate during other solar cycles (King and Slater 1973, Wakai and Matuura 1980) it was felt that a reassuring and useful study could be made to validate the maps for the ionospheric conditions prevailing during the declining phase of solar cycle 21, a period not covered by the above two studies.

Ionosondes on three continents, each close to a Faraday rotation receiving site and spanning a range of latitudes, provided monthly mean data for comparison with CCIR predictions. The co–ordinates of the three sites at Ottawa, Rome and Chung Li are given in Table 5.1 which lists

the ground co–ordinates of the ionosonde sites and the ionospheric points of the Faraday rotation receiving sites. Ionosonde data from 1980, 1982 and 1985 for the four calibration months were examined, a total of 36 station months. The mean deviations and standard deviations between the CCIR Model predictions and the monthly means measured by ionosonde are listed in Tables 5.2 to 5.4. The statistics confirm the accuracy of the CCIR Model; the standard deviation of foF2 at Rome was greater than 1 MHz on only two occasions.

The mean deviation statistics do not reveal any systematic bias for the foF2 predictions at any of the stations The absolute values are typically less than 0.5 MHz, though less than this for low solar activity. The standard deviations of foF2 are frequently less than 1 MHz, display no seasonal variation, and again tend to decrease with solar activity. For the propagation factor, M(3000)F2, the CCIR Model exhibits a positive bias relative to the ionosonde data of approximately 0.05 to 0.20 for low and high solar activity respectively. The standard deviations of M(3000)F2 are approximately 0.15, though decrease to approximately 0.10 for low solar activity.

Differences in the diurnal patterns of the ionosonde data and the CCIR Model predictions can be seen in Figures 5.1 to 5.3. The diagrams show the monthly mean diurnal variation of foF2 and M(3000)F2 as measured by ionosonde and as predicted by the CCIR Model for the month of March at Ottawa during 1980, at Rome during 1982 and at Chung LI during 1985. The magnitude and variation of foF2 is reproduced closely by the CCIR Model and, though the magnitude of the M(3000)F2 is not predicted exactly, the shape of the variation is still similar to that of the ionosonde data.

The findings of King and Slater (1973), expressed in terms of the percentage ratio of the quartile range to the median, quoted a value of 9% for the comparison of predicted and ionosonde foF2 data. If quartile range can be compared to standard deviation, this result agrees with the above findings which are equivalent to approximately 10%. A comparison of M(3000)F2 findings was made when the above results were converted into equivalent peak altitude by the Shimazaki empirical relation (Equation 4.14 with $\Delta M = 0$) (this was the procedure adopted by King and Slater). The results for M(3000)F2 give equivalent standard deviations in peak altitude of between 3 and 6% which agree well with values of 5% reported by King and Slater.

After an investigation employing 36 station months of ionosonde monthly mean data from an epoch of solar cycle 21, the foF2 and M(3000)F2 predictions of the CCIR Model were found to

be consistently accurate during all seasons and over wide ranges of solar activity and latitude. Thus it was confirmed that the CCIR Model could provide a firm foundation for a predictive model of electron content.

5.2 Predictive Model Calibration

The altitude scaling of a Chapman profile is determined by the atmospheric pressure scale height at the peak altitude. Vertical scaling of a Bent profile requires the semi–thicknesses of both the bottomside biparabola and the fitting parabola and the decay coefficients for each of the topside sections.

5.2.1 Chapman Profile

Since the altitude of the ionospheric peak is variable it is necessary to know the scale height as a function of altitude. The scale height, as defined in Equation 1.1, is a function of temperature and composition and consequently is a difficult parameter to model. A simple empirical formula giving the scale height as a function of altitude is quoted in Bent et al (1975) as the NASA Model and is reproduced below as Equation 5.1.

$$H = 24.9 + 0.1245\,h \qquad (5.1)$$

H = scale height (km) h = altitude (km)

A global contour map of the scale height calculated with this equation at 12 UT for a level of solar activity given by a sunspot number of 150 for the month of March (the standard conditions) is presented in Figure 5.4. As a consequence of the formulation, the global pattern of scale height is a scaled and translated version of that of the peak altitude. The greatest scale height is predicted to occur at low latitudes during daytime where its value reaches 80 km. Steep gradients are found towards mid–latitudes and at sunrise. The minimum predicted scale height is slightly less than 60 km at pre–dawn mid–latitudes.

An exact value of the scale height is essential for a Chapman model and so it was thought necessary to formulate a more accurate alternative to Equation 5.1. This was achieved by calculating separate temperature and composition profiles from the Jacchia Thermospheric Model (Jacchia 1965) and then producing scale height profiles from their combination. The empirical equations of the Jacchia Model (see Appendix A) allow calculation of the exospheric

temperature and provide a model temperature profile for a given set of time and space co–ordinates. For a sunspot number of 170 and at a latitude of 45° during March the Jacchia Model predicts an average daily exospheric temperature of 1 200 K which agrees with the prediction of Schatten and Sofia (1987) for 1990 (the year proposed for the launch of ERS1).

When the temperature profile is combined, through Equation 1.1, with the mean composition profile, altitude profiles of scale height can be calculated. Due to the limitations of the data set which calibrated the Jacchia Model, the profiles are only valid for altitudes up to 800 km and above this the model profiles must be considered a theoretical extrapolation. Sampling a set of the resultant profiles, evenly spaced about the world, at a predetermined altitude permits the production of global maps of scale height for that altitude.

Numerical global maps of scale height were generated from the Jacchia Model for equinoctial conditions at altitudes of 300 km, 800 km, 1 000 km and 1 500 km and for levels of solar activity given by sunspot numbers of 0, 50, 100, 150 and 200. The geographic increments were 10° in latitude and 15° in longitude which established the lower limit of resolution. The scale heights at intermediate altitudes, intermediate locations and intermediate sunspot numbers were calculated by four–dimensional linear interpolation between the tabulated values. This technique of calculating scale height from look–up tables was applied for both the value at the Chapman profile peak of Model D and in the calculation of the topside decay coefficients of the Bent profile Model A. In the Bent profile the scale height at the lower edge of the section was used to calculate the decay coefficient for the whole section since it was considered more important for the profile to be accurate at altitudes where the electron density was greatest.

The global contour map in Figure 5.5 depicts the scale height at the peak altitude as calculated by the four–dimensional look–up technique under standard conditions. The pattern is similar to that of Figure 5.4 with the maximum scale height predicted for daytime low–latitudes and the minimum at daytime high–latitudes. The range of variation, though, is slightly greater.

An accurate value of the scale height is most important at the peak for a Chapman profile and around the fitting point for a Bent profile. Bearing this in mind, attention was concentrated on the 200 km to 500 km region and least–squares straight lines were fitted to the scale height profiles generated for 00 LT, 06 LT, 12 LT and 18 LT at solar activity levels given by sunspot numbers of 0, 100 and 200. The fits for a sunspot number of 100 are shown as Figure 5.6. The constants and coefficients of the regression lines and the standard deviations of the profiles about the regression lines are listed in Table 5.5.

Taking a linear interpolation of the values listed in Table 5.5 to a sunspot number of 170 and averaging the results over Local Time results in the empirical formula of Equation 5.2 which is remarkably similar to the NASA Model.

$$H = 21.8 + 0.1365\,h \tag{5.2}$$

5.2.2 Bent Profile

The semi–thicknesses of the parabolic regions of a Bent profile can be found from the formulae given by Rawer and Bilitza (1985). Two indirect relationships of biparabolic semi–thickness with solar activity were suggested, one in terms of noon peak altitude and the other in terms of noontime foF2. The relationship with foF2 is described by Equations 2.1 to 2.5. A standard conditions global map, calculated from the foF2 formulation, displaying the spatial variation of the bottomside semi–thickness is shown in Figure 5.7. The semi–thickness varies from approximately 130 km during daytime to over 180 km in the early morning. The Rawer and Bilitza formulae predict the ionosphere to be thickest during nighttime at low latitudes and thinnest during daytime at mid– and high–latitudes. The thickness of the summer ionosphere is expected to be greater and have a larger diurnal variation than the winter ionosphere. The maximum thickness is predicted to occur between 1 LT and 10 LT depending on season.

Further investigations were made into bottomside electron content using 89 station months of the Faraday rotation data base The intention was to investigate alternative sub–models of biparabolic semi–thickness, based on foF2 and peak altitude for the Bent profile. The data from March, June, September and December of the six years 1980–85, collected at the Goose Bay, Boulder, Patrick and Palehua stations were employed for the calibration study.

The calibration procedure started out with the assumption that the topside model accurately reproduced the electron content from the peak up to 2 000 km. The difference between the predicted topside electron content and the measured Faraday rotation data was then assumed to be the bottomside electron content. Through Equation 4.9 the bottomside electron content (EC1) was then associated with a biparabolic semi–thickness (y_m). Thus for each hour of Local Time the monthly mean electron content provided an estimate of the y_m parameter. The Local Time variation of y_m was then described by the three coefficients of Equation 5.3 (i.e. an offset term A, an amplitude term B and a phase term C). These three coefficients approximated the y_m variation at each station.

$$y_m = A\,\bar{p} - B\,\bar{p}\cos(\,15\,(LT + C)\,) \qquad (5.3)$$

p = peak parameter (foF2 or h_0) (overbars indicate noontime values)

A = offset coefficient B = amplitude coefficient C = phase coefficient

The variation of the A, B and C coefficients for high and low solar activity (1980–82 and 1983–85, respectively) were considered separately. The least–squares regression lines, constrained to pass through the origin, were calculated for both the offset and amplitude coefficients with the corresponding noontime foF2 (Sub–model A1) and with the corresponding noontime peak altitude (Sub–model A2). Since no obvious variation of the phase term with either noontime parameter was evident just the mean was calculated.

The regression coefficients of the offset and amplitude coefficients and the means of the phase term for the noontime foF2 comparison are listed in Table 5.6 with those for the noontime peak altitude listed in Table 5.7. The coefficients listed in both tables exhibit no systematic variation with solar activity since the solar activity variation is sufficiently well accounted for by the behaviour of the corresponding peak parameter. Pronounced seasonal variations, though, are evident.

The means of the high and low solar activity coefficients were taken and the seasonal variations of these means were considered After extensive investigations it was found that day number variations based on cosine curves, as employed by Rawer and Bilitza (1985), were not sufficiently good fits to the calibration data. Neither were more complicated polynomial fits calculated with NAG Library routines found to be any better. Hence, to reproduce the seasonal variation between the calibration months a simple linear interpolation procedure in day number was adopted, this at least ensured accuracy for the four calibration months.

Global maps of y_m predicted by both versions of the calibration are shown in Figures 5.8 and 5.9. The maximum semi–thickness is predicted for the nighttime equatorial region and the minimum for daytime high latitudes. As a result of their formulation the A1 Sub–model has two maxima one either side of the Geomagnetic Equator, whereas the A2 Sub–model has just a single maximum on the geomagnetic Equator itself. The magnitude range of both models is greater than that of the sub–model developed by Rawer and Bilitza, both being below 100 km during the day and over 300 km at night.

Both calibrations predicted the thickest ionosphere in summer and the thinnest in winter with the summer values having the greatest range and winter the least. The equinoctial behaviour was

predicted to be intermediate to that of summer and winter in accordance with that found by Rawer and Bilitza. For all seasons the thickest ionosphere was expected to occur in the early morning between 5 LT and 8 LT.

5.3 Predictive Model Validation

A three stage analysis was undertaken to ascertain which of the five predictive models estimated monthly mean electron content most accurately. For each station month considered a point was awarded to the model whose prediction of the monthly mean diurnal variation of electron content had the lowest standard deviation about the data. The most successful model was judged to be that which accumulated the greatest number of points.

The data employed were collected over six years at eight stations from the four calibration sites at Goose Bay, Boulder, Patrick and Palehua and the four validation sites at Anchorage, Sagamore Hill, La Posta and Lunping. In all a database of 531 station months, of which 93 were employed in the calibration of Models A1 and A2 and 438 for validation purposes. The co–ordinates of all eight stations are listed in Table 3.2.

In the first study two versions of Bent profile based Model A, version A1 with the biparabolic semi–thickness determined by noontime foF2 and version A2 with the semi–thickness determined by noontime peak altitude were compared. This preliminary test involved 147 station months of data and the results are summarized in Table 5.8.

As expected the standard deviations of the electron content predicted from the two versions of Model A were very similar resulting in a fairly even distribution of points. Since the two models were calibrated with half of the data considered, the results for these 93 station months are listed separately in the two left hand columns of Table 5.8. The almost equal distribution of points for these data (A1 48 vs. A2 45) was anticipated. A more reliable test was provided by 77 station months of independent data from the four validation stations. For these data the version A2 has a slight edge over A1 (A1 34 vs. A2 43). On the strength of this version A2 of Model A with the semi–thickness given by the peak altitude was adopted as Predictive Model A for the second stage of the investigation.

The aim of the second stage of the study was to isolate the two most accurate predictive models from the four remaining candidates. This involved comparison of the predictions from the

ABCD Models against monthly mean Faraday data on the above points system. All 531 station months of data were employed in the comparison, though in the case of Model A only 438 could be considered independent, the other 93 having been used in its calibration procedure.

Initially the influence of solar activity on the accuracy of the candidate models was examined. The behaviour of the models during the calibration months at the calibration sites is summarized by Table 5.9 which quantifies the success of each model in terms of a crude solar activity parameter. The years 1980, 1981 and 1982 were considered as times of high activity (H) and 1983, 1984 and 1985 as times of low activity (L). Table 5.9 indicates that in general if a model is successful for a given month it is almost equally successful during both high and low solar activities. From this it was decided to consider all years of the data base together, retaining just the seasonal variation.

Two tables summarize the full set of results and allow study of the seasonal trends, Table 5.10 covers the four calibration sites and Table 5.11 the validation sites. The most apparent result from the tables is that Model D and Model A are the most successful models. The point totals for Models A, B, C and D for the calibration sites are 77, 61, 55 and 88 and for the validation sites are 69, 32, 37 and 112, respectively. Considering that the scale height sub–model of Model D was based on equinoctial conditions with no seasonal variation, good results were achieved for winter, though the model was not quite so successful for summer. Models B and C were quite accurate during summer but less so at other times. Model A was reasonably accurate for all seasons, but not to the same extent as Model D and was, in fact, almost as successful at the validation sites as at its calibration sites.

Since the second stage tests showed Model A and Model D to be the most successful a comparison was made of these to determine how many points each would pick up from the months when Models B and C were most accurate. The results, divided into calibration and validation sites, are presented in Table 5.12. Model D was the most successful since it was most accurate for 143 station months against 138 for Model A at the calibration sites and 149 station months against 101 at the validation sites.

One further test of Model D was made against a new version of itself (Model E) which was designed to be computer efficient. Towards this end the method of calculating the scale height from a look–up table sub–model was replaced by the analytical formula of Equation 5.2. This model ignored the fraction of total electron content found above 800 km (approximately 10% by day) and replaced the NAG Library routine D01BDF with the analytic integral of the Chapman

profile from zero to infinite altitude. In terms of the peak parameters the sub–800 km electron content was then estimated from the total electron content (E_∞) through the simple relation given in Equation 5.4.

$$E_\infty = (2\pi e)^{\frac{1}{2}} N_0 (21.8 + 0.1365\, h_0) \qquad (5.4)$$

The tests of Model E against Model D involving 170 station months of Faraday data are summarized in Table 5.13. The results indicate that Model D is more accurate in the prediction of monthly mean electron content almost twice as often as the simplified Model E and so no further development of Model E was undertaken.

Extensive trials of the four candidate models involving 531 station months of data resulted in the eventual adoption of Model D as the Predictive Model for the radar altimeter ionospheric correction algorithm.

5.4 Predictive Model Analysis

The change in the precision of the model when the peak parameters foF2 and M(3000)F2 were supplied from monthly mean ionosonde data rather than the CCIR Model was first evaluated. Although it has been proven that the CCIR Model quite accurately estimates the monthly mean peak parameters, it was thought that small errors in the parameters could be amplified by the electron content integration process to a level where the differences become significant.

Table 5.14 details the results of this study which utilized the same data set as the previous comparison between ionosonde data and CCIR Model output. The input of ionosonde data in place of the CCIR Model increased the precision of the electron content predictions for 22 of the 36 station months tested (as a matter of interest the figures for the other candidate models were 17, 20 and 24 for A, B and C, respectively).

It would appear that the inclusion of monthly mean ionosonde data has a beneficial effect on model accuracy. An improvement was found for approximately 60% of the station months considered and this figure can be expected to increase if the ionosonde station is co–located with the ionospheric point of the Faraday site. This improvement, though, has to be weighed against the increased complexity of the correction scheme and the inevitable delay involved in the scaling and acquisition of the ionosonde data. Though not insignificant, the increase of accuracy gained

from the input of ionosonde data was abandoned in favour of the simplicity and independence of adopting the CCIR Model values.

The Chapman altitude profiles of Model D for standard conditions at a mid–latitude site are shown in Figure 5.10. The diurnal profile shape changes can be seen to be most significant in the region of the peak. The altitude variation in Local Time of the electron density predicted by Model D is shown in Figure 5.11 which highlights the effect of sunrise in producing steep gradients of electron density which can also be seen in Figure 4.3. The variation of noontime electron density with latitude along the Greenwich meridian under standard conditions is obtained from Model D and is reproduced in Figure 5.12 which has the Equatorial Anomaly as a prominent feature at +20° and –10° latitude. As previously seen in Figures 4.4 and 4.5 the peak altitude increases towards the Equator.

A comparison of the 2 000 km electron content predicted by Model D with actual Faraday rotation data quantifies how well the model represents the real ionosphere and provides the fundamental test of model reliability. The predicted temporal structure of sub–2 000 km electron content for 1980 at the four calibration sites is displayed in Figures 5.13 to 5.16. The figure of both diurnal and seasonal variations compare very well with the equivalent Faraday data presented in a similar fashion in Figures 3.6, and 3.17 to 3.19. The diurnal and anomalous seasonal variation is accurately reproduced at all stations. The predicted magnitudes also stand comparison with the Faraday data, with only a few exceptions. The equinoctial daytime electron content at Palehua is underestimated by approximately 20 ecu and at Goose Bay it is overestimated by approximately 10 ecu suggesting a latitude dependent bias of the model.

The spatial structure of Faraday (i.e. sub–2 000 km) electron content as estimated from the Predictive Model for representative ranges of temporal and solar activity parameters have been reproduced in contour map form. The electron content predicted from Model D for standard conditions is illustrated in Figure 5.17. The features which can be seen from this map are the strong gradients in the ionosphere across the dawn Terminator, the high electron content of the Equatorial Anomaly, the decrease of electron content with increasing latitude and the complex morphology of the ionosphere due to the influence of the geomagnetic field.

Figure 5.18 illustrates the synoptic variation in electron content in six hour intervals of Universal Time. The asymmetrical influence on ionospheric plasma transport caused by the non–alignment of the Earth's rotation and geomagnetic axes necessitates the consideration of both Universal Time and longitude. The pattern of the ionosphere does not simply convect over

the surface of the Earth, that is the electron content cannot be considered to be 'frozen–in'. Figure 5.19 depicts the seasonal variation of the predicted 12 UT electron content; the high electron content found in the equinoctial months, the low values of summer and intermediate winter values are all correctly reproduced. Figure 5.20 illustrates the dominant influence of solar activity over the magnitude of the electron content. For March 12 UT conditions the maximum electron content for a sunspot number of 0 was slightly over 30 ecu, whereas for a sunspot number of 200 the maximum was over 110 ecu. The increase in solar activity also increases the strength of the gradients found at the sunrise Terminator and around the Equatorial Anomaly.

To quantify the accuracy of the Predictive Model the root mean square and mean deviations of its predictions from monthly mean Faraday rotation data were calculated for each of the 531 station months of calibration and validation data. The standard deviation of the predicted mean about the measured mean (t_0 of Equation 4.22) quantifies how precisely the model estimates the true electron content. The mean deviation quantifies any bias between the model and the data. Results for the eight stations are presented in graphical form in Figures 5.21 to 5.28. To clarify the trend with solar activity the twelve–month running mean of both statistics are also plotted.

In general the standard deviation of the predicted about the measured electron content increased with solar activity and towards lower latitudes. The bias of the predictions switched from positive to negative while the sunspot number was still above 100 suggesting the model had a tendency to overestimate electron content for high levels of solar activity and vice versa. The switch was earlier, and lead to more negative biases, for the two equatorial sites. The standard deviations had values up to approximately 20 ecu and the mean deviations were within ±15 ecu. These errors cannot be attributed to the CCIR Model since it has been shown that the Predictive Model accuracy is only slightly improved by the use of monthly mean ionosonde data. They must be attributed to a failure of the Chapman profile to represent properly the vertical figure of the ionosphere.

Considering the intention to run the correction procedure for the ERS1 mission for three years during the maximum of solar cycle 22 when the sunspot number is predicted to be 170±25 (Schatten and Sofia 1987) it must be expected that the Predictive Model will tend to return monthly mean estimates of electron content somewhat greater than the true value. This behaviour should be compared with that of the data depicted by Figure 3.5 and Figures 3.14 to 3.16 which exhibit a saturation of electron content for sunspot numbers greater than 140.

5.5 Chapter Summary

It should be emphasized that all empirical models are data base limited. The Predictive Model described above was based on 531 station months of data covering a range of sunspot numbers from 15 to 164. Since the predicted maximum sunspot number for solar cycle 22 is 170±25 the calibration of the Predictive Model described above should be sufficient to cope with the expected behaviour of electron content, though with the caveat given above that overestimation might be expected for the extremes levels solar activity. Predictive Model estimates of the electron content at the four calibration sites were shown to bear a good comparison to the Faraday data presented earlier.

The potential problem of overestimation of electron content for high levels of solar activity lends increased importance to the performance of the adaptive component of the ionospheric correction model, especially in the light of the predictions of high solar activity for the times of the ERS1 mission. The requirements of the Adaptive Model are to account for the significant variations of electron content on short time scales and to overcome any intrinsic bias in the Predictive Model.

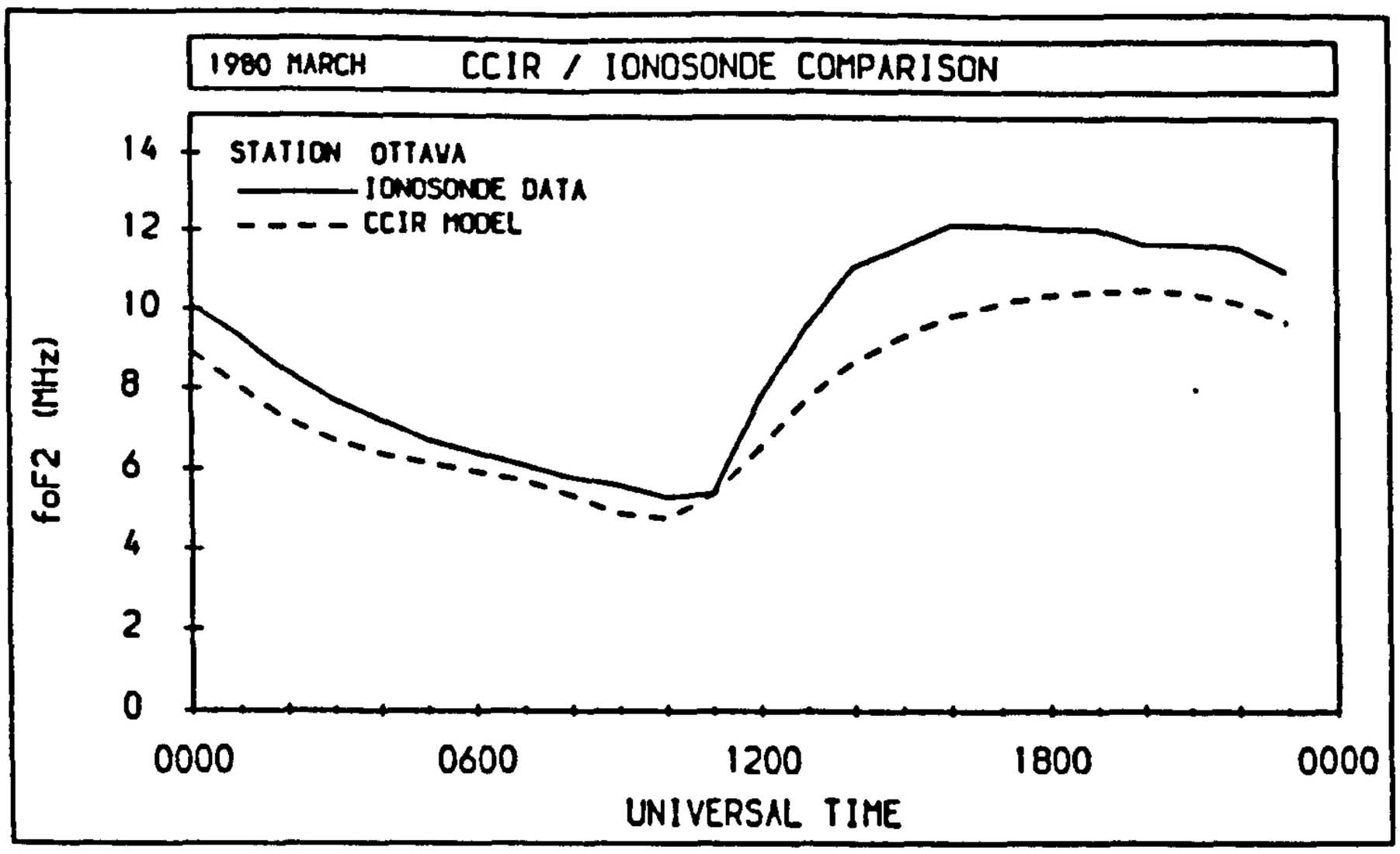

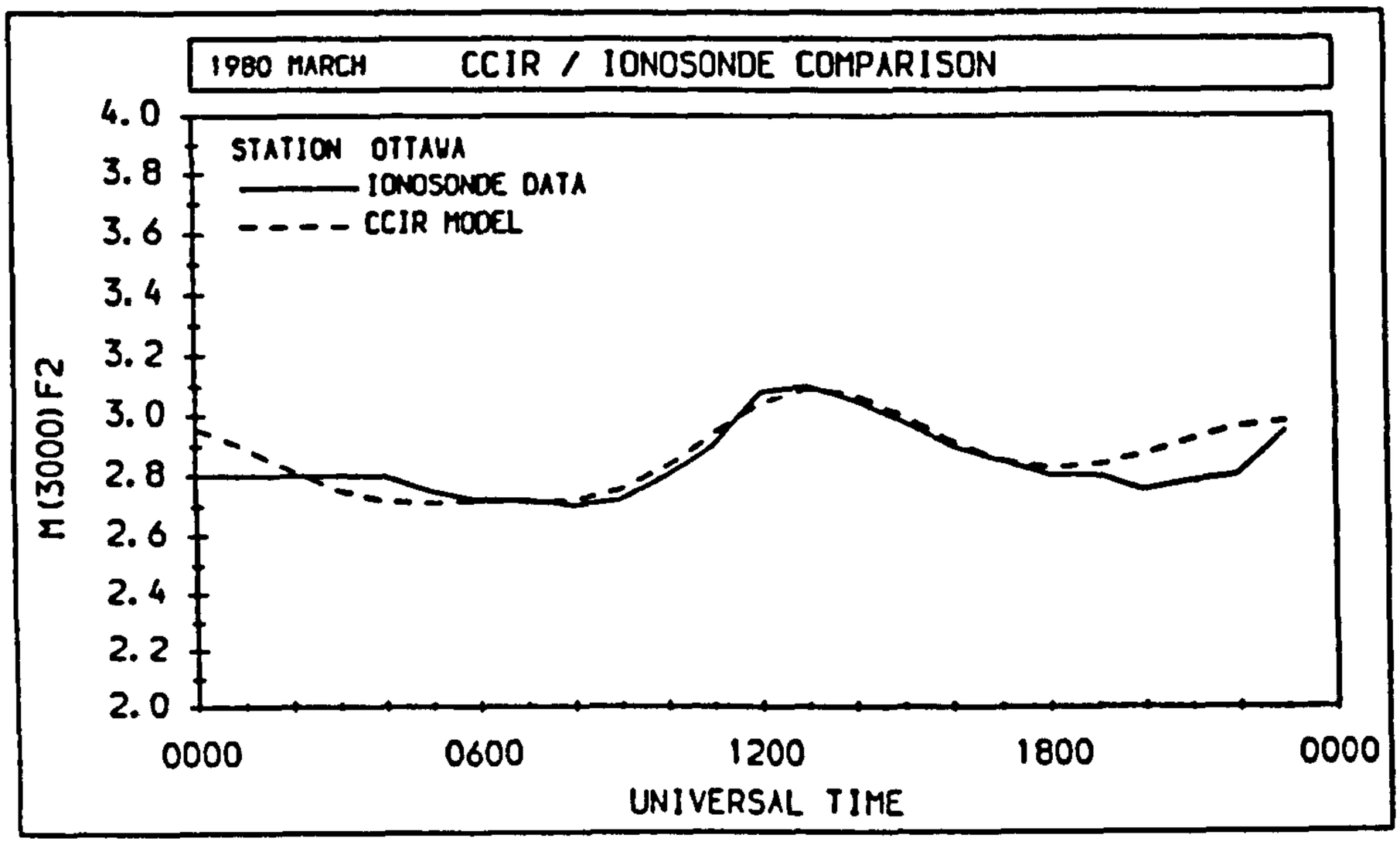

Figure 5.1 The monthly mean variation of foF2 and M(3000)F2 measured during March 1980 from the Ottawa ionosonde compared with the corresponding predictions of the CCIR Model.

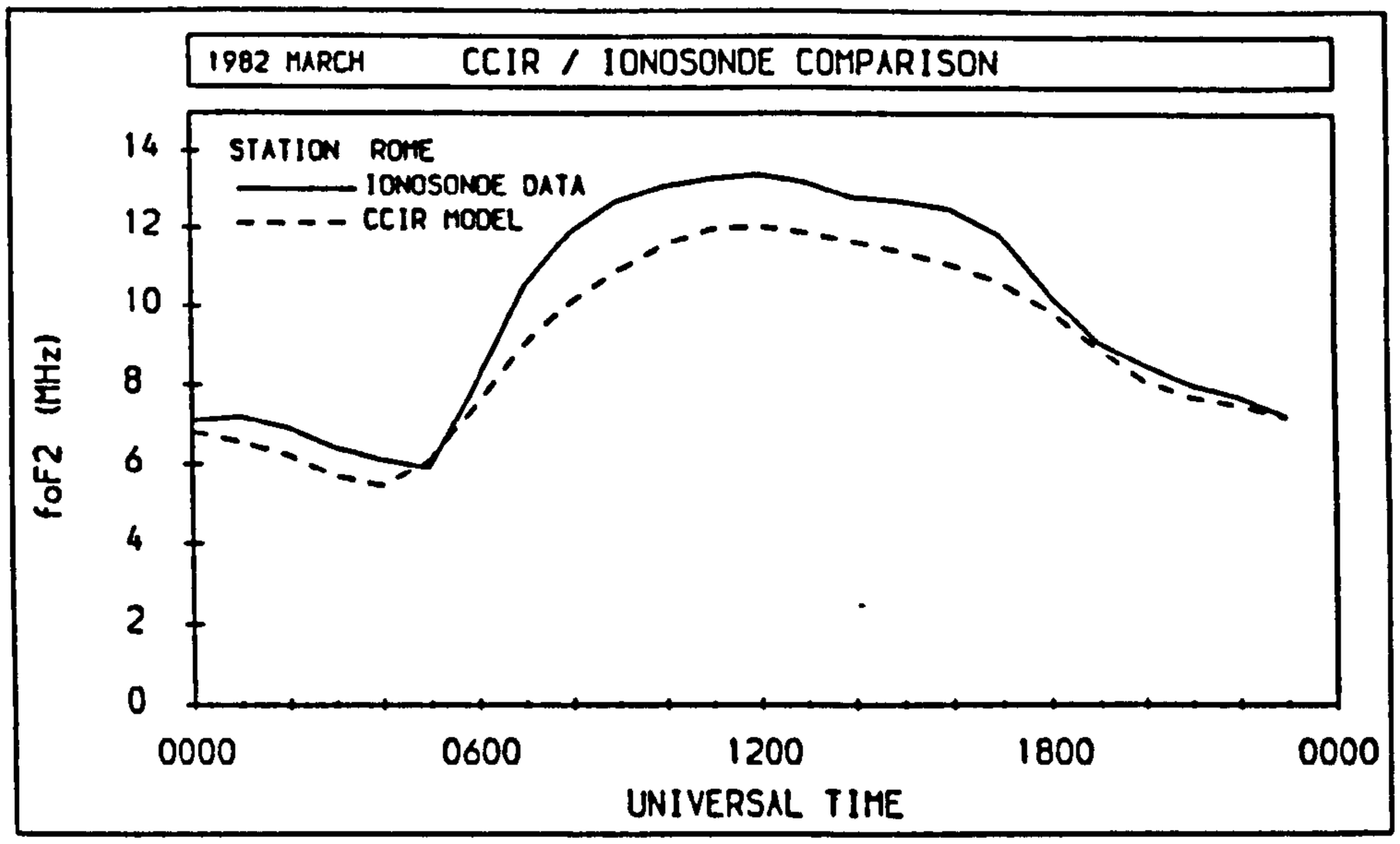

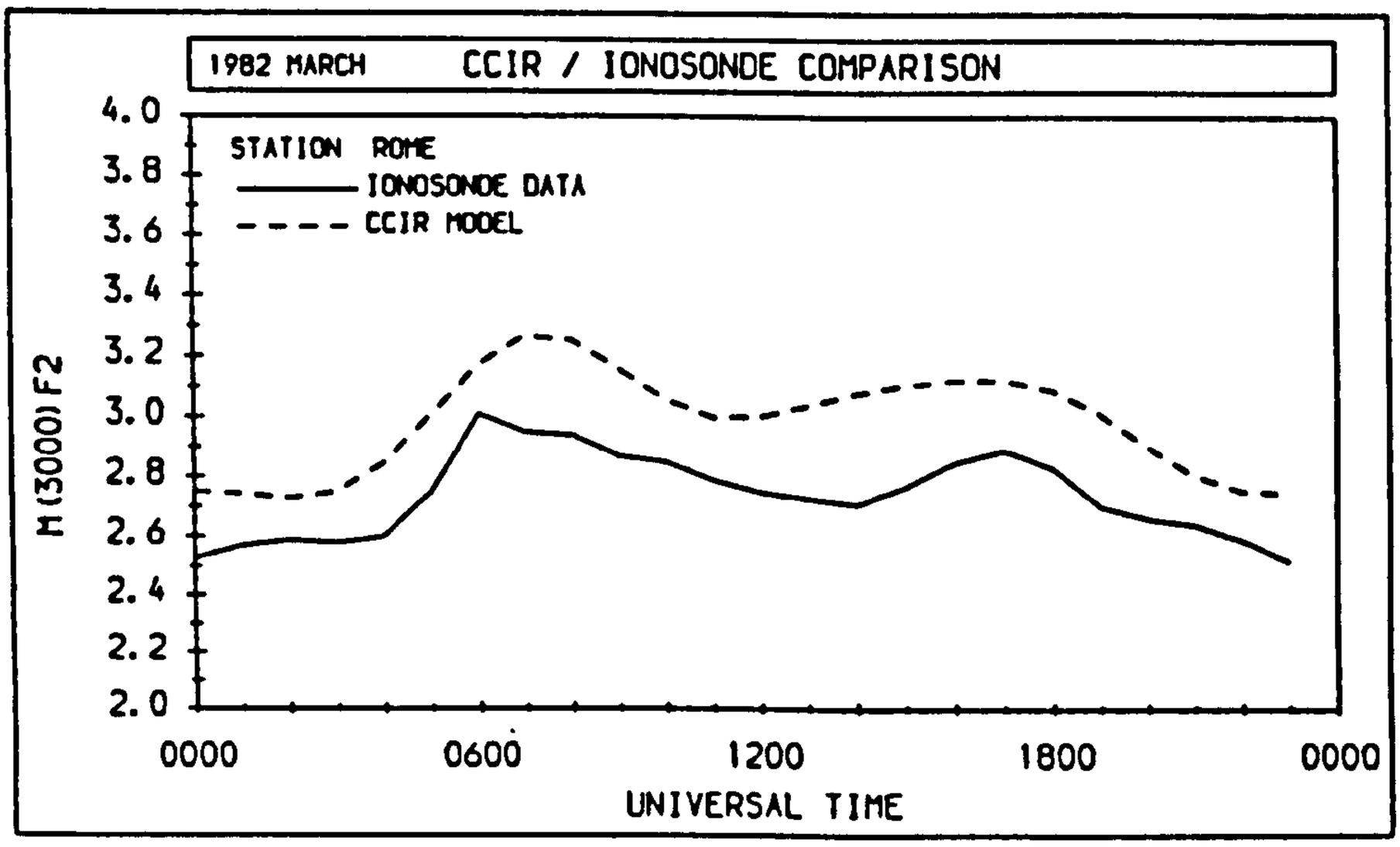

Figure 5.2 The monthly mean variation of foF2 and M(3000)F2 measured during March 1982 from the Rome ionosonde compared with the corresponding predictions of the CCIR Model.

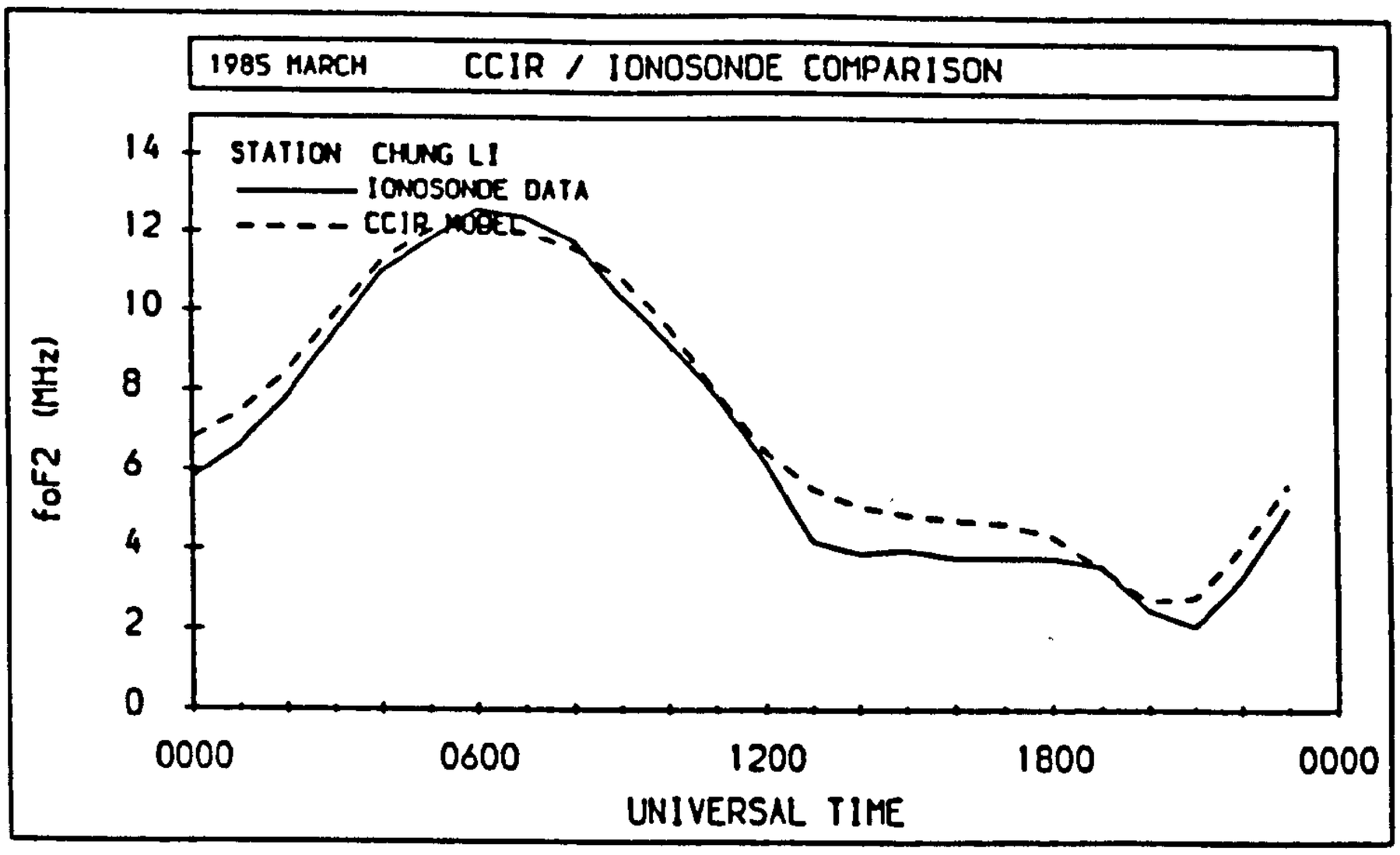

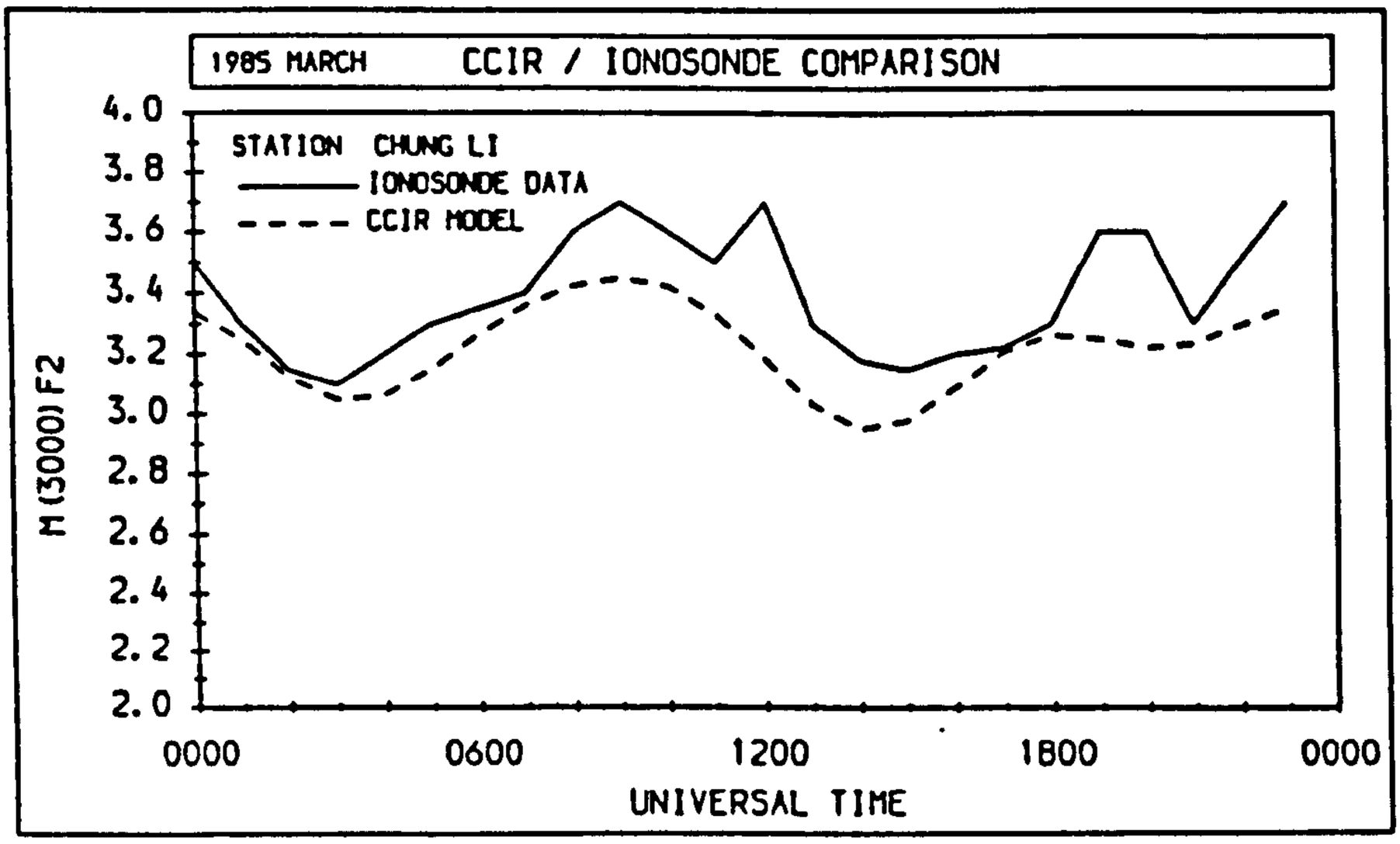

Figure 5.3 The monthly mean variation of foF2 and M(3000)F2 measured during March 1985 from the Chung Li ionosonde compared with the corresponding predictions of the CCIR Model.

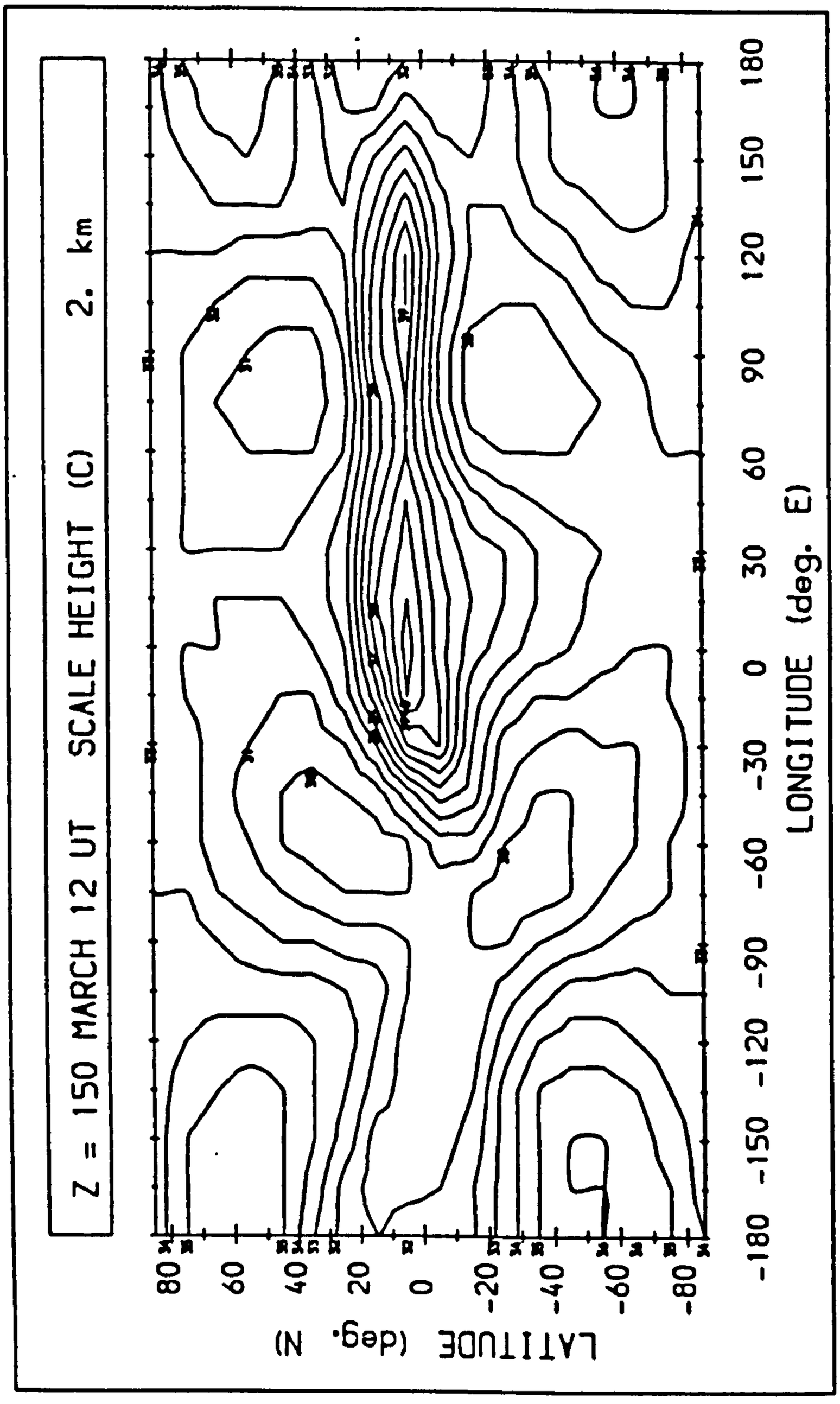

Figure 5.4 A global map of the scale height at the ionospheric peak predicted from the NASA Model under standard conditions. The contour interval is 2 km.

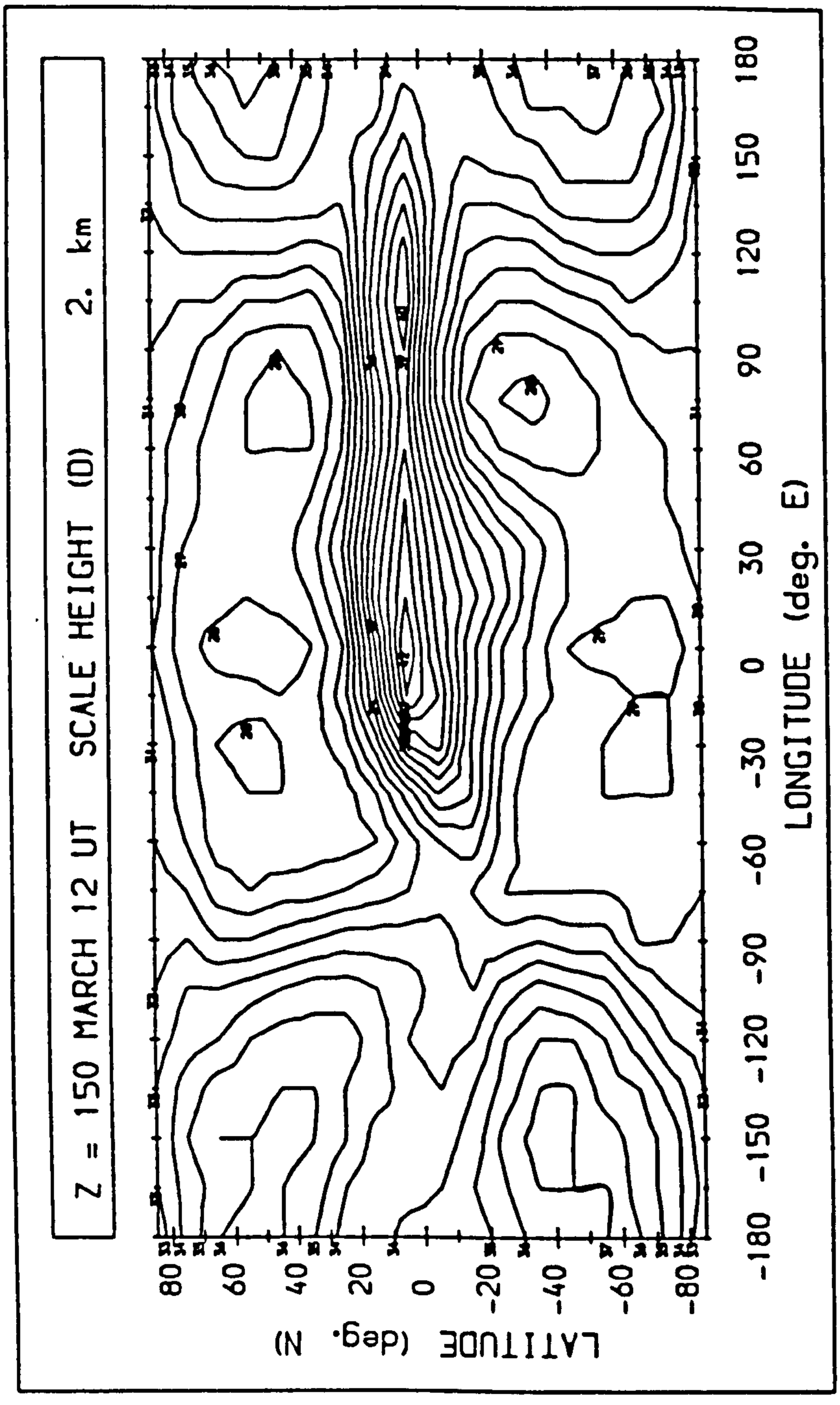

Figure 5.5 A global map of the scale height at the ionospheric peak predicted from the Jacchia Model under standard conditions. The contour interval is 2 km.

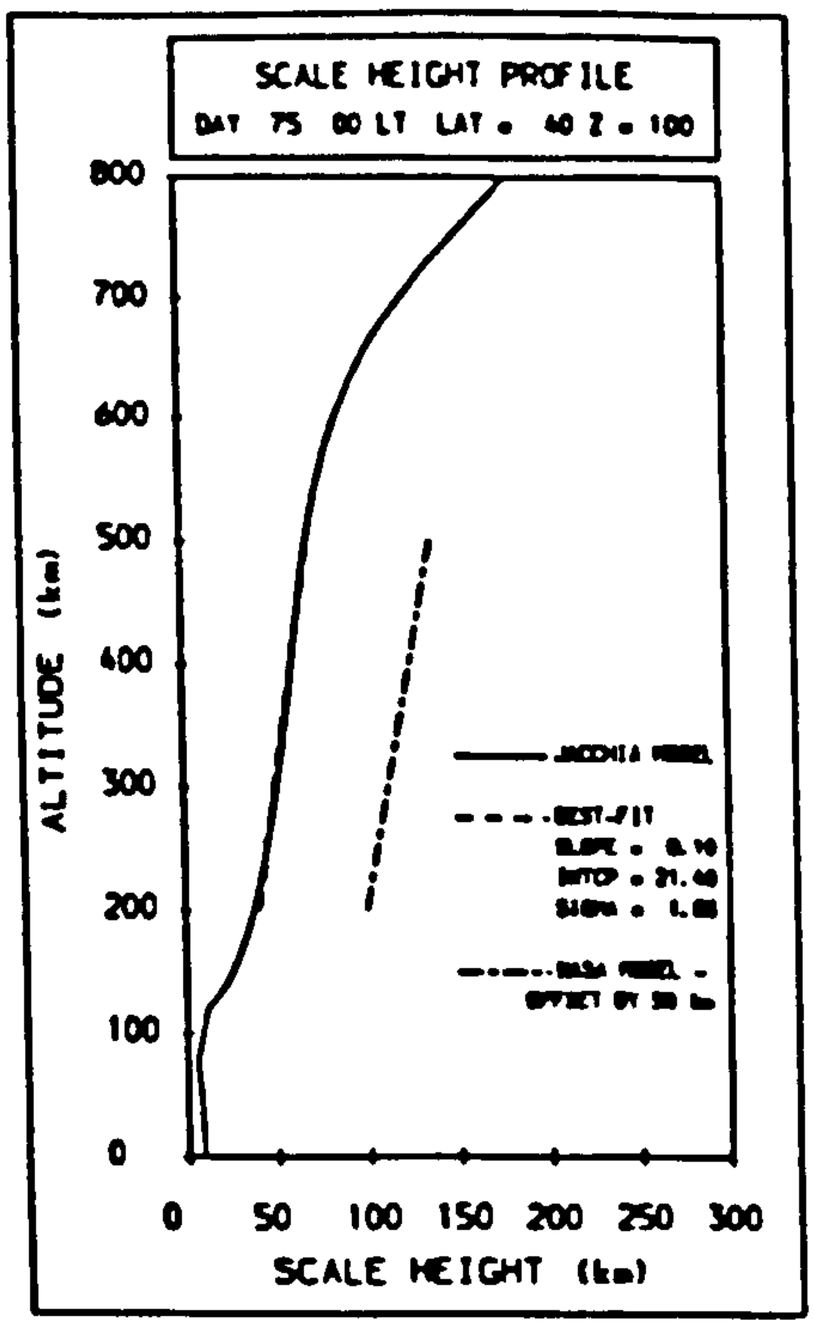

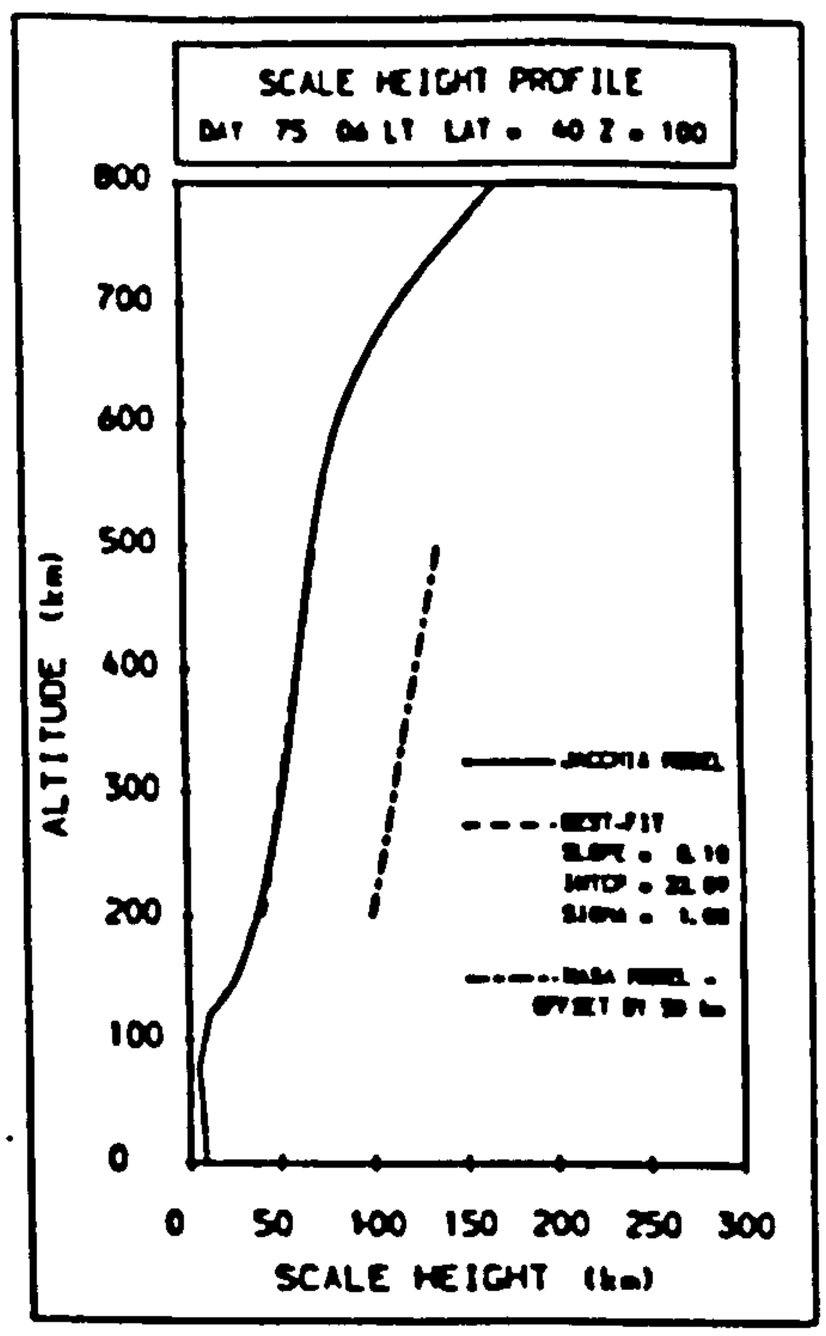

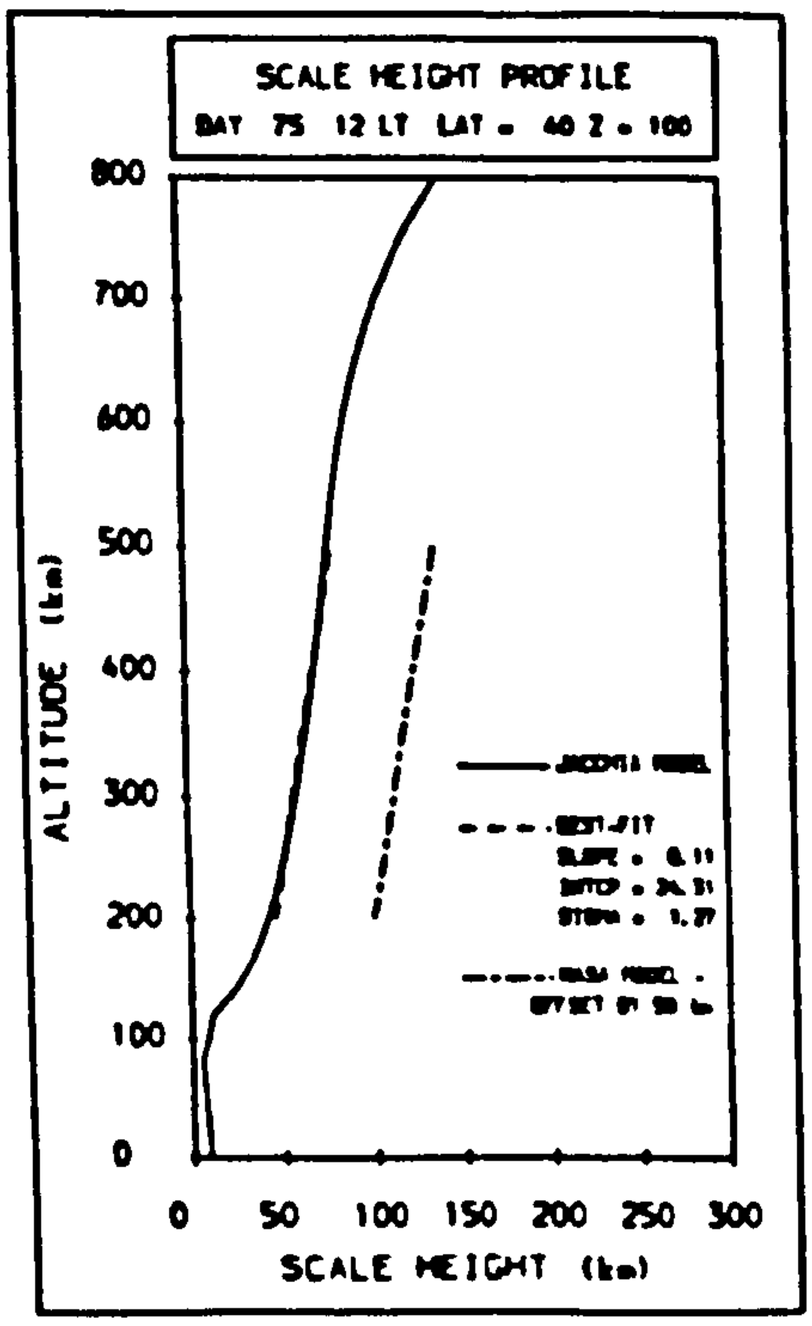

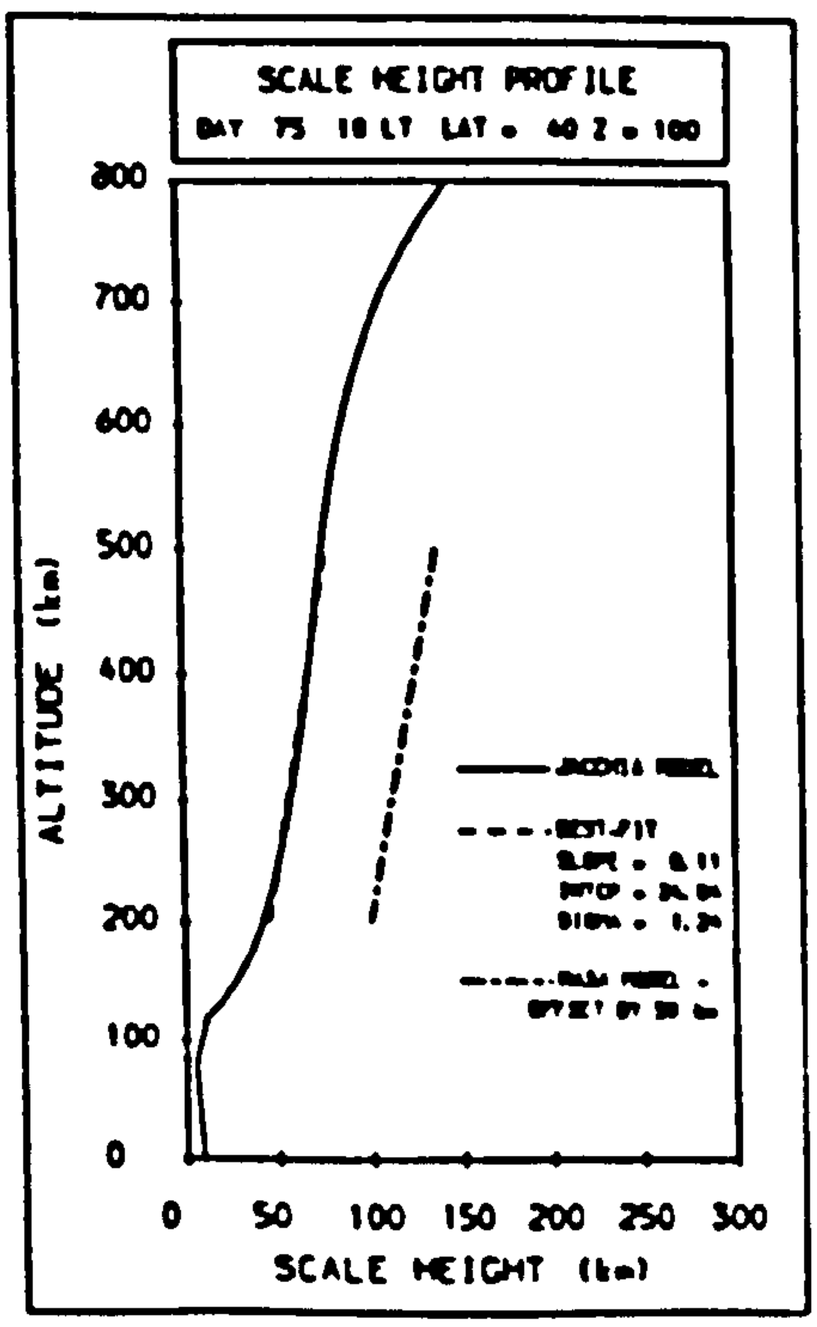

Figure 5.6 Altitude profiles to 800 km of scale height predicted from the Jacchia Thermospheric Model at 00 LT, 06 LT, 12 LT and 18 LT for a site at (40°N,0°E). A best-fit line is plotted for altitudes between 200 and 500 km, its parameters are given on the diagrams. The NASA Model profile is plotted, for comparison purposes, with an offset of 50 km.

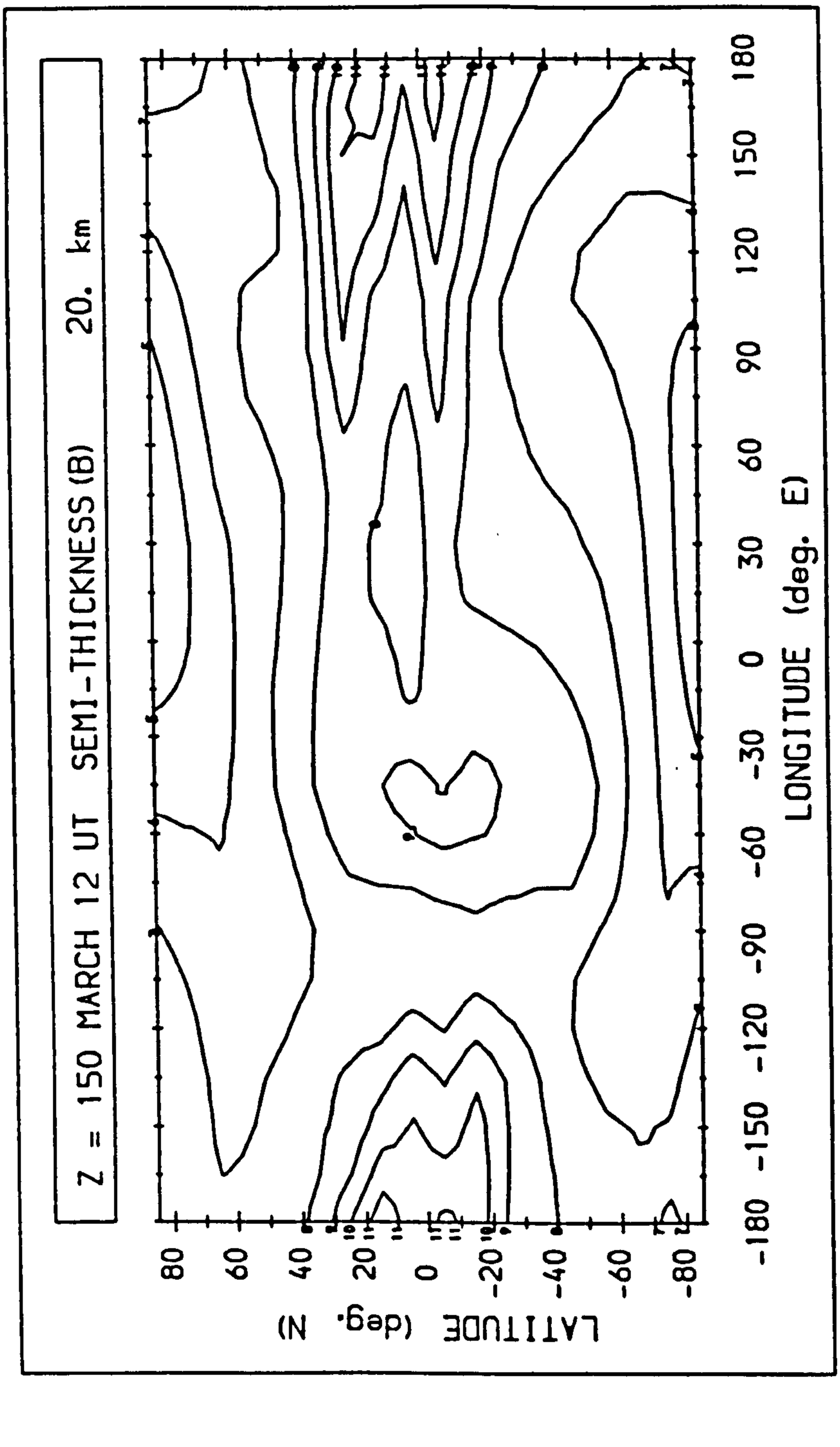

Figure 5.7 A global map of the biparabolic semi-thickness predicted for standard conditions from the formulation of Rawer and Bilitza (1985). The contour interval is 20 km.

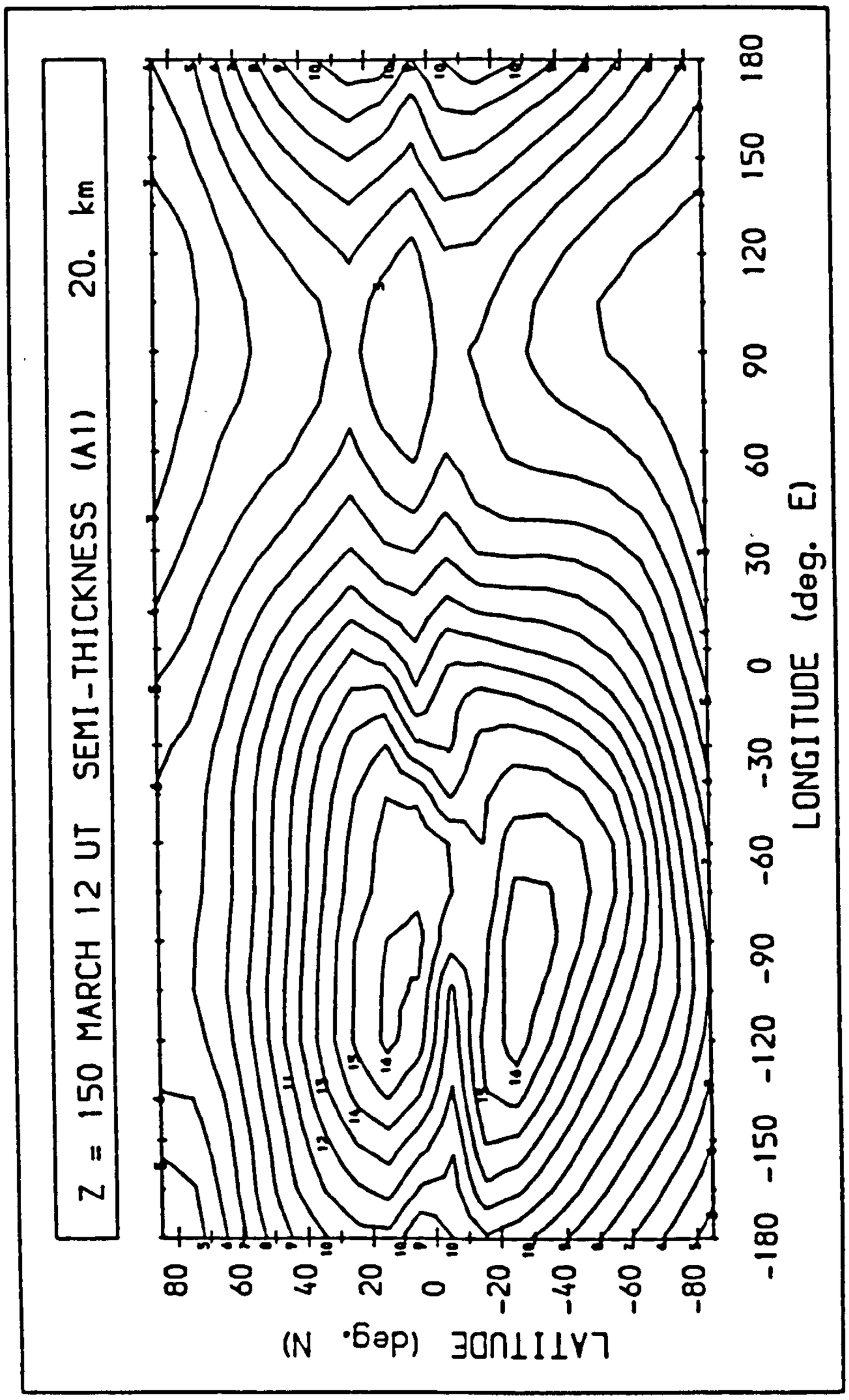

Figure 5.8 A global map of the biparabolic semi-thickness predicted for standard conditions from the bottomside calibration procedure based on noontime foF2 data. The contour interval is 20 km.

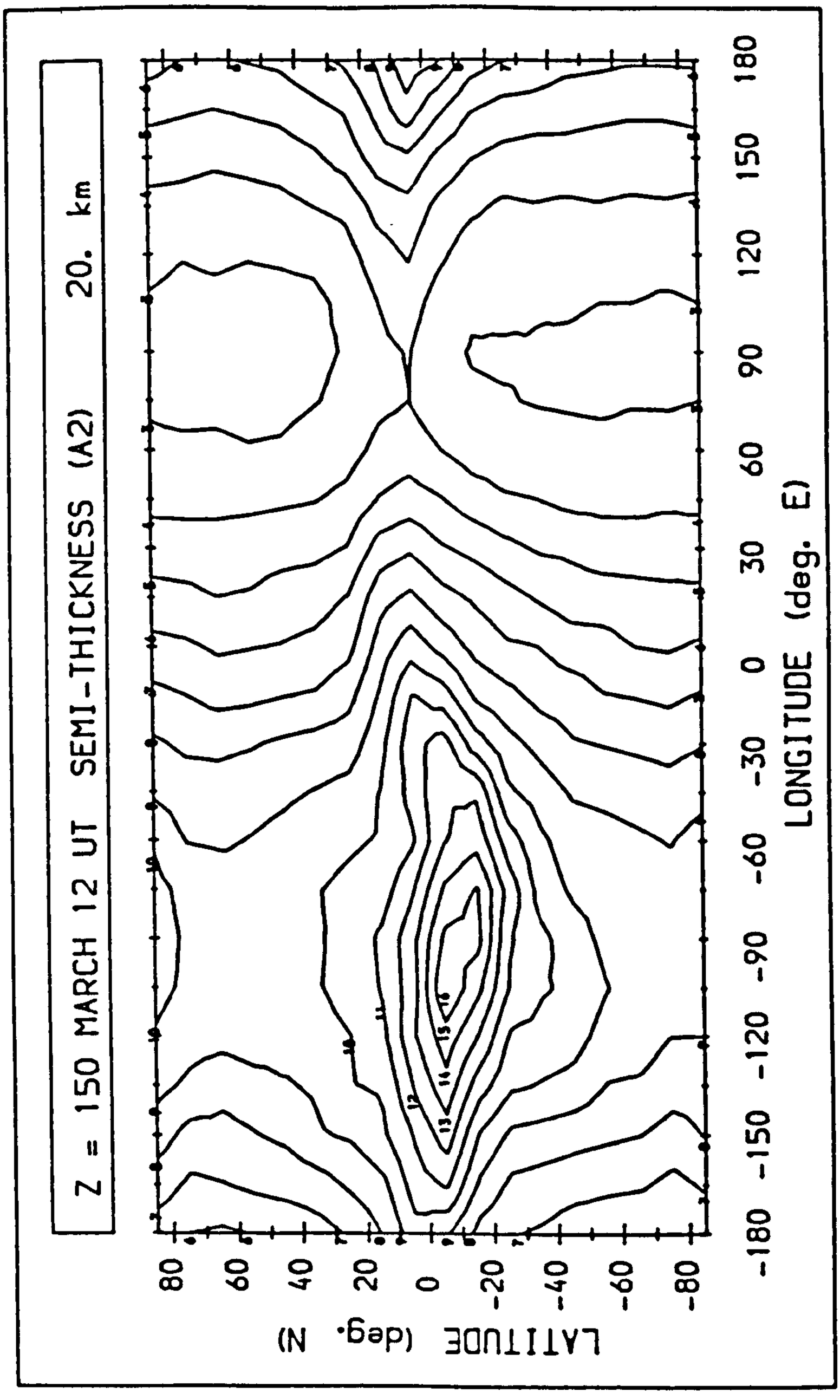

Figure 5.9 A global map of the biparabolic semi-thickness predicted for standard conditions from the bottomside calibration procedure based on noontime peak altitude data. The contour interval is 20 km.

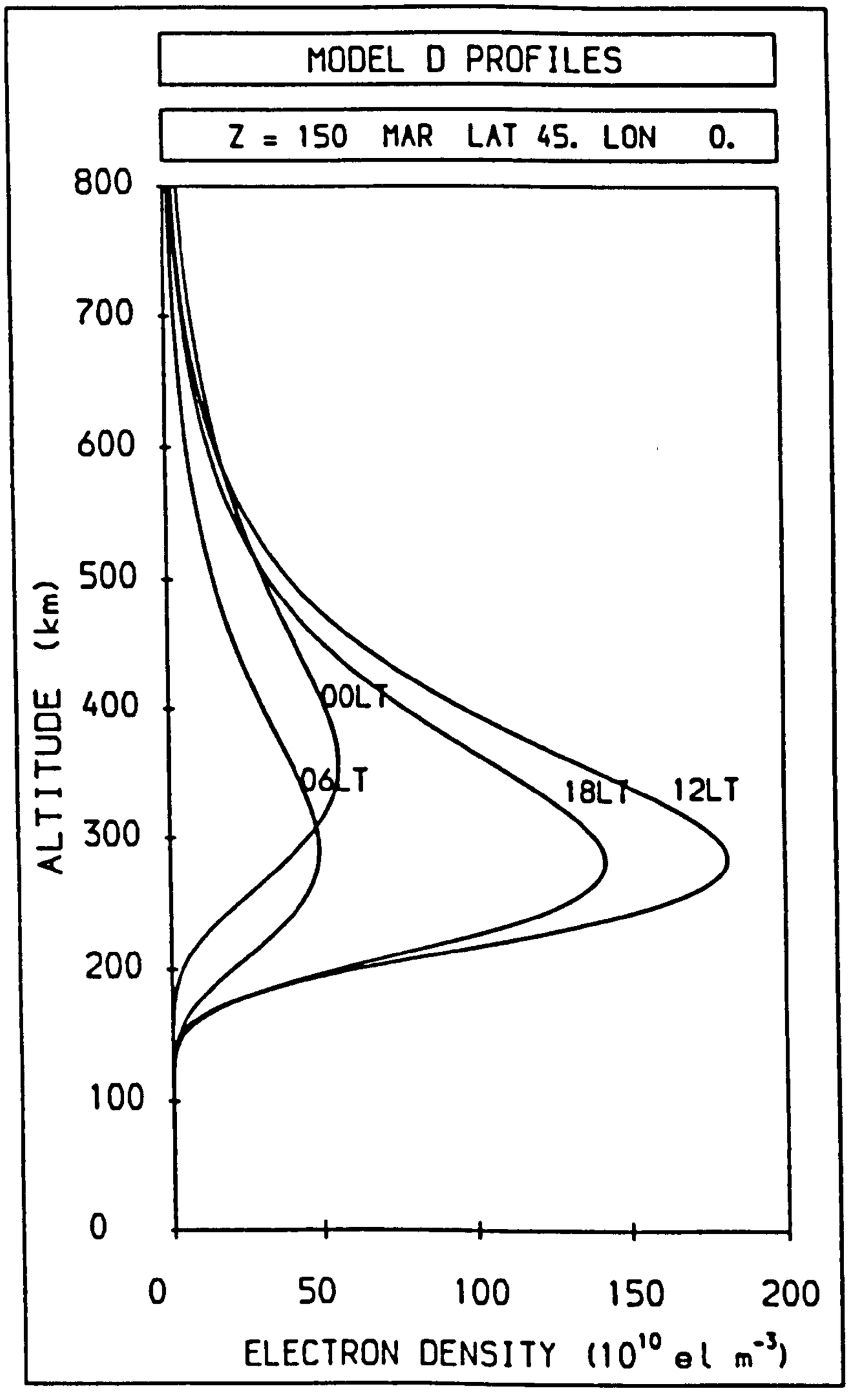

Figure 5.10 Altitude profiles of electron density predicted for a site at (45°N,0°E) at 00 LT, 06 LT, 12 LT and 18 LT from the Predictive Model D under standard conditions.

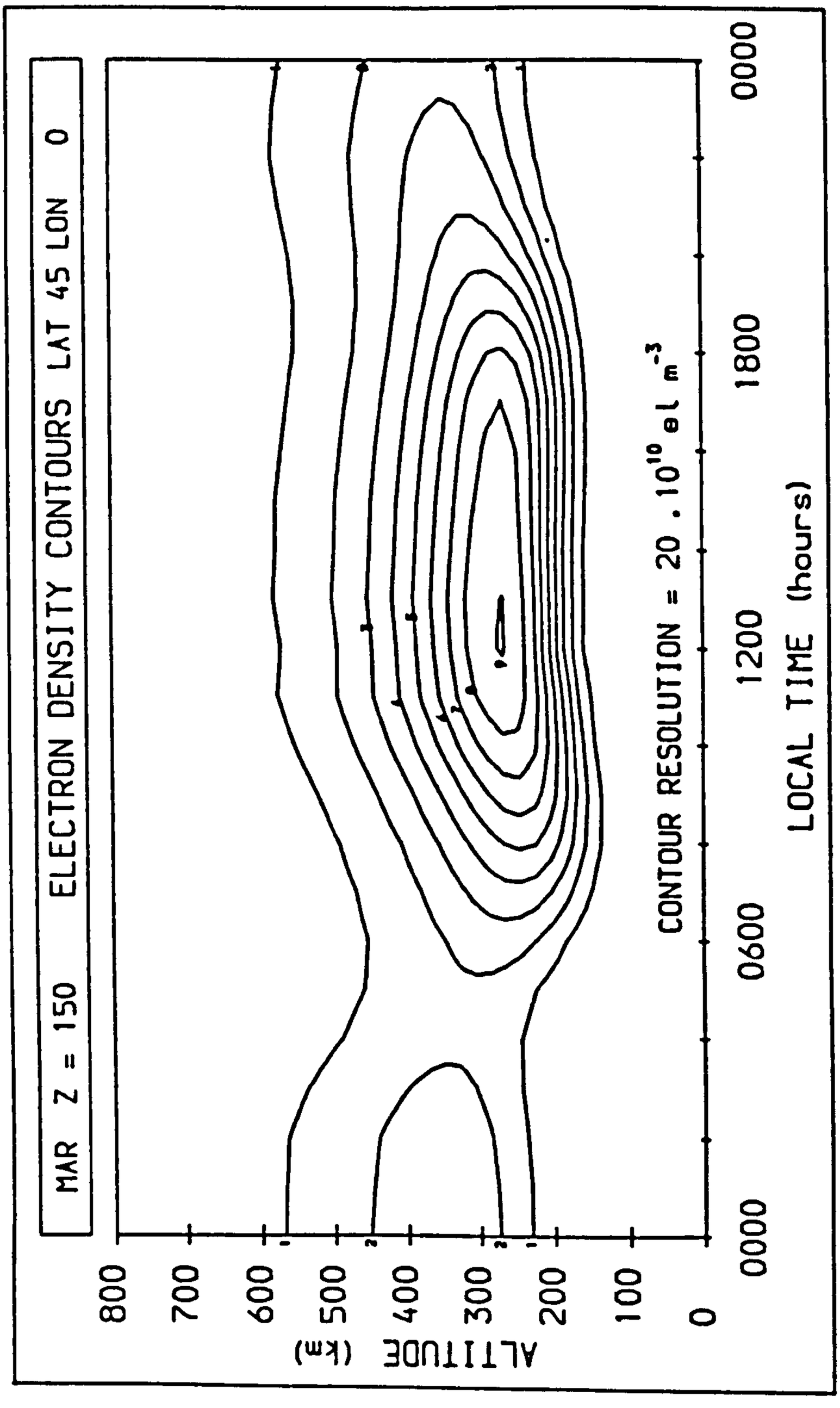

Figure 5.11 The Local Time variation of the sub–800 km electron density altitude profile predicted from the Predictive Model D for a site at (45°N,0°E) under standard conditions. The contour interval is 2.10^{11} m^{-3}.

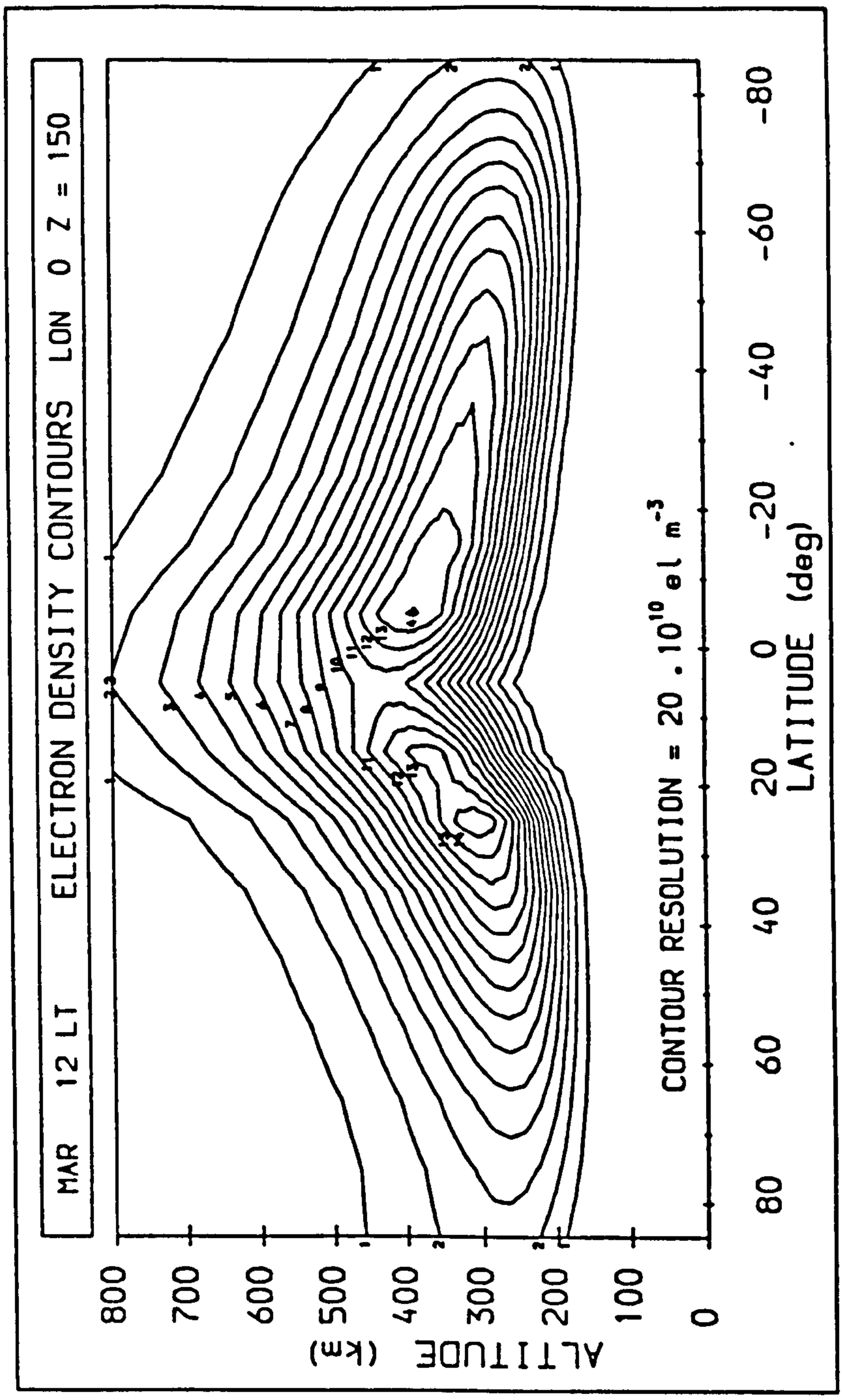

Figure 5.12 The latitudinal variation of the sub–800 km electron density altitude profile predicted from the Predictive Model D for 12 LT under standard conditions. The contour interval is 2.10^{11} m^{-3}.

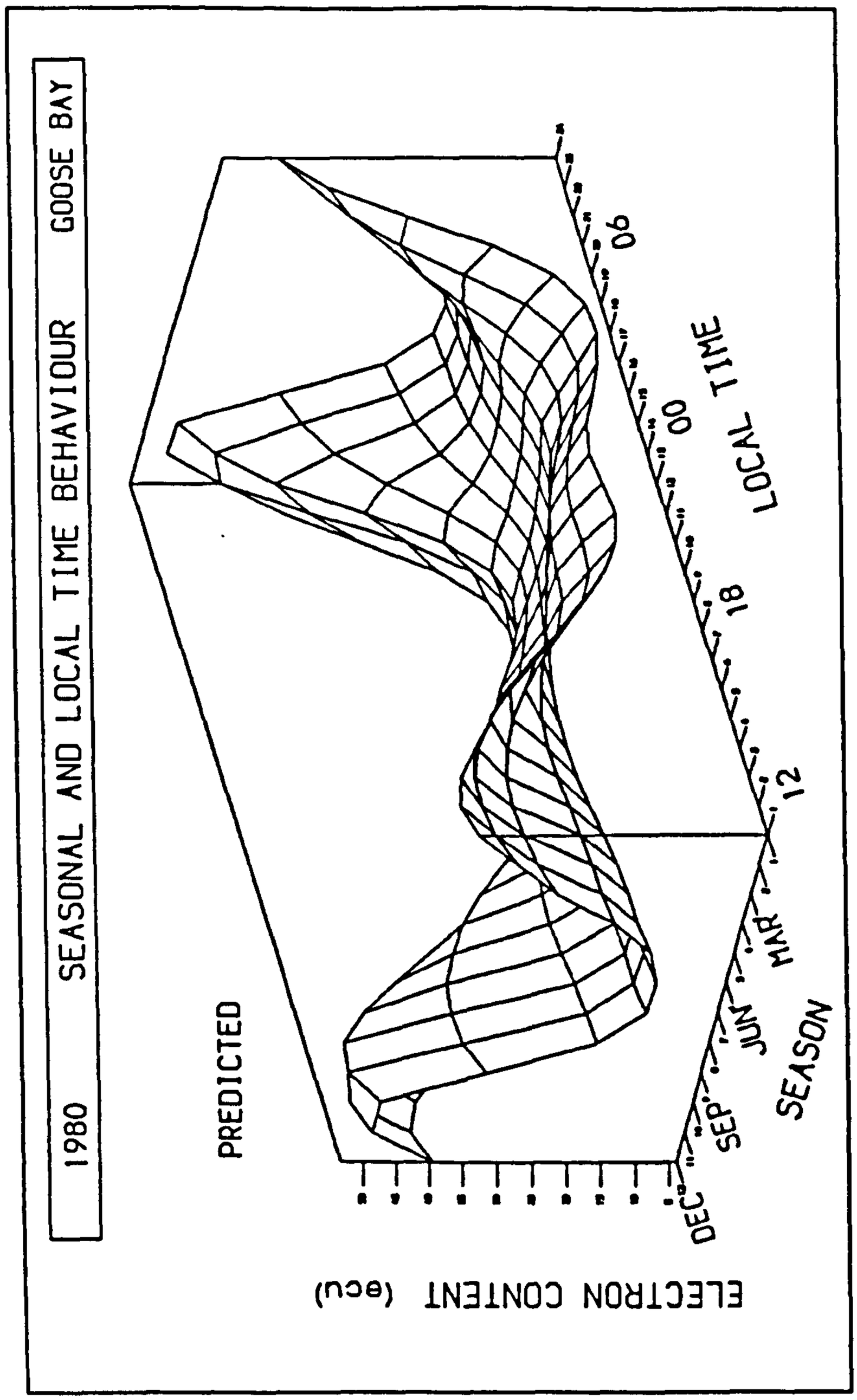

Figure 5.13 The diurnal and seasonal variation of electron content estimated from Predictive Model D for 1980 at Goose Bay.

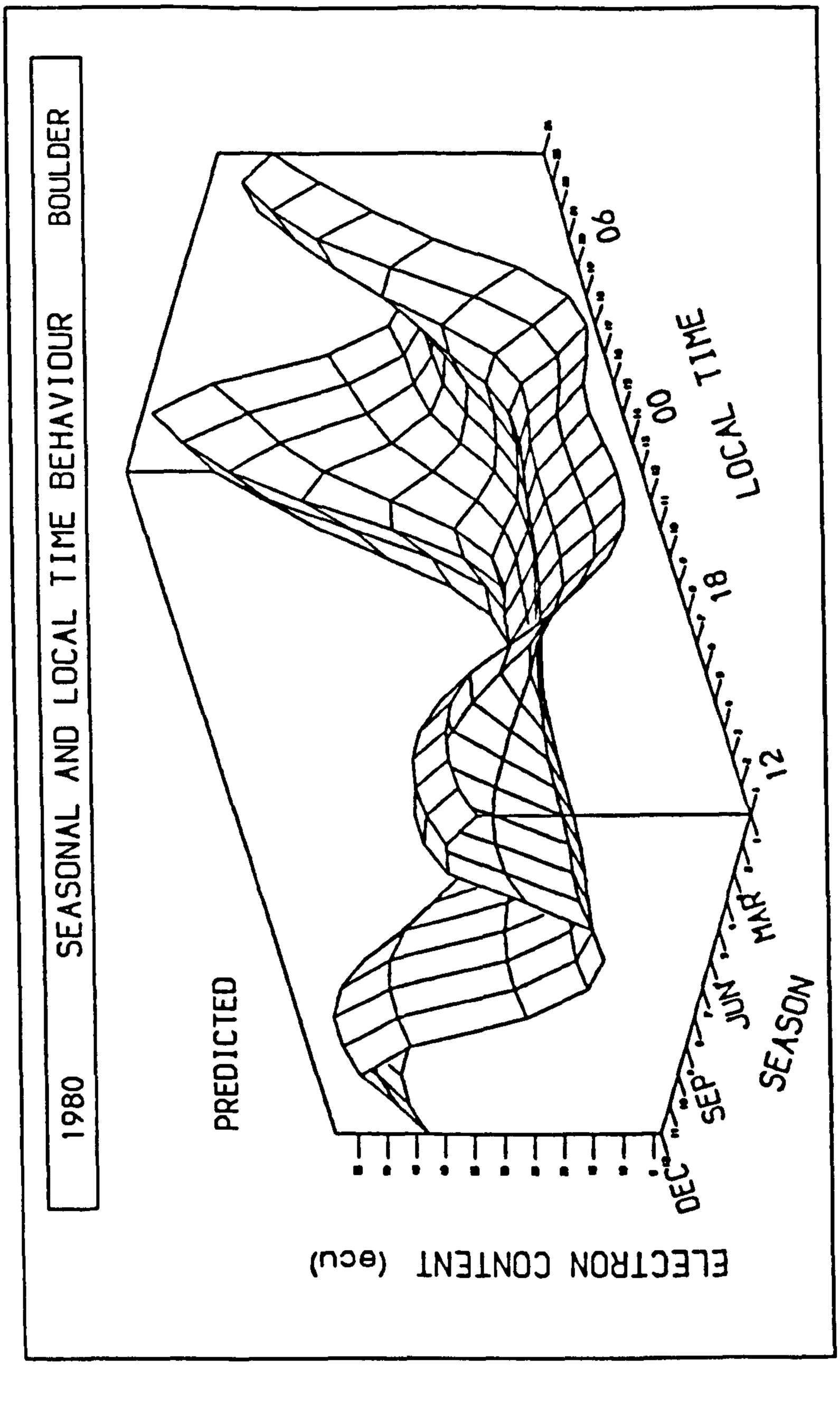

Figure 5.14 The diurnal and seasonal variation of electron content estimated from Predictive Model D for 1980 at Boulder.

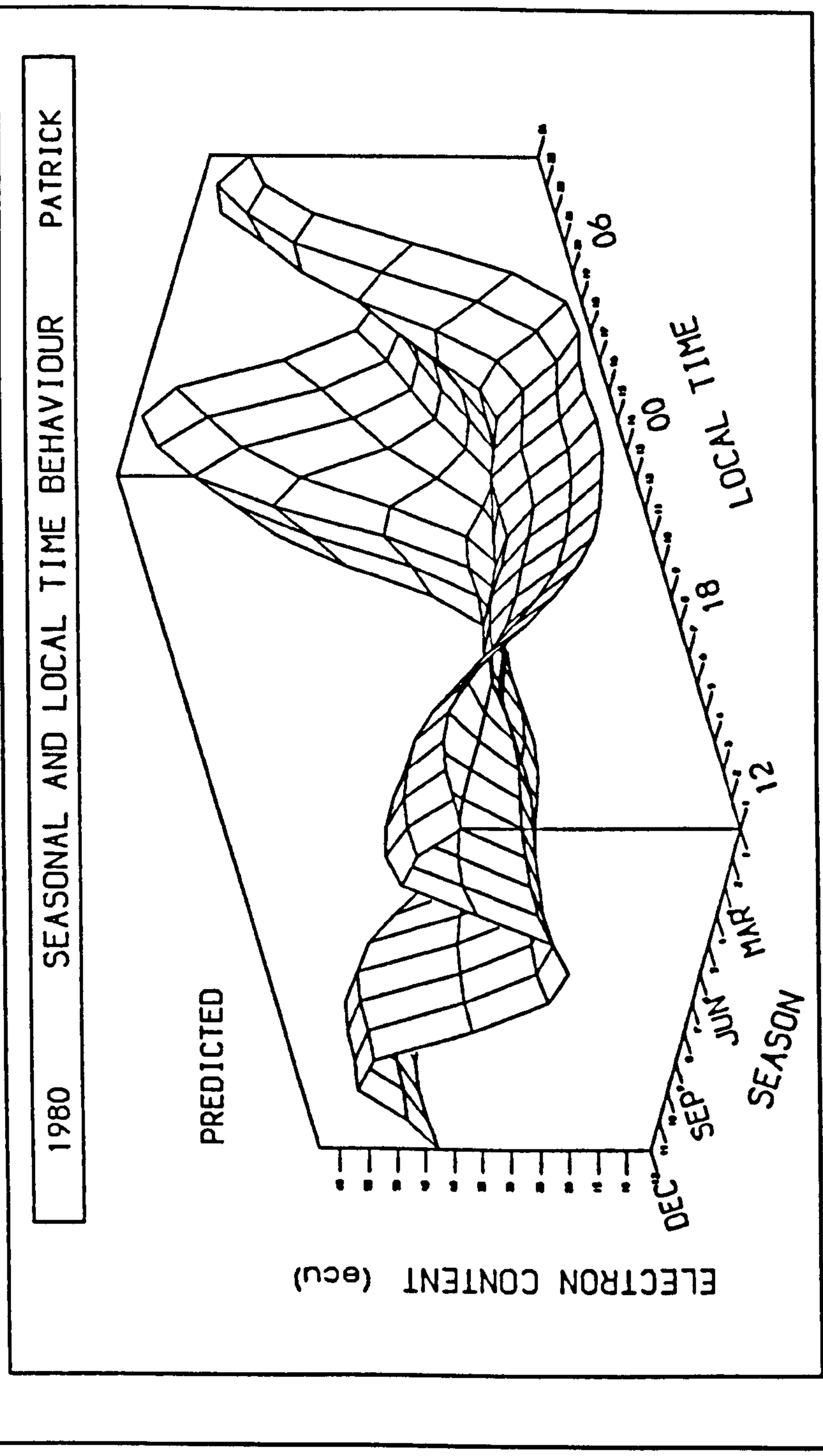

Figure 5.15 The diurnal and seasonal variation of electron content estimated from Predictive Model D for 1980 at Patrick AFB.

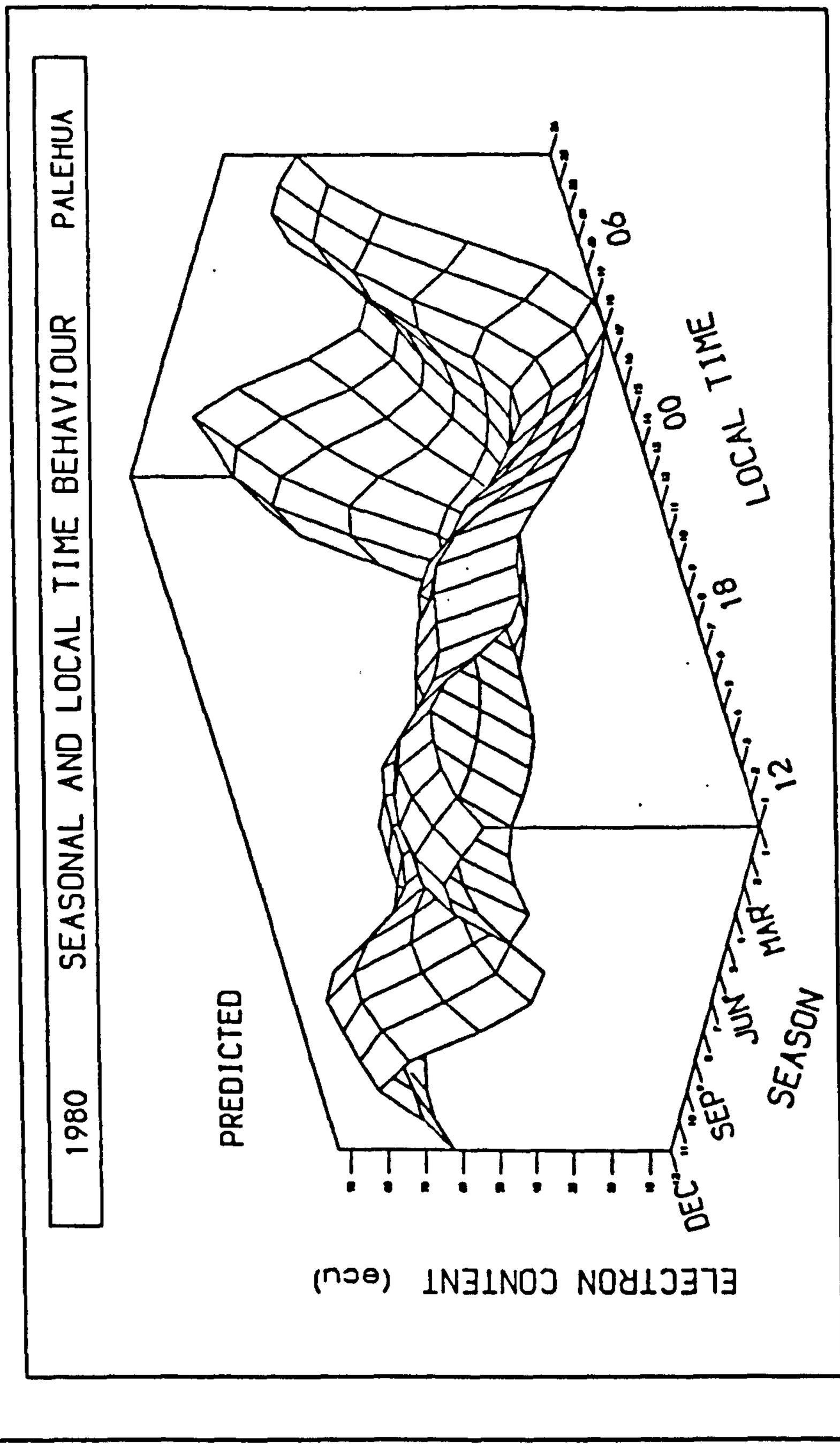

Figure 5.16 The diurnal and seasonal variation of electron content estimated from Predictive Model D for 1980 at Palehua.

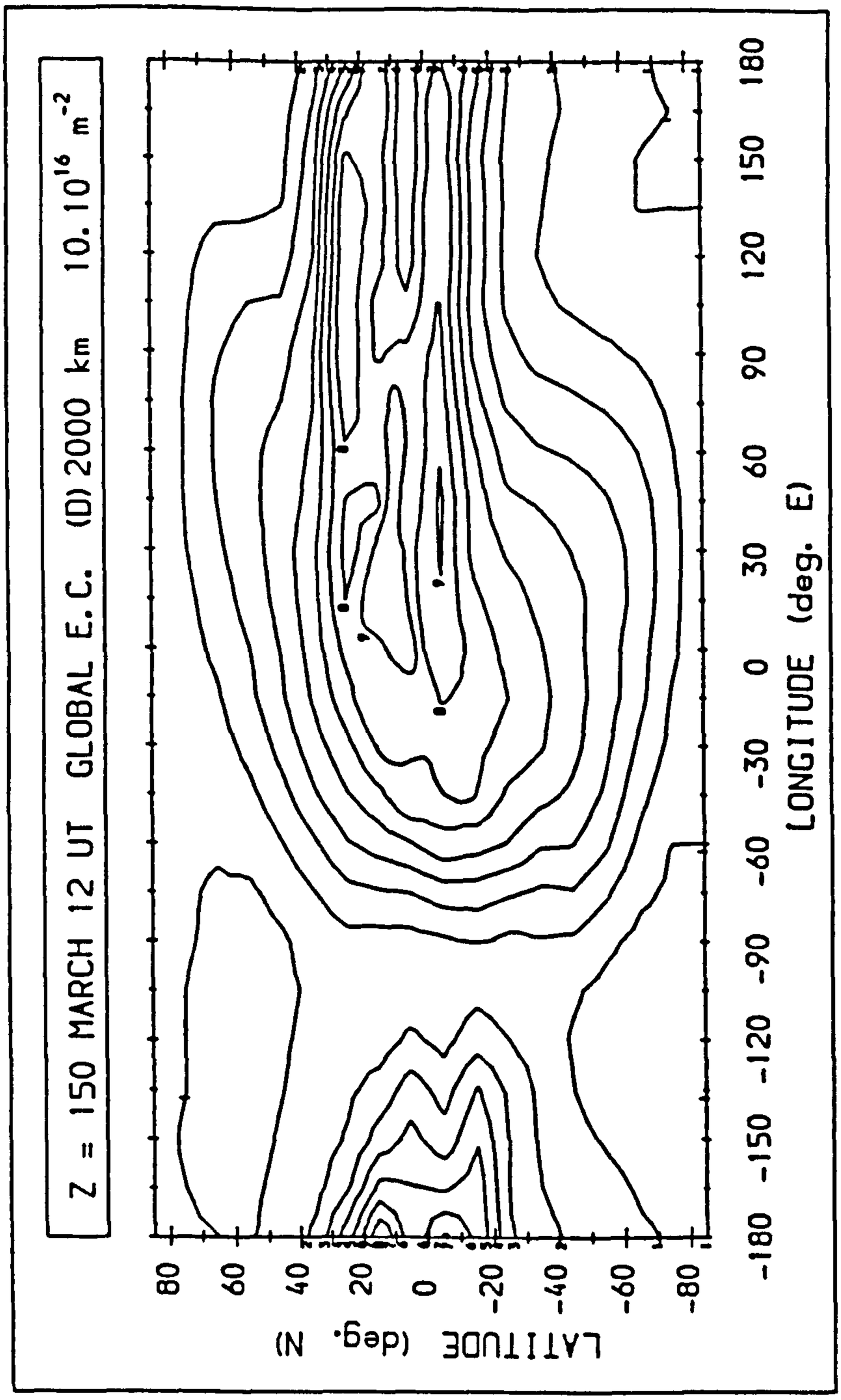

Figure 5.17 A global map of sub–2 000 km electron content estimated from Predictive Model D at 12 UT during March for a sunspot number of 150. The contour interval is 10 ecu.

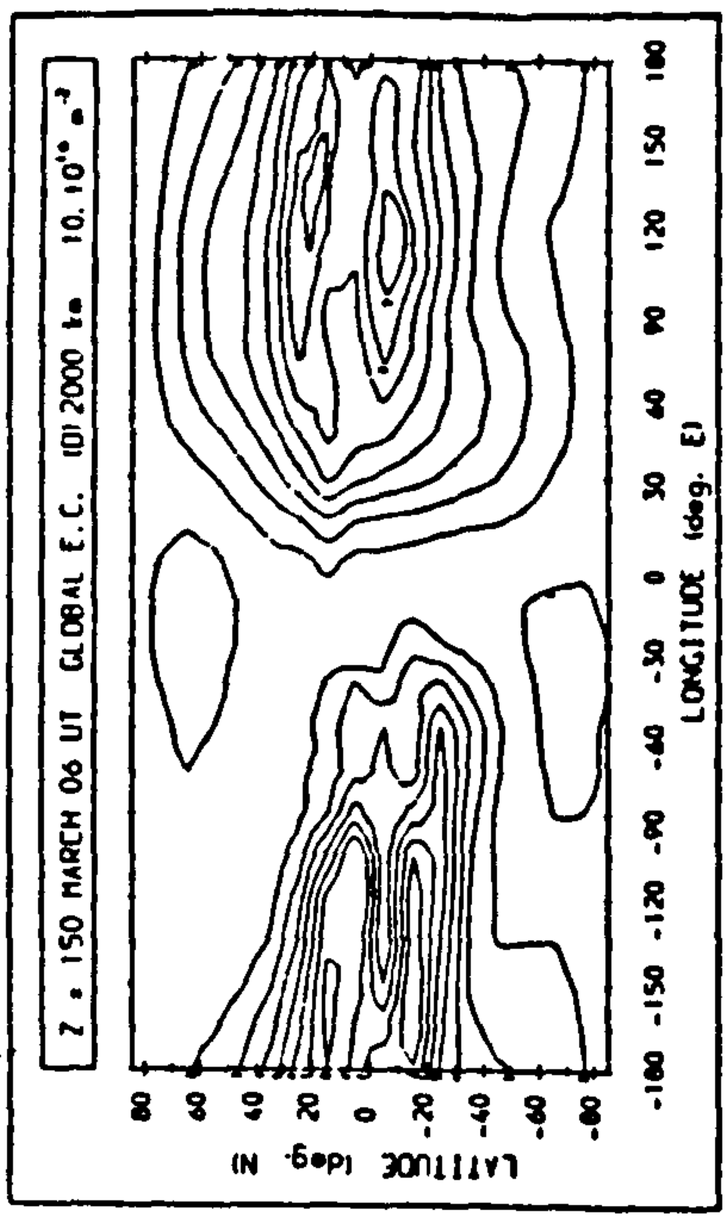

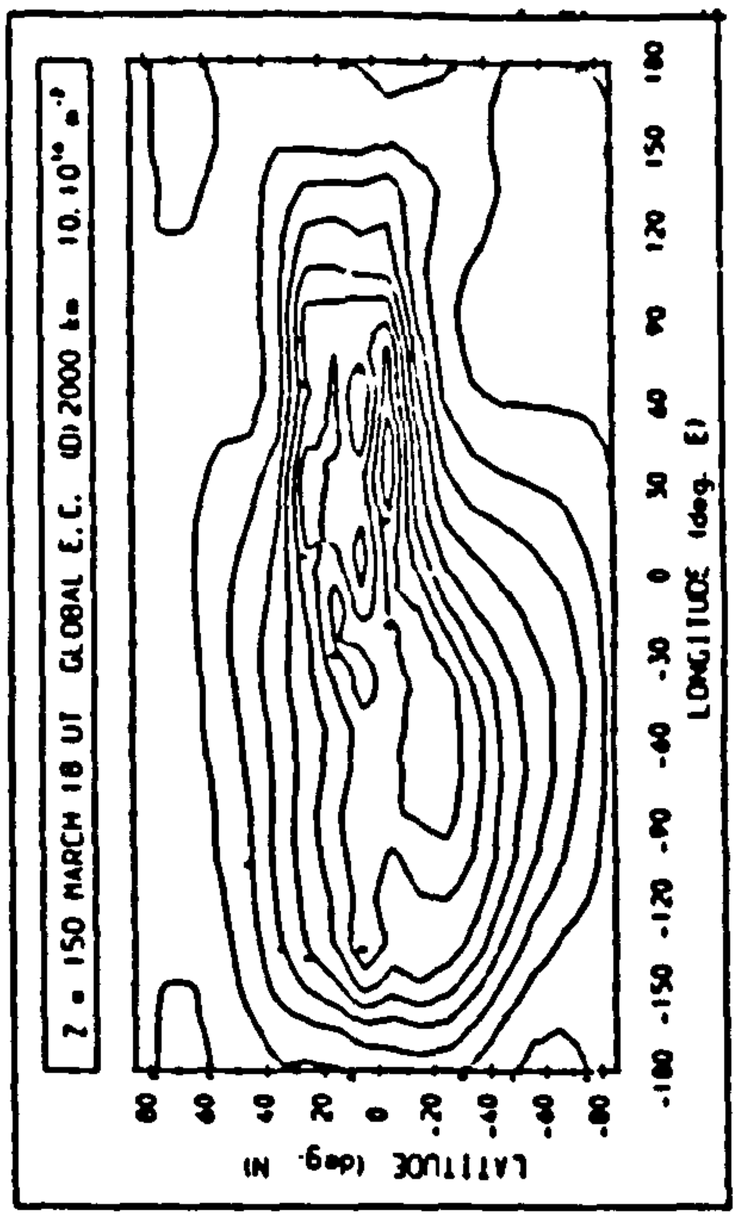

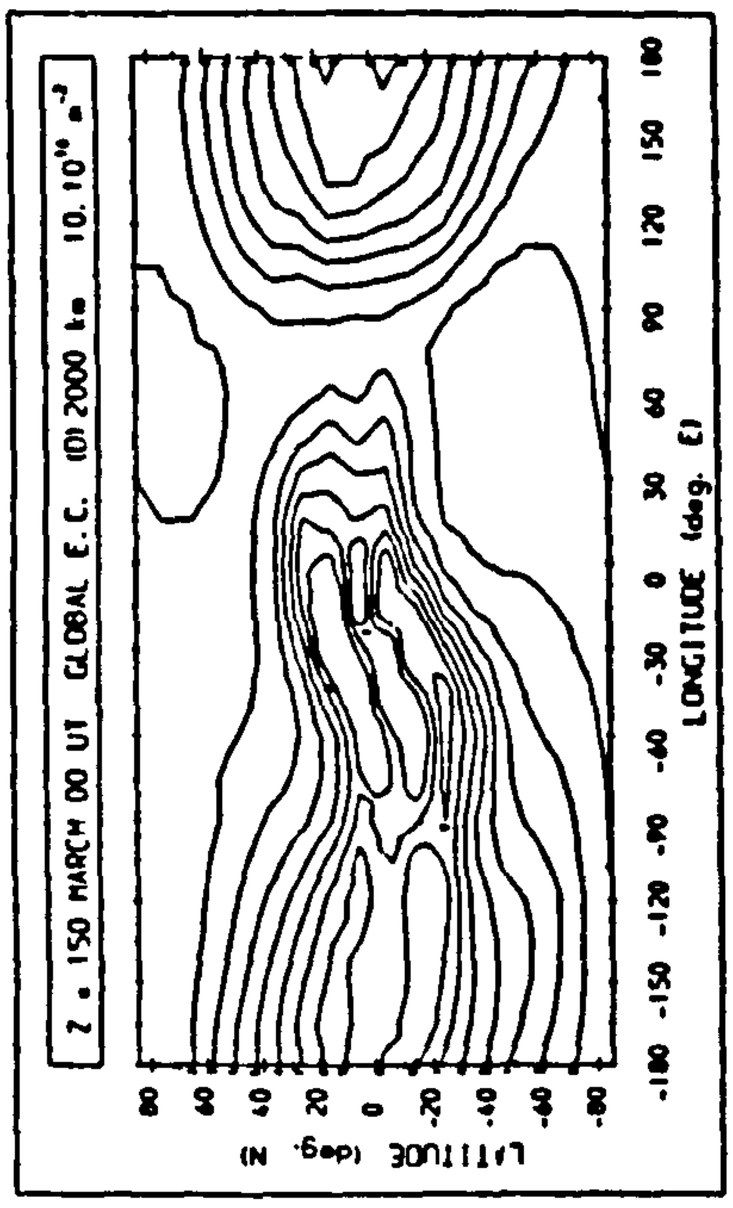

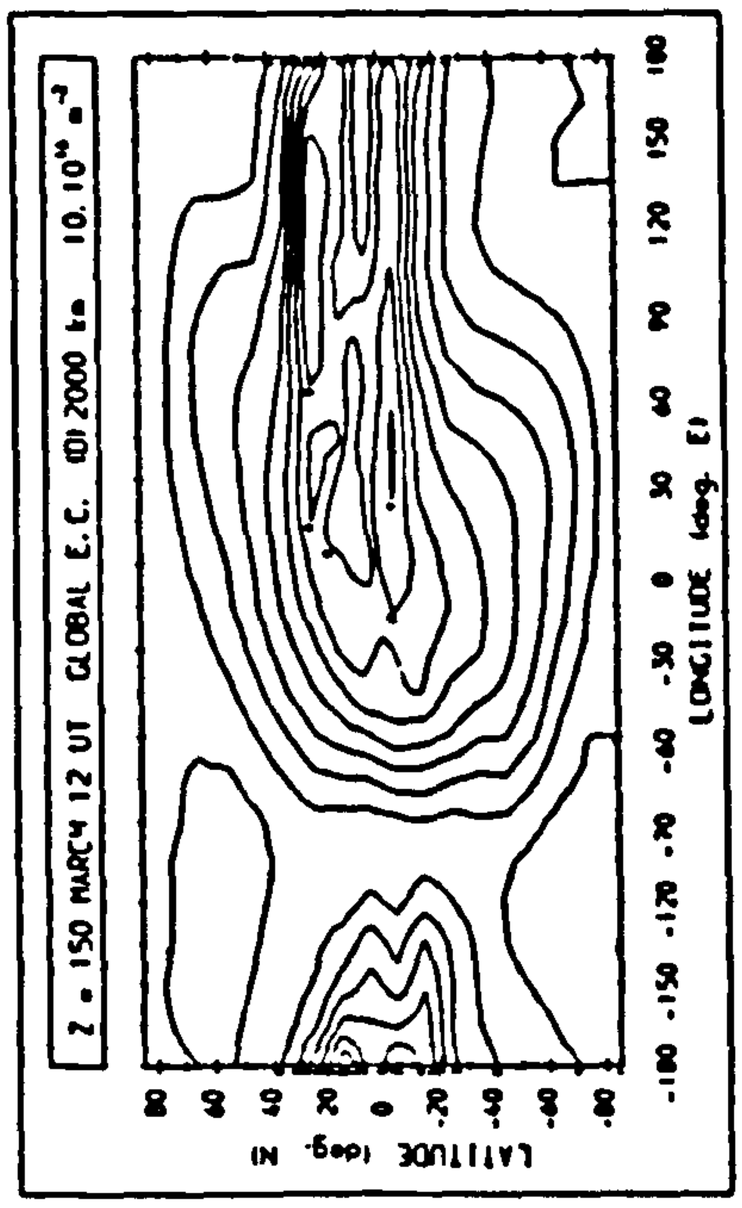

Figure 5.18 Global maps of sub–2 000 km electron content estimated from Predictive Model D at 00 UT, 06 UT, 12 UT and 18 UT under standard conditions. The contour interval is 10 ecu.

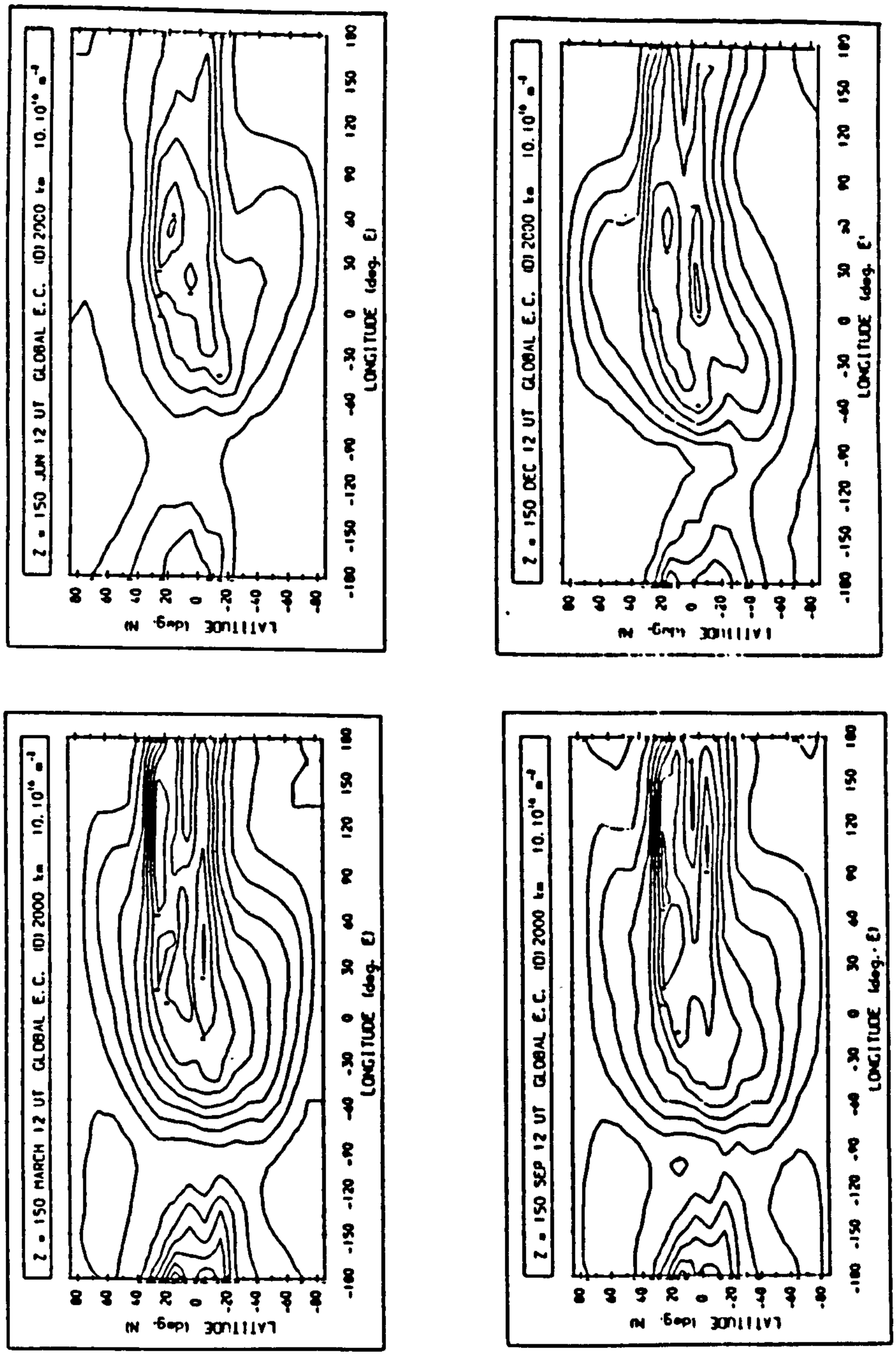

Figure 5.19 Global maps of sub–2 000 km electron content estimated from Predictive Model D for March, June, September and December at 12 UT for a sunspot number of 150. The contour interval is 10 ecu.

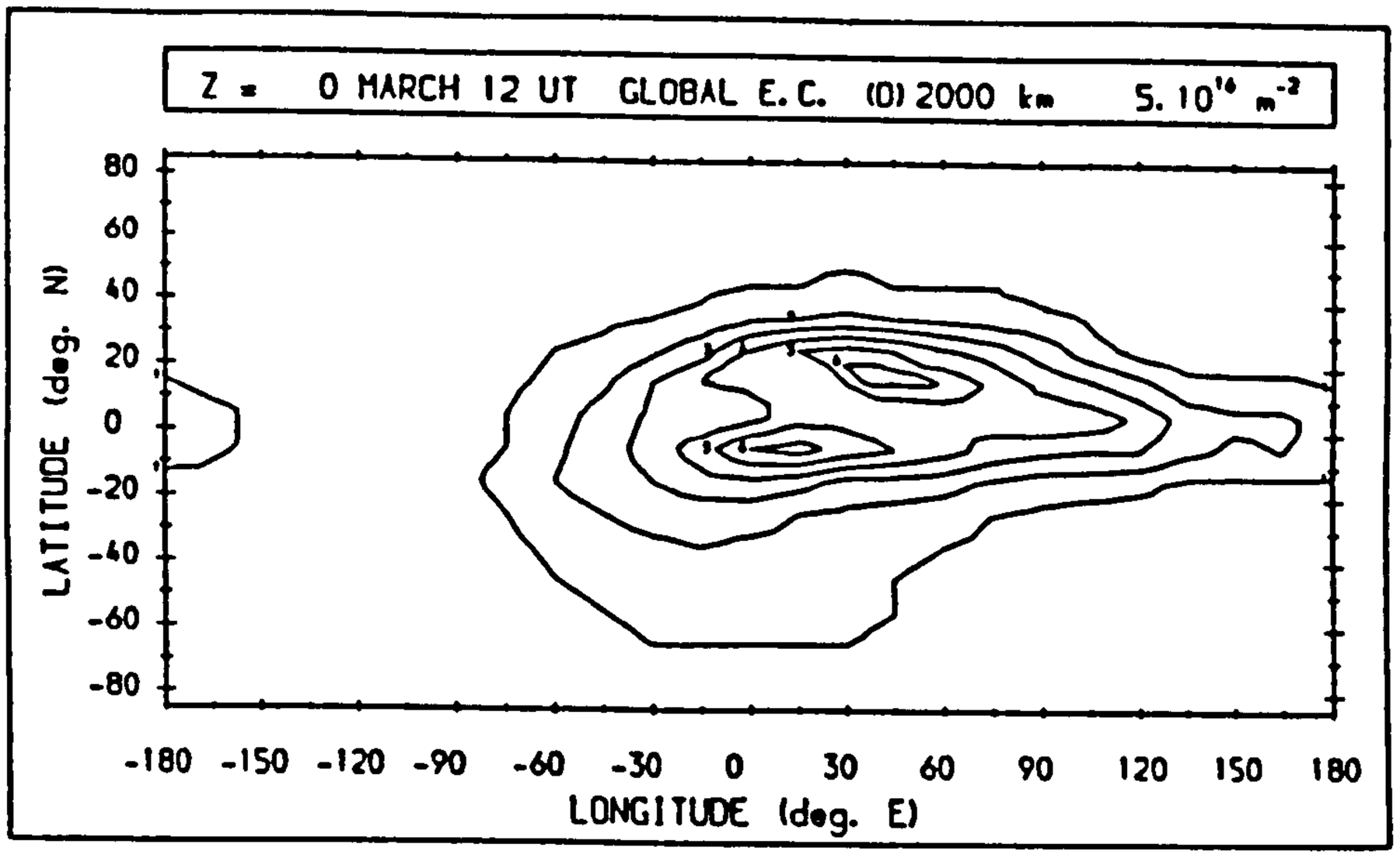

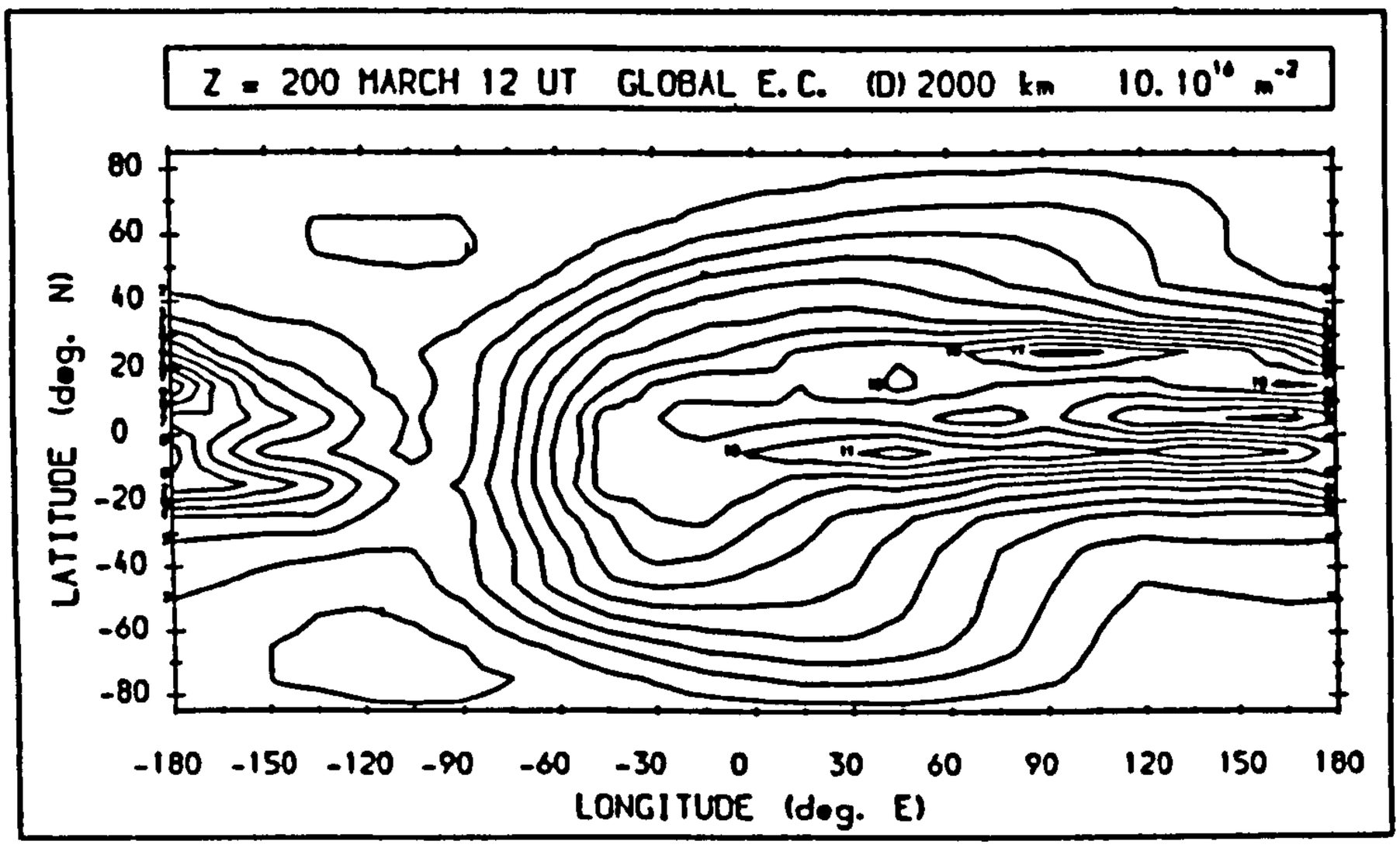

Figure 5.20 Global maps of sub–2 000 km electron content estimated from Predictive Model D for sunspot numbers of 0 and 200 during March at 12 UT. The contour interval is 10 ecu.

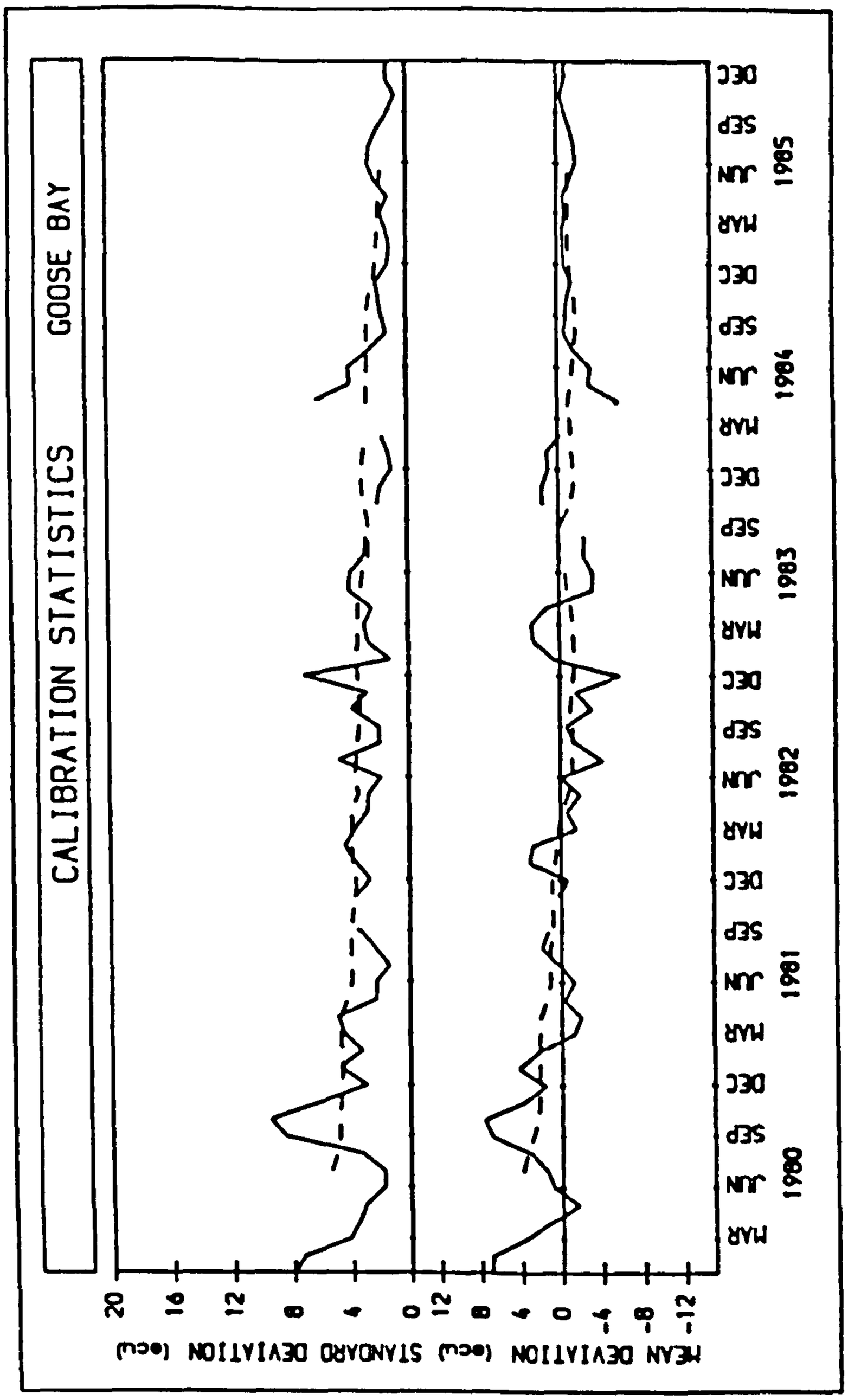

Figure 5.21 The standard deviation and mean deviation of the Model D monthly mean electron content estimates about the monthly mean Goose Bay data between 1980 and 1985, inclusive.

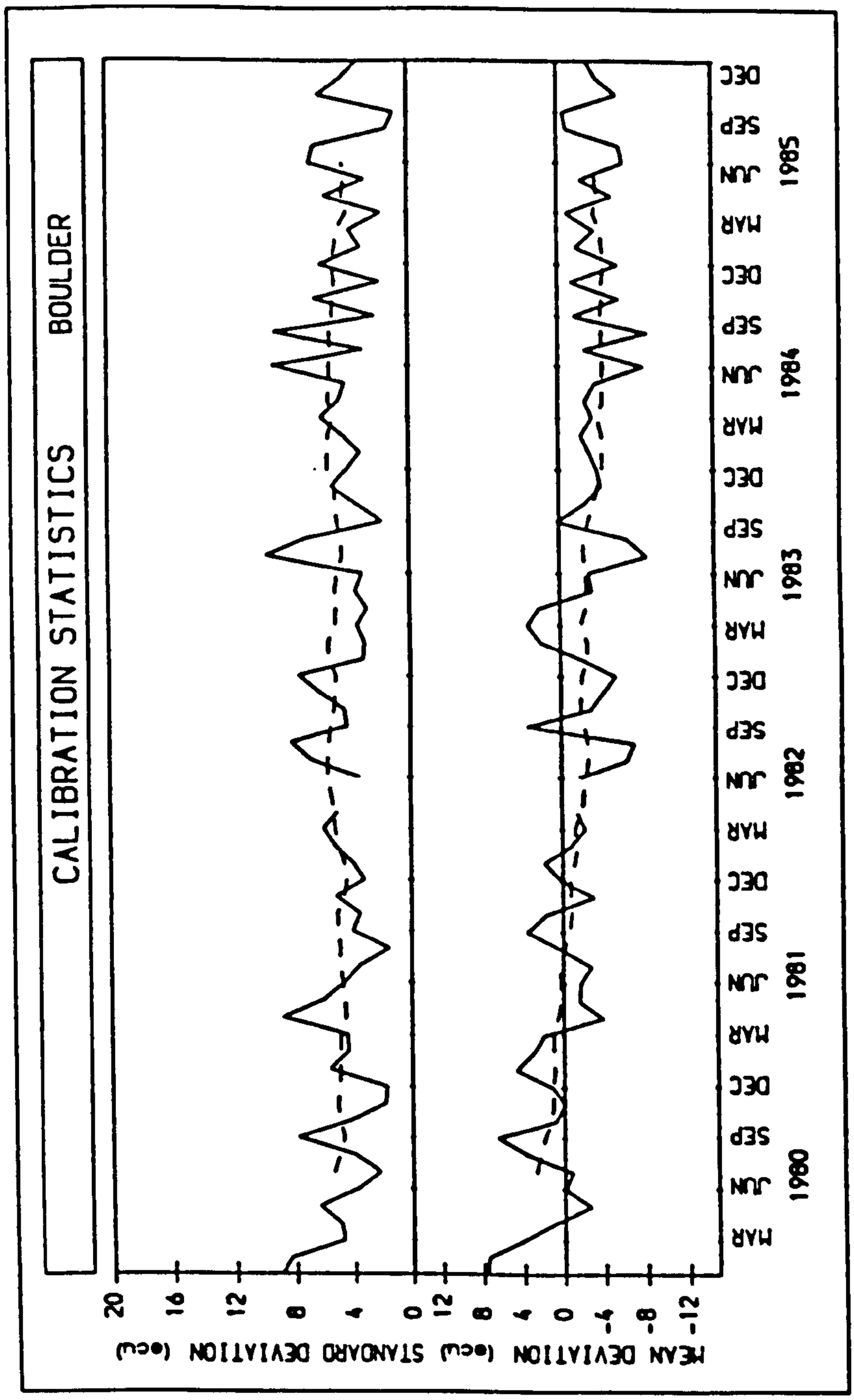

Figure 5.22 The standard deviation and mean deviation of the Model D monthly mean electron content estimates about the monthly mean Boulder data between 1980 and 1985, inclusive.

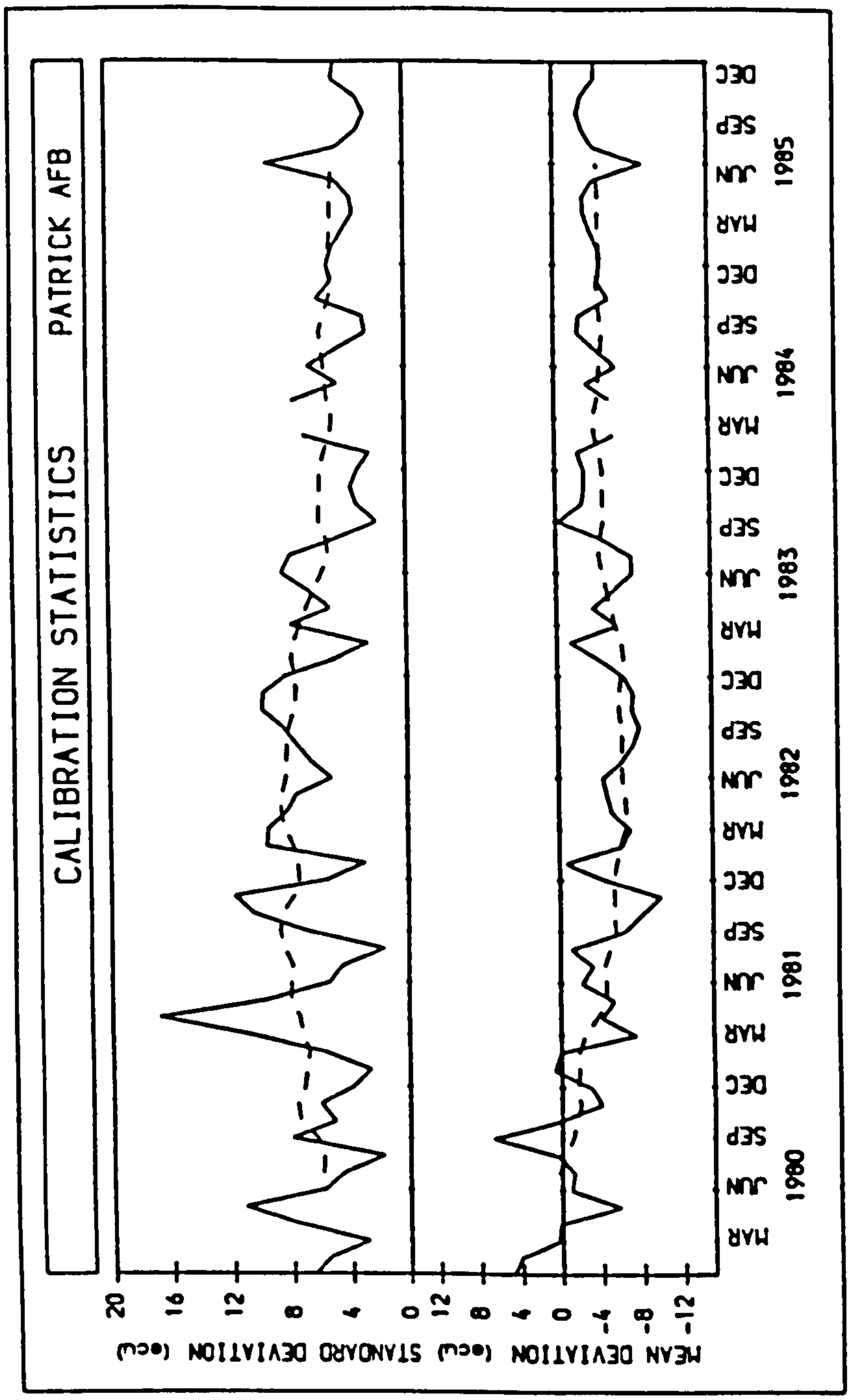

Figure 5.23 The standard deviation and mean deviation of the Model D monthly mean electron content estimates about the monthly mean Patrick AFB data between 1980 and 1985, inclusive.

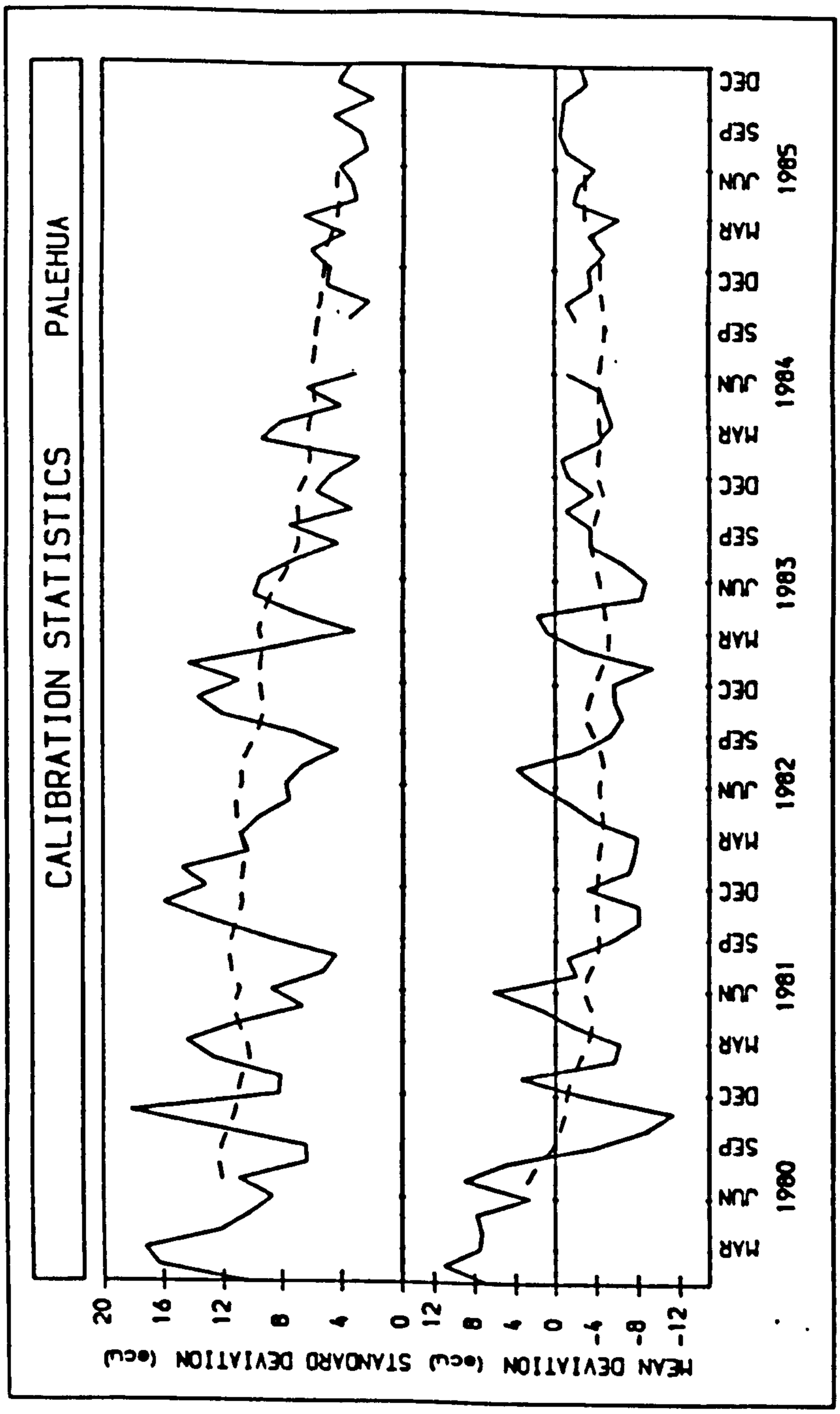

Figure 5.24 The standard deviation and mean deviation of the Model D monthly mean electron content estimates about the monthly mean Palehua data between 1980 and 1985, inclusive.

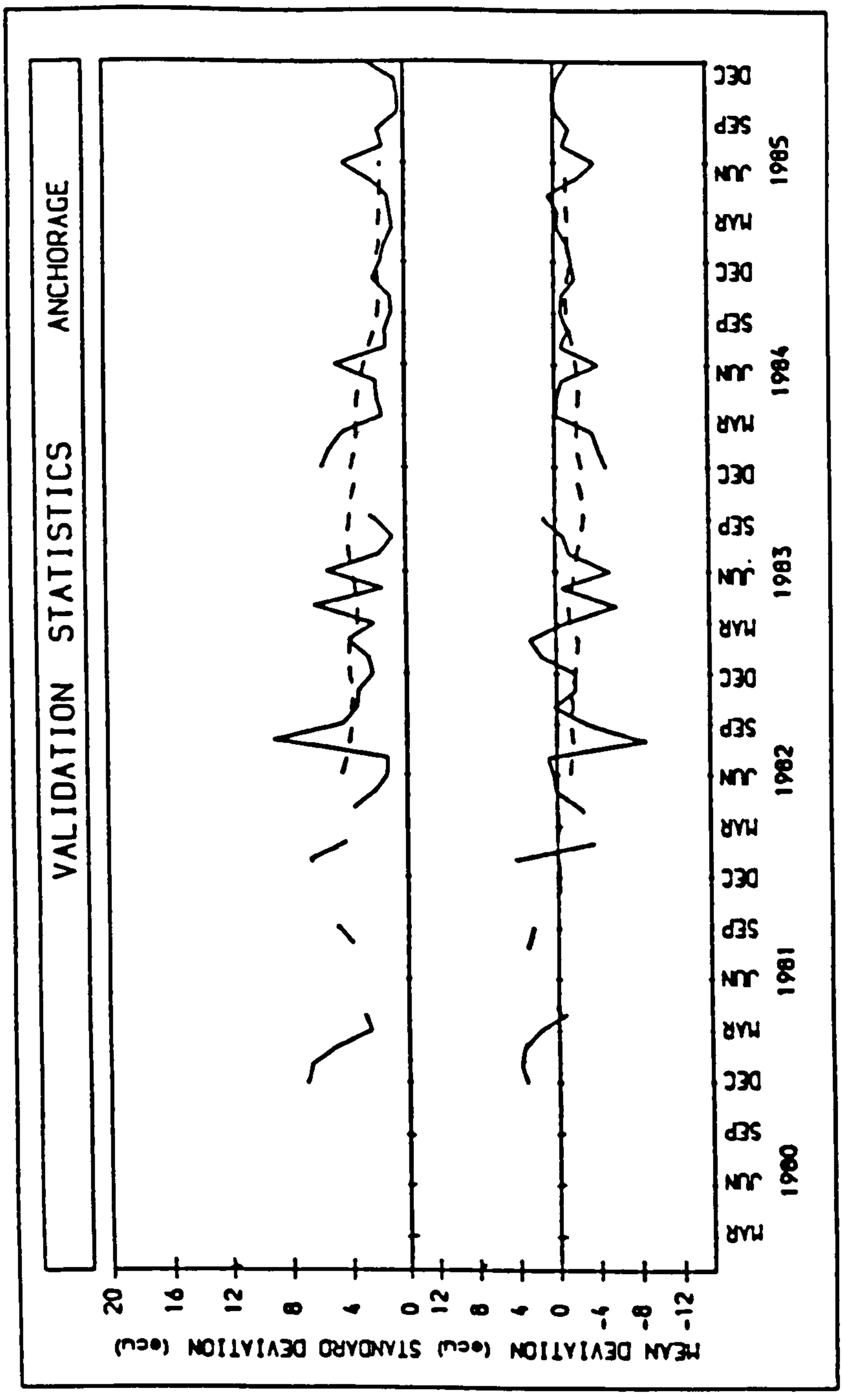

Figure 5.25 The standard deviation and mean deviation of the Model D monthly mean electron content estimates about the monthly mean Anchorage data between 1980 and 1985, inclusive.

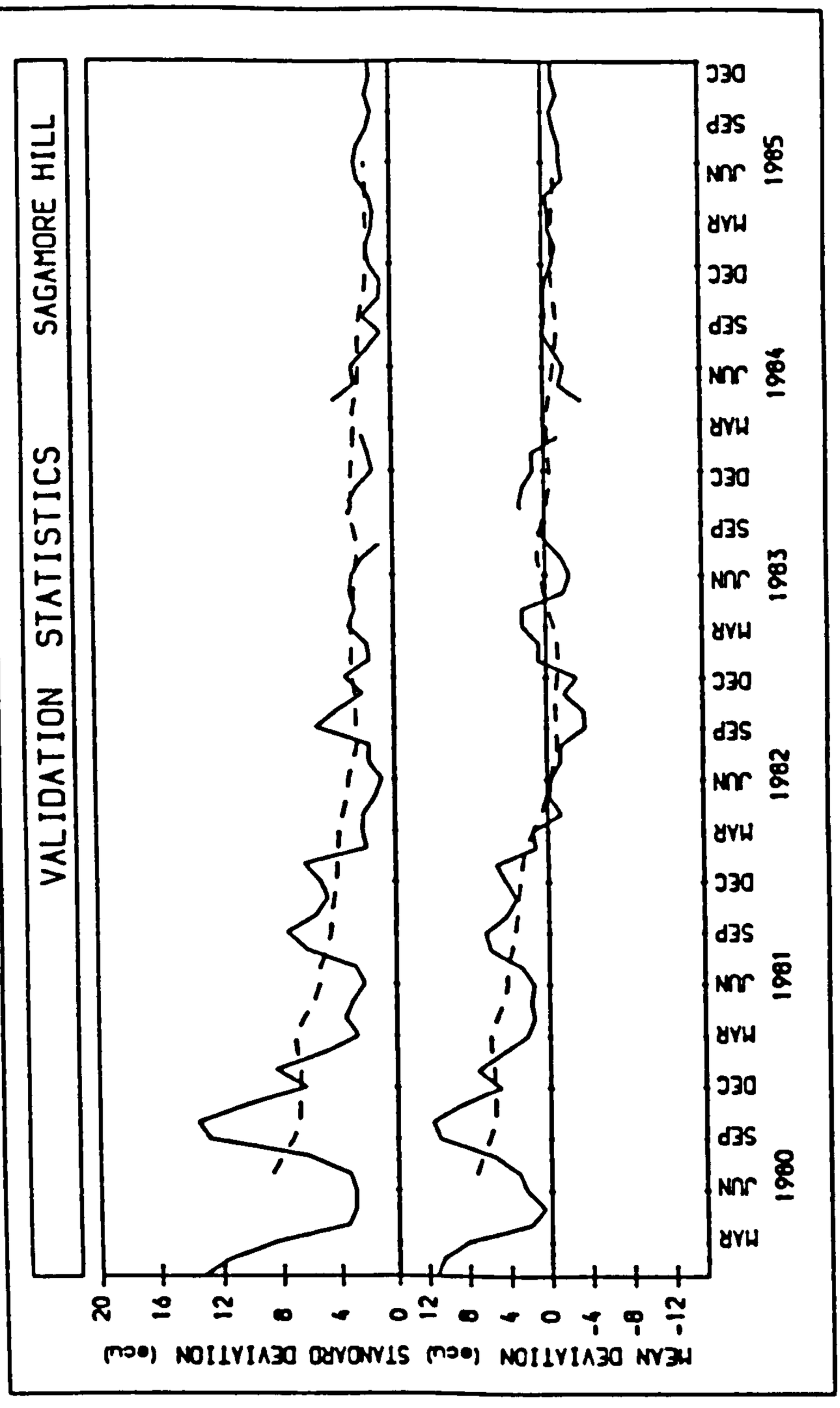

Figure 5.26 The standard deviation and mean deviation of the Model D monthly mean electron content estimates about the monthly mean Sagamore Hill data between 1980 and 1985, inclusive.

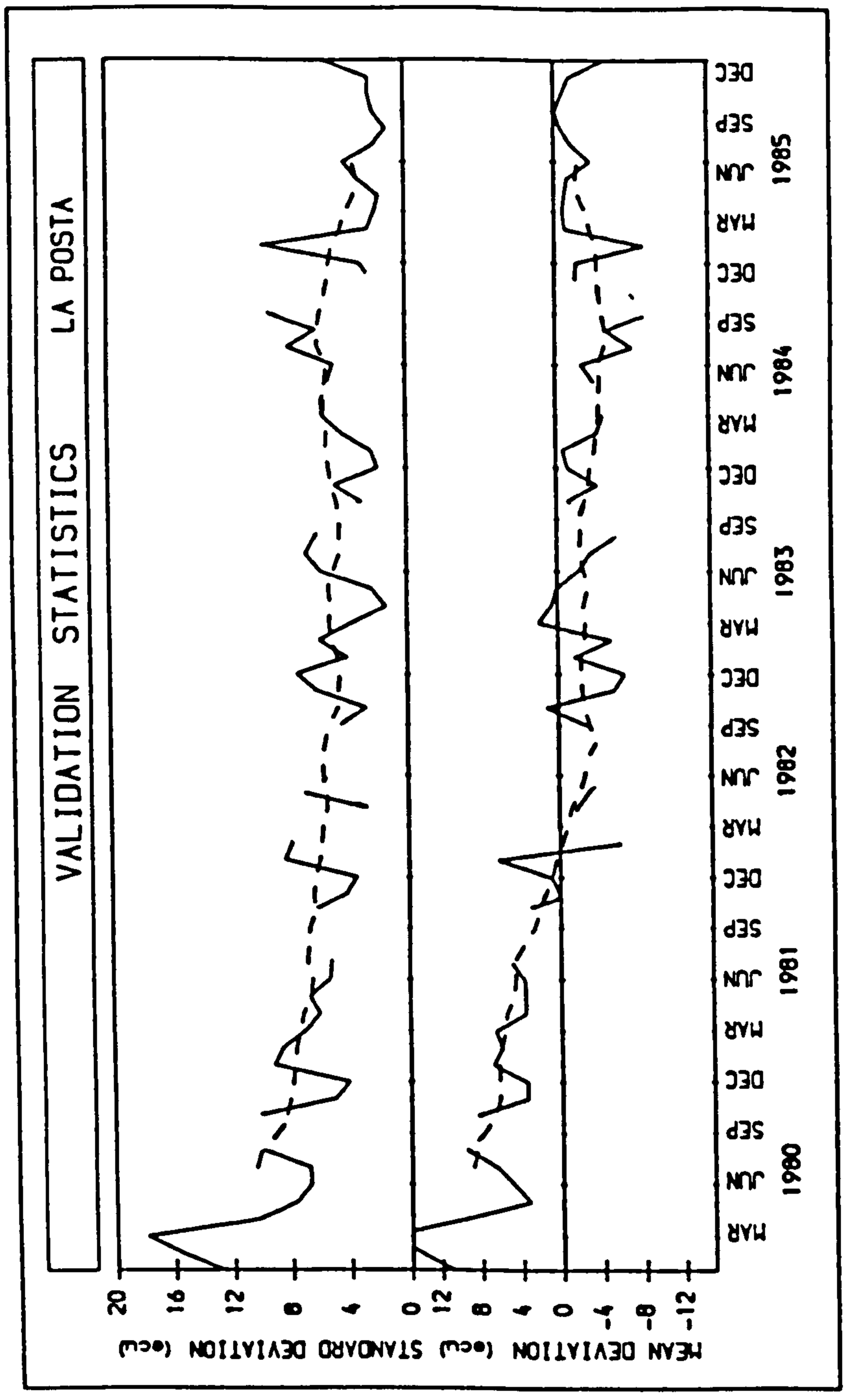

Figure 5.27 The standard deviation and mean deviation of the Model D monthly mean electron content estimates about the monthly mean La Posta data between 1980 and 1985, inclusive.

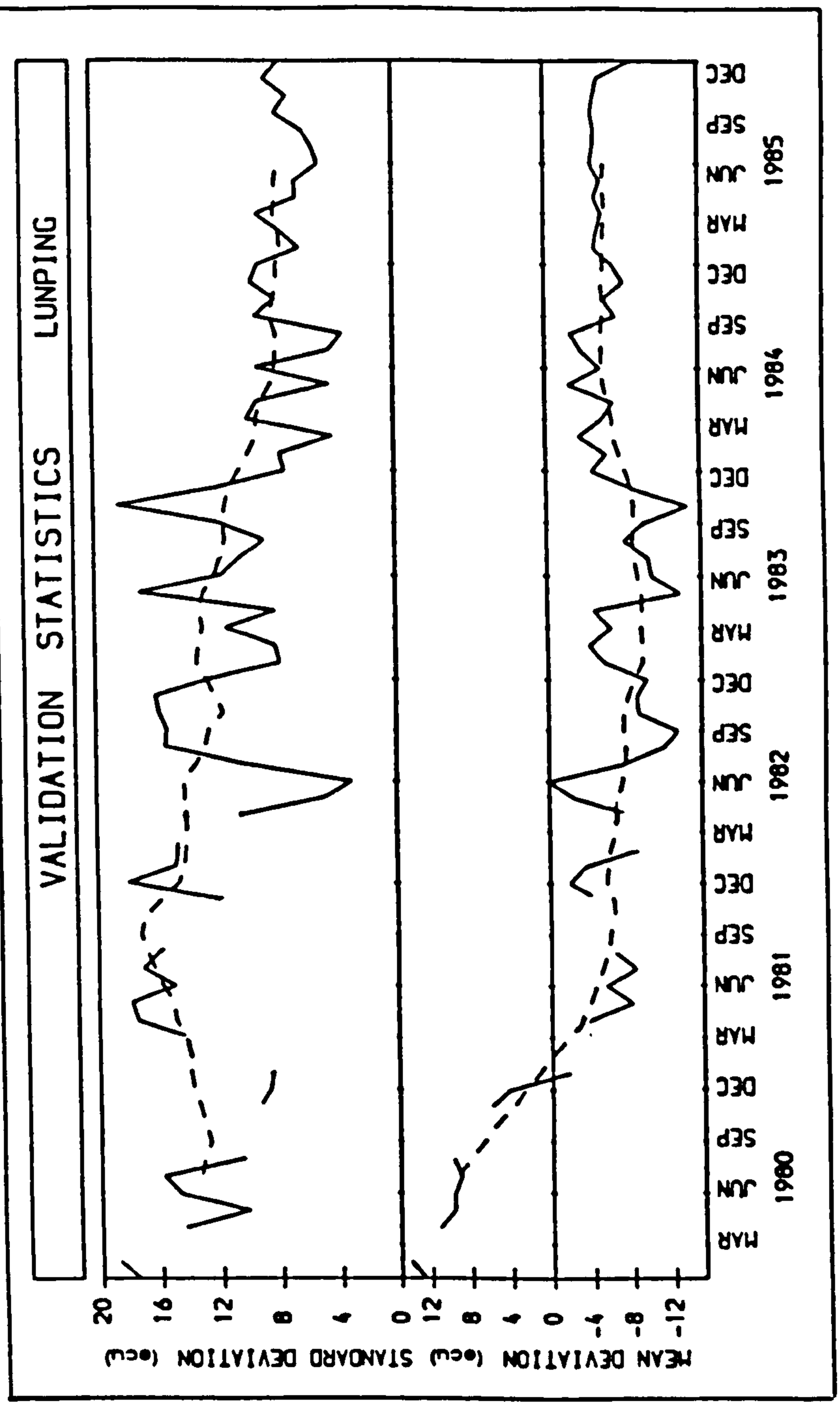

Figure 5.28 The standard deviation and mean deviation of the Model D monthly mean electron content estimates about the monthly mean Lunping data between 1980 and 1985, inclusive.

TECHNIQUE	STATION	LATITUDE (°N)	LONGITUDE (°E)
IONOSONDE	OTTAWA	45	284
FARADAY	GOOSE BAY	48	298
IONOSONDE	ROME	42	13
FARADAY	ATHENS	35	18
IONOSONDE	CHUNG LI	25	121
FARADAY	LUNPING	23	122

Table 5.1 : The Faraday rotation station and ionosonde site pairs utilized as sources of data in the study of the relative accuracies of the CCIR Model and ionosonde data as inputs to the modelling procedure.

		MAR	JUN	SEP	DEC
		foF2 (MHz)			
1980	MD	-1.21	-0.73	0.45	-0.49
	SD	1.37	0.79	0.90	0.59
1982	MD	-1.07	0.27	0.48	-0.63
	SD	1.29	0.51	0.82	1.07
1985	MD	0.12	-0.12	0.02	0.17
	SD	0.22	0.28	0.28	0.27
		M(3000)F2 (dimensionless)			
1980	MD	0.03	0.18	0.08	0.16
	SD	0.07	0.20	0.11	0.18
1982	MD	0.13	0.21	0.13	0.18
	SD	0.14	0.23	0.17	0.19
1985	MD	0.03	0.09	0.02	0.13
	SD	0.08	0.12	0.09	0.16

Table 5.2 : Mean deviation (MD) and standard deviation (SD) of the predictions of the CCIR maps of foF2 and M(3000)F2 about the corresponding monthly mean ionosonde data for the calibration months at the Ottawa ionosonde location.

		MAR	JUN	SEP	DEC
		foF2 (MHz)			
1980	MD	0.00	-0.48	0.50	-0.29
	SD	0.52	0.62	0.66	0.73
1982	MD	-0.86	0.25	0.19	-0.71
	SD	1.04	0.36	0.39	1.08
1985	MD	0.32	0.10	0.10	0.09
	SD	0.41	0.19	0.43	0.21
		M(3000)F2 (dimensionless)			
1980	MD	0.16	0.23	0.15	0.26
	SD	0.19	0.24	0.15	0.27
1982	MD	0.24	0.17	0.20	0.26
	SD	0.25	0.17	0.21	0.27
1985	MD	0.04	0.06	-0.09	0.04
	SD	0.09	0.08	0.10	0.08

Table 5.3 : Mean deviation (MD) and standard deviation (SD) of the predictions of the CCIR maps of foF2 and M(3000)F2 about the corresponding monthly mean ionosonde data for the calibration months at the Rome ionosonde location.

		MAR	JUN	SEP	DEC
		foF2 (MHz)			
1980	MD	0.63	-1.23	-0.04	-1.18
	SD	1.12	1.71	1.11	1.67
1982	MD	-0.72	-0.24	-0.19	-2.50
	SD	1.05	0.42	0.82	2.83
1985	MD	0.49	-0.30	0.48	-0.19
	SD	0.67	0.57	1.26	0.57
		M(3000)F2 (dimensionless)			
1980	MD	-0.02	0.08	-0.03	0.08
	SD	0.15	0.13	0.09	0.14
1982	MD	0.03	0.03	0.06	0.15
	SD	0.13	0.08	0.09	0.19
1985	MD	-0.17	-0.08	-0.10	-0.08
	SD	0.22	0.11	0.14	0.14

Table 5.4 : Mean deviation (MD) and standard deviation (SD) of the predictions of the CCIR maps of foF2 and M(3000)F2 about the corresponding monthly mean ionosonde data for the calibration months at the Chung Li ionosonde location.

SUNSPOT NUMBER		LOCAL TIME (hours) 00	06	12	18
0	m	0.10	0.10	0.09	0.09
	c	8.76	11.18	17.65	16.96
	s	1.95	1.50	0.80	0.81
100	m	0.10	0.10	0.11	0.11
	c	21.40	22.09	24.31	24.04
	s	1.03	1.08	1.27	1.24
200	m	0.12	0.13	0.18	0.17
	c	25.10	24.91	16.34	18.84
	s	1.51	1.66	2.58	2.45

m = regression coefficient (= 0.1245 in the NASA Model)

c = regression constant (= 24.9 in the NASA Model)

s = standard deviation about the regression line

Table 5.5 : Details of the best–fit lines to the 200 km to 500 km section of scale height altitude profiles generated from the Jacchia Thermospheric Model.

		MAR	JUN	SEP	DEC
A	HIGH	13.4	16.3	14.6	9.4
	LOW	14.8	16.5	15.1	9.5
B	HIGH	7.1	8.9	11.2	5.1
	LOW	7.9	11.0	7.5	4.0
C	HIGH	5	7	6	8
	LOW	6	7	7	7

Table 5.6 : The regression coefficients of the offset (A) and amplitude (B) coefficients and the means of the phase (C) coefficients of the semi-parabolic thickness sub-model as a function of F2-region critical frequency. The parameters were calculated separately for the four months characteristic of the seasons and separately for high and low solar activity.

		MAR	JUN	SEP	DEC
A	HIGH	0.40	0.51	0.39	0.34
	LOW	0.46	0.54	0.46	0.30
B	HIGH	0.23	0.33	0.22	0.24
	LOW	0.27	0.36	0.26	0.17
C	HIGH	5	7	6	8
	LOW	6	7	7	7

Table 5.7 : The regression coefficients of the of the offset (A) and amplitude (B) coefficients and the means of the phase (C) coefficients of the semi–parabolic thickness sub–model as a function of peak altitude. The parameters were calculated separately for the four months characteristic of the seasons and separately for high and low solar activity.

	CALIBRATION DATA				VALIDATION DATA			
	A1		A2		A1		A2	
MAR	14		8		9		8	
JUN	13		11		8		13	
SEP	7		16		7		10	
DEC	14		10		10		12	
	48	(TOTAL 93)	45		34	(TOTAL 77)	43	

Table 5.8 : The numbers of successes of the two versions of predictive model A for each month between 1980 and 1985 at the eight calibration and validation sites.

CALIBRATION DATA

		A	B	C	D
MAR	H	5	3	2	2
	L	3	2	1	4
JUN	H	5	2	1	4
	L	1	7	1	3
SEP	H	5	0	2	5
	L	4	0	2	5
DEC	H	5	1	2	4
	L	1	5	2	4
(TOTAL 93)		29	20	13	31

Table 5.9 : The numbers of successes of each of the four predictive models for each calibration month between 1980 and 1985 at the four calibration sites.

CALIBRATION DATA

	A	B	C	D
JAN	3	4	2	15
FEB	13	5	2	4
MAR	8	5	3	6
APR	7	6	5	6
MAY	4	5	8	6
JUN	6	9	2	7
JUL	3	7	7	6
AUG	4	5	5	9
SEP	9	0	4	10
OCT	6	4	7	6
NOV	8	5	6	5
DEC	6	6	4	8
(TOTAL 281)	77	61	55	88

Table 5.10 : The numbers of successes of each of the four predictive models at the four calibration sites between 1980 and 1985 inclusive.

VALIDATION DATA

	A	B	C	D
JAN	3	2	4	14
FEB	6	2	1	13
MAR	5	1	2	9
APR	7	4	6	5
MAY	8	6	3	5
JUN	3	3	7	8
JUL	7	3	2	10
AUG	4	2	3	12
SEP	6	1	2	8
OCT	8	2	0	8
NOV	6	3	4	10
DEC	6	3	3	10
(TOTAL 250)	69	32	37	112

Table 5.11 : The numbers of successes of each of the four predictive models at the four validation sites between 1980 and 1985 inclusive.

	CALIBRATION DATA			VALIDATION DATA		
	A	D		A	D	
JAN	7	17		5	18	
FEB	18	6		8	14	
MAR	13	9		6	11	
APR	13	11		11	11	
MAY	9	14		14	8	
JUN	15	9		6	15	
JUL	10	13		10	12	
AUG	9	14		6	15	
SEP	9	14		7	10	
OCT	10	13		10	8	
NOV	13	11		9	14	
DEC	12	12		9	13	
	138	(TOTAL 281)	143	101	(TOTAL 250)	149

Table 5.12 : The successes of predictive models A and D compared over the full calibration and validation data sets.

	CALIBRATION DATA		VALIDATION DATA	
	D	E	D	E
MAR	15	7	9	8
JUN	14	10	15	6
SEP	14	9	10	7
DEC	16	8	16	6
	59 (TOTAL 93)	34	50 (TOTAL 77)	27

Table 5.13 : The successes of predictive models D and E for the four months representative of the seasons in the calibration and validation data sets.

IONOSONDE/CCIR COMPARISON

GOOSE BAY / OTTAWA = 1 ATHENS / ROME = 2 LUNPING / CHUNG LI = 3

	MAR			JUN			SEP			DEC			TOTAL
	1	2	3	1	2	3	1	2	3	1	2	3	D / I
1980	I	I	D	I	I	I	D	D	D	I	I	I	4 / 8
1982	I	I	I	D	I	I	D	I	I	I	I	I	2 / 10
1985	I	D	D	I	I	D	D	D	D	D	I	D	8 / 4
TOTAL	3 / 6			2 / 7			7 / 2			2 / 7			14 / 22
D / I													

Table 5.14 : The table displays the results of an investigation into the improvement in the accuracy of the Predictive Model through the use of monthly mean ionosonde data. Model I employed monthly mean ionosonde data and Model D the CCIR Model to provide peak parameters over the twelve calibration months. A comparison was made between the model output and data from the Faraday receiving site closest to the ionosonde station; the station pairs are shown in the list immediately above.

Chapter 6 : Calibration and Validation of the Adaptive Model

The purpose of this chapter is to outline the various investigations which have been made into the spatial and temporal coherence of electron content variability. This is followed by a brief description of the use of the spatial and temporal coherence functions in the Adaptive Model. Even a predictive model with the capability to reproduce exactly the monthly average electron content would be vulnerable to the day–to–day variability characteristic of electron content. Given the coherence functions and a suitable measurement of electron content the Adaptive Model can adjust the monthly mean, estimated by the Predictive Model, to account for the conditions prevailing in the local ionosphere. The outline of coherence theory given below is based on the tutorial of Papoulis (1965).

6.1 Definition of Coherence

The statistical process on which the Adaptive Model is based is the deviation of electron content from its mean level, denoted as D in Equation 6.1.

$$D(r, t) = E(r, t) - \langle E(r, t) \rangle \qquad (6.1)$$

r = location co–ordinate t = time co–ordinate

$E(r, t)$ = electron content at position r and time t

$\langle E(r, t) \rangle$ = corresponding monthly mean value $D(r, t)$ = corresponding deviation

Equation 6.2 defines the temporal covariance for a real process as the expectation of the product of the deviations at two points separated in time. Similarly Equation 6.3 defines the spatial covariance for a real process as the expectation of the product of the deviations at two points separated in space. The zero–lag covariance ($\sigma = 0$ and $\tau = 0$) is equivalent to the variance of electron content.

$$C_T(r, t, \tau) = E[D(r, t)\, D(r, t+\tau)] \qquad (6.2)$$

$$C_S(r, \sigma, t) = E[D(r, t)\, D(r+\sigma, t)] \qquad (6.3)$$

$C_S(r, \sigma, t)$ = spatial covariance $\quad$ σ = spatial separation

$C_T(r, t, \tau)$ = temporal covariance $\quad$ τ = temporal separation

The temporal correlation coefficient of the electron content between two times at a given site is defined in Equation 6.4 as the ratio of the covariance at the two times to the square root of the product of the corresponding variances. Similarly the spatial correlation coefficient between two sites is defined in Equation 6.5 as the ratio of the covariance of the instantaneous electron content at the two positions to the square root of the product of the corresponding variances.

$$R_T(r, t, \tau) = \frac{C_T(r, t, t+\tau)}{\left(C_T(r, t, t) \;\; C_T(r, t+\tau, t+\tau) \right)^{\frac{1}{2}}} \tag{6.4}$$

$$R_S(r, \sigma, t) = \frac{C_S(r, r+\sigma, t)}{\left(C_S(r, r, t) \;\; C_S(r+\sigma, r+\sigma, t) \right)^{\frac{1}{2}}} \tag{6.5}$$

$R_T(r, t, \tau)$ = temporal correlation coefficient $\quad (-1 \le R_T \le 1)$

$R_S(r, \sigma, t)$ = spatial correlation coefficient $\quad (-1 \le R_S \le 1)$

The coherence of a process can be considered to be a measure of the persistence of a deviation of the process from its mean level.

Considering the second order central statistics of electron content to be locally homogeneous allows the covariance equations to be rewritten in the simpler forms of Equations 6.6 to 6.9.

$$R_T(\tau) = \frac{C_T(0, \tau)}{\left(C_T(0, 0) \;\; C_T(\tau, \tau) \right)^{\frac{1}{2}}} \tag{6.6}$$

$$R_T(\tau) = \frac{C_T(\tau)}{C_T(0)} \tag{6.7}$$

$$R_S(\sigma) = \frac{C_S(0, \sigma)}{\left(C_S(0, 0) \;\; C_S(\sigma, \sigma) \right)^{\frac{1}{2}}} \tag{6.8}$$

$$R_S(\sigma) = \frac{C_S(\sigma)}{C_S(0)} \tag{6.9}$$

$C_T(0)$ = variance of electron content in the locality of the station.

$C_S(0)$ = variance of electron content in the locality of the two stations.

Since most of the data were contiguous over complete months it was possible to calculate coherence values for the process without resorting to the ergodic assumption. Arrays of electron content data from each hour of Universal Time were constructed from the ensemble of measurements taken during a particular month. These arrays of electron content were then converted to arrays of differences from the monthly mean and then employed in the calculation of the spatial and temporal correlation coefficients on an hourly basis; the expectation being calculated over the days of the month.

The above theory deals with autocorrelation which is a statistical test of a single process. Crosscorrelation is employed to test the degree of correspondence between two processes. The crosscovariance for two real central processes is defined by Equation 6.10 as the expectation of the product of their deviations from their means. The crosscorrelation coefficient is then given, as in Equation 6.11, as the ratio of the crosscovariance to the square root of the product of the variances of the individual processes.

$$B_{IL}(0) = E[\, i(0)\, L(0)\,] \tag{6.10}$$

$$X_{IL}(0) = \frac{B_{IL}(0)}{\left(C_I(0)\;\; C_L(0) \right)^{\frac{1}{2}}} \tag{6.11}$$

I(0) = process one (e.g. a geomagnetic index)

L(0) = process two (e.g. a characteristic time)

$B_{IL}(0)$ = crosscovariance of the processes I and L

$C_I(0)$ = the zero–lag covariance (i.e. variance) of process one

$C_L(0)$ = the zero–lag covariance of process two

$X_{IL}(0)$ = crosscorrelation coefficient

The zero arguments are retained as a reminder that simultaneous values of the two processes are considered. Crosscorrelation coefficients in this form will be employed to study the strength of relationships between geomagnetic indices and coherence times and between geographic latitude and coherence times.

6.2 Temporal Coherence of Electron Content

The investigation of temporal coherence of electron content employed data from ten stations collected over six years, in all a total of 664 station months. Due to the large volume of data an important consideration was to reduce the electron content values to some measure of temporal coherence as early as possible to facilitate the observation of patterns and trends in the data.

Equation 6.12 gives, in array notation, the L–th lag temporal covariance for I hours Universal Time. The array D(I,J) contains the differences of electron content from the monthly mean with the I index running from 0 to 23 and the J index running over the day of the month.

$$C(I, L) = \frac{1}{N} \sum_{J=1}^{N} D(I, J)\ \ D(I + L, J) \qquad (6.12)$$

I = Universal Time in units of hours
L = Universal Time lag in units of hours
J = day number of the month
N = number of days in the month

The temporal covariance of electron content was calculated for each hour out to a maximum time lag of five hours (i.e. L = 0 to 5). The covariances were then divided by the zeroth lag covariance to calculate correlation coefficients. The decorrelation was found to follow a linear trend, hence a best–fit line, constrained to pass through unity at zero lag, was calculated for the set of six correlation coefficients. The best–fit line allowed calculation of the time lag at which the correlation coefficient had fallen to 0.7. This time lag quantified the strength of the temporal correlation and was defined as the Coherence Time (T70).

The diurnal variations of the Coherence Times at the Boulder station for the calibration months of 1980 are shown in Figure 6.1. The standard deviations of the correlation coefficients about the linear fit are plotted as error bars and their low values indicate a linear decorrelation with time, at least in the short term. No consistent diurnal variation of the Coherence Time can be observed in this case. This finding conflicts with those of other researchers who generally found lower correlation coefficients during the pre–dawn period than at other times. This type of behaviour was observed at other stations, however. Patrick data, for example, regularly had daytime Coherence Times which were from five to fifteen minutes longer than nighttime values. The Local Time behaviour of the Coherence Time, though, was inconsistent and, hence, impossible to describe in the succinct mathematical format necessary for an ionospheric correction algorithm. Therefore it was decided, in light of the inconsistency and small errors likely to arise, to take an average of the Coherence Times over Local Time. This analysis produced a characteristic Coherence Time for the whole month. No attempt was made to separate magnetically disturbed

times from magnetically quiet times since the Adaptive Model was required to operate under all geomagnetic conditions.

The monthly Coherence Times and their standard deviations calculated from data collected during 1980 and 1985 at the four calibration sites are shown in Figure 6.2. The plots reveal no systematic seasonal variation of the Coherence Time at any of the four sites. The Coherence Times found at the Boulder station for the 71 months of available data are listed in Table 6.1. The calculations of the Coherence Times from the other five years confirm the lack of a seasonal variation. Bearing all this in mind, the search for a seasonal variation was abandoned and it was decided to average the Coherence Times over the months of each year to produce a characteristic annual value for each of the receiving sites, the weights used in the averaging process were calculated with the rules set out by Barford (1967).

Annual values of T70 for each of the ten stations involved in the temporal coherence investigation are listed in Table 6.2. The characteristic times range from 62 to 104 minutes. To reveal trends in latitude the Coherence Times for each year were plotted against the geographic latitude of the receiving station ionospheric point. The graphs of Figures 6.3 to 6.5 reveal a changing relationship between T70 and latitude according to the prevailing level of solar activity. As the solar activity decreases so does the strength of their relationship which is confirmed by the decrease of the crosscorrelation coefficient. The crosscorrelation coefficients between T70 and latitude are also set out in Table 6.3 and decrease monotonically from 0.75 for 1980, the year of highest solar activity, down to 0.27 for 1985, the year of lowest solar activity. Table 6.3 lists, for each year, the Coherence Times at latitudes 0°N and 60°N which are extrapolated from the best–fit lines. The 60°N latitude Coherence Times, which span the range from 104 to 74 minutes, exhibit a stronger solar cycle dependence than the corresponding 0°N Coherence Times, which are in the range 63 to 76 minutes. This behaviour implies that at higher latitudes the Coherence Time is controlled more strongly by solar activity than that at lower latitudes. Or, equivalently, that the low–latitude ionosphere is highly variable at all levels of solar activity.

However, the crosscorrelation coefficients, with the possible exception of that for 1980, are not high enough to substantiate a significant relationship between latitude and Coherence Time. Allied with the fact that the ionospheric points of the ten stations spanned only 36° of latitude it was decided to take the average of the Coherence Times from all ten stations to calculate one time which was characteristic of the annual median solar activity.

Referring back to Table 6.2, a definite trend in solar activity can be seen in the Coherence Times found at all the stations, though this is less pronounced at the low–latitude stations of Palehua and Lunping. The characteristic annual values of T70 of each year for which data were available are listed in Table 6.7; at this stage fluctuations on time scales other than that of the solar cycle have been averaged out. In Figure 6.6 the annual Coherence Times are plotted against the annual median twelve–month running mean sunspot number (which is subsequently referred to as the annual sunspot number and taken to represent the mean power of the solar ionizing flux). The best–fit line through the data suggests that for a level of solar activity represented by the twelve–month running mean sunspot number the Coherence Time is given, in minutes, by Equation 6.13. Hence, the temporal correlation coefficient for a given time lag is given by Equation 6.14.

$$T70 = 67.2 + 0.14\,Z \tag{6.13}$$

$$R_T = 1.0 - 0.3\,\frac{t}{T70} \tag{6.14}$$

T70 = Coherence Time (minutes) Z = twelve–month running mean sunspot number

t = time lag (minutes) R_T = temporal correlation coefficient

The increase of Coherence Time with solar activity agrees with the findings of other researchers detailed previously. The crosscorrelation coefficient between the annual Coherence Times and the annual sunspot number is also listed in Table 6.7. The value of 0.98 for this coefficient confirms the strong relationship between solar activity and the temporal coherence of electron content variability. The physical interpretation of this quality is that the deviations of electron content from the mean level endure for longer when the sun is active than when the sun is quiet.

6.3 Spatial Coherence of Electron Content

The investigation of spatial coherence of electron content employed data from six stations collected over six years, in all a total of 413 station months. Figure 6.7 is a schematic map of the stations which gives a guide to their orientations and their great circle separations. Table 6.4 lists the approximate separations in the North–South (NS) and East–West (EW) directions of the four station pairs chosen to investigate the spatial decorrelation in the two directions.

The North–South Coherence Distance (N70) and the East–West Coherence Distance (E70) were calculated separately in order to investigate the anisotropy found by Klobuchar and

Johanson (1977). For each direction four of the six stations listed in Table 6.4 were employed giving a total of six combinations of station–pair separations.

Correlation coefficients between the electron content deviations at two sites were calculated for each hour of Universal Time. In the light of the inconsistencies found in the diurnal variation of the temporal coherence a diurnal average of these coefficients was taken. When repeated for the six combinations of station pairs a best–fit line – constrained to pass through unit correlation at zero separation – was drawn through the set of coefficients plotted against their corresponding separations. The linear fit allowed calculation of the separation at which the spatial correlation coefficient fell to 0.7 which was then taken as characteristic of the spatial coherence for the month and direction.

The monthly values of N70 are tabulated in Table 6.5 and those of E70 in Table 6.6; inspection reveals three properties of the Coherence Distances. Firstly there is no apparent variation of either N70 or E70 with season. This opinion is reinforced by Figure 6.8 which shows, for both directions, plots of Coherence Distance against month during 1980. Secondly both N70 and E70 exhibit a positive correlation with solar activity. The previous two observations have parallels in the behaviour of Coherence Time. The third trait is uncovered through a comparison of the two Coherence Distances which reveals the spatial coherence of electron content variability to be anisotropic, the East–West Coherence Distance being greater than that in the North–South direction.

Dismissing the seasonal variation and averaging over the twelve months of each year results in an annual Coherence Distance for both directions. These annual values are listed in Table 6.7 where the variation with annual sunspot number can clearly be seen. The annual Coherence Distances are plotted against the annual median twelve–month running mean sunspot number in Figures 6.9 and 6.10 which also shows the best–fit line for both sets of data. For a level of solar activity represented by a twelve–month running mean sunspot number the Coherence Distances are given by Equations 6.15 and 6.16.

$$N70 = 550.4 + 4.46\,Z \qquad (6.15)$$

$$E70 = 686.6 + 5.02\,Z \qquad (6.16)$$

N70 = NS Coherence Distance (km) E70 = EW Coherence Distance (km)

The anisotropy of electron content spatial coherence exhibited by Equations 6.15 and 6.16 can be summarized by the eccentricity of a Coherence Oval whose axes are defined by the

Coherence Distances. For a solar activity level defined by a sunspot number of 100 the Coherence Distances are approximately 1 000 km North–South and 1 200 km East–West, equivalent to an eccentricity of 0.55. To make a fair comparison with the eccentricity of 0.78 . calculated from the results of Klobuchar and Johanson (1977) it should be remembered that the data employed in the East–West calculations were from a time of higher solar activity than that for the North–South calculations. The East–West data was collected during 1969 which had an annual median sunspot number of 106. The North–South data was collected between late 1972 and 1974 and the median sunspot number for this period was 55. Calculating Coherence Distances from Equations 6.15 and 6.16 with these sunspot numbers gives a Coherence Oval with an eccentricity of approximately 0.76 which compares very well indeed with the 0.78 value of the Klobuchar and Johanson data.

The spatial correlation coefficients can be represented in an equivalent manner to the temporal coefficients by Equations 6.17 and 6.18.

$$R_N = 1.0 - 0.3 \frac{r_N}{N70} \tag{6.17}$$

$$R_E = 1.0 - 0.3 \frac{r_E}{E70} \tag{6.18}$$

R_N = NS spatial correlation coefficient R_E = EW spatial correlation coefficient

r_N = NS separation (km) r_E = EW separation (km)

Table 6.7 lists the crosscorrelation coefficients between the annual Coherence Distances and the annual sunspot number. The crosscorrelation coefficients are 0.96 for the North–South direction and 0.90 for the East–West direction. These high values confirm the strong relationship between solar activity and the spatial coherence of electron content variability. The physical interpretation of this is that a deviation of electron content at a given site is more likely to be sustained over a wider area during solar maximum than during solar minimum.

Even though the coherence functions were calculated from sub–2 000 km electron content data they should still be valid for the sub–800 km behaviour since most of the variability occurs around the ionospheric peak which is well below 800 km. Just as for the Predictive Model, the Adaptive Model, incorporating the coherence functions found above, needs to be validated before it can be confidently incorporated into the ionospheric correction algorithm.

6.4 Validation of the Adaptive Model

The Adaptive Model was validated with data from two stations, Boulder and La Posta, collected during March, June and December of 1980. The first stage considered each site individually and involved calculation of the adaptive adjustment to electron content, given measurements from several hours previous, to test the temporal update capability. The presumption that a reduction should occur in the uncertainty as the time lag decreased was then authenticated. This process was then repeated, though with data from the alternative site being used as the input to the Adaptive Model to test the spatial update capability. This was performed with the assumption that the standard deviations of electron content at the two sites were the same. The two sites are separated by approximately 1 000 km.

The results for the first stage are quoted in Table 6.8 in terms of the standard deviation of the adjusted data about the true values along with the standard deviation of the unadjusted values. The time lag of the measurements provided to the adaptive procedure ranged from three to zero hours. The table clearly proves that as the time lag between the measurement and update decreases then the uncertainty in the predicted electron content also decreases. A significant decrease is not seen, though, until the correlation coefficient is greater than the 0.6 level. When the time lag is zero the correlation is, of course, perfect and the predicted mean can be adjusted to give the exact value of electron content, hence the zero standard deviations.

For the second stage, where data from a remote observing site is used to update the monthly mean electron content prediction, the benefit to update accuracy is somewhat less, as demonstrated by Table 6.9. Even for zero time lag the correlation coefficient is only slightly greater than 0.7 just taking the measurements inside the coherence horizon. In this case it is only the remote update at zero time lag which is useful in the adaptive procedure.

The data presented in Tables 6.8 and 6.9 validates the capability of the Adaptive Model to improve on the accuracy of the Predictive Model. The efficacy of the 0.7 coherence horizon is also established by the results. From these findings the model can be confidently incorporated into the full ionospheric correction technique.

6.5 Influence of Geomagnetic Activity

What follows is brief discussion of the behaviour of temporal coherence of electron content during magnetic storms. As described previously, magnetic storms exert a strong and peculiar influence on the electron content of the ionosphere, particularly in the high–latitude region. The principal effect is either a positive or negative sustained deviation from the monthly mean electron content which would result in a climatological model being consistently in error over several days. Thus, magnetic storms cause problems in modelling and any correction procedure should be capable of dealing with the effects they produce. The large scale effect of the storms suggests that during storm times the temporal coherence would be greater during these events since like deviations about the mean persist for many hours. This stronger coherence, though, may be tempered by the greater variability of the perturbed electron content.

February 1982 was a geomagnetically active month, the average of the daily sum of the logarithmic Kp geomagnetic index (ΣKp) over the month was 32 and that of the linear AE index was 387. These may be compared with the corresponding values for March 1982 which were 21 and 221 respectively. Although the time scales of ionospheric storms are of the order of days, the high frequency of storms during February 1982 should provide an indication of storm influence even on the monthly average Coherence Times. The mid–latitude Patrick station was chosen to test this hypothesis since the earlier description of the 12th February 1982 geomagnetic storm showed the electron content to be consistently enhanced at this site over several days.

Indeed this is the case as illustrated by Figure 6.11 which depicts the temporal decorrelation at Patrick for February and March 1982. As suggested above the temporal coherence of the electron content fluctuations is significantly stronger for February than for March, the February Coherence Time of 159 minutes being significantly greater than the value of approximately 85 minutes calculated from Equation 6.13, the March Coherence Time of 104 minutes is closer to this calculated value.

In order to examine the Coherence Time of electron content fluctuations during a particular storm, it is necessary to invoke the ergodic assumption for the process D(r,t) which to be valid requires that the time average of the process equals its ensemble average (Papoulis 1965). With the assumption of ergodicity, the temporal correlation coefficient can be calculated from the time average of a finite sample of the ensemble of one month of electron content data.

$$C(L) = \frac{1}{24} \sum_{I=0}^{23} D(I) \quad D(I+L) \tag{6.19}$$

C = covariance I = ensemble sample time index L = time lag in integer hours

The correlation coefficient is given, from Equation 6.19, by the ratio of the L–th lag covariance to the zeroth lag covariance. By applying this technique for calculating correlation coefficients the coherence behaviour at Patrick during the 12th to 14th of February 1982 ionospheric storm was investigated and the results are plotted in Figure 6.12. This graph displays correlation coefficients calculated from a 77 hour sample of February 1982 electron content data with the Coherence Times for the three days of the storm listed along with the corresponding ΣKp and AE indices. The times for the 13th and 14th are over three times the February average though that for the 12th is much closer to that predicted by Equation 6.13.

The shorter Coherence Time for the first storm day could almost be anticipated from the behaviour of electron content at Patrick during the storm, also shown in Figure 6.12. On the first day of the storm the content was slightly below the mean until 11 LT when it became enhanced. The heightened variability at the onset of the ionospheric storm reduced the increase of coherence on the first day. Significantly increased coherence was experienced, however, during the following two days when the electron content was consistently enhanced.

The increase of Coherence Time noted during this ionospheric storm prompted a further investigation of the relationship between Coherence Time and geomagnetic activity with the aim of identifying a magnetic index which could predict such an increase. For nine months during high solar activity an ergodic correlation coefficient was calculated for each day at Anchorage, Sagamore Hill and the four calibration sites which was then crosscorrelated with the corresponding ΣKp and AE indices. The ΣKp index was chosen as it represents the state of the planetary magnetic field and the AE index because it represents the state of the high–latitude field which is more susceptible to disturbances. The crosscorrelation coefficients found between the magnetic indices and the Coherence Times are listed in Tables 6.10 and 6.11.

The crosscorrelation coefficients of T70 with ΣKp and AE are much less than 0.7 which would seem not to support the hypothesis that Coherence Times are increased during magnetic storms. In addition the coefficients for both indices, though similar to each other, exhibit neither a seasonal nor a latitudinal dependence as can be seen from the the tables. However, a possible

explanation for this unexpected behaviour, which may preserve the hypothesis, is that the ΣKp and AE indices record a magnetic storm rather than an ionospheric storm and so do not represent properly the activity of the ionosphere. In other words a time delay between the magnetic and ionospheric storms would mean the increases in magnetic index and T70 would be out of phase and hence less correlated. Also the indices provide only a summary of the average behaviour of the geomagnetic field in one 24 hour period, whereas the electron content is variable on timescales at least as short as the one hour measurement interval.

Mendillo (1973) demonstrated that the crosscorrelation between the Kp index and the electron content was inadequate to predict whether or not an ionospheric storm would have an initial positive phase prior to a storm time depletion. It was postulated that the Kp index was unable to do this since, firstly, it does not discriminate between the phases of a magnetic storm and, secondly, it is an average over three hours of magnetometer data in which time the electron content can change significantly.

An alternative to the ΣKp and AE magnetic indices is the ΣK index prepared, on much shorter time scales than those of the planetary indices, from data taken at individual magnetometer stations. Even though not a true planetary index a ΣK index would be valuable in a prediction scheme because of its fast production time. Table 6.12 lists the crosscorrelation coefficients between the Coherence Times and the ΣK index calculated at the Eskdalemuir magnetometer station (55°N,357°E). The crosscorrelation coefficients for the local ΣK index themselves are as low as those for the ΣKp and AE indices which can only be taken as further proof of the absence of a link between simultaneous Coherence Times and geomagnetic indices. It must be concluded that it would not be beneficial to include a geomagnetic index into a scheme to predict magnetic storm enhanced Coherence Times.

The crosscorrelation coefficients between the ΣKp, ΣK and AE geomagnetic indices were calculated and these are listed in Table 6.13. As might be expected very high correlations exist between all of the three indices.

6.6 Chapter Summary

The methods for calculating the electron content coherence functions have been described and applied to the calibration and validation of the Adaptive Model. The calibration involved the

investigation and calculation of spatial and temporal coherence functions of electron content as a function of latitude, Local Time, season and solar activity. It was proven that a reduction in the residual error of a predictive model due to the day–to–day variability is possible through the application of an adaptive adjustment procedure. In addition an investigation was made into the effect of magnetic storms on the coherence of electron content which found no significant correlation between Coherence Time and the prevailing level of magnetic activity as reflected by three different geomagnetic indices.

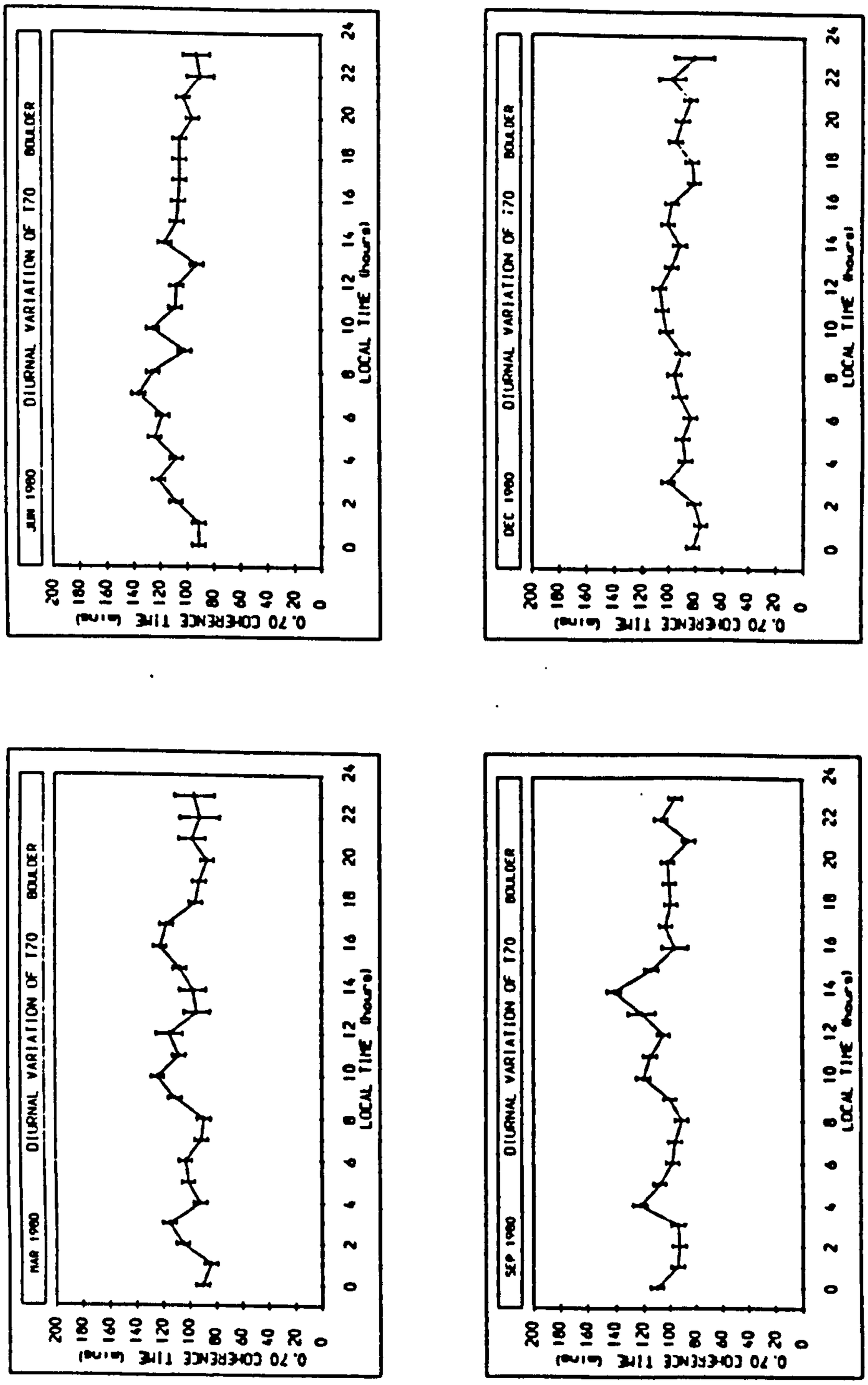

Figure 6.1 : The diurnal variation of Coherence Time calculated from data taken at the Boulder site during the calibration months of 1980.

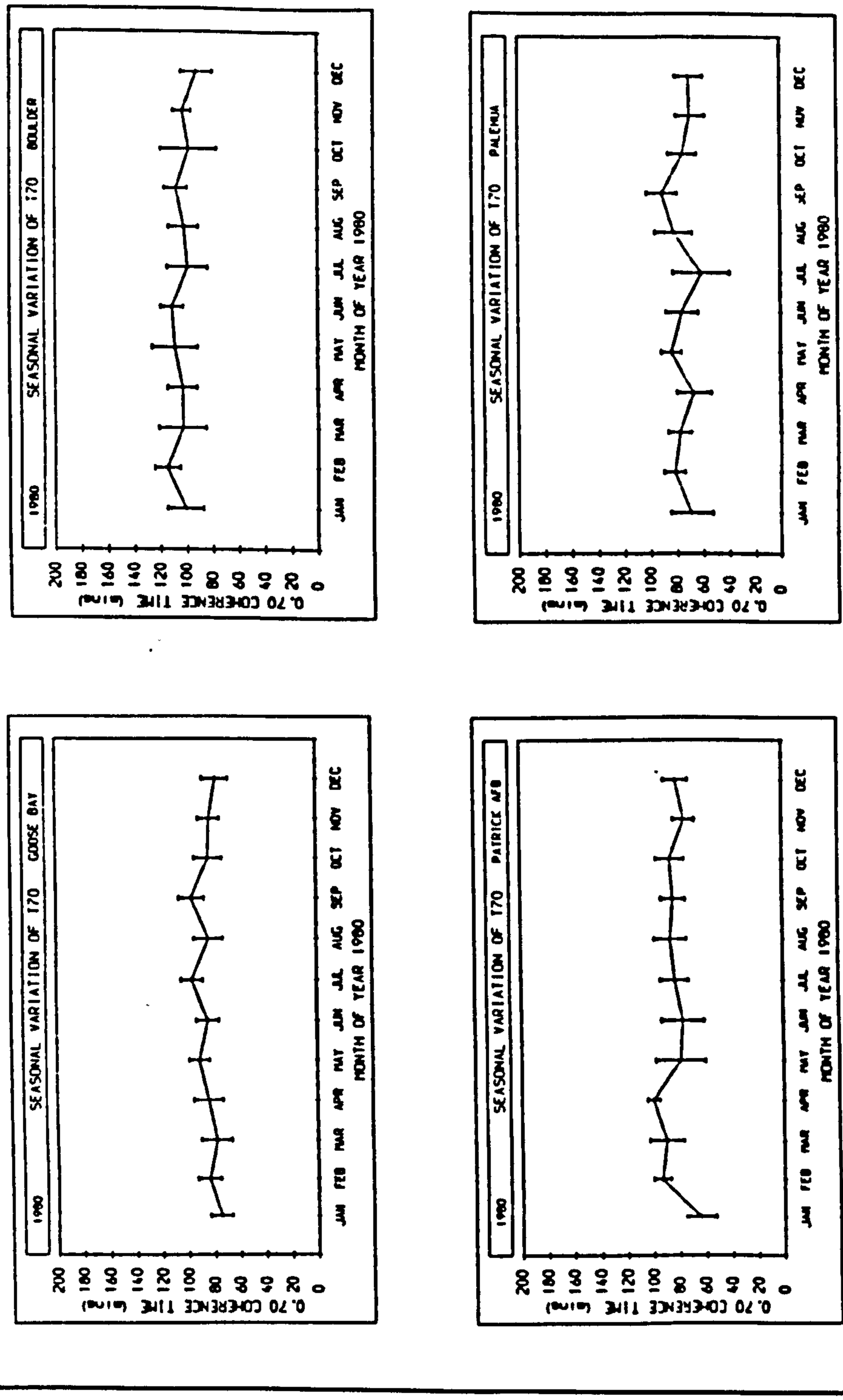

Figure 6.2 : The seasonal variation of Coherence Time calculated from data taken at the four calibration sites sites during 1980.

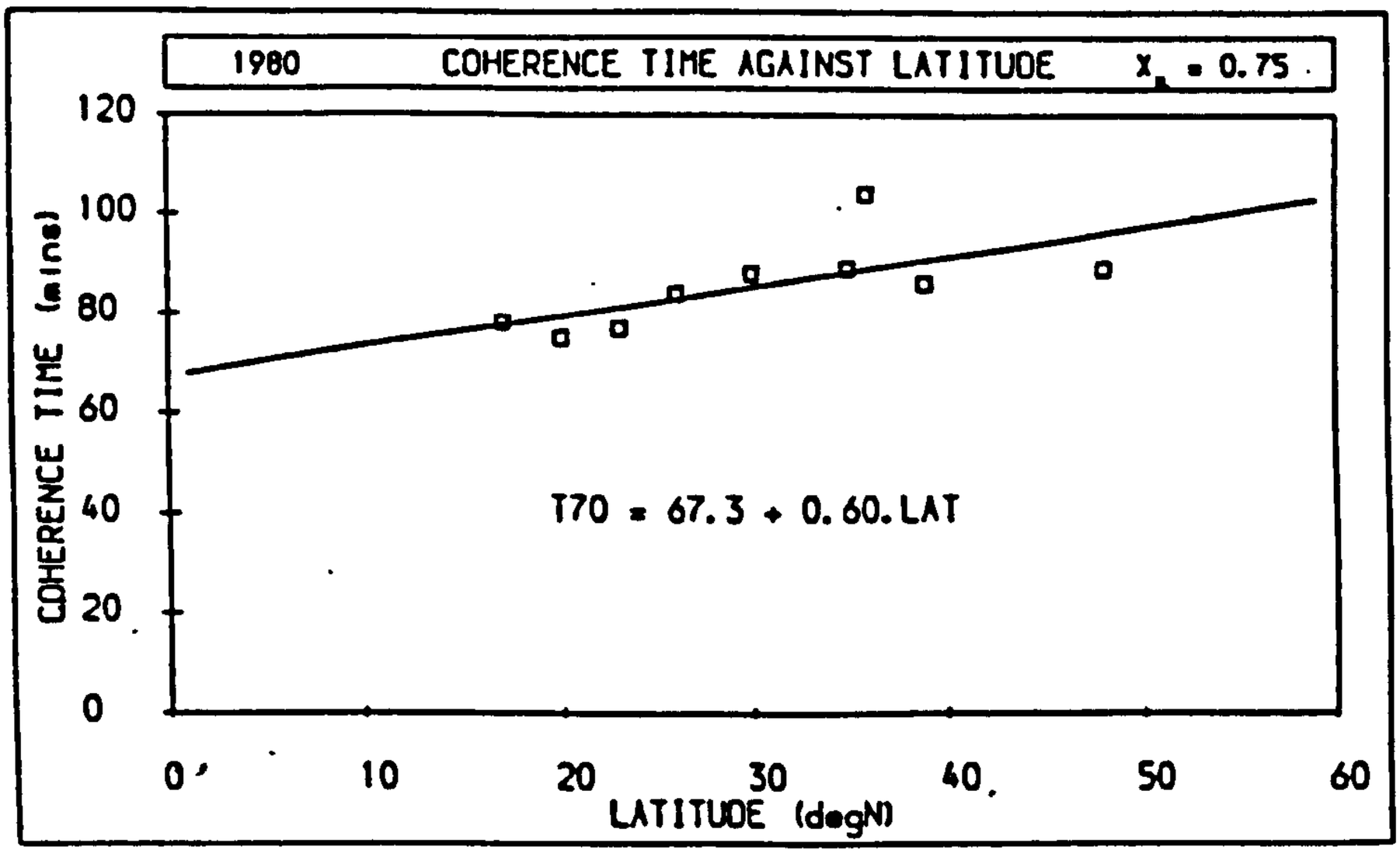

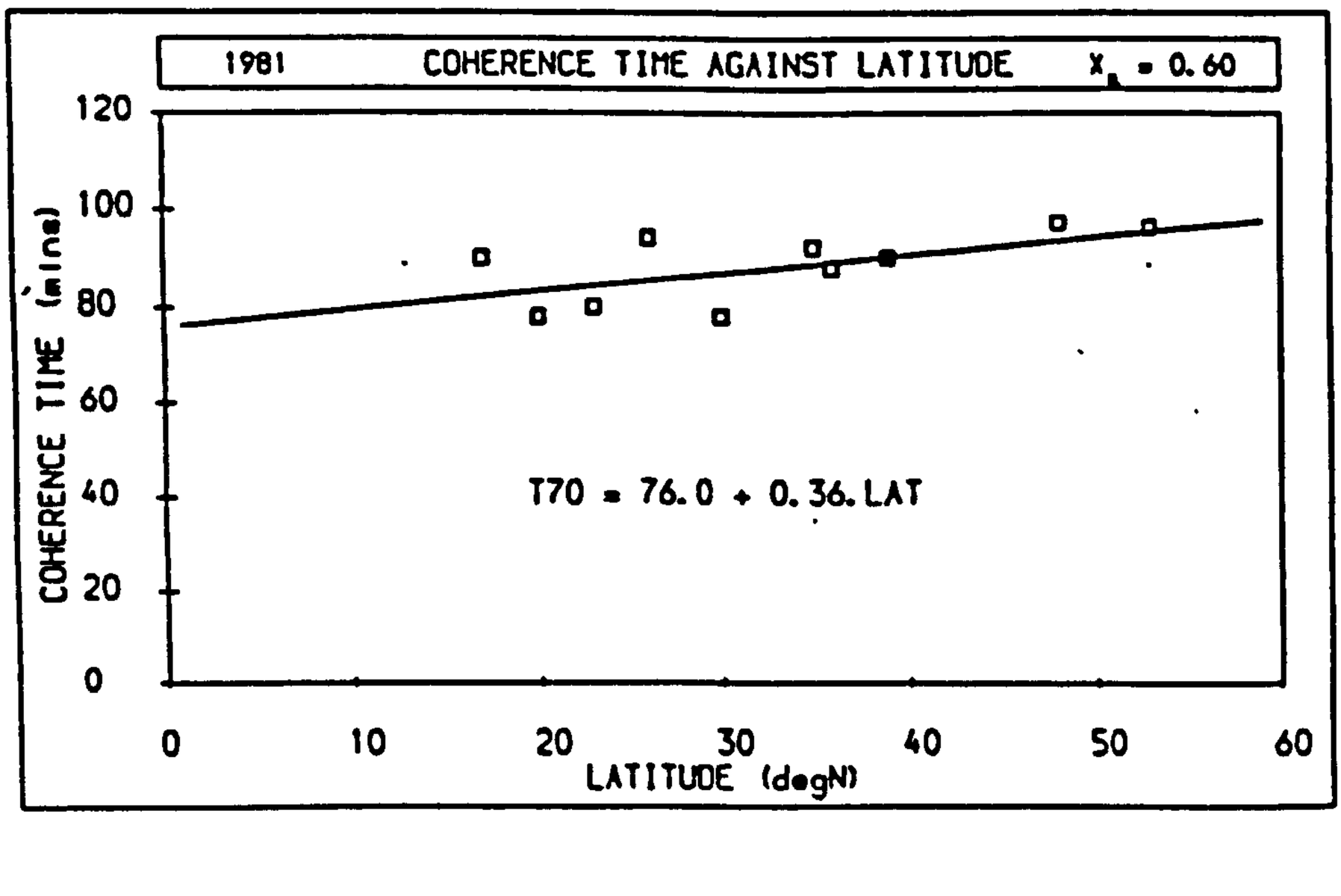

Figure 6.3 : The variation of annual mean Coherence Time (T70) with geographic latitude (LAT) during 1980 and 1981. The best-fit line is also drawn.

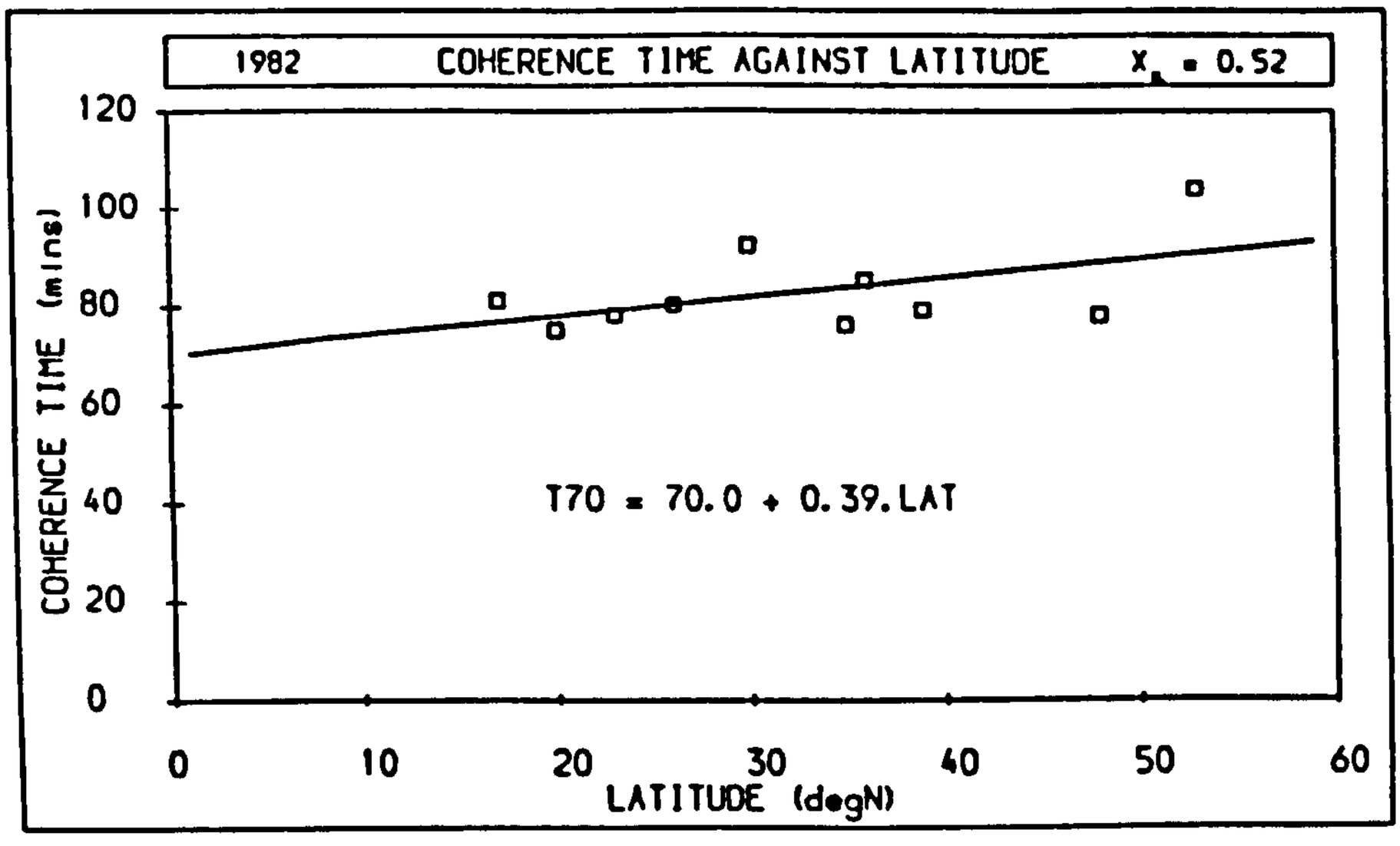

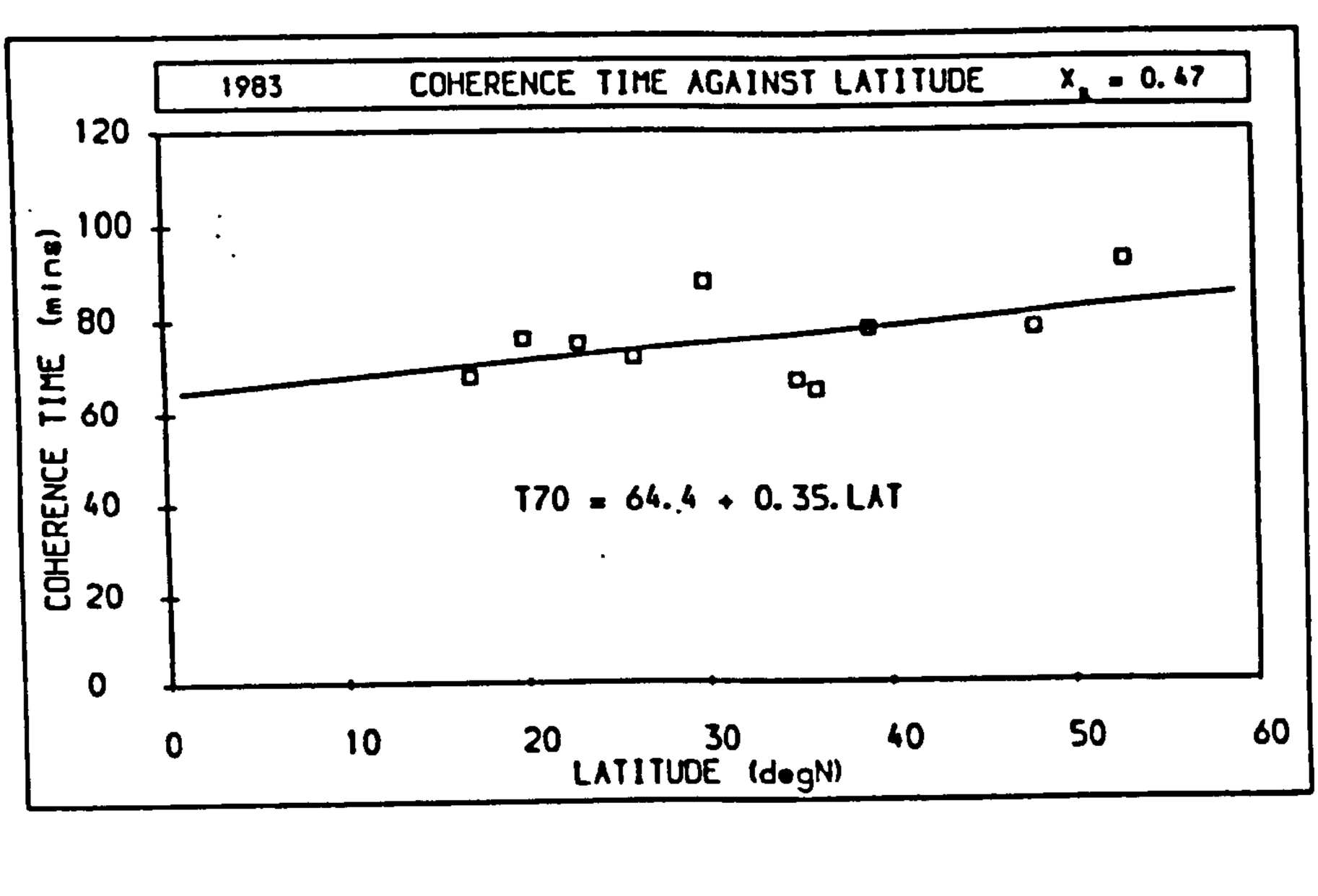

Figure 6.4 : The variation of annual mean Coherence Time (T70) with geographic latitude (LAT) during 1982 and 1983. The best-fit line is also drawn.

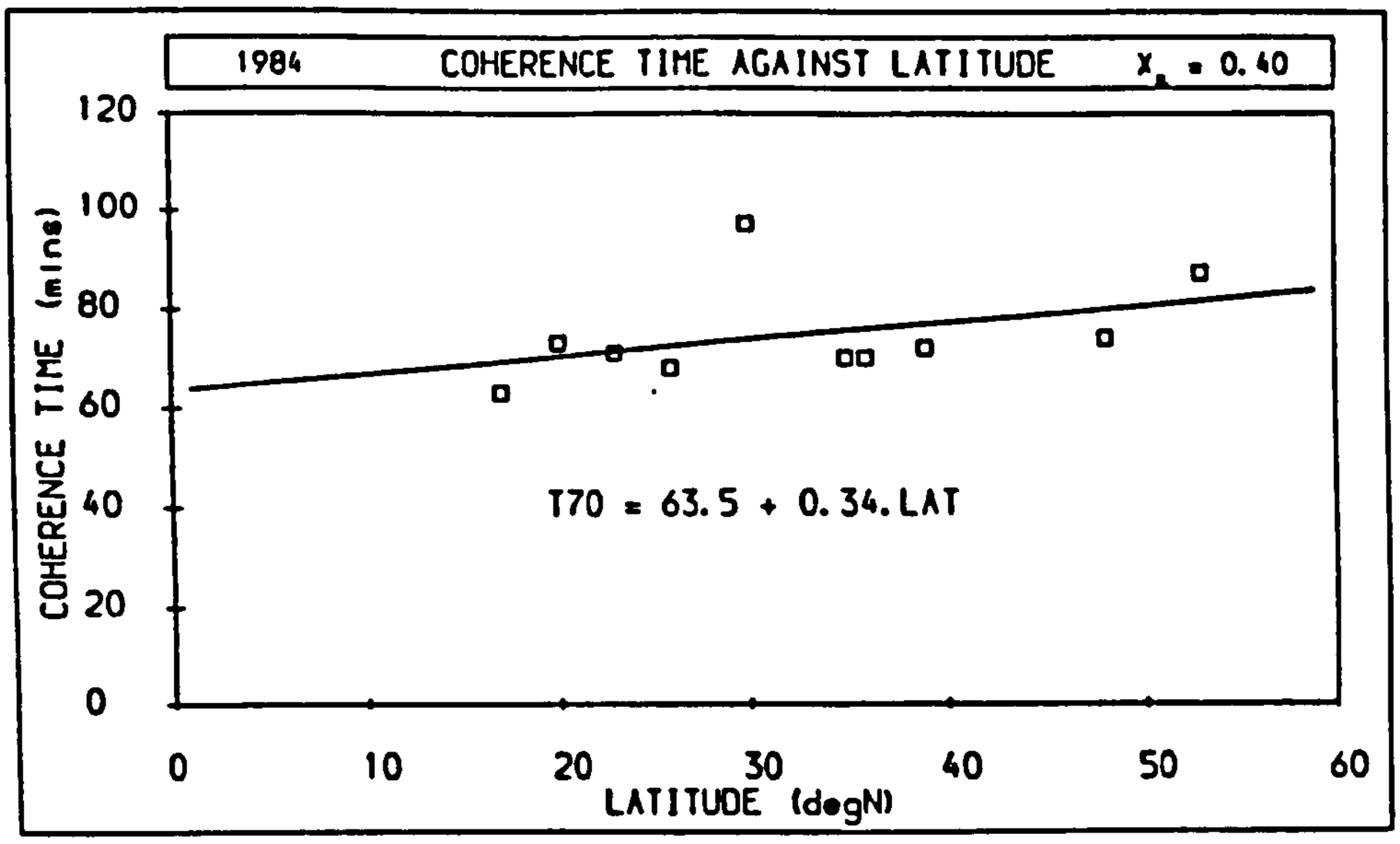

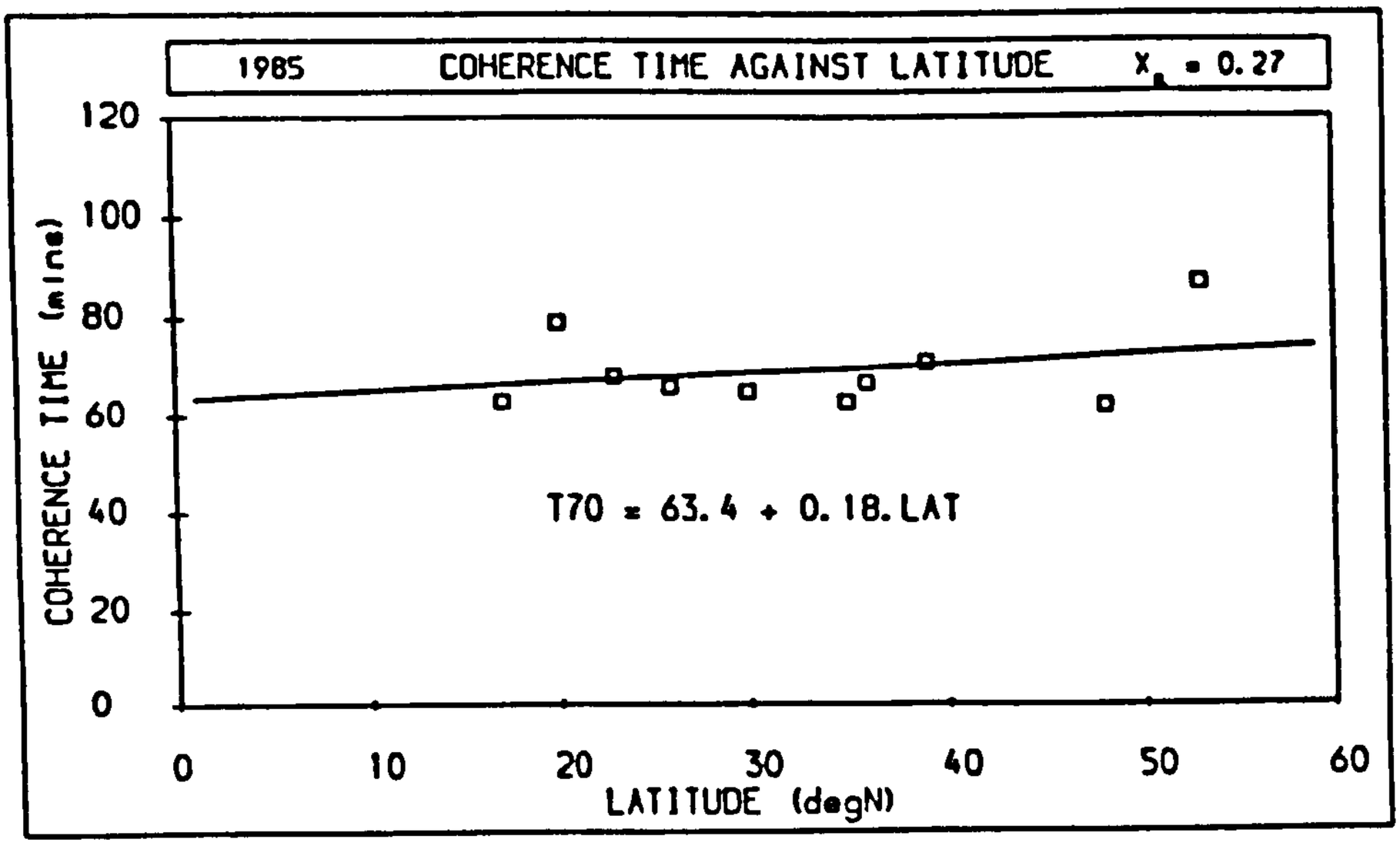

Figure 6.5 : The variation of annual mean Coherence Time (T70) with geographic latitude (LAT) during 1984 and 1985. The best–fit line is also drawn.

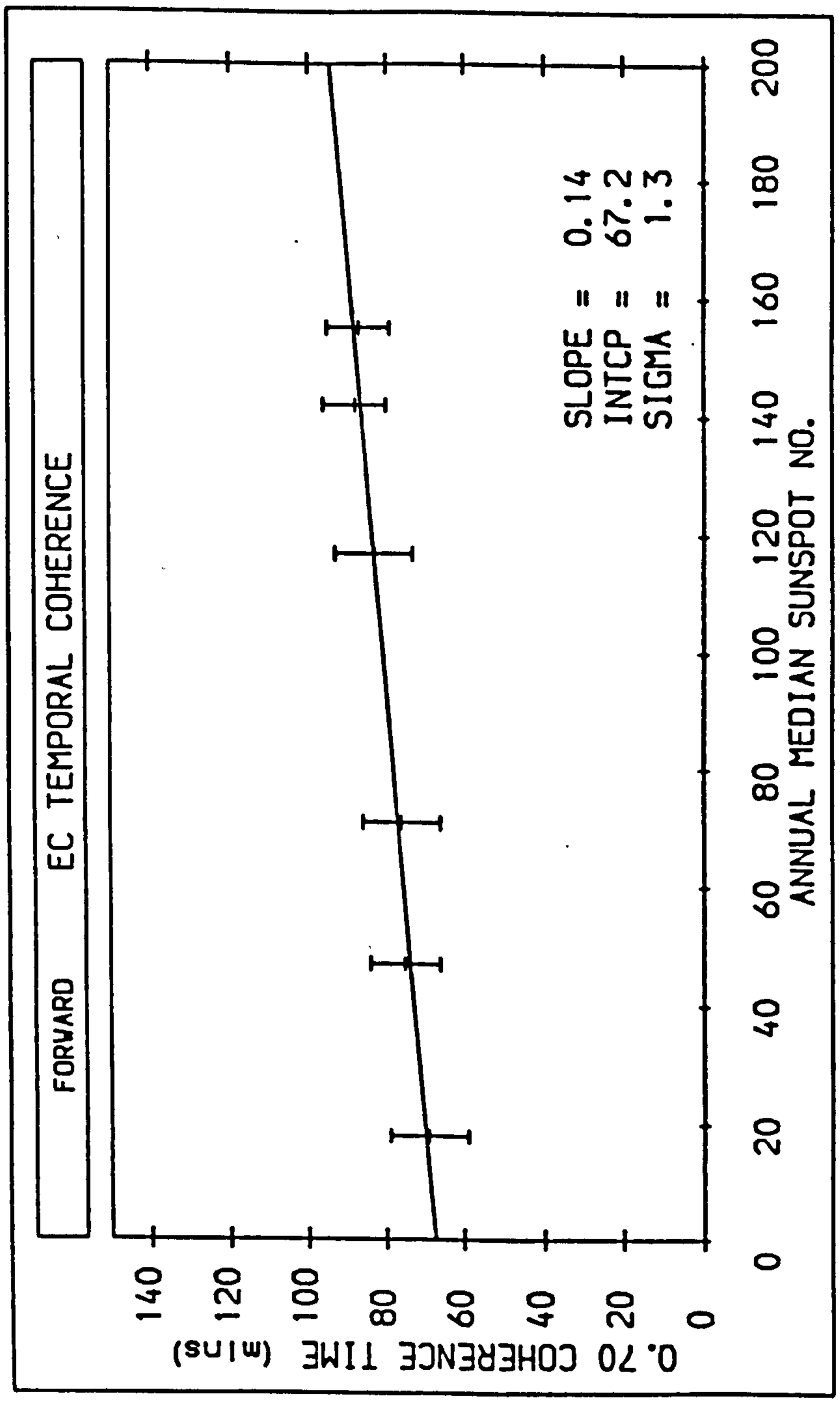

Figure 6.6 : The variation of the annual mean Coherence Time with the annual median twelve–month running mean sunspot number. The best–fit line is also drawn.

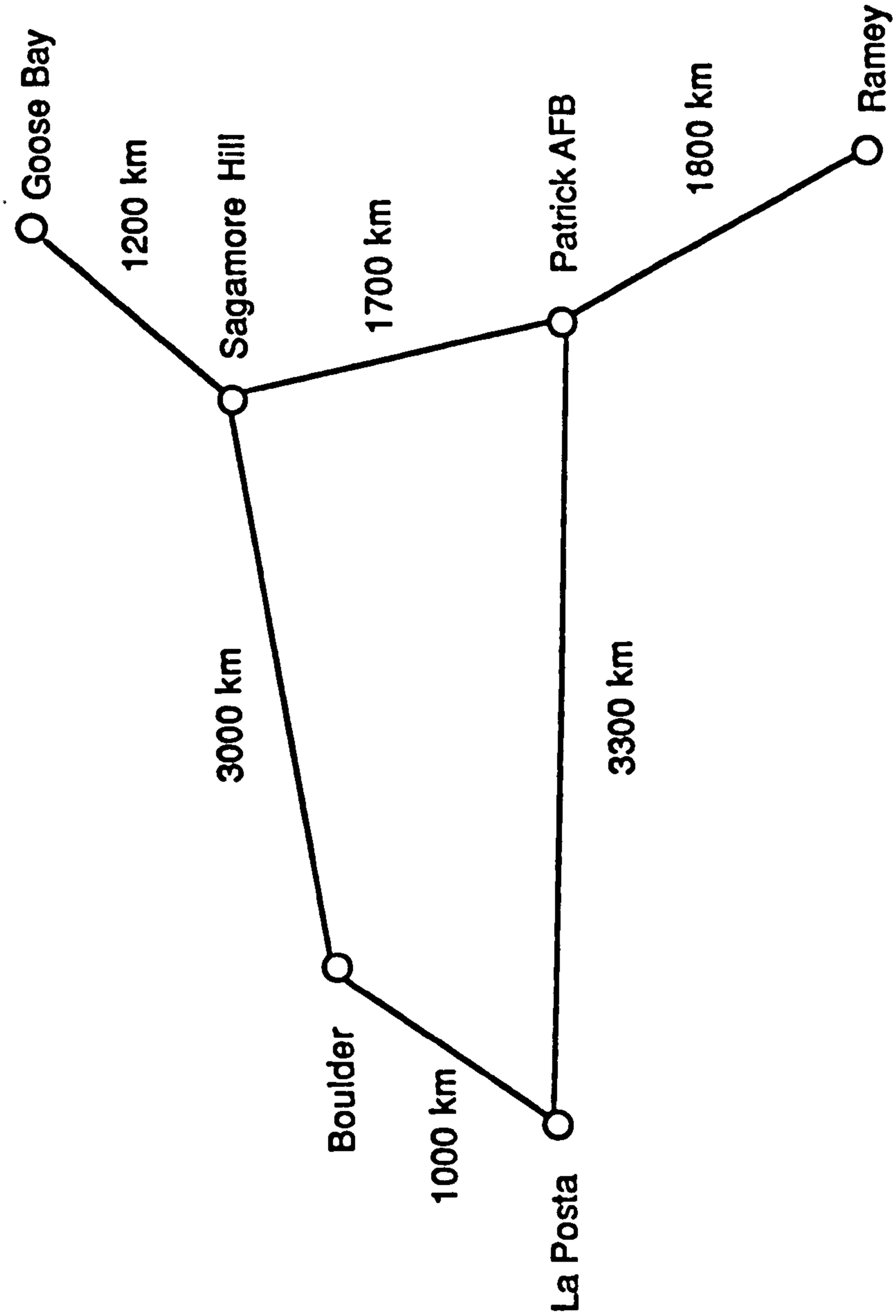

Figure 6.7 : A sketch map of the relative orientations and approximate great circle separations of the six Faraday rotation receiving sites employed in the study of the spatial coherence of electron content.

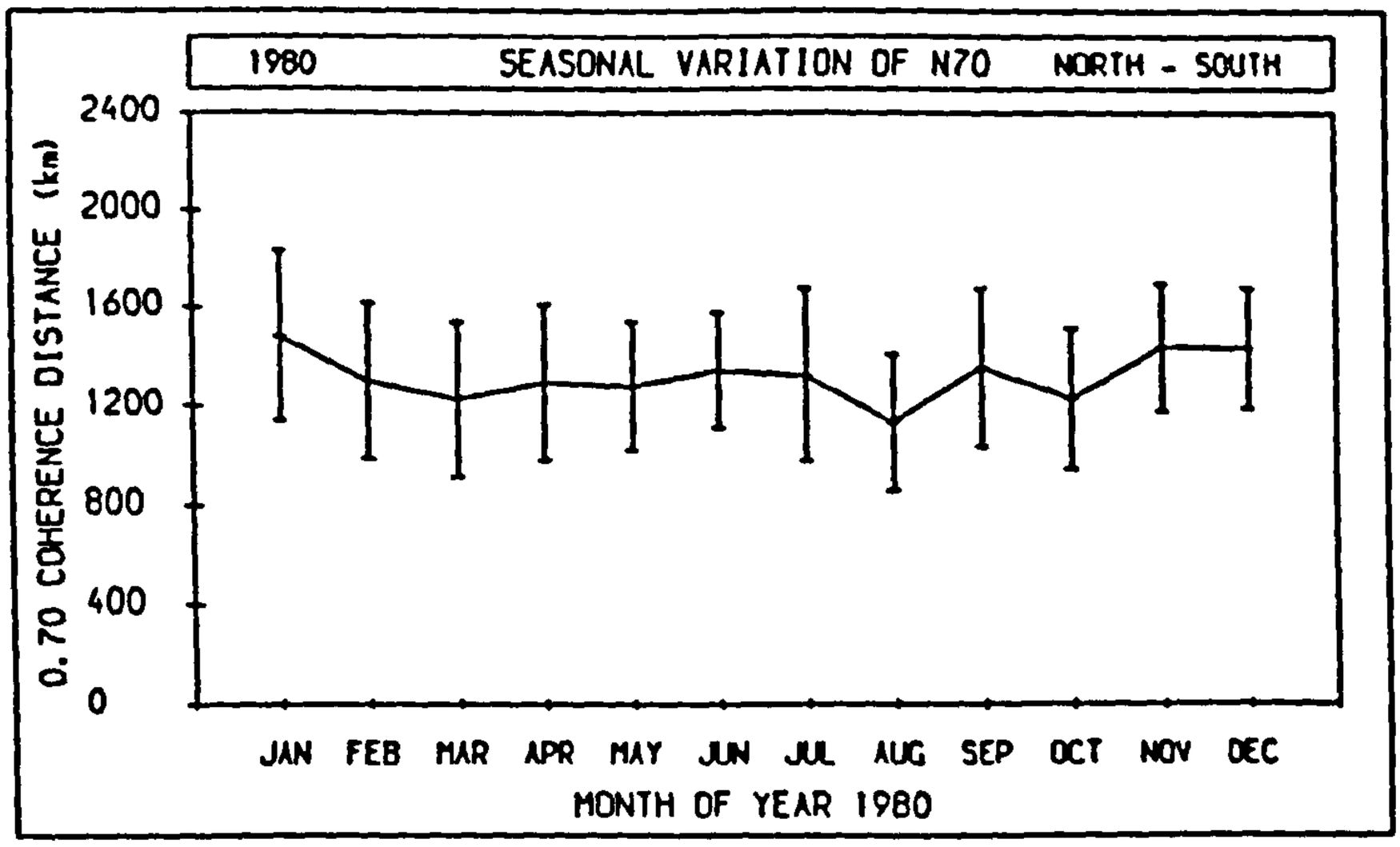

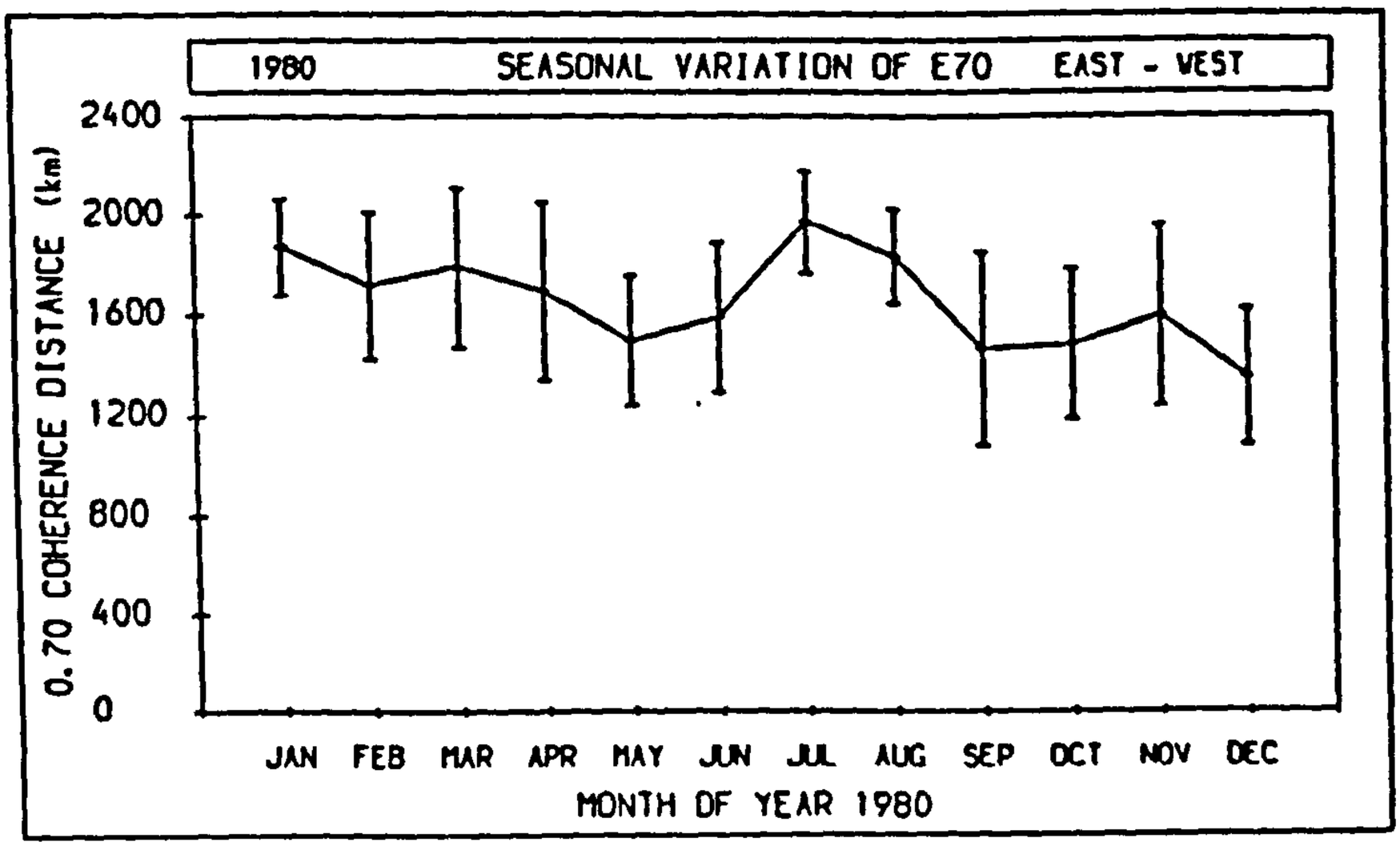

Figure 6.8 : The seasonal variation of the North–South and East–West Coherence Distances calculated from data taken during 1980.

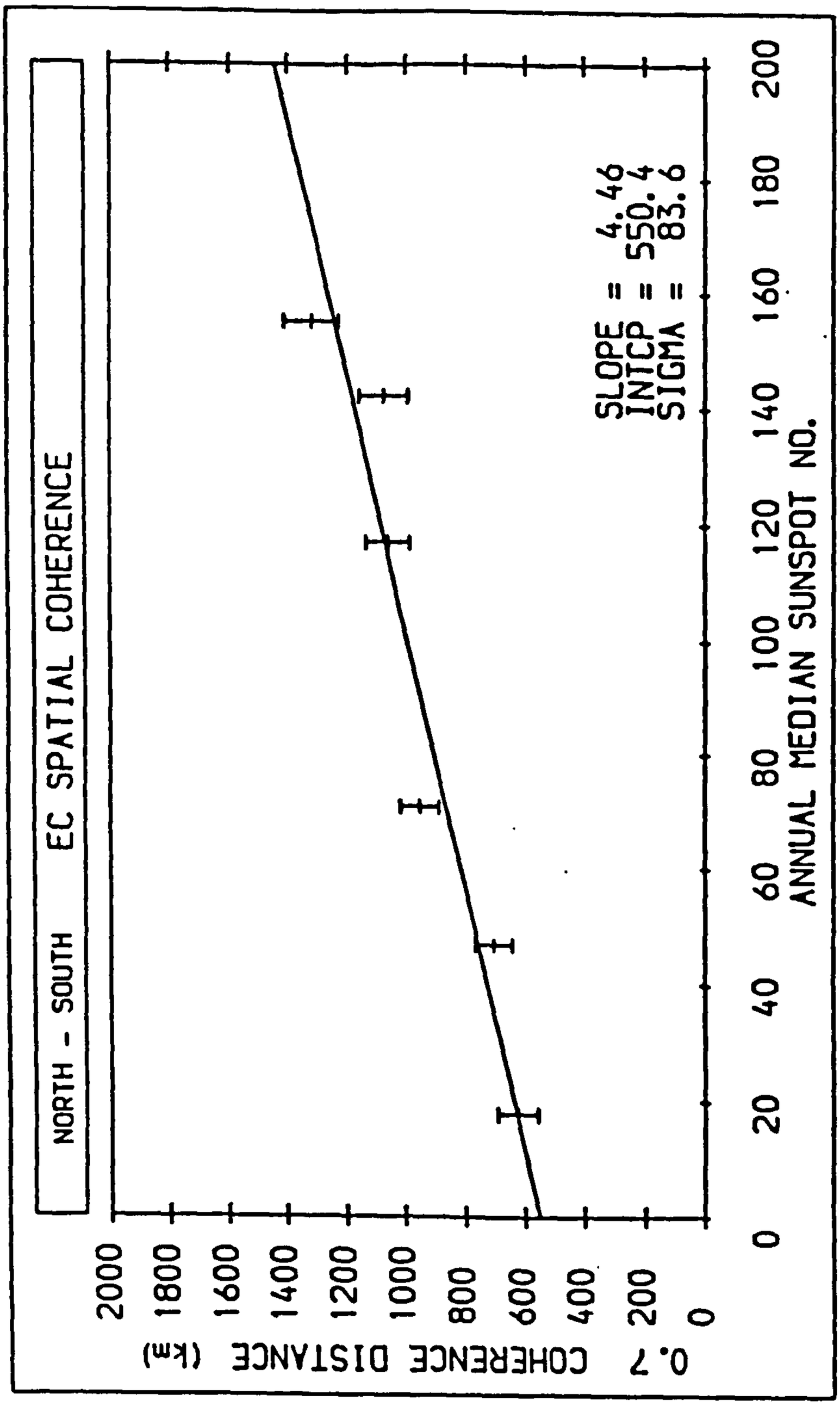

Figure 6.9 : The variation of the annual mean North–South Coherence Distance with the annual median twelve–month running mean sunspot number. The best–fit line is also drawn.

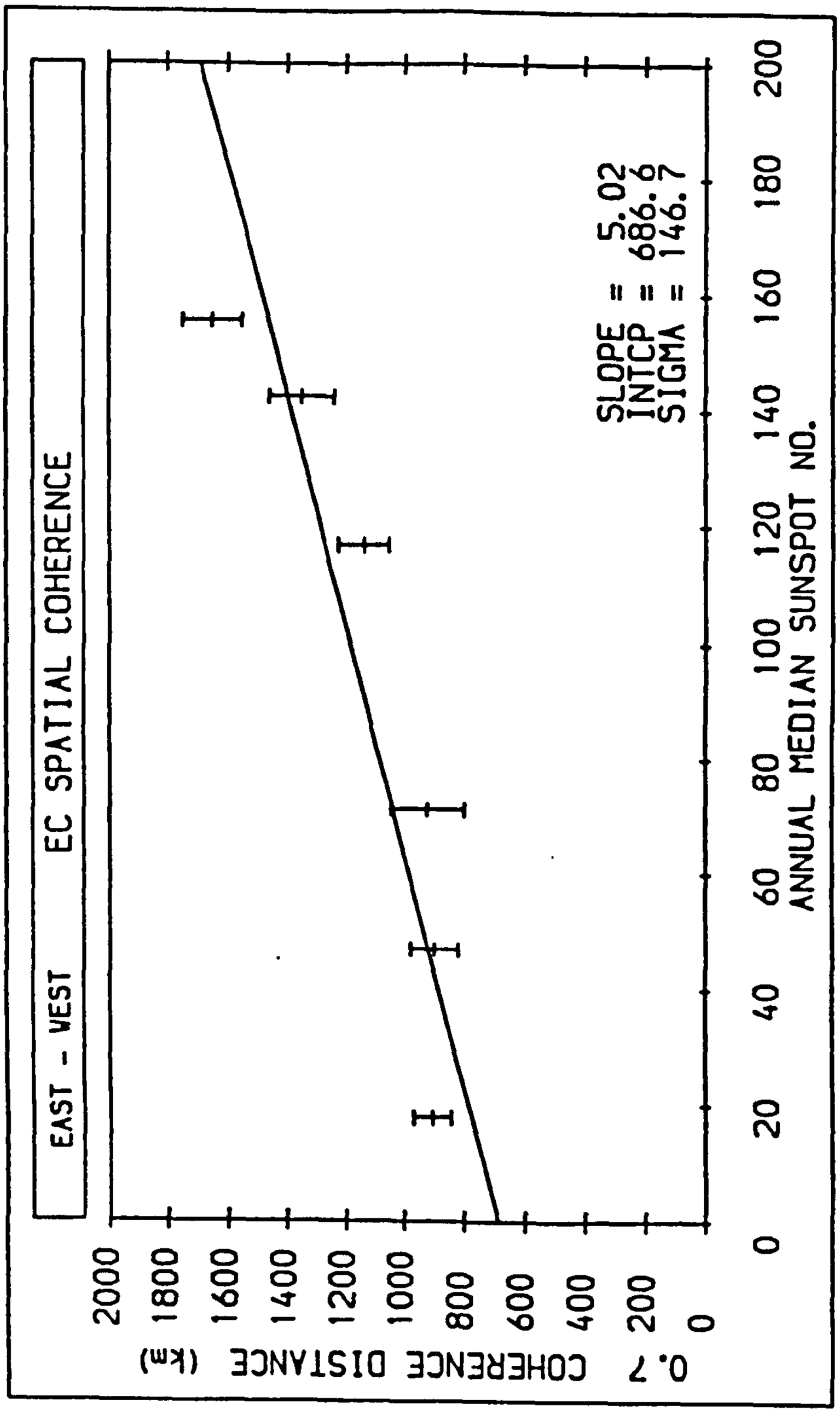

Figure 6.10 : The variation of the annual mean East–West Coherence Distance with the annual median twelve–month running mean sunspot number. The best–fit line is also drawn.

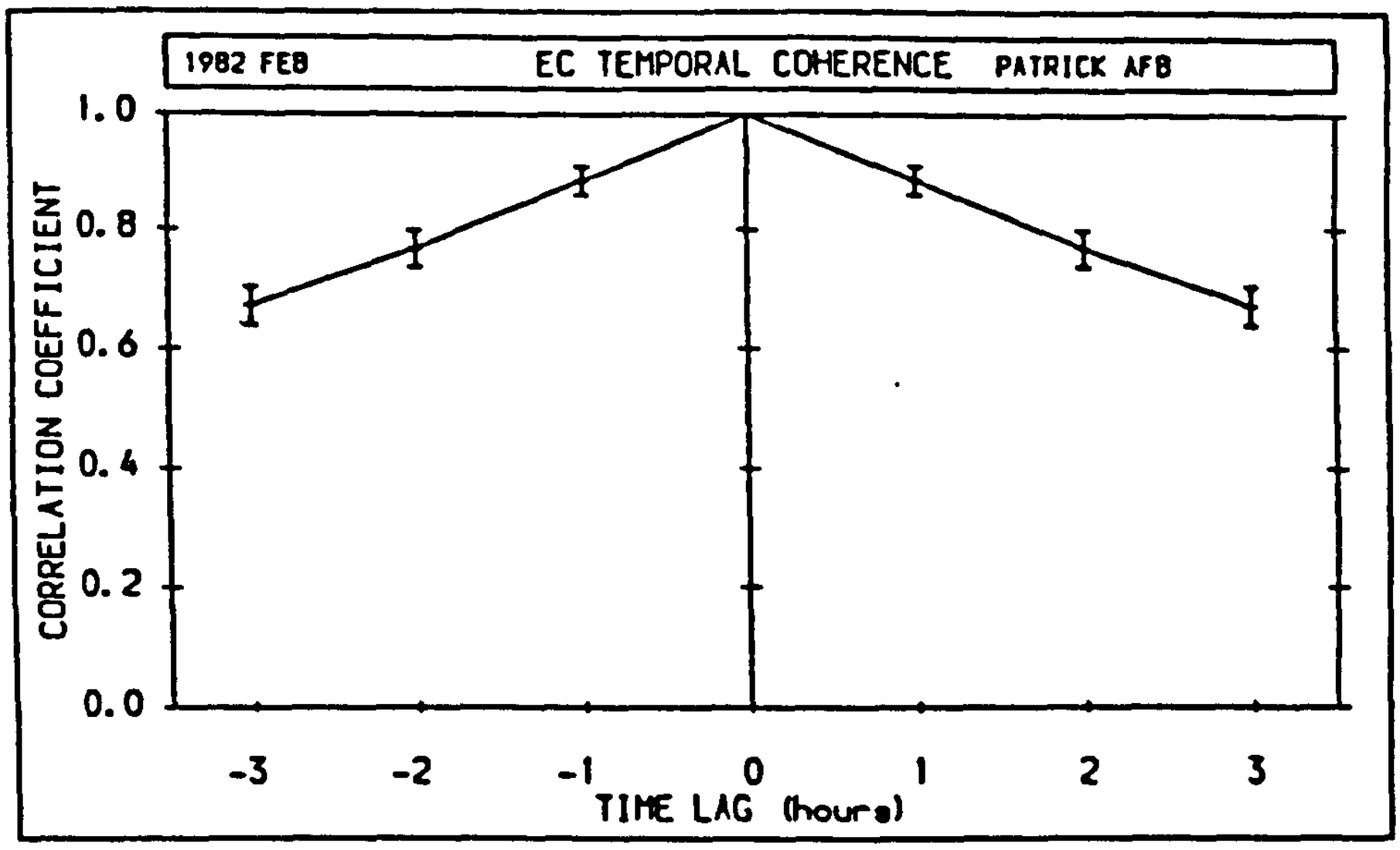

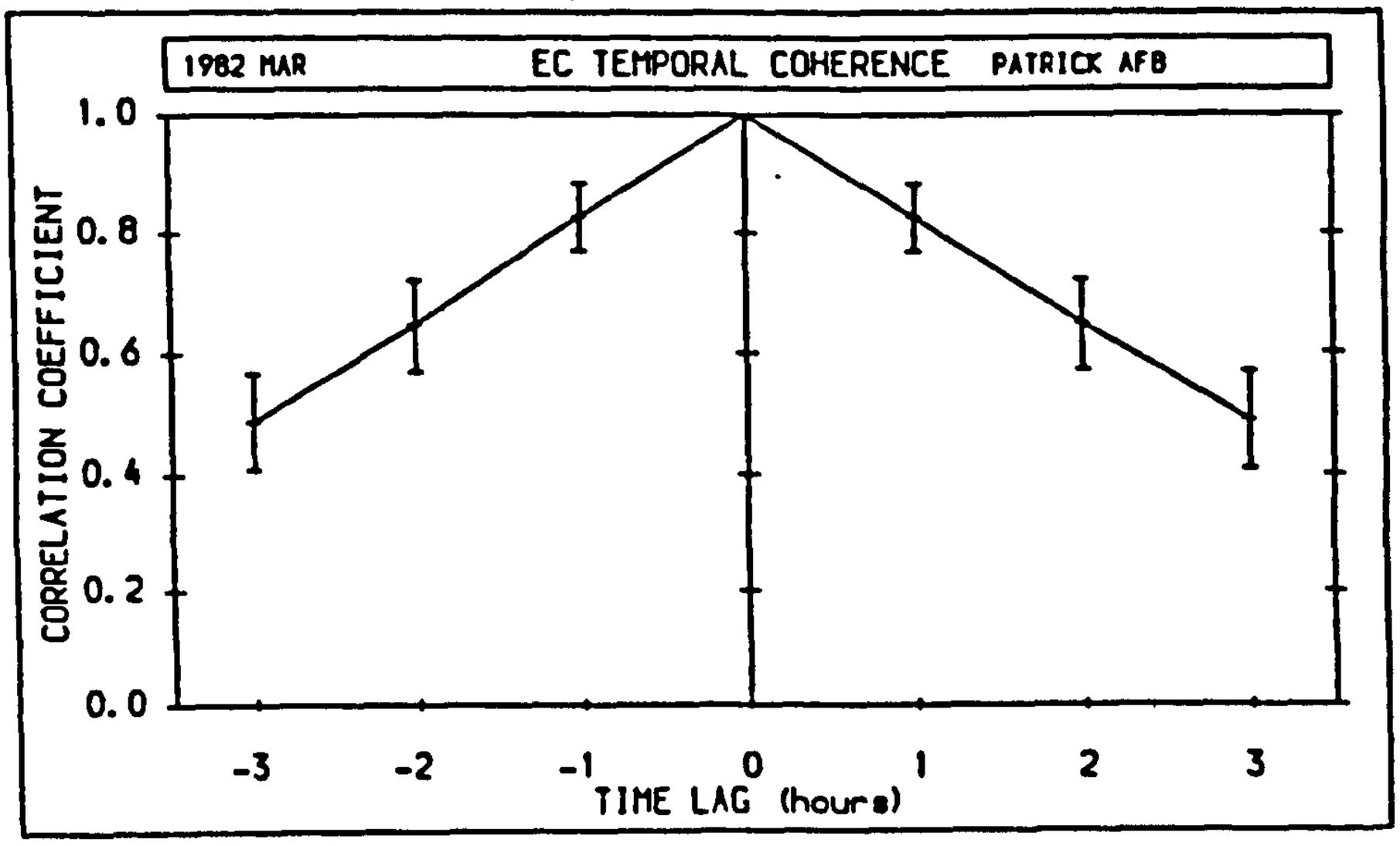

Figure 6.11 : The temporal decorrelation of the Patrick AFB data taken during February and March 1982. Note the almost linear decorrelation.

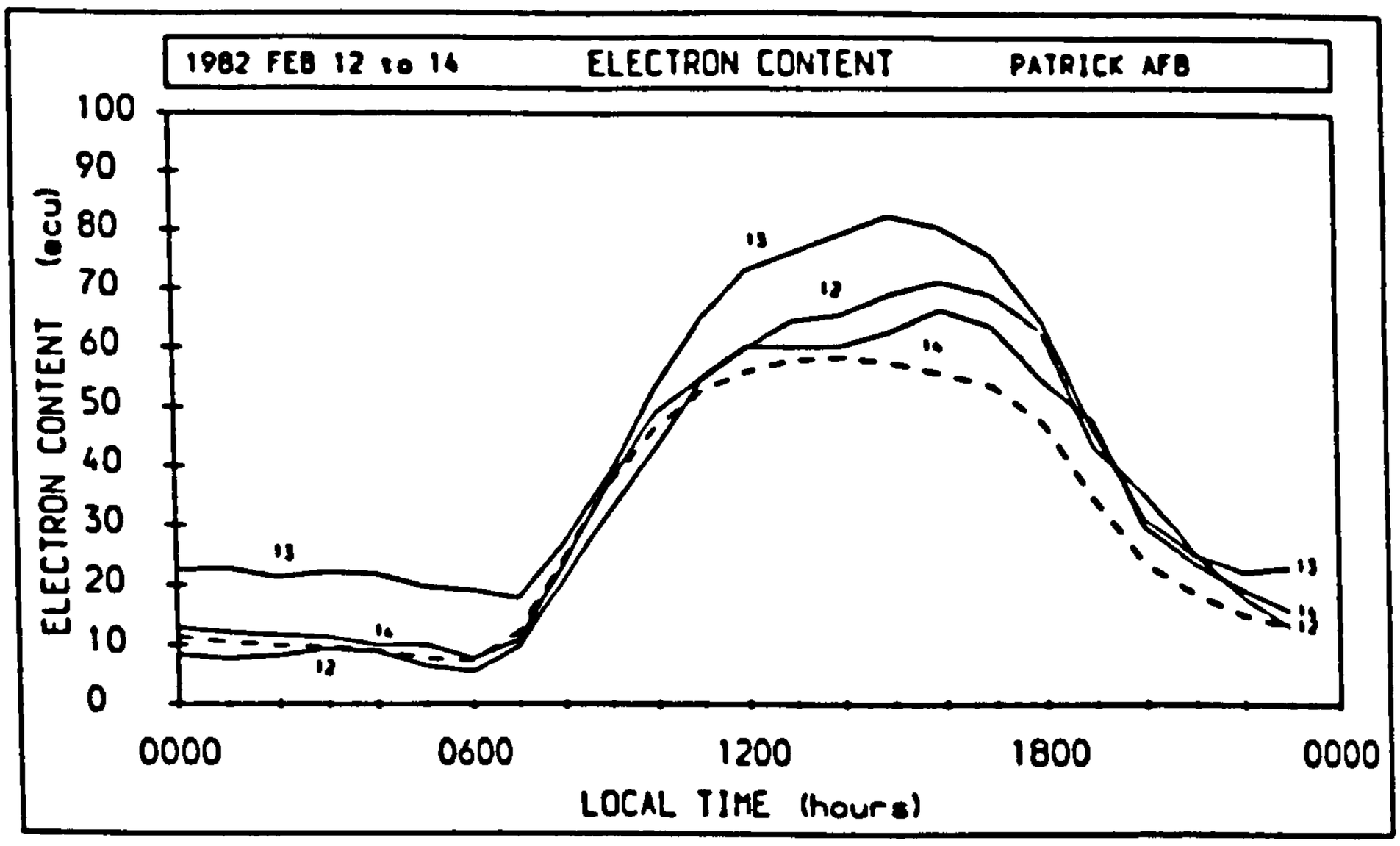

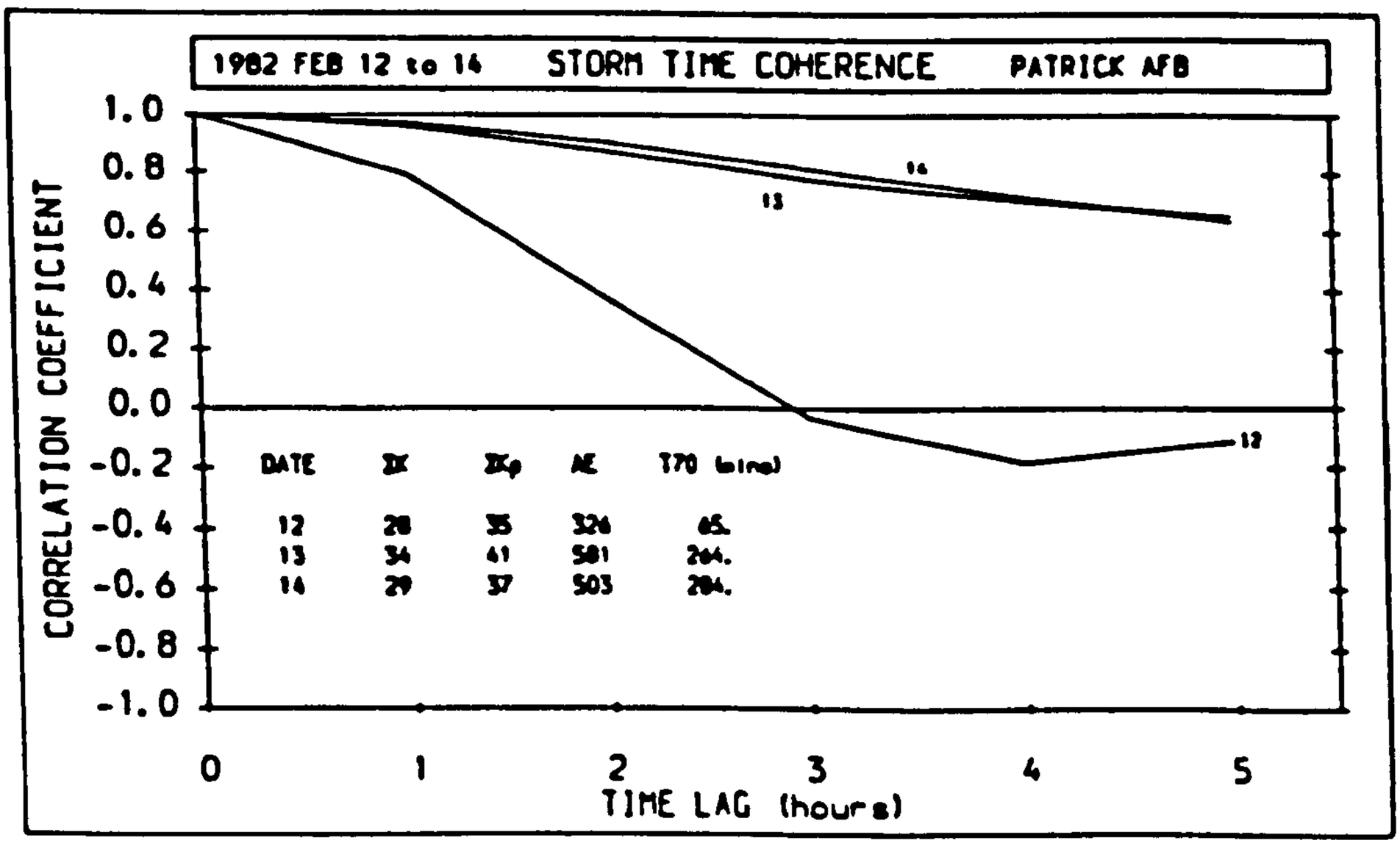

Figure 6.12 : (top) The electron content data from 12th–14th February 1982 and the February 1982 monthly mean (shown dashed) taken from Patrick and (below) its zero to five hour lag correlation coefficients. The prevailing magnetic indices are also shown.

Table 6.1 : The Coherence Times calculated with electron content data taken from the Boulder site between January 1980 and December 1985, inclusive.

	COHERENCE TIMES (mins) AT BOULDER												
	JAN	FEB	MAR	APR	MAY	JUN	JUL	AUG	SEP	OCT	NOV	DEC	AVERAGE
1980	101	115	103	103	109	111	99	102	108	98	103	92	104
1981	89	100	82	76	88	93	90	86	91	77	102	83	88
1982	93	94	87	87	—	81	79	77	97	78	77	78	84
1983	60	65	69	73	69	72	73	66	56	53	53	67	65
1984	89	67	71	72	74	74	64	63	72	71	68	61	70
1985	70	58	72	63	66	69	74	72	54	65	64	73	67

Table 6.2 : The annual mean Coherence Times calculated with electron content data measured between 1980 and 1985 from the ten receiving sites. Also listed is the annual mean of the Coherence Times at the ten sites.

YEAR	ANCH	ATHE	BLDR	GBAY	POST	PALE	PAFB	RAMY	SAGA	TAIW	AVERAGE
1980	-	89	104	89	88	75	84	78	86	77	86
1981	96	92	88	97	78	78	94	90	90	80	88
1982	104	76	84	78	92	75	80	81	79	78	83
1983	92	67	65	78	88	76	72	68	78	75	76
1984	87	70	70	74	97	73	68	63	72	71	75
1985	87	63	67	62	65	79	66	63	71	68	69

YEAR	1980	1981	1982	1983	1984	1985
T70 (latitude 0°N)	67	76	70	64	64	63
T70 (latitude 60°N)	103	98	94	85	84	74
CROSS-CORRELATION COEFFICIENT	0.75	0.60	0.52	0.47	0.40	0.27

Table 6.3 : Coherence Times at 0°N and 60°N latitude for the six years of the full data set interpolated from the best-fit line to the variation of Coherence Time with geographic latitude.

NORTH – SOUTH SEPARATION OF RECEIVING SITES (km)

	GOOSE BAY	SAGAMORE HILL	PATRICK AFB	RAMEY
GOOSE BAY	--	1000	2450	3450
SAGAMORE HILL	1000	--	1450	2450
PATRICK AFB	2450	1450	--	1000
RAMEY	3450	2450	1000	--

EAST – WEST SEPARATION OF RECEIVING SITES (km)

	LA POSTA	BOULDER	PATRICK AFB	SAGAMORE HILL
LA POSTA	--	750	3250	3850
BOULDER	750	--	2400	3000
PATRICK AFB	3250	2400	--	850
SAGAMORE HILL	3850	3000	850	--

Table 6.4 : A list of the Faraday sites and their relevant separations employed in the study of the spatial coherence of electron content.

Table 6.5 : The North–South Coherence Distances calculated with electron content data, measured between 1980 and 1985 inclusive, from the sites listed in Table 6.4.

	NORTH – SOUTH												
	JAN	FEB	MAR	APR	MAY	JUN	JUL	AUG	SEP	OCT	NOV	DEC	AVERAGE
1980	1484	1300	1227	1295	1283	1345	1325	1133	1354	1228	1435	1429	1320
1981	1166	1039	1021	1083	1161	1091	1051	1185	1041	1169	922	991	1077
1982	1057	1136	997	1169	1185	952	1245	1115	959	917	1029	996	1063
1983	1037	985	994	1034	931	1084	725	927	1004	923	991	823	955
1984	710	667	720	685	656	762	736	825	620	737	681	710	709
1985	697	546	653	657	590	776	929	576	501	376	638	604	629

Table 6.6 : The East-West Coherence Distances calculated with electron content data, measured between 1980 and 1985 inclusive, from the sites listed in Table 6.4.

	EAST – WEST												
	JAN	FEB	MAR	APR	MAY	JUN	JUL	AUG	SEP	OCT	NOV	DEC	AVERAGE
1980	1870	1717	1789	1692	1495	1585	1971	1832	1460	1477	1593	1345	1652
1981	1434	1698	1483	1375	1446	1353	1265	1112	1260	1253	1271	1268	1352
1982	1307	1215	1253	1222	1167	1154	1137	1141	1028	989	1102	993	1142
1983	1025	1002	947	1078	901	887	804	843	899	973	807	939	925
1984	884	898	832	881	915	920	845	853	907	934	953	987	901
1985	848	959	979	981	910	949	919	949	893	713	890	897	907

YEAR	MEDIAN SUNSPOT NO.	0.7 COHERENCE TIME (mins)		NS 0.7 COHERENCE DISTANCE (km)		EW 0.7 COHERENCE DISTANCE (km)	
1980	155	86	(8)	1320	(91)	1652	(97)
1981	142	88	(8)	1077	(84)	1352	(111)
1982	117	84	(10)	1063	(74)	1142	(86)
1983	71	76	(10)	955	(64)	925	(123)
1984	47	76	(9)	709	(61)	901	(79)
1985	18	69	(10)	629	(68)	907	(63)
CROSSCORRELATION WITH SUNSPOT NUMBER		0.98		0.96		0.90	

Table 6.7 : A summary of the annual mean Coherence Times and Coherence Distances of electron content along with their corresponding standard deviations (shown in brackets). The annual mean sunspot number for 1980 to 1985 inclusive and the crosscorrelation coefficients between the coherence values and these sunspot numbers are also tabulated.

BOULDER

LAG (hours)	LAG (km)	CORREL. COEFFICIENT	MAR	JUN	DEC
			(3.7)	(4.2)	(3.5)
3	0	0.40	3.0	2.6	2.8
2	0	0.60	2.4	2.0	2.4
1	0	0.80	1.6	1.4	1.8
0	0	1.00	0.0	0.0	0.0

LA POSTA

LAG (hours)	LAG (km)	CORREL. COEFFICIENT	MAR	JUN	DEC
			(3.6)	(4.7)	(2.3)
3	0	0.40	3.3	3.3	1.9
2	0	0.60	2.8	2.7	1.8
1	0	0.80	2.0	1.9	1.4
0	0	1.00	0.0	0.0	0.0

Table 6.8 : Reduction of the standard deviation of predicted electron content at Boulder and La Posta after adjustment with recent data. The more recent the data the greater the reduction. Unadjusted values are shown in brackets.

BOULDER – LA POSTA

LAG (hours)	(km)	CORREL. COEFFICIENT	MAR	JUN	DEC
			(3.7)	(4.2)	(3.5)
3	1000	0.29	3.6	4.0	3.2
2	1000	0.43	3.7	4.4	3.1
1	1000	0.57	3.0	3.3	3.0
0	1000	0.72	2.6	2.4	2.3

LA POSTA – BOULDER

LAG (hours)	(km)	CORREL. COEFFICIENT	MAR	JUN	DEC
			(3.6)	(4.7)	(2.3)
3	1000	0.29	3.5	4.3	2.2
2	1000	0.43	3.5	4.3	2.2
1	1000	0.57	3.4	3.7	2.1
0	1000	0.72	2.5	2.7	2.0

Table 6.9 : An illustration of the reduction the standard deviation of predicted electron content after adjustment with remote data. La Posta data is used to update predictions for Boulder and vice versa. Unadjusted standard deviations are shown in brackets.

	1980				1982				
STATION	MAR	JUN	SEP	DEC	FEB	MAR	JUN	SEP	DEC
				AE					
GOOSE BAY	-0.01	0.05	0.20	-0.26	-0.33	-0.33	0.23	0.27	-0.29
ANCHORAGE	---	---	---	---	-0.05	-0.28	-0.27	0.49	-0.13
SAGAMORE HILL	0.28	-0.03	0.24	-0.15	-0.21	-0.13	-0.15	0.22	-0.07
BOULDER	0.10	0.44	0.06	-0.13	0.05	-0.32	-0.21	0.18	-0.18
PATRICK AFB	0.24	0.14	-0.31	-0.31	0.09	-0.11	-0.06	0.21	-0.27
PALEHUA	0.20	0.36	0.03	-0.28	0.31	-0.10	0.19	0.02	-0.36

Table 6.10 : The crosscorrelation coefficients between the electron content Coherence Times measured at six sites and the magnetic index AE for data from the representative months of 1980 and 1982 and from February 1982.

	1980				1982				
STATION	MAR	JUN	SEP	DEC	FEB	MAR	JUN	SEP	DEC
					ΣKp				
GOOSE BAY	0.05	0.02	0.04	-0.23	-0.32	-0.38	0.19	0.17	-0.40
ANCHORAGE	--	--	--	--	-0.04	-0.38	-0.24	0.51	-0.10
SAGAMORE HILL	0.21	0.00	0.21	-0.14	-0.23	-0.13	-0.01	0.13	-0.17
BOULDER	0.17	0.32	-0.11	-0.15	0.05	-0.13	-0.24	0.16	-0.21
PATRICK AFB	0.24	0.15	-0.23	-0.21	0.02	-0.06	-0.05	0.16	-0.32
PALEHUA	0.16	0.41	0.14	-0.36	0.30	-0.04	0.20	0.04	-0.33

Table 6.11 : The crosscorrelation coefficients between the electron content Coherence Times measured at six sites and the magnetic index ΣKp for data from the representative months of 1980 and 1982 and from February 1982.

	1980				1982				
STATION	MAR	JUN	SEP	DEC	FEB	MAR	JUN	SEP	DEC
				ΣK					
GOOSE BAY	0.22	0.05	0.11	-0.24	-0.33	-0.38	0.24	0.14	-0.40
ANCHORAGE	—	—	—	—	-0.06	-0.30	-0.25	0.54	-0.09
SAGAMORE HILL	0.41	-0.03	0.36	-0.11	-0.17	-0.13	-0.11	0.10	-0.19
BOULDER	0.32	0.31	-0.07	-0.21	0.08	-0.16	-0.21	0.14	-0.22
PATRICK AFB	0.43	0.20	-0.12	-0.21	0.02	-0.11	-0.04	0.18	-0.36
PALEHUA	0.15	0.36	0.02	-0.30	0.29	-0.04	0.29	0.03	-0.51

Table 6.12 : The crosscorrelation coefficients between the electron content Coherence Times measured at six sites and the magnetic index ΣK for data from the representative months of 1980 and 1982 and from February 1982.

	1980				1982				
	MAR	JUN	SEP	DEC	FEB	MAR	JUN	SEP	DEC
$\Sigma Kp * AE$	0.87	0.93	0.83	0.90	0.91	0.91	0.84	0.93	0.90
$AE * \Sigma K$	0.60	0.88	0.65	0.90	0.85	0.90	0.83	0.90	0.90
$\Sigma K * \Sigma Kp$	0.56	0.97	0.88	0.95	0.96	0.97	0.94	0.99	0.99

Table 6.13 : The crosscorrelation coefficients between the three magnetic indices ΣK, ΣKp and AE for the representative months of 1980 and 1982 and February 1982.

Chapter 7 : Ionospheric Correction Algorithm

This chapter explains how the Predictive and Adaptive Models are combined into a satellite radar altimeter ionospheric correction system. The orbit configuration is a necessary input to the correction procedure and a tranche of that of the Seasat mission is employed in a mission simulation. The output from the new algorithm, referred to as the LEI Model, will be compared to that of the ionospheric correction procedure developed for the Seasat altimeter at the US Jet Propulsion Laboratory.

7.1 Generation of the Predictive Correction

The principal aim of a model ionosphere is the reproduction of the properties of the real ionosphere as closely as possible for a restricted set of input conditions. Table 7.1 lists the number of increments of each input variable of the Predictive Model and compares them to the number suggested by Nisbet (1975) for an empirical model.

The first stage of the ionospheric correction technique is the prediction of monthly mean electron content at the sub–altimeter point. When running the procedure on a computer, efficient storage of data and fast program execution is desirable, hence the system was based on the look–up table principle. The Predictive Model was used to generate global numerical maps of sub–800 km electron content with a resolution of 10° of latitude by 15° of longitude. The digital maps were produced at each hour of Universal Time for each month and for five levels of solar activity (sunspot numbers of 0 to 200 in steps of 50). Although the Predictive Model was calibrated with sub–2 000 km data the bulk of the electron content, and particularly its variability, is found at altitudes of a few hundred kilometres around the peak. This implies that the Predictive Model should still be accurate after truncation of the profile at the nominal 800 km altitude of ERS1.

After input of the temporal and spatial co–ordinates from the orbit configuration, a simple linear interpolation program calculates the sub–800 km electron content for values of sunspot number, day number, Universal Time and latitude and longitude between the grid points of the tables.

Given the altimeter transmission frequency, Equation 1.17 is then utilized to calculate the monthly mean subtractive ionospheric correction for the sub–satellite point.

Examples of the output from the Predictive Model in terms of electron content are given in Figures 7.1 to 7.3 which illustrate the Local Time and seasonal variation estimated for the ionospheric point of the Boulder station between 1990 and 1992, the proposed duration of the ERS1 mission. Since the year 1990 is in the ascending phase of solar cycle 22 the magnitude of the daytime electron content at the autumnal equinox is greater than at the vernal equinox; the opposite situation to that during 1980, illustrated in Figure 3.6, which is in the descending phase of solar cycle 21.

7.2 Generation of the Adaptive Correction

Due to the day–to–day variability of electron content the Predictive Model cannot be expected to provide a sufficiently accurate value of the sub–satellite electron content. This problem can be rectified by the Adaptive Model which incorporates electron content measurements into the prediction system. The principal source of electron content data is expected to be the Precise Range And Range–rate Equipment (PRARE), an autonomous microwave radar system designed principally to measure the ERS1 ephemeris (Hartl 1984).

The dual frequency downlink transmissions (on 2.2 GHz and 8.5 GHz) of the space–based component of PRARE and the dispersive nature of the ionosphere permits calculation of the electron content along the line–of–sight from the PRARE ground station to the satellite from the differential delay of the S– and X–band signals (Wilmes et al 1987). The measurement rate is planned to be 1 Hz. The PRARE design limits its operation to ground zenith angles (ζ in Figure 1.9) of less than 70° and hence the equivalent vertical electron content can be calculated from simple multiplication by the cosine of the ionospheric zenith angle (McNamara 1983). The configuration of the PRARE/ERS1 system for the extreme 70° ground zenith angle condition is depicted by Figure 7.4. The maximum ionospheric zenith angle is 62°. The range accuracy of the PRARE system, which will be checked during the mission by laser ranging calibration, is expected to be better than 10 mm at the 8.5 GHz frequency; equivalent to 1.8 ecu in terms of electron content.

At present three PRARE ground stations are under construction by the Institut für Navigation, Stuttgart which will be supported by a global network of smaller transponder units. Depending on

the extent of industrial co–operation, a total of eighteen sites is envisaged, distributed as in Figure 7.5. The greater the number of sites the greater the number of opportunities there will be to invoke the Adaptive Model.

The upper part of Figure 7.6 illustrates the anisotropic electron content spatial correlation horizon, due to the coherence distance being greater East–West than North–South. The lower figure is the isocoherent surface of the 0.7 correlation horizon which is centred on the space–time co–ordinates of the altimeter sounding. All points on the surface of this figure have a correlation coefficient of 0.7 and represent the extremes of space–time separation between the measurement and sounding which still permit operation of the Adaptive Model. The Adaptive Model can be invoked for all space–time points inside the surface, but those outside are beyond the coherence horizon. In correlation space this figure would, of course, be a sphere.

In addition to the measurement of electron content the Adaptive Model also requires the monthly mean electron content at the measurement point which is provided by the Predictive Model and the combined space–time correlation coefficient (Equation 4.27). Given the spatial and temporal separation of the measurement and sounding points the correlation coefficient can be calculated from the Equations 6.13 to 6.14 and 6.15 to 6.18.

Due to the zenith angle limit of the PRARE system the maximum ground to satellite line–of–sight range is 1711 km and the maximum measurement point to sounding point separation in the ionosphere is only 593 km. Hence, for a pass along the meridian of a PRARE ground station the altimeter will be inside the operation limit for approximately 400 s. During this time the adaptive adjustment to the ionospheric correction only need consider the spatial decorrelation between the measurement and sub–altimeter points, since for each altimeter sounding a simultaneous PRARE electron content measurement will be available. The proximity of the sounding and measurement lead to a high combined correlation coefficient and make the Adaptive Model a highly effective correction procedure within these constraints.

Beyond the limit of PRARE operation both temporal and spatial decorrelation of the last electron content measurement must be considered. This measurement can repeatedly adjust the forecast until its spatial and temporal separation from the altimeter sounding takes it beyond the correlation horizon (at a correlation coefficient of 0.7). Since it is not necessary to make the ionospheric correction in real time the electron content measurement made when the ground station first makes contact with the satellite can be utilized to make the adjustment to the series of values predicted previously back out to the coherence horizon.

A prototype algorithm code is given in Appendix C in terms of an Algorithm Design Language.

7.3 Seasat Mission Simulation

The environment of an altimeter mission was simulated to provide a trial for the ionospheric range correction algorithm. The orbit configuration of latitude, longitude and Universal Time was supplied from a three revolution tranche of the Seasat mission orbit. The ionospheric correction procedure employed for the Seasat mission was developed at the US Jet Propulsion Laboratory, (JPL) and is described in Appendix B. An extensive comparative analysis of the estimated ionospheric corrections from the new LEI Model and the JPL Model was undertaken for the spatial and temporal co–ordinates of the three revolutions. The limited data set results in poor temporal sampling, but good spatial sampling due to the wide coverage of latitude, to ±72° over each revolution.

To provide the ionospheric correction for the sub–altimeter points the JPL Model employed electron content data collected at one northern hemisphere and one southern hemisphere ground station as the basis of a non–linear extrapolation procedure which calculated ionospheric correction values to the nearest 10 mm. Although it is accepted that in prediction procedures the use of real time data is advantageous, a loss of accuracy is likely to result from the large distances over which extrapolation is required. In general these distances are much greater than the coherence distances of electron content. The overall accuracy of the JPL Model was estimated as 30 mm in altitude at 13.6 GHz (Lorell et al 1982).

The JPL Model output for day number 256 of 1978 was validated with a more complicated, independent, solar radiation based model. The subtractive corrections supplied by the two models for part of revolution 1 117 are compared in Figure 7.7. The solar radiation model predicted greater extremes of electron content and distinguished the Equatorial Anomaly more clearly than the JPL Model, though the magnitudes of the corrections were broadly similar and in phase.

The global structure of sub–800 km ionospheric correction predicted by the LEI Model during July 1978 for an altimeter frequency of 13.8 GHz is illustrated by Figure 7.8. The LEI Model corrections range from below 10 mm to over 100 mm and strong gradients are evident in the regions of the Equatorial Anomaly and the sunrise Terminator.

Figure 7.9 shows the corresponding ground tracks of revolutions 472, 473 and 474 of the Seasat orbit which had a nominal altitude of 800 km and an inclination of 108°. Revolution 472 was tagged at the northward equatorward crossing over Sumatra, 473 south of the Indian sub–continent and 474 over the Horn of Africa. The three Seasat revolutions considered in the comparison are from the orbit configuration on day number 211 (29th July) of 1978 beginning at 0009 UT and ending at 0609 UT. The Seasat data set was reduced from one correction per second to one per thirty seconds which left approximately 200 JPL ionospheric corrections and corresponding ground track locations per revolution. The ground track co–ordinates were then used as the input to the LEI Predictive Model which generated predictions of ionospheric corrections at the same sub–altimeter locations as the JPL Model.

The corrections predicted by both the LEI and JPL Models for an altimeter frequency of 13.8 GHz over revolutions 472, 473 and 474 are presented in graphical form in Figures 7.10 to 7.12 respectively. The Local Times of the northward equatorward crossings were 0631 LT, 0451 LT and 0311 LT, respectively. It is clear that the two models exhibit variations in the predicted correction which are approximately in phase. However, the magnitude of the LEI Model predictions is somewhat larger. The greatest value of the JPL correction set is 60 mm, whereas that of the LEI Model is almost 100 mm.

As the satellite progressed along its ground track the magnitude of the correction changed, depending primarily on the geographical location of the satellite footprint. At the start of each of the three revolutions the altimeter footprint was within the nightside equatorial zone, which resulted in a predicted correction of between 30 and 40 mm from both models. As the latitude increased into the nightside northern hemisphere the LEI Model predictions decreased to be approximately 15 mm at the northernmost point of the orbit. In contrast the JPL Model predictions remained constant at 30 mm, about twice the LEI value. The LEI Model corrections rose again during the traversal of the dayside northern hemisphere until at mid–latitudes the two models predicted similar corrections of approximately 40 mm. The LEI corrections exhibited a sharp gradient in the dayside equatorial zone, the correction doubling to almost 100 mm within five minutes (an approximate along–track distance of 2 000 km). The JPL set on the other hand predicted a shallower gradient giving a maximum correction of 60 mm. The LEI Model revealed more explicitly the double peak structure of the dayside Equatorial Anomaly. The gradient of the predictions coming out into the southern hemisphere Equatorial Anomaly was just as steep as the one leading in. The two models again agreed for mid–latitude regions with the corrections of approximately 30 mm. Over the southernmost part of the orbit, about 75 minutes

in, the LEI Model returned corrections of around 20 mm, whereas the JPL Model was down to 10 mm. The two models were again close at 20 and 30 mm for the return path through the nightside southern mid–latitudes. This comparison highlighted the broad similarities between the two models, especially in mid–latitude regions.

Further, it is useful to note that at approximately 93 minutes into revolution 472 the sub–satellite point passed within 1 500 km of the southern JPL ground station at Armidale. This is sufficiently close to the coherence horizon to provide a valuable point of comparison between the two models. From Figure 7.11 the two models agree to within 10 mm at this point which, at least, lends some degree of confidence to the LEI Model.

The distribution of corrections predicted by the JPL and LEI Models over all three revolutions are shown in Figures 7.13 and 7.14, respectively, binned in 10 mm ranges. The mode of the JPL corrections lies in the 30 mm bin and the distribution is only slightly skewed to higher values. The upper bound of the JPL corrections occurs at 60 mm. The LEI corrections have a more varied structure, however. The most occupied bin is still that centred on 30 mm, though the range of corrections is such that even the 100 mm bin is occupied.

The distributions of the differences between the two models over the three revolutions are shown in Figures 7.15 to 7.17 where the fractional occurrence of a given difference is plotted as a histogram. All three revolutions exhibit a similar form of distribution, the majority of differences are clustered within ±20 mm. There is, however, a small proportion of large positive differences due to the LEI Model response to the dayside equatorial zone which skews the distribution towards positive values. The statistics of the differences between the two models are listed in Table 7.2. On average over each revolution the LEI Model predicted greater values of ionospheric correction than those returned by the JPL Model. The standard deviation of the two sets of predictions is somewhat below 20 mm for each revolution.

When compared to the JPL Model, the LEI Model is more finely structured, predicts a greater range of corrections and tends to predict higher corrections for the dayside and lower corrections for the nightside. The predictions from the two models are largely in phase along the ground tracks of the orbit. The along–track structure of the LEI Model predictions, though, had a broad similarity to the predictions of the solar radiation model shown in Figure 7.7. These conclusions can only be considered tentative, though, since only about six hours of data have been considered.

As a matter of interest, and to contrast the two models in a similar light, Figure 7.18 shows the LEI Model corrections for revolution 474 rounded to the nearest 10 mm along with the JPL Model corrections offset by 1 mm. The differences between the two sets of predictions highlighted above are still evident despite this rounding. Figure 7.19 shows the LEI Model predictions for revolution 472 calculated individually every 30 seconds and demonstrates the improvement in smoothness which could be gained from increasing the spatial resolution of the global maps by a factor of five.

Unfortunately, in this case, no data was available to invoke the adaptive element of the LEI Model. The influence of the Adaptive Model on the predicted electron content is demonstrated in Figure 7.20 which shows the monthly mean electron content and equivalent ionospheric correction at Boulder for March 1980 and the actual values measured on the 12th of the month. The line joining the two curves plots the ionospheric correction predicted by the LEI Model given one measurement of electron content at 12 LT. The coherence horizon in this situation lies at a time lag of approximately two hours and it can be seen that after 14 LT the model predicts a value very close to the mean level. Notice in this case the sign of the adjustment is negative. The model allows the predicted electron content to follow the true electron content more closely for the couple of hours that the measurement is within the coherence horizon, though the improvement is marginal for predictions at greater temporal separations.

7.4 Chapter Summary

The methodology for production of the monthly mean electron content by the Predictive Model was outlined and the monthly mean predictions at the Boulder site for the proposed duration of the ERS1 mission were presented. A comparison was made between the LEI and JPL Predictive Models and the areas of similarity and difference noted. The PRARE system was then proposed as the principal source of electron content data for the Adaptive Model. The behaviour of the LEI Adaptive Model was seen to make an adaptive forecast of the electron content which, as expected, was closer to the true value than the mean itself. The above examples have demonstrated the capability of the LEI Model to provide ionospheric corrections to altimeter data under conditions similar to those proposed for the ERS1 altimeter mission.

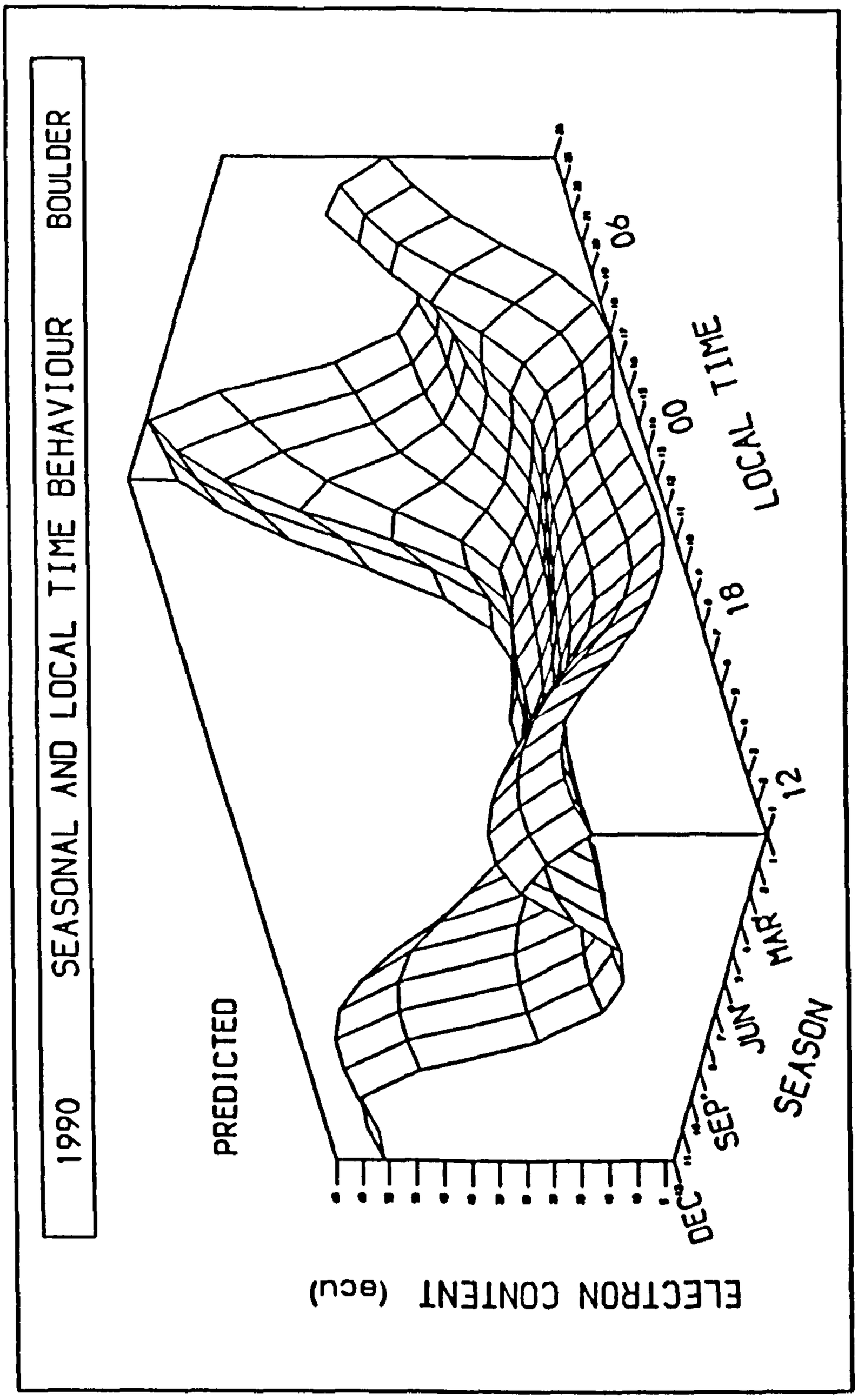

Figure 7.1 : The Local Time and seasonal variation of electron content at the Boulder site estimated from the Predictive Model for 1990.

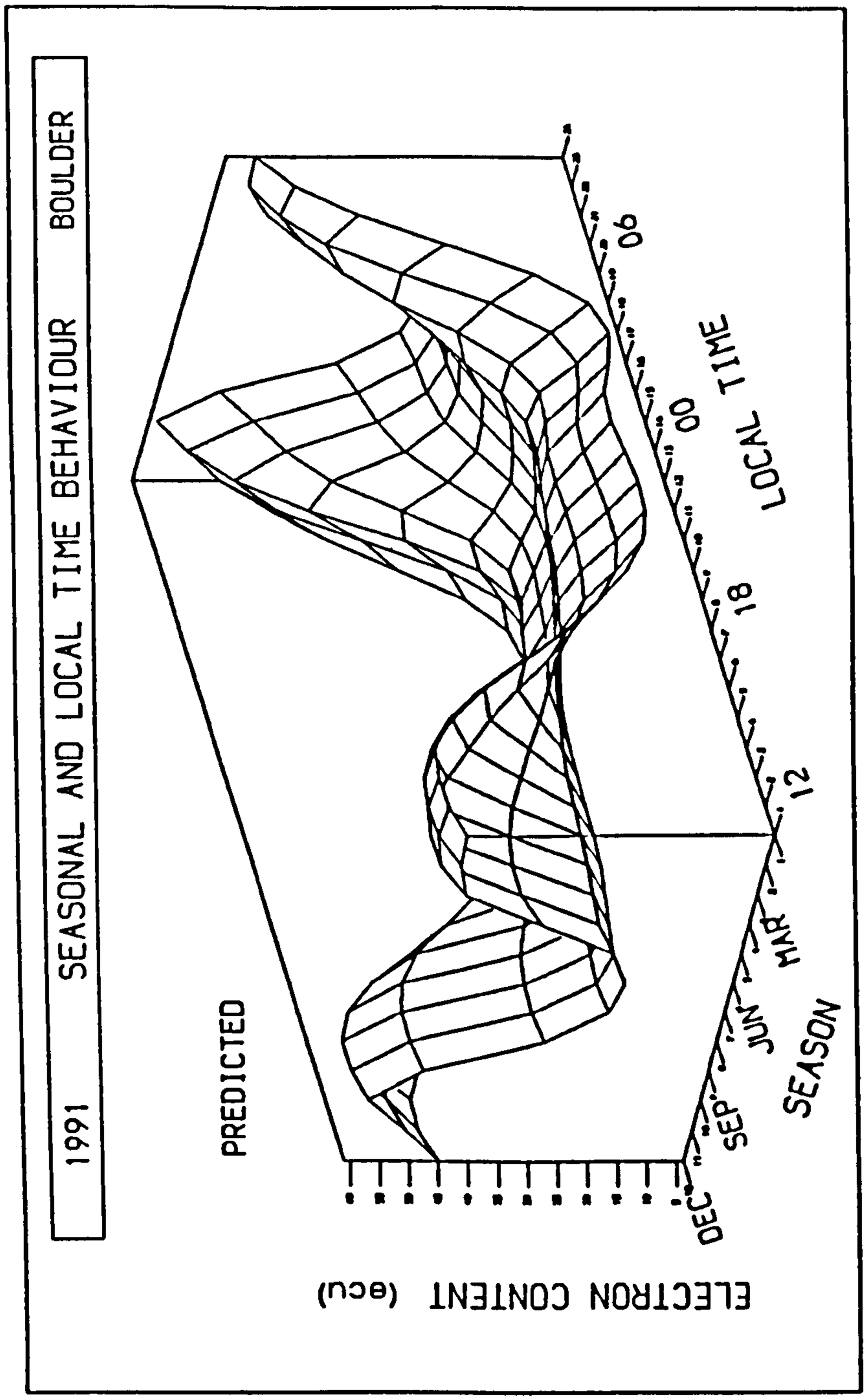

Figure 7.2 : The Local Time and seasonal variation of electron content at the Boulder site estimated from the Predictive Model for 1991.

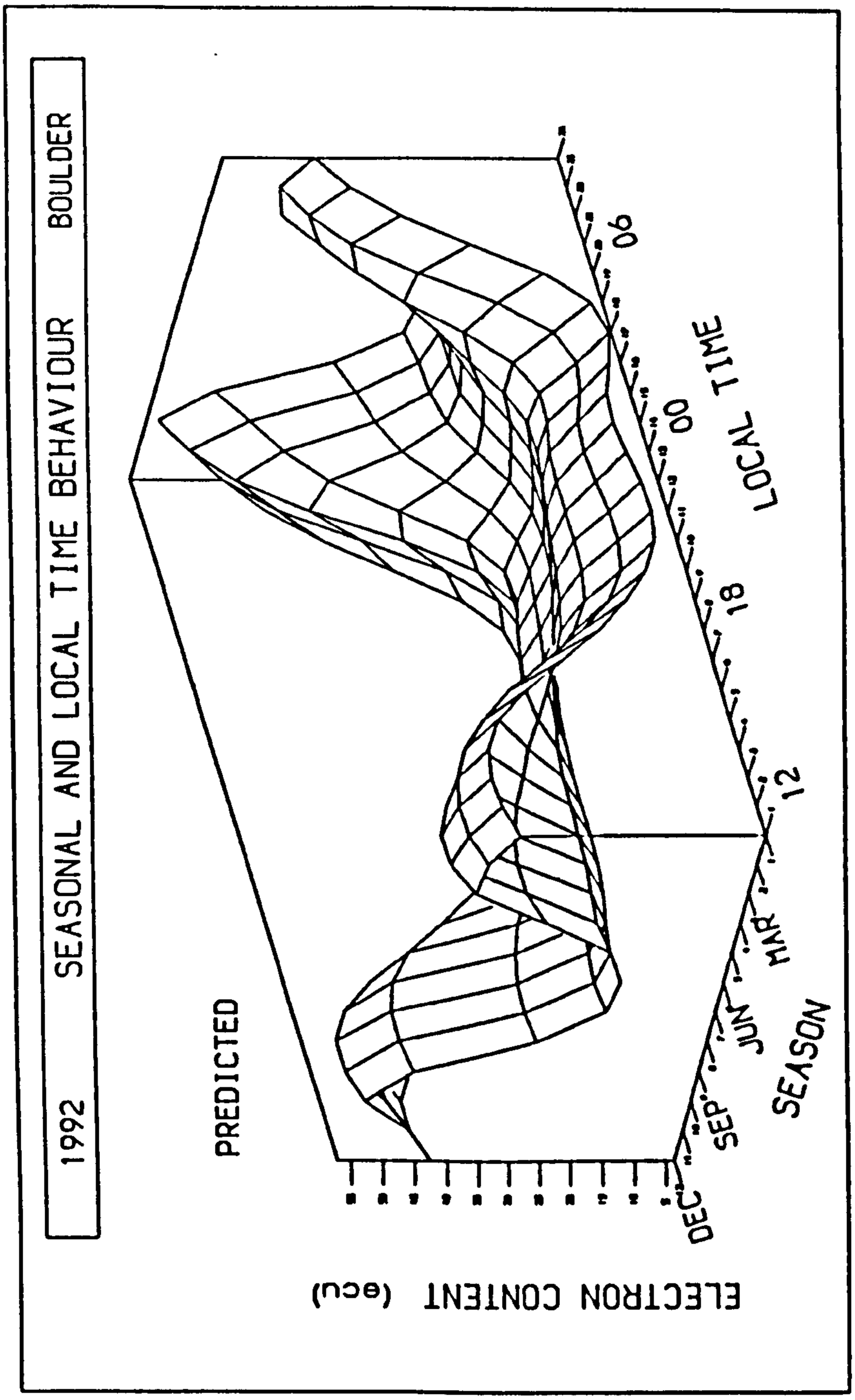

Figure 7.3 : The Local Time and seasonal variation of electron content at the Boulder site estimated from the Predictive Model for 1992.

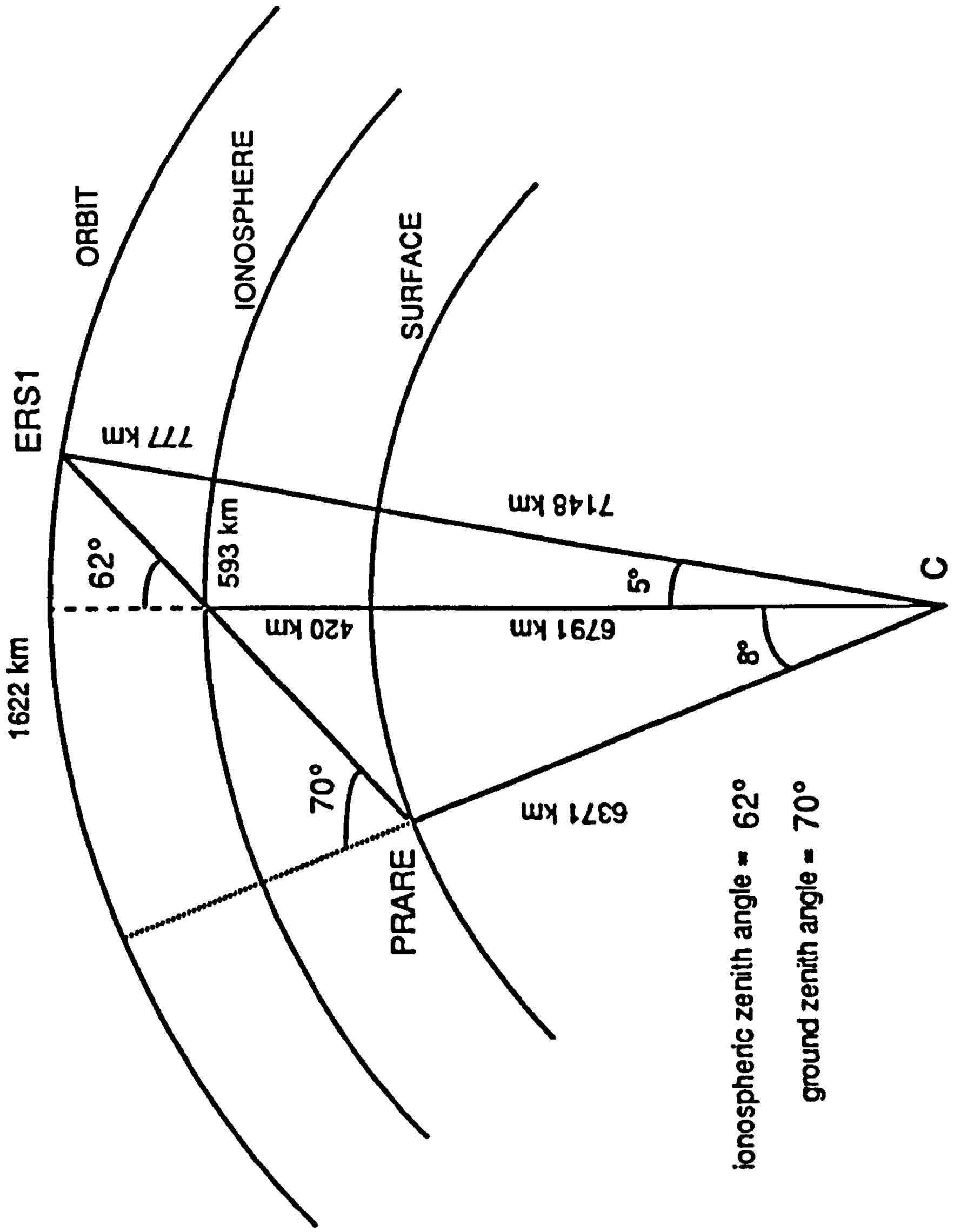

Figure 7.4 : The configuration of the PRARE-ERS1 system at its maximum ground zenith angle of 70°.

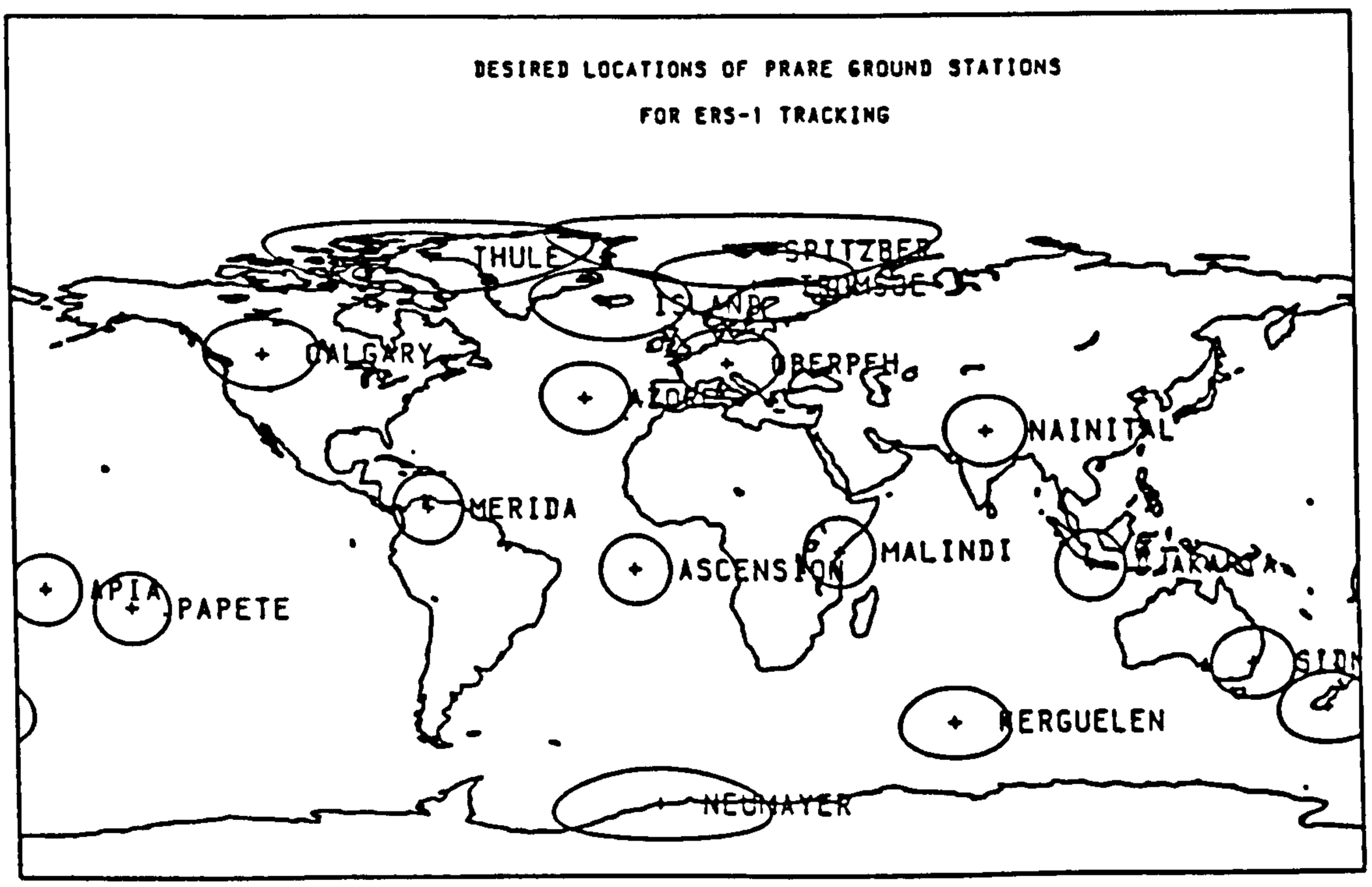

Figure 7.5 : The proposed global distribution of eighteen PRARE ground sites (after Wilmes et al 1987). Their operational horizons are also shown.

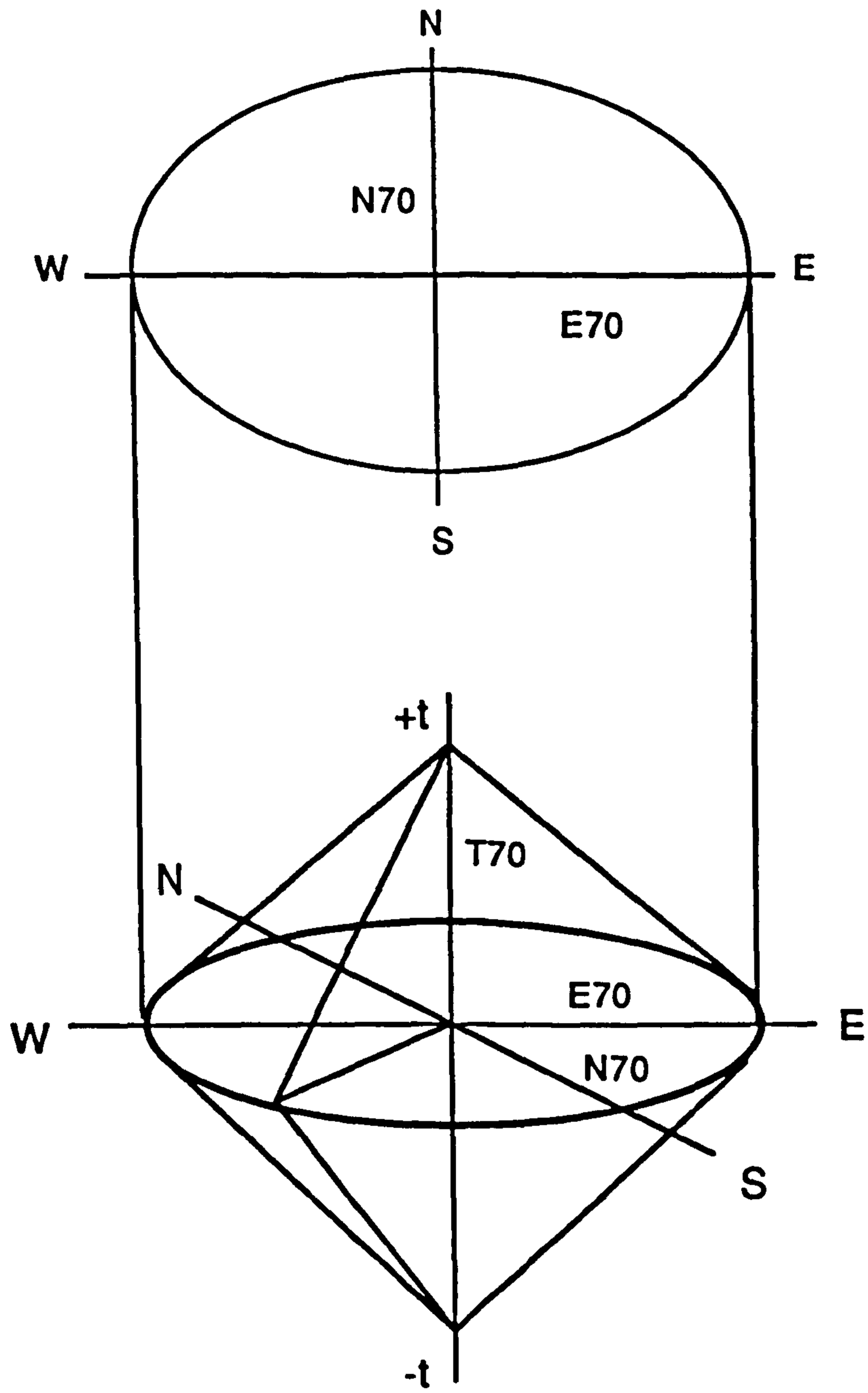

Figure 7.6 : The 0.7 isocoherent space–time surface which depicts the spatial anisotropy and the linear decorrelation of electron content.

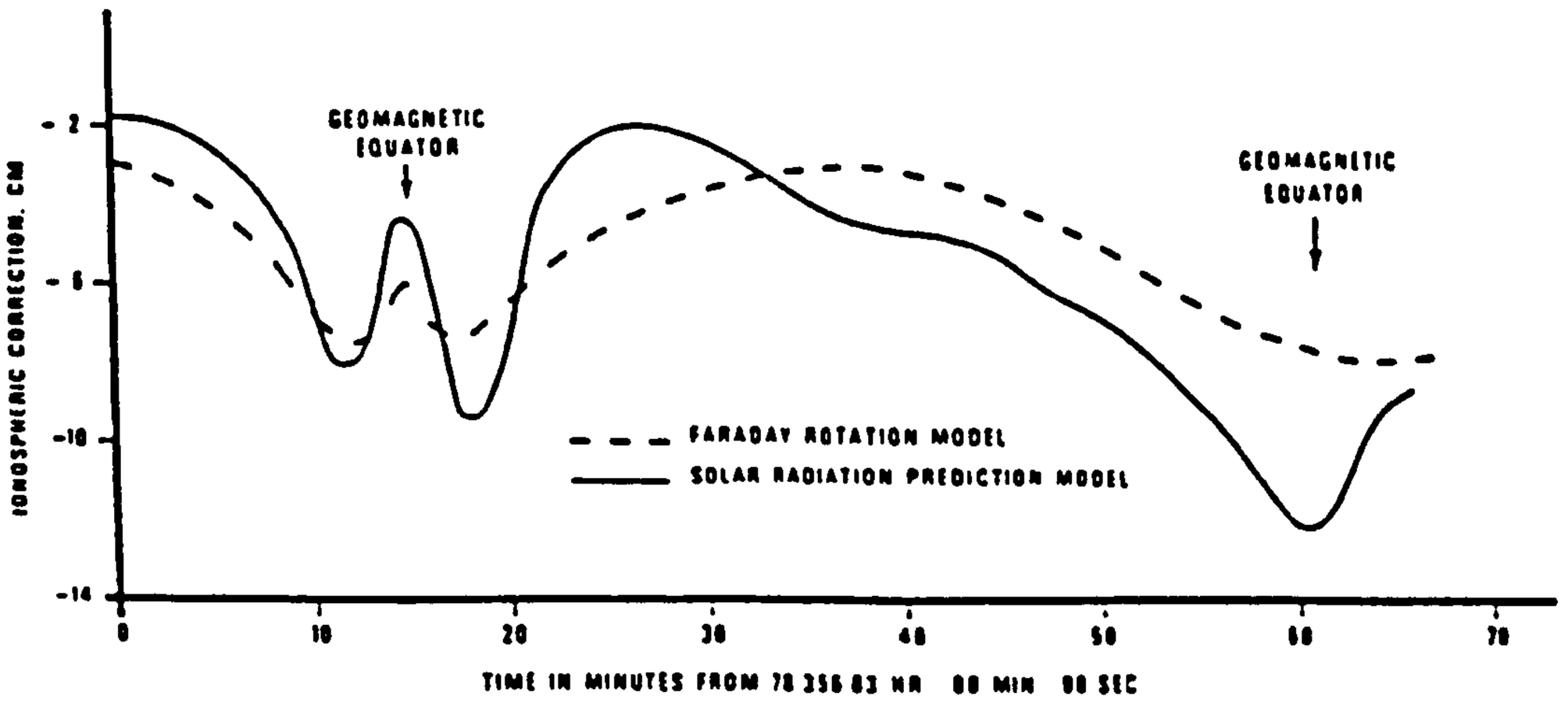

Figure 7.7 : A comparison between the JPL Model and a more complicated solar radiation model (after Lorell et al 1982).

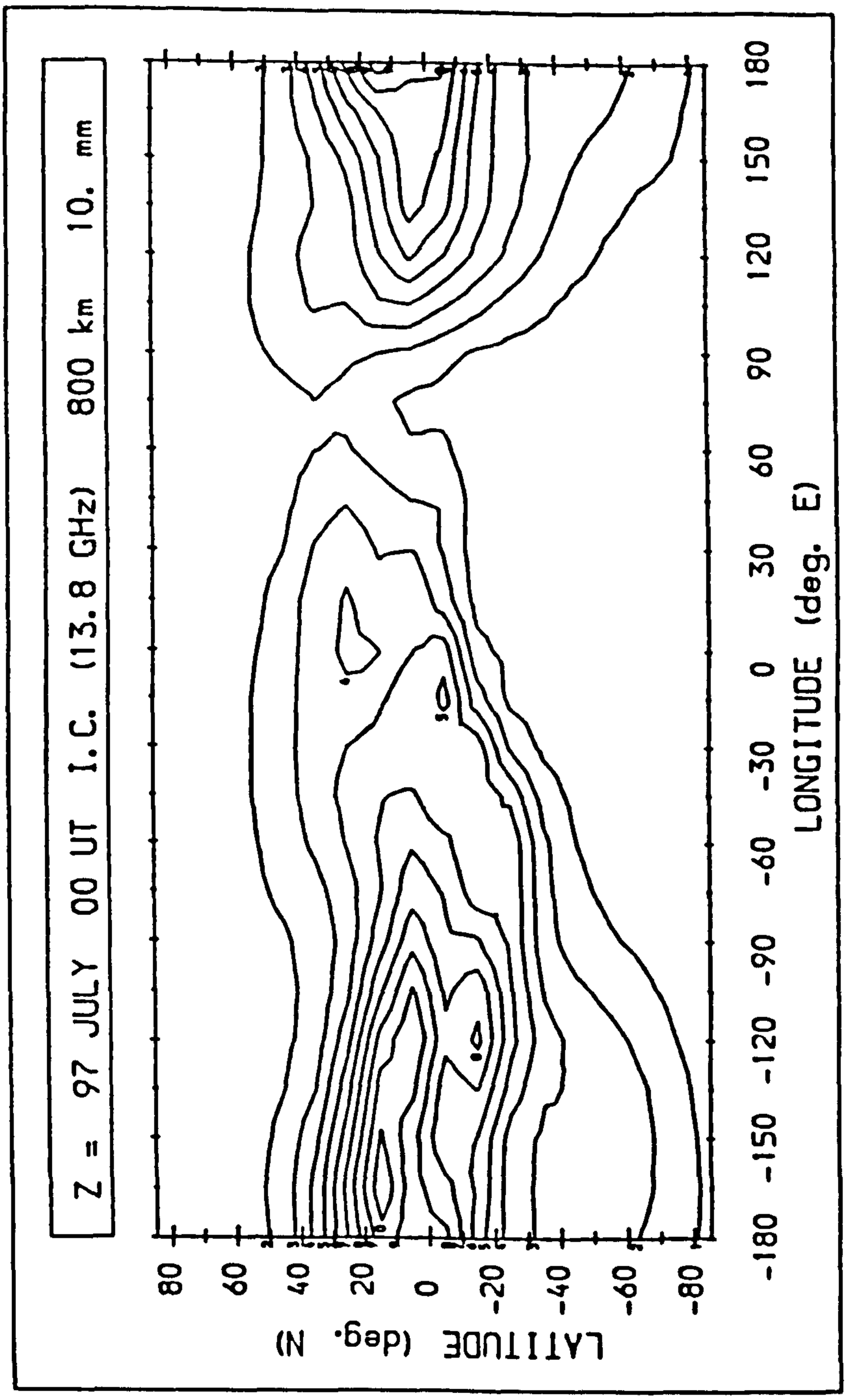

Figure 7.8 : The global morphology of ionospheric group delay correction predicted by the LEI Model for 00 UT July 1978 with an altimeter operating at 13.8 GHz at an orbit altitude of 800 km.

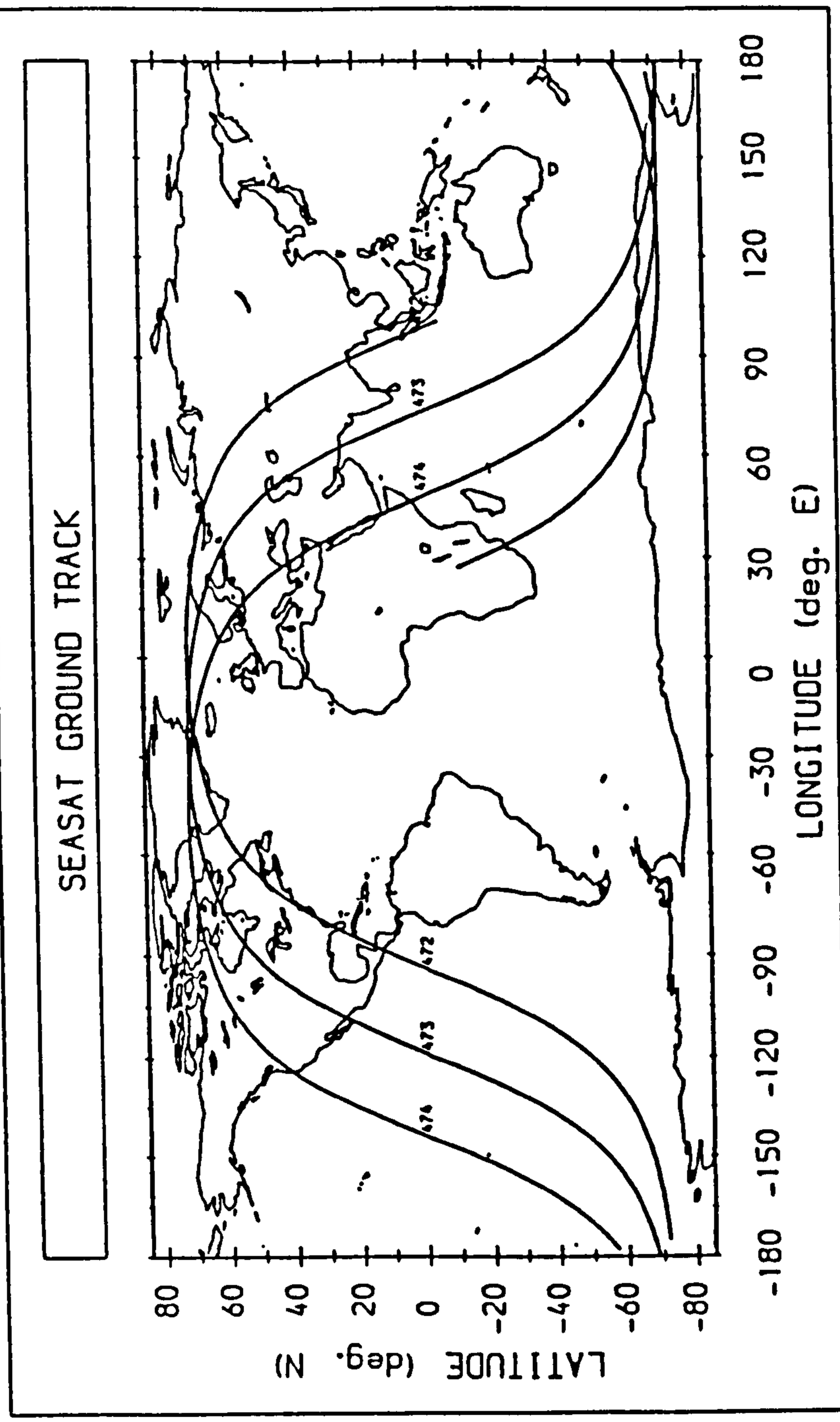

Figure 7.9 : The ground tracks of Seasat revolutions 472–474 superimposed upon a map of the world.

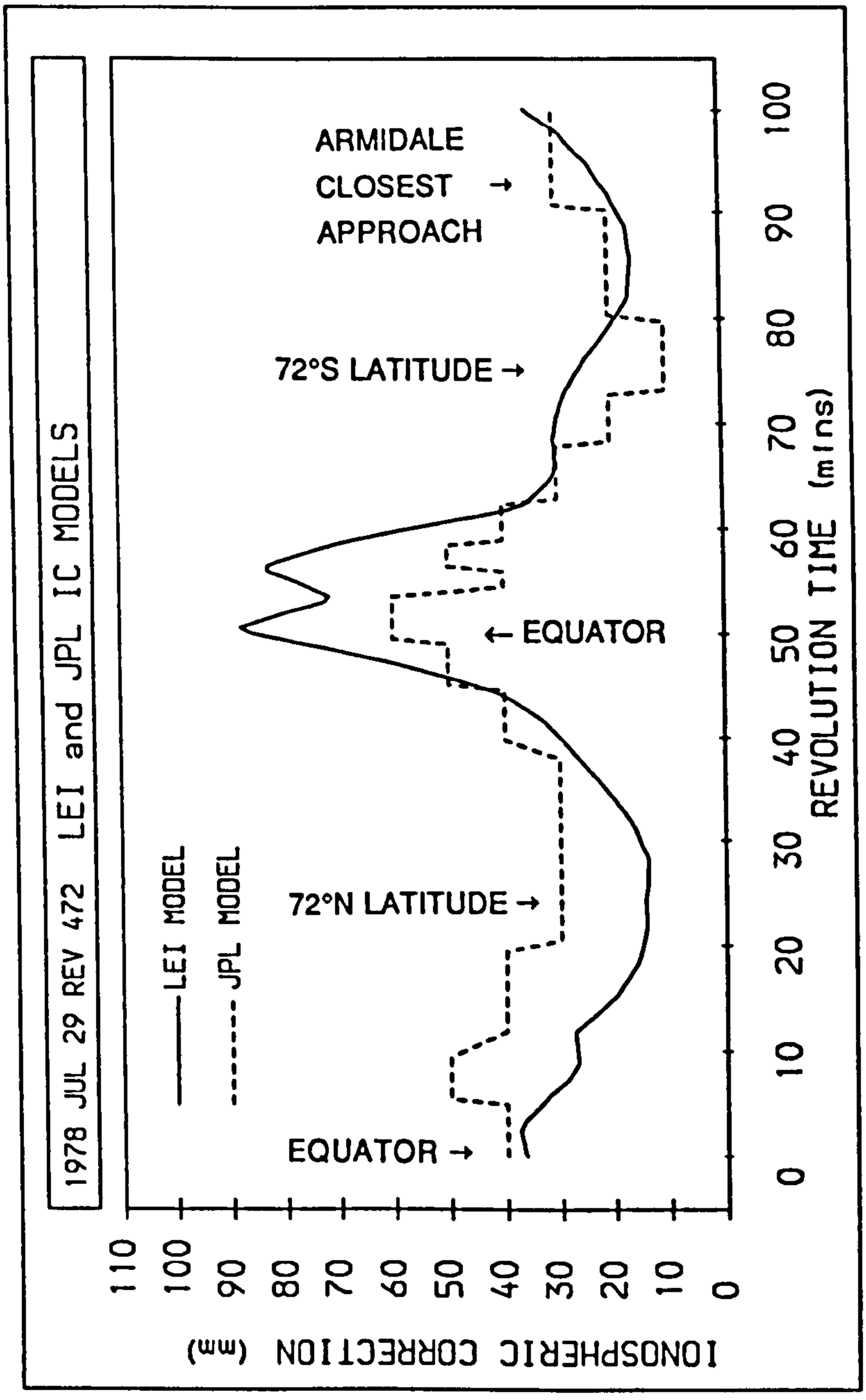

Figure 7.10 : The ionospheric correction to the Seasat altimeter as estimated from the Predictive Model for Seasat revolution 472. Also shown is the actual correction employed for the mission supplied by the JPL Model.

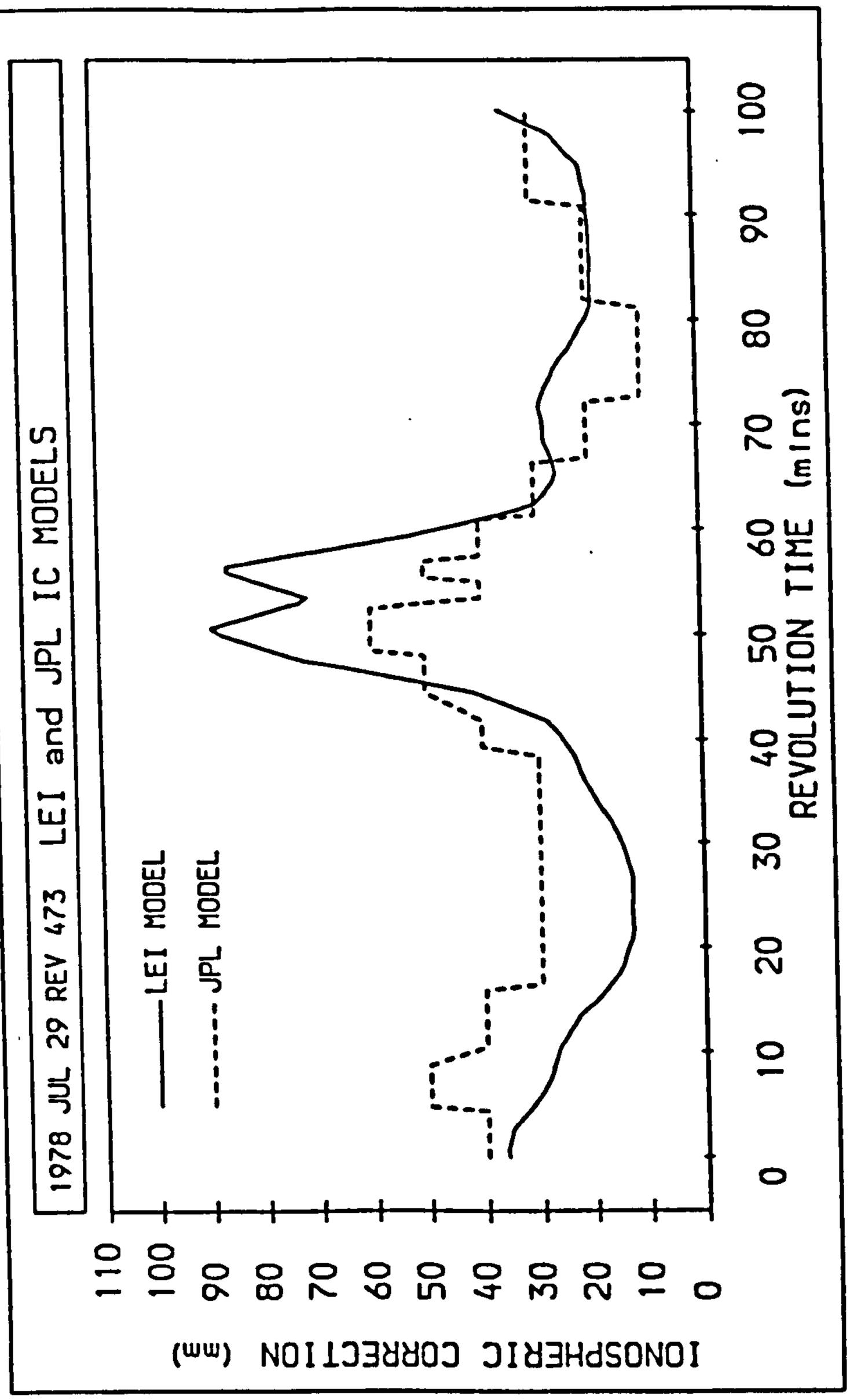

Figure 7.11 : The ionospheric correction to the Seasat altimeter as estimated from the Predictive Model for Seasat revolution 473. Also shown is the actual correction employed for the mission supplied by the JPL Model.

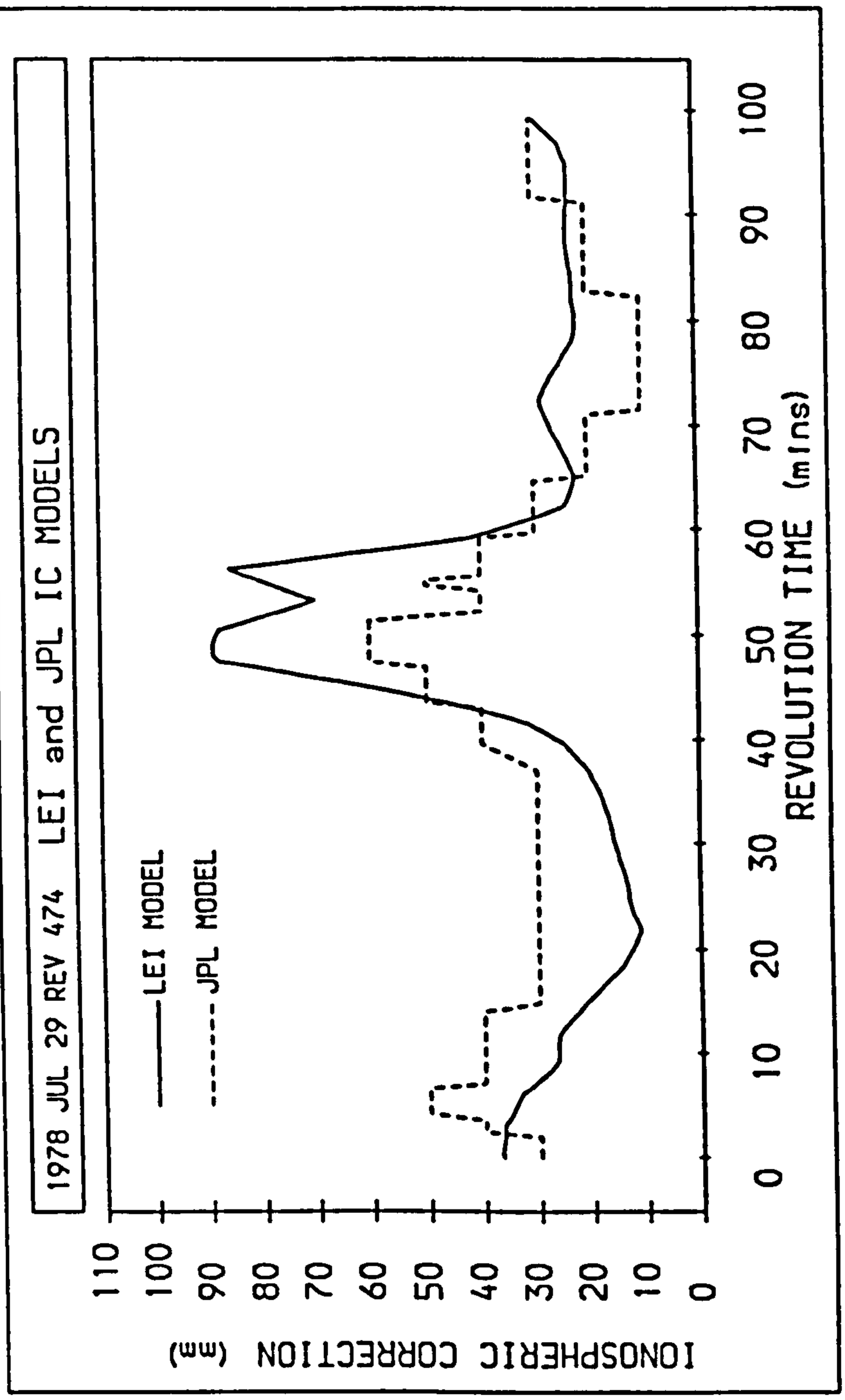

Figure 7.12 : The ionospheric correction to the Seasat altimeter as estimated from the Predictive Model for Seasat revolution 474. Also shown is the actual correction employed for the mission supplied by the JPL Model.

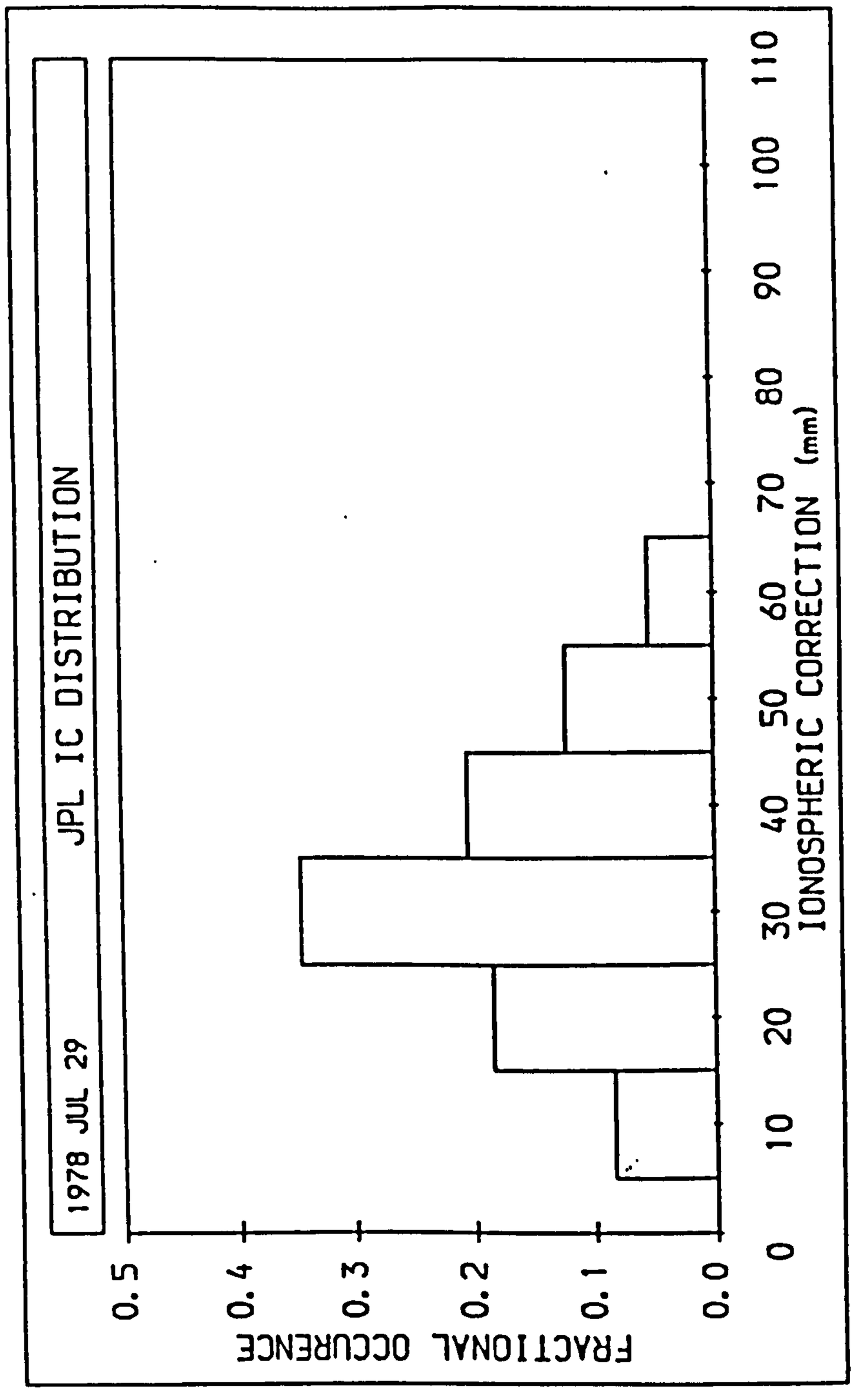

Figure 7.13 : Histogram depicting the distribution of ionospheric corrections estimated from the JPL Model over the three Seasat revolutions 472–474.

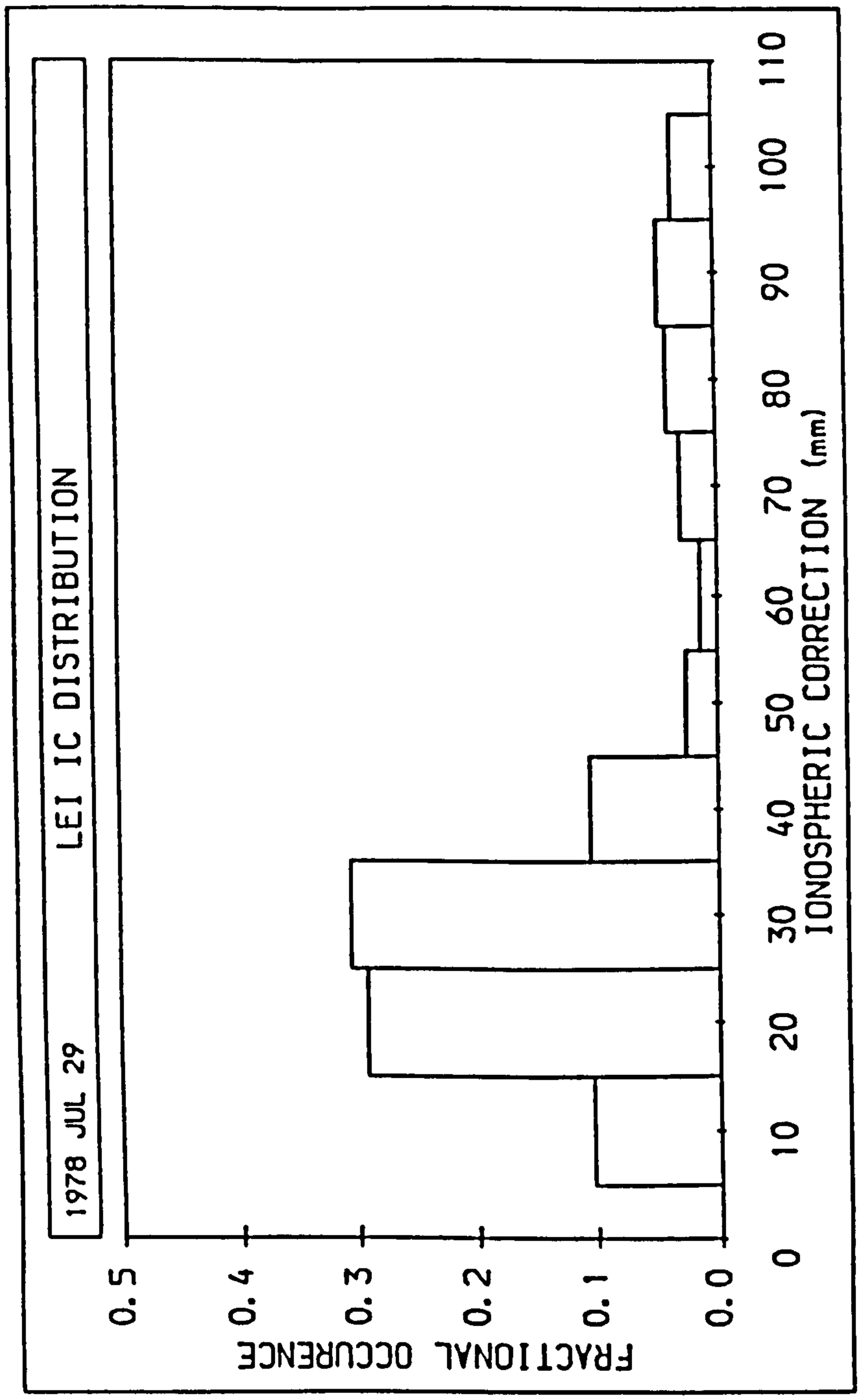

Figure 7.14 : Histogram depicting the distribution of ionospheric corrections estimated from the LEI Model over the three Seasat revolutions 472–474.

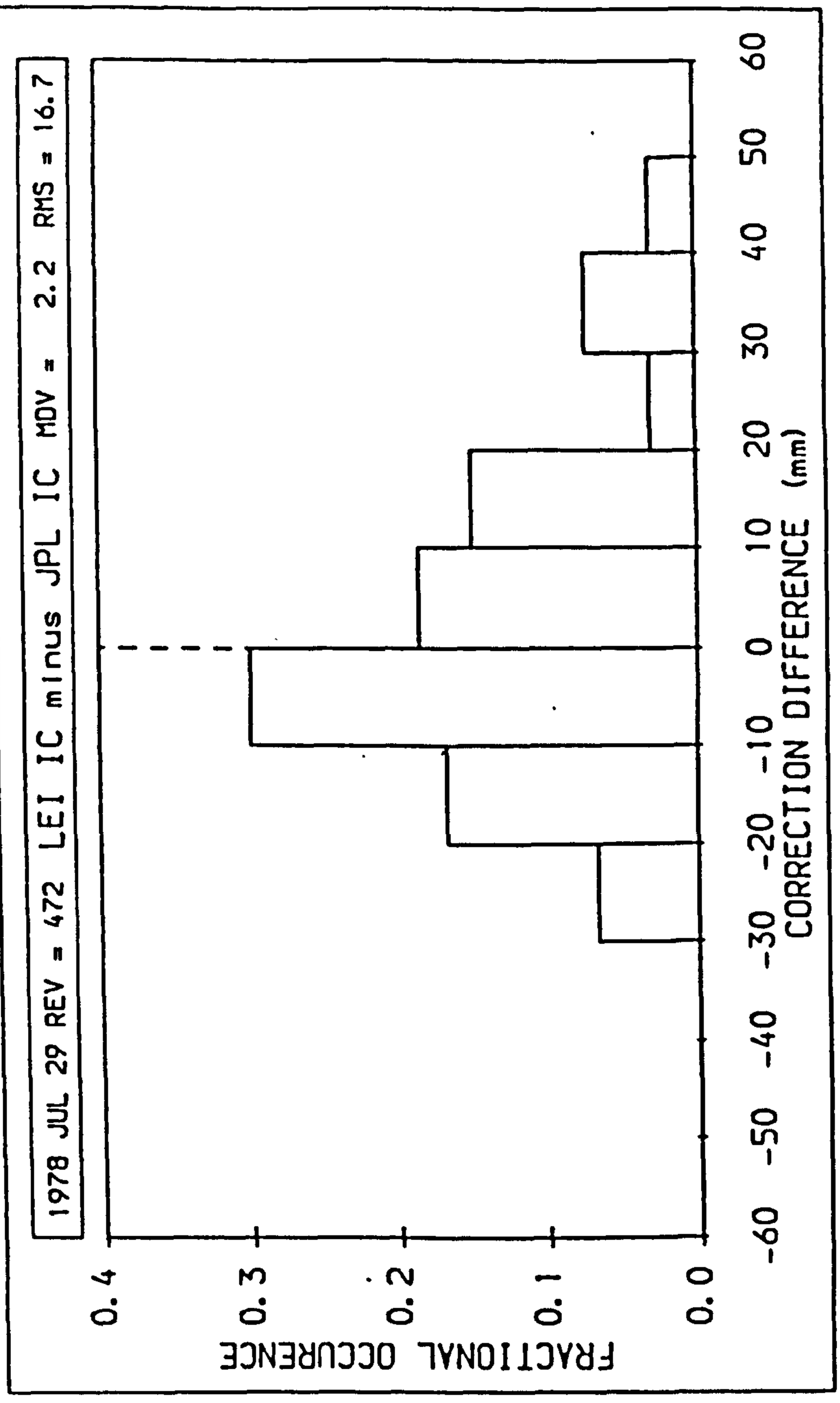

Figure 7.15 : Histogram depicting the distribution of differences between the ionospheric corrections estimated from the LEI and JPL Models over revolution 472 of the Seasat mission.

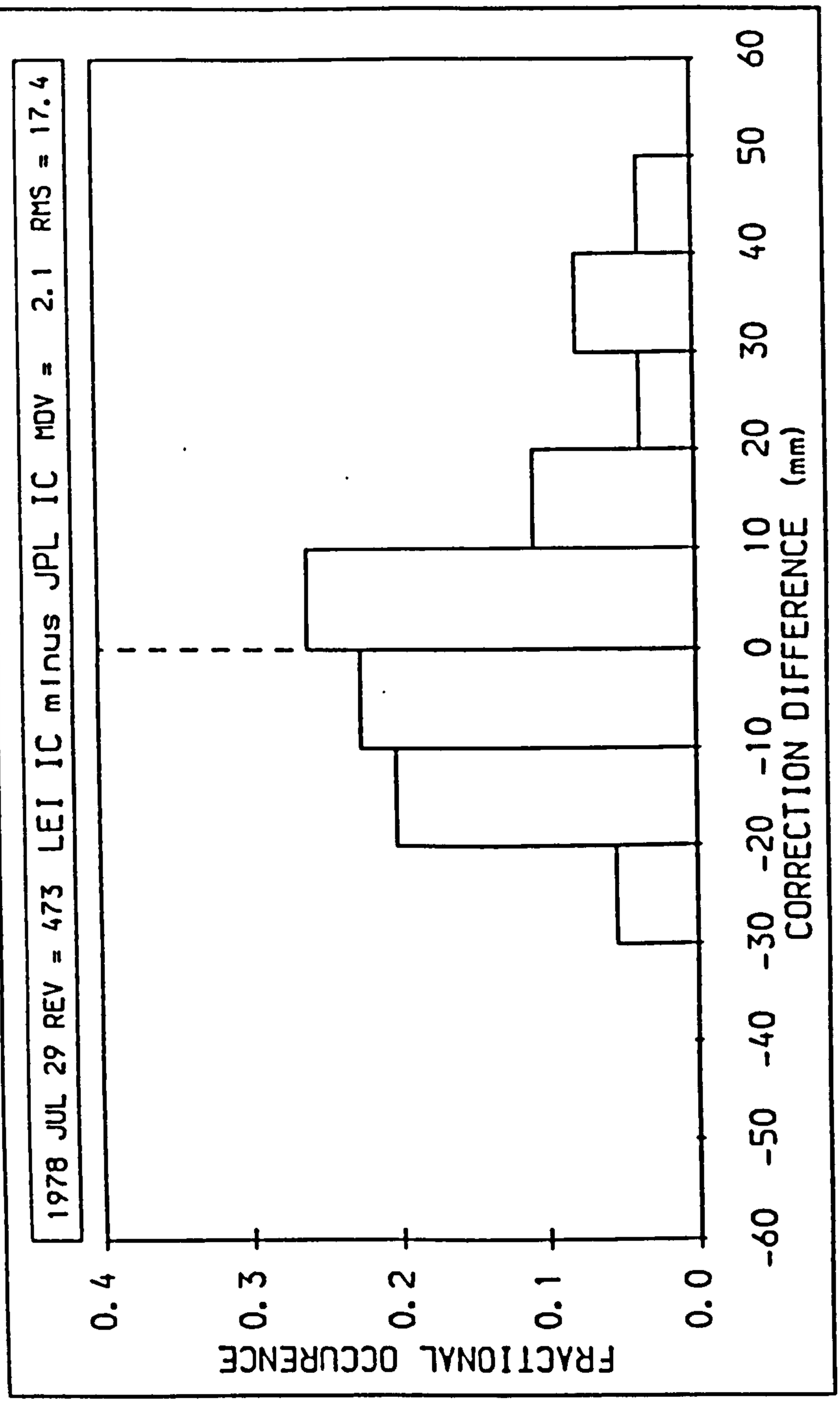

Figure 7.16 : Histogram depicting the distribution of differences between the ionospheric corrections estimated from the LEI and JPL Models over revolution 473 of the Seasat mission.

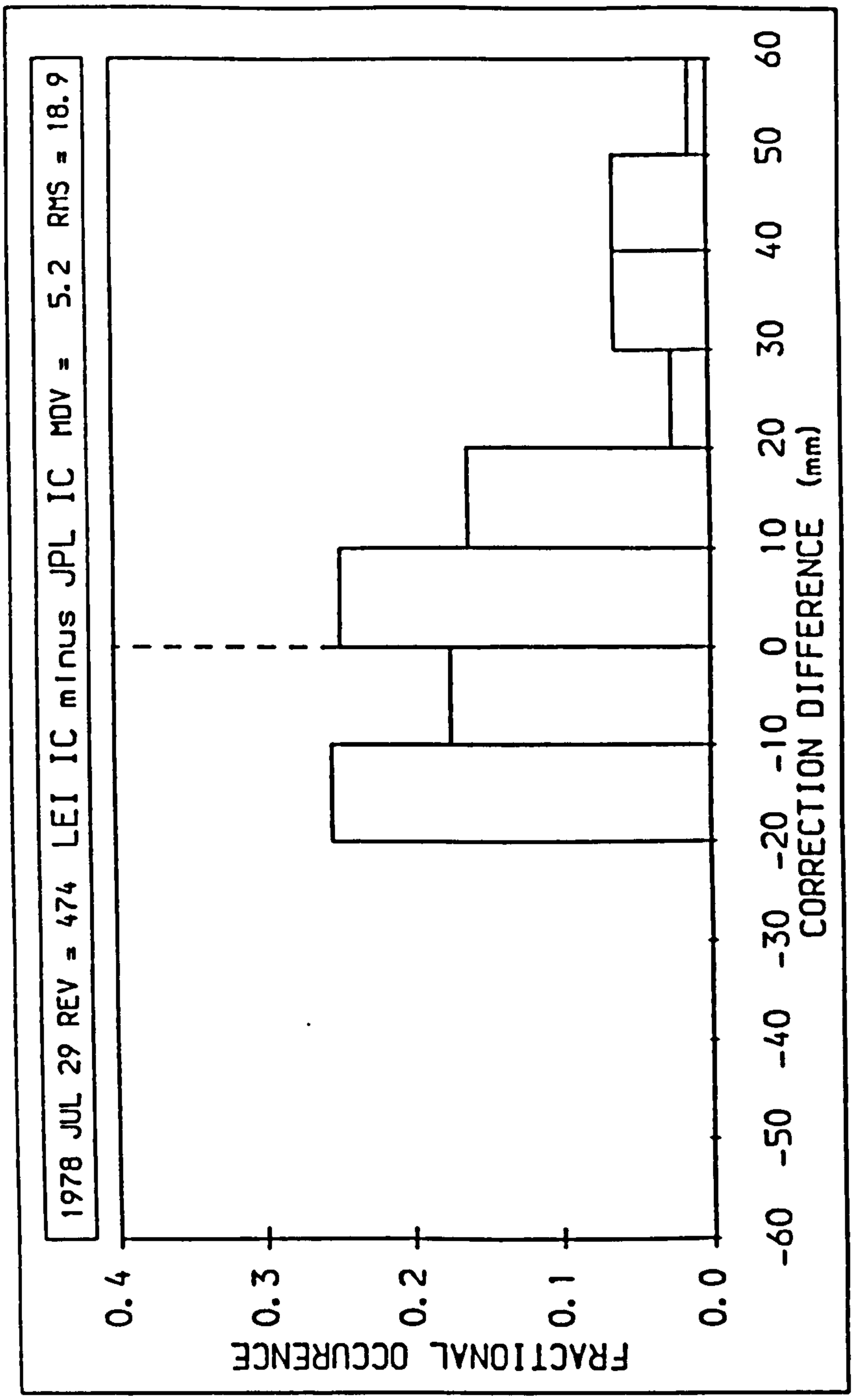

Figure 7.17 : Histogram depicting the distribution of differences between the ionospheric corrections estimated from the LEI and JPL Models over revolution 474 of the Seasat mission.

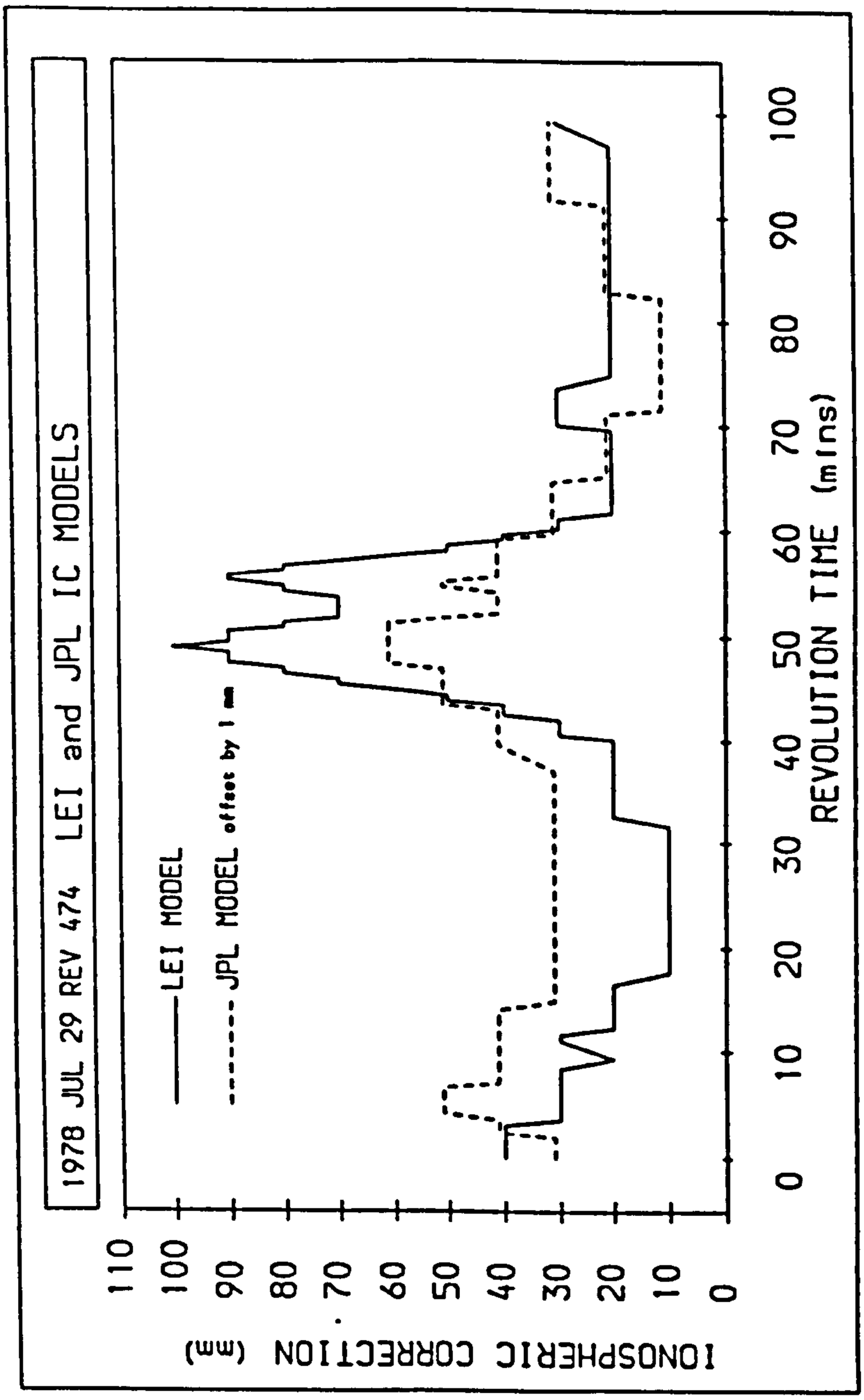

Figure 7.18 : The LEI ionospheric correction for Seasat revolution 474 rounded to the nearest 10 mm. For clarity the JPL Model corrections have been offset by 1 mm.

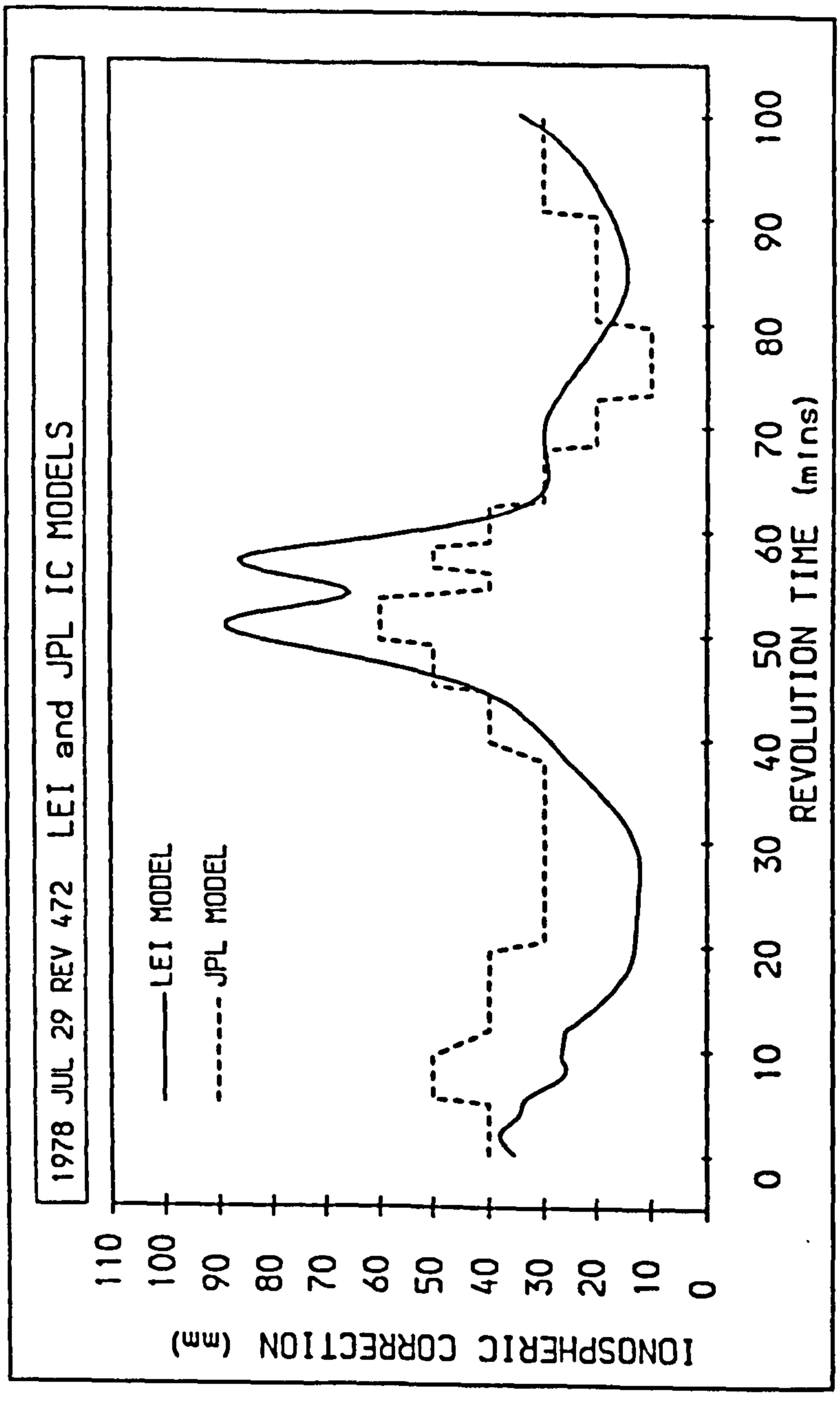

Figure 7.19 : The LEI ionospheric correction for Seasat revolution 472 derived from a version of the model with five-times the resolution of the original.

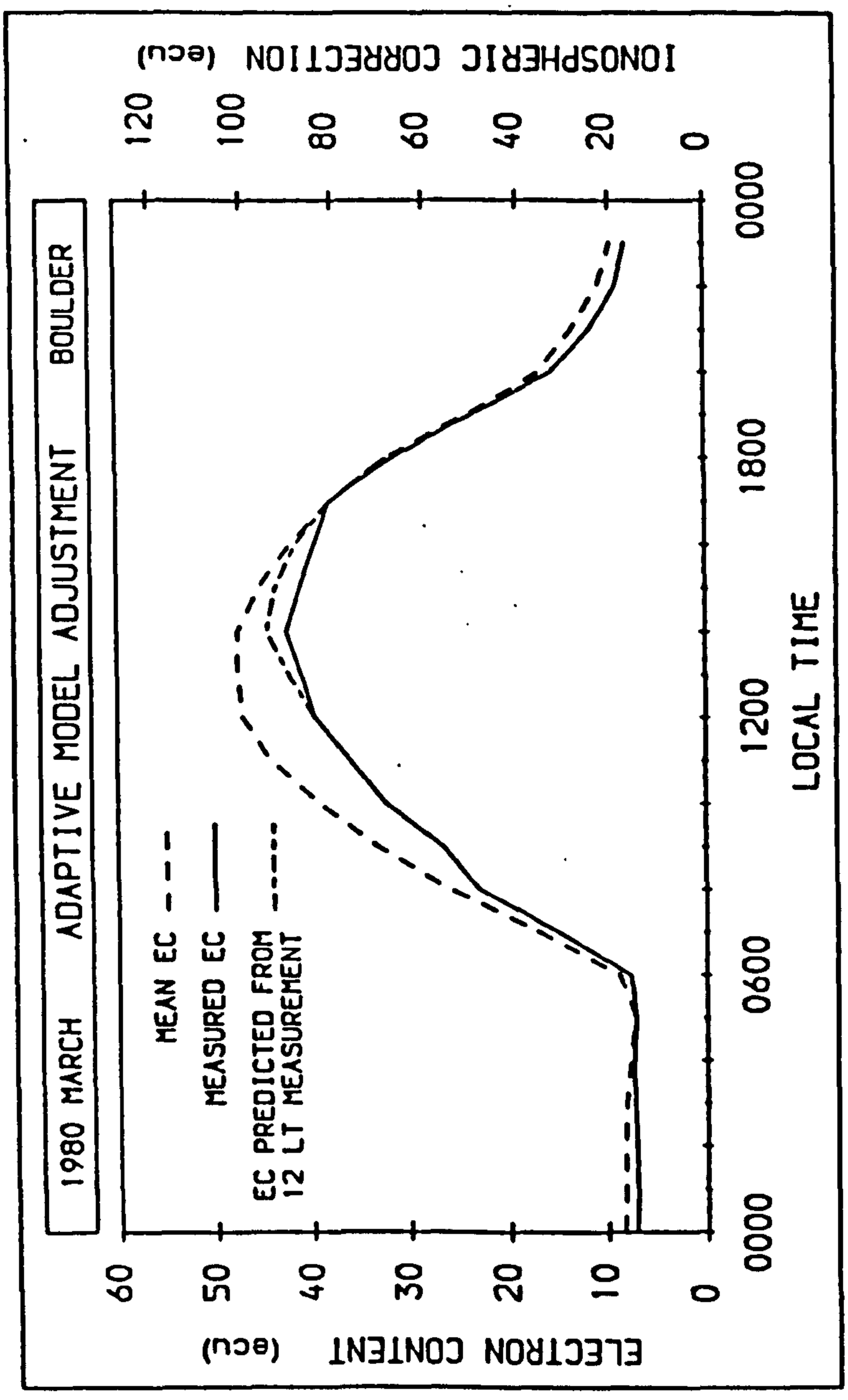

Figure 7.20 : The adaptive adjustment of monthly mean data. The monthly mean signature of March 1980 is adjusted with a measurement taken at local noon on the 12th of the month. The decay of the adjusted electron content back to the monthly mean as the time lag increases is evident.

VARIABLE	NISBET SUGGESTION	LEI PREDICTIVE MODEL
LATITUDE	17	18
LONGITUDE	36	24
TIME	24	24
SEASON	6	12
GEOMAGNETIC ACTIVITY	3	1
SOLAR ACTIVITY	5	5
TOTAL	91	84

Table 7.1 : Number of increments of the LEI Predictive Model input variables compared with the number suggested by Nisbet (1975).

LEI MODEL vs. JPL MODEL STATISTICS

REVOLUTION NUMBER	472	473	474
MEAN DEVIATION (mm)	+2.2	+2.1	+5.2
STANDARD DEVIATION (mm)	16.7	17.4	18.9

Table 7.2 : The mean deviation and standard deviation statistics between ionospheric corrections calculated from the LEI Model and JPL Model the over three revolutions 472–474 inclusive.

Chapter 8 : Conclusion

This final chapter seeks to evaluate the work presented in the previous chapters and makes suggestions for future work.

8.1 Critical Evaluation of the Modelling Technique

The limitations of the LEI Model are manifold and should be borne in mind when employing the model to generate altimetric corrections. These limitations inevitably lead to a reduction in the accuracy of the output from the model and, consequently, are more important in a situation where an ionospheric correction is required to a trans–ionospheric transmission in the VHF or UHF bands. For example, for a 400 MHz radar pulse a 20% uncertainty in an electron content prediction of 100 ecu would lead to a range correction uncertainty of over 60 m. The shortcomings of the model can be classified as to whether they are associated with the predictive or the adaptive elements of the algorithm.

The principal weakness of the Predictive Model is that it was only validated with electron content data for the mid– and low–latitude northern hemisphere. All empirical models are limited primarily by the data base which went into their construction. The absence of any high–latitude electron content data and the complete lack of any data from the southern hemisphere must lead to some uncertainty as to the accuracy of the Predictive Model in these regions. The station which provided calibration data from the highest invariant latitude was Goose Bay at $L = 3.8$, whereas $L = 4.0$ is usually taken as the value arbitrarily dividing mid– and high–latitudes. One mitigating factor is that, at least on a monthly mean basis, the electron content is strongly influenced by the maximum electron density and the CCIR technique for calculating this was validated for the southern hemisphere (Wakai and Matuura 1980). Though this still does not confer any confidence in model accuracy in the high–latitude regions of either hemisphere.

The Predictive Model generated a set of numerical maps of electron content which constituted the foundation of the LEI Model. A set of global neutral atmosphere scale height look–up tables were employed in the generation of these numerical maps to scale vertically the Chapman profile

before the electron content was calculated by height integration. This set of scale height look–up tables was generated for equinoctial conditions and did not allow for any seasonal variation which may have caused problems for the prediction of electron content for the summer and winter seasons. From the results listed in Tables 5.10 and 5.11, though, this does not seem to be a major problem.

The altimeter will measure the mean ocean range at a rate of 1 Hz which corresponds to an along–track distance of 6.6 km (or approximately 0.06° of latitude), a spatial scale much less than that of the numerical maps of electron content. The global maps of electron content stored in the look–up tables had a spatial resolution of 10° in latitude by 15° in longitude. The Nyquist Sampling Theorem states that in this case only spatial features of electron content with a scale size greater than 20° x 30° can be resolved. On a monthly mean basis this essentially restricts the model to the reproduction of large–scale electron content gradients such as the Equatorial Anomaly and the Terminator boundary.

The Adaptive Model also has limitations. The first arises from the assumption that the ratio of the standard deviations of electron content at the measurement and adjustment points is unity. This may not be valid under all circumstances, even though it need only be true within one Coherence Distance. Assuming that the spatial variation of the standard deviation of electron content is a purely latitudinal effect Figure 3.12 and Figures 3.22 to 3.24 can give an indication of the standard deviations in four latitude bands. The standard deviations at Goose Bay, Boulder and Patrick, covering a latitude range between 26°N and 48°N, are all broadly similar. The Palehua site at 20°N, though, has standard deviations approximately four times those found at the Patrick site which is separated in latitude by approximately half the North–South Coherence Distance. This difference may be due to the difference in magnetic latitude of the two sites, Palehua being at 20°MN and Patrick at 37°MN, placing the Palehua in the highly variable Equatorial Anomaly region and Patrick in the more quiescent mid–latitudes. Clearly if a measurement of electron content were made in the mid–latitude region and were used to adjust the mean prediction at a point inside the coherence horizon, but in the Equatorial Anomaly region, the assumption of a ratio of standard deviation of unity could result in an underestimate of the adjustment by a factor of four. This is a drawback which should be borne in mind if any PRARE ranging sites are located in such a position to make this situation possible.

Some difficulties are associated with the necessity for an independent source of electron content data. An ideal source would provide worldwide electron content with a spatial resolution on the scale of the coherence horizon. Such a system would be prohibitively expensive and would

prove difficult to install over the oceans. Though the final number of PRARE sites is still unknown a figure of eighteen has been suggested as a minimum requirement (Wilmes et al 1987). Although this number may be sufficient for tracking purposes, the coverage is inadequate to supply a continuous stream of electron content data to the Adaptive Model and some thought should be given to an alternative source of data. One possible source is the Navstar Global Positioning System (GPS) a proposed constellation of eighteen navigation satellites each equipped with multi–frequency radio beacons (Yunck et al 1985). The differential group delay on any two frequencies will allow calculation of the line–of–sight electron content. The continuous global coverage of the constellation makes GPS a promising electron content data source.

One final cautionary note was sounded by McNamara and Wilkinson (1984) on the very principle of adaptive adjustment. It was argued that the strength of coherence is greatest for a disturbed ionosphere and that such times contribute to the coherence of electron content to an extent out of proportion to their duration. On more quiescent days the correlation coefficient was proposed to be much smaller than during disturbed times. The consequence of this was thought to be that the adaptive technique provides an adequate adjustment during disturbed times, but offers no great improvement of prediction accuracy during quieter times.

This opinion was supported by Milsom (1984), who suggested that the decorrelation of ionospheric parameters has two phases; one due to 'quiet–time' behaviour and the other due to 'disturbed–time' behaviour. It was argued that F2–region parameters decorrelate rapidly over the first few minutes due to the transient variations present on quiet days, but on disturbed days the coherence remains high because of the persistent deviation of the parameter from its mean level.

The achievements of the modelling technique can be summarized as the calibration and validation of a Predictive and Adaptive Model of ionospheric electron content. This was achieved with 664 station months of electron content data, measured at ten northern hemisphere sites by the Faraday rotation method and through a successful comparison with the results of a model developed at JPL under the simulated conditions of the ERS1 altimeter mission.

8.2 Suggestions for Future Work

The suggestions for future work can, again, be conveniently divided into those related to predictive and those related to adaptive electron content modelling. Most of the

recommendations for further development of the model stem from the criticisms outlined in the previous section.

It is recognized that as a consequence of the high variability of the F2–region it is difficult to extrapolate measurements of foF2 from one point to another with the same degree of accuracy as is possible with, for example, the more regular critical frequency of the E–region. The numerical maps of F2–region peak parameters are, then, the greatest potential source of error in empirical models of the ionosphere; the Predictive Model being a typical example of such a model. Over inaccessible area such as the oceans, therefore, the accuracy of the maps deteriorates.

A new version of the coefficients for the CCIR numerical maps of foF2 and M(3000)F2 will soon be available which provides improvements over the previous versions by the application of a novel data extrapolation technique. The extrapolation method has been described by Rush et al (1983) and involves the use of a theoretical ionospheric model to calculate values of foF2 over the oceans from boundary conditions measured by ionosonde. The theoretical values and measured data were then both reduced into the tables of coefficients for the generation of global maps of foF2. It is hoped that the new coefficient tables will return more accurate values of foF2 over the oceans, which cover wide areas particularly of the southern hemisphere, and so should be ideally suited to a model dedicated to ionospheric correction of ocean remote sensing data.

The CCIR Model does not claim to be accurate in the high–latitude regions of the ionosphere since the short time scale variability and small scale structure make this region particularly difficult to model. Nevertheless, it is necessary for the Predictive Model to return accurate values in this region since the inclination of Earth surveillance satellite orbits take them to these high–latitudes. One of the principal structures of the high–latitude ionosphere is the Main Trough which occurs for 98% of the hours of darkness. The model of Halcrow and Nisbet (1977) can adjust the CCIR Model predictions to allow for the abnormally low F2–region peak electron densities of the Main Trough and, hence, improve the scaling of the theoretical ionospheric profile in this region. This feature should be incorporated in the LEI Model.

The long term prediction of ionospheric parameters is usually based upon their strong correlations with the smoothed sunspot number; the sunspot number being a qualitative measure of the strength of solar radiations in the ionizing frequency bands. This holds good over a wide range of solar conditions, but saturation occurs for very high levels of solar activity as evidenced by Figure 3.5 and Figures 3.14 to 3.16. It would be preferable, therefore, to have the strength of euv radiation as a direct input to a prediction scheme for ionospheric parameters since it is these

radiations which are responsible for the production of atmospheric plasma. With euv data available from satellite observatories such as the Atmospheric Explorer series this is now feasible. Lakshmi et al (1988) recommended the use of euv data for forecasting purposes since plots of foF2 against euv fluxes gave a more linear relation than against smoothed sunspot numbers.

Further improvement in the accuracy of the Predictive Model could be gained from the use of a more accurate neutral atmosphere model to replace the Jacchia Thermospheric Model in the calculation of scale height numerical maps. A candidate model for this task is the MSIS–86 Thermospheric Model (Mass Spectrometer Incoherent Scatter Model) described by Hedin (1987). Unlike the previous implementation, the MSIS–86 Model should admit a seasonal variation into the global maps of scale height, rather than just mapping the scale height under equinoctial conditions.

The lack of calibration sites in the southern hemisphere for the Predictive Model is considered to be a serious weakness in the constitution of the model. A definite improvement in confidence, if not necessarily in accuracy, stands to be gained from validation of the Predictive Model with southern hemisphere electron content data. Similarly the extent of the comparison with the JPL Model should be expanded to cover at least one complete 24 hour period in order to increase the temporal sampling of the LEI Model.

One final area which may lead to an improvement in the accuracy of the estimates returned by the Predictive Model is in the shape of the theoretical ionospheric profile. The total electron content of a Chapman profile is determined uniquely by the electron density and atmospheric scale height at the peak altitude and is scaled by an integration factor representative of the mathematical description of the profile. For an α–Chapman profile the integration factor as given in Equation 4.12 is $(2\pi e)^{1/2}$. A modified Chapman profile is described by Equation 8.1 for which the integration factor takes the more general form given in Equation 8.2.

$$N = N_0 \ \mathrm{EXP}\left(a(1 - z - e^{-z}) \right) \tag{8.1}$$

$$E = N_0 H_0 \ \frac{\mathrm{EXP}(a)}{a^a} \ \Gamma(a) \tag{8.2}$$

Γ = the Gamma function a = modification parameter

For the special case of a = 0.5 corresponding to the α–Chapman profile the integration factor reduces to $(2\pi e)^{1/2}$. The modification parameter would provide an extra dimension of flexibility for fitting Equation 8.2 to electron content data which could be particularly beneficial in low–latitude

regions. Figure 8.1 illustrates the fractional increase of total electron content of the Chapman profile as a function of the modification parameter. The classical α–Chapman profile is given by a = 0.5 and provides the reference level for the diagram. Values of the modification parameter greater than 0.5 result in lower electron content, for example a Chapman profile with a modification parameter of 0.7 has approximately 81% of the total electron content of the α–Chapman profile. Conversely, values of the modification parameter less than 0.5 result in greater electron content, for example a modification parameter of 0.42 gives an approximate 10% increase of total electron content. Studies incorporating unambiguous electron density profiles derived from incoherent scatter radar measurements would be especially useful for determining patterns in the electron density profile shape and, hence, in calculating suitable values of the modification parameter.

Future work on the adaptive element of the model should concentrate on an attempt to prove or refute the claim of McNamara and Wilkinson (1984) that the adaptive procedure is unreliable for quiescent ionospheric conditions. This could be achieved through a study of electron content coherence under quiet and disturbed conditions. If, indeed, there is seen to be a significant and consistent reduction in coherence for quiet times then the Faraday rotation data should be divided into quiet and disturbed data and a set of coherence functions calculated from each of the two. Incorporation of such a procedure into the model would need some measure of the state of the ionosphere as a further input. A geomagnetic index is probably not a suitable candidate for a disturbance indicator, since the work described previously demonstrated the lack of correlation between three daily geomagnetic indices and the Coherence Time.

The post–ERS1 generation of radar altimeters are designed to be dual–frequency instruments. This means that the altimeters themselves will have the capability to mitigate atmospheric delays to a much greater accuracy than is possible with any model. The ionospheric correction to the altitude measured on the upper frequency is given by Equations 8.3 and 8.4.

$$\varepsilon_1 = \frac{f_2^2}{f_1^2 - f_2^2} c\,\Delta t \qquad (8.3)$$

$$\Delta t = t_2 - t_1 \qquad (8.4)$$

c = free space light speed

f_1 = upper altimeter frequency $\quad f_2$ = lower altimeter frequency

t_1 = return time of upper frequency pulse $\quad t_2$ = return time of lower frequency pulse

ε_1 = ionospheric correction to altitude measured by the upper frequency

For SHF altimetry the self–compensation capability requires a differential measurement to sub–nanosecond accuracy, especially if the two frequencies are closely spaced (Rush 1979). Previously this limitation, and the increased complexity and noise of the transmitter/receiver system and concurrent reduced reliability of the instrumentation, have discouraged the dual–frequency option. The configuration, though, will be implemented on the NASA–CNES joint TOPEX/Poseidon mission with frequencies of 5.3 GHz and 13.6 GHz (Chase et al 1987).

To achieve the 20 mm accuracy required by the TOPEX/Poseidon project an altimeter operating on these two frequencies through a sub–altimeter electron content of 100 ecu must be able to measure the return times to better than 0.07 ns. The 20 mm accuracy could never be achieved by a predictive empirical model because it is similar to the magnitude of electron content standard deviations. A secondary benefit of a dual–frequency altimeter system is its use as an electron content monitoring device, the inverse of the problem discussed in this thesis. The near–global coverage of a high inclination satellite altimeter and the planned long duration of altimeter missions would make the dual–frequency altimeter a valuable source of ionospheric electron content data.

8.3 Concluding Remarks

The research presented in this thesis has covered the development of a computer model to provide ionospheric group delay corrections to satellite radar altimeter systems. Initially this involved the study of mean and disturbed electron content behaviour and the calculation of spatial and temporal coherence functions. A brief investigation was made into the effect of geomagnetic activity on Coherence Time. Sub–models of the ionosphere including theoretical altitude profiles of electron density, the CCIR numerical maps of peak parameters and the Jacchia Model of the Thermosphere were combined into a Predictive Model of monthly mean electron content. The Adaptive Model was then outlined which allowed the incorporation of measured electron content data with the aim of improving the accuracy of the estimates of the Predictive Model. Both the Predictive and the Adaptive Models were validated independently. Finally the ionospheric correction model developed by the Jet Propulsion Laboratory for the Seasat mission was compared with the Predictive Model in a simulation of the ERS1 mission.

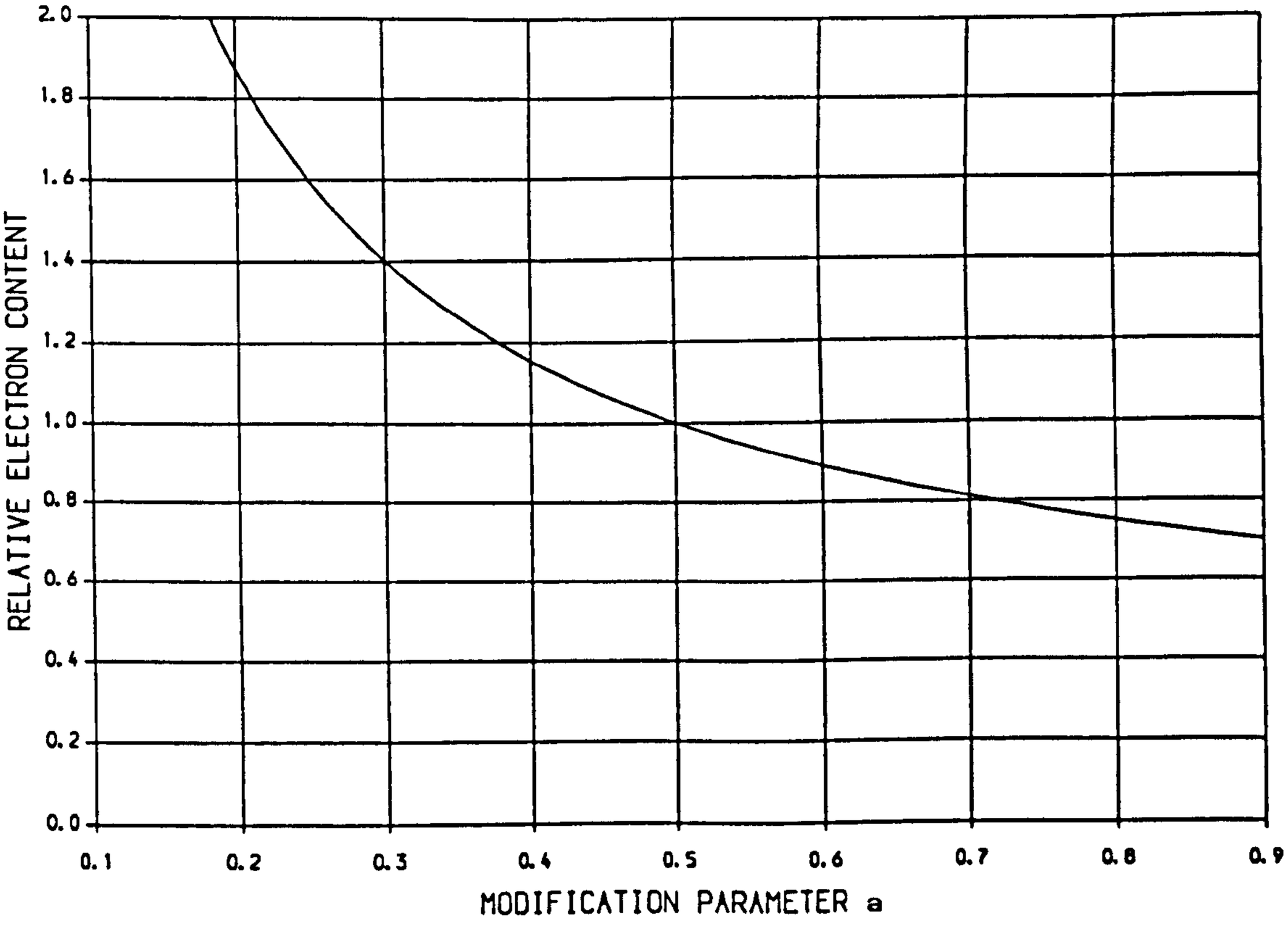

Figure 8.1 : The total electron content of a modified Chapman profile relative to that of an α–Chapman profile as a function of the modification parameter.

Appendix A : The Jacchia Thermospheric Model

The Jacchia Thermospheric Model (Jacchia 1965) considers a five component atmosphere in diffusive equilibrium. The model, which was developed initially for satellite–drag studies, requires Local Time, day number, geomagnetic activity, solar activity and geographic location as inputs.

The composition sub–model takes as its foundation an invariant set of boundary conditions at an altitude of 120 km for the temperature and the partial densities of Helium, molecular Nitrogen and atomic and molecular Oxygen. The 120 km boundary conditions are listed in Table A.1. The fifth component, Hydrogen, does not come into diffusive equilibrium until 500 km and is only then included in the calculations, its density there being calculated from the asymptotic exospheric temperature with Equation A.1.

$$LOG_{10}(n(H)_{500}) = 73.1 - 39.4\, LOG_{10}(T_\infty) + 5.5\, (LOG_{10}(T_\infty))^2 \qquad (A.1)$$

$n(H)_{500}$ = concentration of Hydrogen at 500 km T_∞ = exospheric temperature

Starting from the boundary conditions, the concentrations of the individual components were calculated as a function of altitude by numerical integration of the Diffusion Equation (Equations A.2 to A.4). From the density profiles of the five components the mean molecular mass altitude profile was calculated in steps of 1 km.

$$\frac{dn_i}{n_i} = -\frac{dh}{H_i} - \frac{dT}{T}(1+\alpha) \qquad (A.2)$$

$$H_i = \frac{k\,T}{m_i\,g} \qquad (A.3)$$

$$g = 9.81 \quad (1 + \frac{h}{R_E})^{-2} \qquad (A.4)$$

n_i = concentration (partial density)of the i th component

H_i = scale height of the i th component

α = thermal diffusion factor (= -0.38 for Helium, = 0 otherwise)

k = Boltzmann's constant g = acceleration due to gravity

T = temperature of the neutral atmosphere

m_i = mean molecular mass of the i th atmospheric component

R_E = mean radius of the Earth (= 6371 km)

The section of the Jacchia Model which deals with atmospheric temperature takes an invariant 120 km boundary condition of 355 K and, given the exospheric temperature, represents the profile by exponential curves of the form of Equations A.5 to A.7.

$$T = T_\infty - (T_\infty - T_{120})\ \mathrm{EXP}(-u\,(h - 120)) \tag{A.5}$$

$$u = 0.0291\ \mathrm{EXP}(-\frac{v^2}{2}) \tag{A.6}$$

$$v = \frac{T_\infty - 800}{750 + 1.722.10^{-4}\,(T_\infty - 800)^2} \tag{A.7}$$

T_{120} = 120 km boundary temperature (= 355 K)

In addition to the empirical formulae given above the exospheric temperature is the variable which is required in order to compute the temperature profile. The exospheric temperature is variable on solar cycle, seasonal, solar rotation and diurnal time scales as well as with geomagnetic activity. The small corrections introduced by the solar rotation and geomagnetic terms were held at their mean level for all the calculations (a constant +61 K accounting for both a level of geomagnetic activity given by Kp = 2 and for the average over three solar rotations) which left just the stronger solar, seasonal and diurnal variations.

The dependence of mean daytime and nighttime exospheric temperature on the solar activity, described by the Covington Index (solar noise flux at 2 800 MHz), is given by Equations A.8 and A.9. A relationship between the twelve–month running mean sunspot number and the solar flux is given by Equation A.10 (Joachim 1966). For a sunspot number of 170 Equation A.10 predicts a solar flux of 196 which compares well with the prediction of 210 for the peak of solar cycle 22 predicted by Schatten and Sofia (1987).

$$\bar{T}_0 = 418 + 3.6\,\bar{F}_{10.7} \tag{A.8}$$

$$\bar{T}_1 = 1.28\,\bar{T}_0 \tag{A.9}$$

$$\bar{F}_{10.7} = Z + 26 + 23^{\frac{-Z}{20}} \tag{A.10}$$

$F_{10.7}$ = Covington index (10^{22} $Wm^{-2}Hz^{-1}$)

T_0 = nighttime exospheric temperature

T_1 = daytime exospheric temperature

(overbars indicate smoothed values over three solar rotations)

The seasonal variation of T_0 is described by Equation A.11, where d is the day number of the year.

$$T_0 = \bar{T}_0 + (0.37 + 0.14 \, SIN (2\pi \frac{d-151}{365})) \, \bar{F}_{10.7} \, SIN (4\pi \frac{d-59}{365}) \qquad (A.11)$$

The exospheric temperature at a given time and location can then be calculated from Equations A.12 to A.15.

$$T = T_0 (1+R \, SIN^m\theta) (1 + R \frac{COS^m\eta - SIN^m\theta}{1 + R \, SIN^m\theta} COS^n\frac{\tau}{2}) \qquad (A.12)$$

$$\eta = \frac{1}{2}(\lambda - \delta) \qquad (A.13)$$

$$\theta = \frac{1}{2}(\lambda + \delta) \qquad (A.14)$$

$$\tau = A + a + p \, SIN (A + b) \qquad (A.15)$$

$-\pi < \tau < \pi$ A = the hour angle of the Sun

R = 0.30 m = 2.2 n = 3.0

a = –37° p = 6° b = 43°

λ = geographic latitude δ = solar declination

Where the values of these parameters are taken from the CIRA 72 model (COSPAR 1972), rather than the values quoted by Jacchia in the original paper. The a term determines the lag of the maximum exospheric temperature with respect to midday and the p term causes an asymmetry into the temperature variations which is located by the b term. The constants m and n determine, respectively, the mode of the latitudinal and longitudinal temperature variations.

The Jacchia Thermosphere Model was employed to calculate scale height profiles of the neutral atmosphere which allowed scaling of the Predictive Model D and the topside regions of Predictive Model A.

JACCHIA MODEL 120 km ALTITUDE BOUNDARY CONDITIONS

TEMPERATURE	355 K

ATMOSPHERIC COMPONENT	DENSITY (m^{-3})
MOLECULAR NITROGEN	$4.0 \cdot 10^{11}$
MOLECULAR OXYGEN	$7.5 \cdot 10^{10}$
ATOMIC OXYGEN	$7.6 \cdot 10^{10}$
HELIUM	$3.4 \cdot 10^{7}$

Table A.1 The 120 km altitude boundary conditions of the Jacchia Thermospheric Model.

Appendix B : The JPL Electron Content Model

The JPL Electron Content Model was developed at the US Jet Propulsion Laboratory, Pasadena, California, originally for deep space tracking of interplanetary probes (Yip et al 1975). The model is based on the precarious assumption that, in a sun–fixed reference frame, the ionosphere is only slowly changing. A version specific to the requirements of the Seasat mission is described by Lorell, Colquitt and Anderle (1982). The Local Time effect is described by Equations B.1 and B.2.

$$E = E_{min} + (E_{max} - E_{min}) \cos^{\alpha}\chi \qquad |\chi| \leq 90° \qquad \text{(B.1)}$$

$$E = E_{min} \qquad |\chi| > 90° \qquad \text{(B.2)}$$

E = electron content

χ = modified solar zenith angle

α = dimensionless exponent

The minimum and maximum values refer to local extremes of electron content. A least–squares technique was used to calculate the values of E_{min}, E_{max} and α for the measurements of electron content taken during each twenty four hour period at the northern hemisphere site at Goldstone, California (35°N,243°E) and the southern hemisphere site at Armidale, Australia (31°S,152°E). The Faraday rotation technique was used to measure the electron content from the transmissions of the ATS1 and ATS2 satellites. An interpolation procedure was then used to calculate the electron content at the required point.

The modified zenith angle is found from Equations B.3 to B.5 and accounts for the asymmetrical Local Time development of electron content about its maximum near local noon.

$$\cos\chi = \sin\lambda \sin\delta + \cos\lambda \cos\delta \cos\omega A \qquad \text{(B.3)}$$

λ = geographic latitude

δ = solar declination

ω = terrestrial angular rotation frequency (15° per hour)

t = Local Time (hours)

A = modified hour angle

$$A = t - 12 \qquad 5 \le t < 11 \qquad \text{(B.4)}$$

$$A = t - 12 - 11\left(\frac{t - 11}{18}\right)^r \qquad 11 \le t < 24 + 5 \qquad \text{(B.5)}$$

The exponent, r, is given empirically by Equation B.6.

$$r = 1.75 - 0.75 \cos^{10} \beta \qquad \text{(B.6)}$$

β = geomagnetic latitude

The spatial variation of electron content, apart from that incorporated in the modified zenith angle, is modelled by a multiplicative factor (G, Equation B.7) which depends on geomagnetic latitude. This factor incorporates an anomaly factor (H, Equations B.8 to B.11) which describes the structure near the geomagnetic Equator.

$$G(\beta,t) = H(\beta,t)\,(1 + \cos^2\beta) \qquad \text{(B.7)}$$

$$H(\beta,t) = 1 - F(t)\,(1.15\ \text{SINC}\sqrt{35\pi|\beta|} - 0.146) \qquad |\beta| \le \pi/6 \qquad \text{(B.8)}$$

$$H(\beta,t) = 1 \qquad |\beta| > \pi/6 \qquad \text{(B.9)}$$

$$F(t) = 0.25\ \text{SIN}\sqrt{\frac{(t - 11).\pi}{18}} \qquad 11 \le t < 29 \qquad \text{(B.10)}$$

$$F(t) = 0 \qquad 5 \le t < 11 \qquad \text{(B.11)}$$

The JPL Model was employed for the one hundred day duration Seasat mission and is compared and contrasted with the new LEI Model in this thesis.

Appendix C : Algorithm Design Language Computer Program

This appendix describes a prototype design for an ionospheric range correction algorithm suitable for radar altimetry. The program is expressed in terms of an Algorithm Design Language (ADL). ADL is a non–compilable language which expresses the structure of an algorithm in a semi–formal manner without being bound by the explicit syntax of a particular programming language.

```
Procedure: MAIN
input sources :<orbit> orbit configuration
                <table>     electron content look–up tables
                <prare>     prare delta–range data
output sources :<primary>   primary processing data stream
                <status>    process status report
<start>
initialize all variables to zero
PERFORM ESTAB                       acquire data from orbit file to configure the algorithm
PERFORM SOLAR                       acquire sunspot number from intrinsic look–up table
PERFORM CHOOSER                     determine files which contain relevant look–up tables
PERFORM READER                      read in four look–up tables defined by sunspot number and month
LOOP FOR number of sounding locations in one revolution
    PERFORM INITIAL                 input spatial and temporal location of the altimeter sounding and prare
                                    data flag
    PERFORM LIMITER                 pitch sounding longitude within standard range (0°–360°) for
                                    consistency
    PERFORM FACTORY                 calculate residual fractions of altimeter co–ordinates between look–up
                                    table grid points
    PERFORM LOOKUP                  acquire grid values of electron content from look–up table 1 and
                                    interpolate in Universal Time, latitude and longitude
    PERFORM LOOKUP                  acquire grid values of electron content from look–up table 2 and
                                    interpolate in Universal Time, latitude and longitude
    PERFORM LOOKUP                  acquire grid values of electron content from look–up table 3 and
                                    interpolate in Universal Time, latitude and longitude
    PERFORM LOOKUP                  acquire grid values of electron content from look–up table 4 and
                                    interpolate in Universal Time, latitude and longitude
    PERFORM INTERPOL                interpolate one pair of results in date
    PERFORM INTERPOL                interpolate other pair of results in date
    PERFORM INTERPOL                interpolate in sunspot number to calculate the predictive electron
                                    content at the sounding point
    IF prare flag = unity THEN
        PERFORM PRARE               input prare station geocentric co–ordinates and delta–range data
        PERFORM CONVERT             calculate slant electron content from prare delta–range
        PERFORM CORD                calculate latitude and longitude of prare ground site
        PERFORM LIMITER             pitch prare ground station longitude within standard range for
                                    consistency
        PERFORM IPOINT              calculate the ionospheric point of the prare measurement
        PERFORM LIMITER             pitch ionospheric point longitude within standard range for consistency
        PERFORM COHERFNS            calculate spatial correlation coefficient between prare data and
                                    altimeter sounding
        PERFORM CZECH               establish whether remote prare data is suitable for correction purposes
```

PERFORM *FACTORY* — calculate residual fractions of ionospheric point co–ordinates between look–up table grid points

PERFORM *LOOKUP* — acquire grid values of electron content from look–up table 1 and interpolate in Universal Time, latitude and longitude

PERFORM *LOOKUP* — acquire grid values of electron content from look–up table 2 and interpolate in Universal Time, latitude and longitude

PERFORM *LOOKUP* — acquire grid values of electron content from look–up table 3 and interpolate in Universal Time, latitude and longitude

PERFORM *LOOKUP* — acquire grid values of electron content from look–up table 4 and interpolate in Universal Time, latitude and longitude

PERFORM *INTERPOL* — interpolate one pair of results in date

PERFORM *INTERPOL* — interpolate other pair of results in date

PERFORM *INTERPOL* — interpolate in sunspot number to calculate the predictive electron content at the ionospheric point

PERFORM *ADAPT* — calculate adaptive adjustment at the sub–altimeter point

ENDIF

PERFORM *DECIDER* — decide between predictive and adaptive estimates of electron content

PERFORM *RANGE* — convert electron content to altimeter ionospheric range correction

PERFORM *DELIVER* — append ionospheric range correction to primary altimeter data stream

ENDLOOP

<end>

procedure : *ESTAB*

input sources :<orbit> orbit configuration

output sources: <status> process status report

<start>

INPUT <orbit> — year number, month number, date, Universal Time, latitude, longitude of altimeter sounding, flag for presence of prare data (at 1 Hz)

store these month and year numbers as references

IF year is a leap year THEN

set leap year flag = 1

ELSE

set leap year flag = 0

ENDIF

rewind orbit configuration file

IF end of file THEN

OUTPUT <status> — report end of file detected

ENDIF

<end>

procedure : *SOLAR*

input sources : none

output sources : none

<start>

CALCULATE — given year and month numbers look–up sunspot number from internal table

IF sunspot number greater than 200 THEN

set sunspot number to 200

ENDIF

<end>

procedure : *CHOOSER*

input sources : none

output sources : none

<start>

IF sunspot number < 50 THEN

set look–up table parameter = 00

ELSEIF sunspot number < 100 THEN

set look–up table parameter = 01

```
ELSEIF sunspot number < 150 THEN
        set look–up table parameter = 02
ELSE
        set look–up table parameter = 03
ENDIF
<end>

procedure : READER
input sources :<table>          electron content look–up tables
output sources :        none
<start>
LOOP FOR month number to month number + 1
        LOOP FOR look–up table parameter to look–up table parameter + 1
                INPUT <table>           corresponding look–up table to common block array
        ENDLOOP
ENDLOOP
<end>

procedure : INITIAL
input sources :<orbit> orbit configuration
output sources:         <status>        process status report
<start>
INPUT <orbit>                                   year number, month number, date, Universal Time, latitude, longitude
                                                of altimeter sounding, flag for presence of prare data
CALCULATE                                       latitude in degrees (from microdegrees)
CALCULATE                                       longitude in degrees (from microdegrees)
CALCULATE                                       Universal Time in hours (from seconds)
IF change in month number or year number THEN
        OUTPUT <status>                 report month/year boundary detected
ENDIF
IF end of file THEN
        OUTPUT <status>                 report end of file detected
ENDIF
<end>

procedure : LIMITER
input sources :none
output sources:         none
<start>
IF longitude is less than 0° THEN
        add 360° to longitude
ELSEIF longitude is greater than 360° THEN
        subtract 360° from longitude
ENDIF
<end>


procedure : FACTORY
input sources :none
output sources:         <status>        process status report
<start>
IF month number less than one or greater than twelve THEN
        OUTPUT <status>                 report month number out of range
ENDIF
CALCULATE                                       look–up number of days in month from internal table given month
                                                number
IF month number equals two THEN
        add leap flag to number of days
ENDIF
LOOP FOR Universal Time, date, sunspot number, latitude, longitude
```

CALCULATE — remainder after division by look–up table interval as a fraction of the interval

ENDLOOP
<end>

procedure : *LOOKUP*
input sources :none
output sources: none
<start>
CALCULATE — acquire eight values of electron content from common block array for interpolation purposes
CALCULATE — linearly interpolate between the eight grid points in Universal Time, longitude and latitude

<end>

procedure : *INTERPOL*
input sources :none
output sources: none
<start>
CALCULATE — linearly interpolate between the results of the *LOOKUP* procedure in date and sunspot number

<end>

procedure : *PRARE*
input sources :<prare> prare delta–range measurements
output sources: none
<start>
INPUT <prare> — the four prare data file records which include delta–range data and the geocentric co–ordinates of the prare ground site

<end>

procedure : *CONVERT*
input sources :none
output sources: none
<start>
CALCULATE — slant path electron content from measurement of the range difference on the two microwave frequencies of the spaceborne component of prare

<end>

procedure : *CORD*
input sources :none
output sources: none
<start>
CALCULATE — latitude and longitude of prare site from its geocentric co–ordinates
<end>

procedure : *IPOINT*
input sources :none
output sources: none
<start>
CALCULATE — zenith angle and ionospheric point of prare measurement.
<end>

procedure : *COHERFNS*
input sources :none
output sources: none
<start>

```
CALCULATE                                   spatial correlation coefficient of electron content between prare
                                            measurement and altimeter sounding
<end>

procedure : CZECH
input sources :none
output sources:      <status>      process status report
<start>
IF correlation coefficient is less than 0.7 THEN
        OUTPUT <status>                     report correlation coefficient out of range
        set prare flag to zero
ENDIF
<end>

procedure : ADAPT
input sources :none
output sources:      none
<start>
CALCULATE                                   adaptive adjustment to predictive electron content estimated for the
                                            altimeter sounding point
<end>

procedure : DECIDER
input sources :none
output sources:      none
<start>
IF prare flag equals unity THEN
        CALCULATE                           electron content as predictive electron content plus adjustment
ELSE
        CALCULATE                           electron content as predictive electron content
ENDIF
<end>

procedure : RANGE
input sources :none
output sources:      <status>      process status report
<start>
CALCULATE                                   ionospheric range correction from sub-altimeter electron content
IF range correction is negative or greater than 1.000 m THEN
        set warning flag to unity
        OUTPUT <status>                     report warning flag set
ELSE
        set warning flag to zero
ENDIF
<end>

procedure : DELIVER
input sources :none
output sources :     <primary>     primary data processing stream
<start>
CALCULATE                                   latitude in degrees (from microdegrees)
CALCULATE                                   longitude in degrees (from microdegrees)
CALCULATE                                   Universal Time in seconds (from hours)
OUTPUT <primary>                            year, month number, date, Universal Time, latitude, longitude,
                                            prare flag, warning flag, ionospheric correction
<end>
```

References

Reference 1 Proceedings of the International Beacon Satellite Symposium on Radio Beacon Contribution to the Study of Ionization and Dynamics of the Ionosphere and to Corrections to Geodesy and Technical Workshop, Oulu, Finland, 1986.

Reference 2 Proceedings of the Symposium on the Effect of the Ionosphere on Space Systems and Communications, Arlington, Virginia, 1975.

Reference 3 Proceedings of the Symposium on the Effect of the Ionosphere on Space and Terrestrial Systems, Arlington, Virginia, 1978.

Reference 4 Proceedings of the International Symposium on Beacon Satellite Studies of the Earth's Environment, New Delhi, India, 1983.

Anderson D. N. and J. A. Klobuchar (1983) J. Geophys. Res. 88 8020
Modeling the Total Electron Content Observations Above Ascension Island.

Appleton E. V. and W. J. G. Beynon (1947) Proc. Phys. Soc. London 59 58
The Application of Ionospheric Data to Radio Communication Problems – Part 2.

Appleton E. V. and W. J. G. Beynon (1940) Proc. Phys. Soc. London 52 518
The Application of Ionospheric Data to Radio Communication Problems – Part 1.

Appleton E. V. (1932) J. Inst. Elec. Eng. 71 642
Wireless Studies of the Ionosphere.

Barford N. C. (1967) Addison–Wesley
Experimental Measurements : Precision, Error and Truth.

Bauer S. J. (1973) Springer–Verlag
Physics of Planetary Ionospheres.

Bent R. B., S. K. Llewellyn, G. Nesterczuk and P. E. Schmid (1975) Reference 2
The Development of a Highly Successful Worldwide Empirical Ionospheric Model and its Use in Certain Aspects of Space Communications and Worldwide Total Electron Content Investigations.

Bhuyan P. K. and T. R. Tyagi (1986) Reference 1
Spatial Correlation of Ionospheric Electron Content at Low–latitudes for Solar Minimum.

Bhuyan P. K., L. Singh and T. R. Tyagi (1984) Indian J. Rad. Spa. Phys. 13 185
Simultaneous Observations of IEC from Two Geostationary Satellites and their Spatial Correlation.

Bhuyan P. K. and T. R. Tyagi (1983) Reference 4
Low–latitude Features of Annual and Semi–annual Periodicities in IEC in the Indian Zone.

Bhuyan P. K., T. R. Tyagi, L. Singh and Y. V. Somayajulu (1983)
Indian J. Rad. Spa. Phys. 12 84
Ionospheric Electron Content Measurements at a Northern Low Mid–latitude Station Through Half a Solar Cycle.

Bilitza D. (1986) Rad. Sci. 21 343
International Reference Ionosphere: Recent Developments.

Bilitza D., N. M. Sheikh and R. Eyfrig (1979) Telecom. J. 46 549
A Global Model for the Height of the F2–peak Using M3000 Values from the CCIR Numerical Map.

Callahan P. S. (1984) Marine Geology 8 249
Ionospheric Variations Affecting Altimeter Measurements : A Brief Synopsis.

Chapman S. (1931) Proc. Phys. Soc. London 43 26
The Absorption and Dissociative or Ionizing Effect of Monochromatic Radiation in an Atmosphere on a Rotating Earth.

Chase R. R. P., R. A. Bindschaller, G. Born, L. L. Fu,P. Mouginis–Mark, C. Parsons and B. Tapley
NASA EOS 2h (1987) Altimetric System Panel Report.

Cheney R. E. (1982) J. Geophys. Res. 87 3247
Comparison Data for Seasat Altimetry in the Western North Atlantic.

Ching B. K. and Y. T. Chiu (1973) J. Atmos. Terr. Phys. 35 1615
A Phenomenological Model of Global Ionospheric Electron Density in the E-, F1- and F2-regions.

Comité Consultatif International des Radiocommunications (1967)
Union Int. des Telecom. CCIR Atlas of Ionospheric Characteristics Report 340.

Comité Consultatif International des Radiocommunications (1975)
Union Int. des Telecom. CCIR Atlas of Ionospheric Characteristics Supplement 2 to Report 340.

Committee on Space Research (1972) North-Holland
COSPAR International Reference Atmosphere CIRA 1972.

da Rosa A. V. (1974) Akademie-Verlag
Space Research XIV.

Davies K. (1981) Rad. Sci. 16 1407
Review of Recent Progress in Ionospheric Predictions.

Davies K., R. B. Fritz and T. B. Gray (1976) J. Geophys. Res. 81 2825
Measurements of the Columnar Electron Contents of the Ionosphere and Magnetosphere.

Davies K. (1968) AGARD LS-29 1-1
Magneto-ionic Theory of Radio Propagation.

Dodson A. H. (1986) Int. J. Rem. Sens. 7 515
Refraction and Propagation Delays in Space Geodesy.

Donatelli D. E. and R. S. Allen (1981) Rad. Sci. 16 261
Time Cells for Adaptive Prediction of Total Electron Content.

Donatelli D. E. and R. S. Allen (1978) Reference 3
Temporal Variability of Ionospheric Refraction Correction.

DuLong D. D. (1977) ADA 046 166 AFGL-TR-77-0125
Reduction of the Uncertainty of Radar Range Correction.

Essex E. A (1979) J. Atmos. Terr. Phys. 41 951
The Effects of Geomagnetic Activity on the F-region of the Ionosphere.

Essex E. A. (1978) J. Atmos. Terr. Phys. 40 1019
Ionospheric Total Electron Content at Southern Mid-latitudes during 1971-74.

Faraday M. (1846) Phil. Trans. Roy. Soc. London 1
Experimental Researches in Electricity - nineteenth series : On the Magnetization of Light and the Illumination of Magnetic Lines of Force.

Feen M. M., V. L. Pisacane and M. Sturmanis (1975) Reference 2
Prediction Techniques for the Effect of the Ionosphere on Ranging from Satellites.

Fleury R. (1986) Reference 1
Study of the Total Electron Content Variability with Applications to Altimetric Measurements.

Flock W. L. (1987) NASA Reference Publication 1108 (02)
Propagation Effects on Satellite Systems at Frequencies below 10 GHz.

Fu L. L., J. Vazquez and M. Parke (1986)
Institute of Oceanographic Sciences WOCE Newsletter, number 3
Seasonal Variability of the Gulf Stream as Observed from Satellite Altimetry.

Fu L. L. (1983) Rev. Geophys. Spa. Phys. 21 1657
Recent Progress in the Application of Satellite Altimetry to Observing the Mesoscale Variability and General Circulation of the Oceans.

Garriott O. K., F. L. Smith and P. C. Yuen (1963) Planet. Spa. Sci. 13 829
Observations of Ionospheric Electron Content using a Geostationary Satellite.

Garriott O. K. (1960) J. Geophys. Res. 65 1139
The Determination of Ionospheric Electron Content and Distribution from Satellite Observations.

Garriott O. K. and C. G. Little (1960) J. Geophys. Res. 65 2025
The Use of Geostationary Satellites for the Study of Ionospheric Electron Content and Ionospheric Radio–Wave Propagation.

Gautier T. N. and D. H. Zacharisen (1965) Conference Record, First Annual IEEE Communications Convention
Use of Space and Time Correlation in Short Term Ionospheric Predictions.

Georges T. M. (1968) Proceedings of the Second ESRIN–ESLAB Symposium : Low Frequency Waves and Irregularities in the Ionosphere, Frascati, Italy, 1968.
Effects of Ionospheric Motions and Irregularities on HF Radio Propagation.

Green D. W., V. W. Lam and H. N. Royden (1980) Proceedings of the AIAA/AAS Astrodynamics Conference, Paper 80–1650, Danvers, Massachusetts, 1980
Effects of the Charged Particle Environment on Voyager Navigation at Jupiter and Saturn.

Griffiths H. D. (1986) University of London Ph. D. thesis
Studies of Radar Altimetry Over Topographic Surfaces.

Halcrow B. W. and J. S. Nisbet (1977) Rad. Sci. 12 815
A Model of F2 Peak Electron Densities in the Main Trough Region of the Ionosphere.

Hanson W. B. (1965) Stanford University Press
Satellite Environment Handbook (ed. F. S. Johnson).

Hargreaves J. K. (1979) Van Nostrand Reinhold
The Upper Atmosphere and Solar Terrestrial Relations.

Hartl P. (1984) Proceedings of the ESA Workshop on ERS–1 Data Products, Frascati, Italy, 1984
The Precise Range and Range Rate Equipment (PRARE) and its Possible Support to the Radar Altimeter Measurements for ERS–1.

Hawkins G. S., and J. A. Klobuchar (1975) Reference 2
Seasonal and Diurnal Variations in the Total Electron Content of the Ionosphere at Invariant Latitude 54 degrees.

Hedin A. E. (1987) J. Geophys. Res. 9 4649
MSIS–86 Thermospheric Model.

Huang T. X. (1983) Reference 4
Average Horizontal Gradients and Spatial Correlation of Mid–latitude Total Electron Content at Solar Minimum.

Huang Y. N. (1984) J. Geophys. Res. 89 9823
Spatial Correlation of the Ionospheric Total Electron Content at the Equatorial Anomaly Crest.

Huang Y. N. (1981) Preprints of the Symposium on the Effect of the Ionosphere on Radio Systems, Washington DC, 1981
Some Results of Ionospheric Total Electron Content and Scintillation Observations at Lunping.

Huang Y. N. (1978) J. Atmos. Terr. Phys. 40 733
Solar Cycle Variation in the Total Electron Content at Sagamore Hill.

Hultqvist B. (1973) Universitetsforlaget
Cosmical Geophysics.

Hunsucker R. D. and J. K. Hargreaves (1988) J. Atmos. Terr. Phys 50 167
A Study of Gravity Waves in Ionospheric Electron Content at L = 4.

Iyer K. N. and O. P. Nagpal (1983) J. Atmos. Terr. Phys. 45 667
On Medium Scale Travelling Ionospheric Disturbances as Seen Through Total Electron Content Power Spectra.

Jacchia L. G. (1965) Smithson. Contr. Astrophys. 8 215
Static Diffusion Models of the Upper Atmosphere with Empirical Temperature Profiles.

Jakowski N., A. Jungstand, L. Lois and B. Lazo (1986) Reference 1

Nighttime Enhancement of the Ionospheric Electron Content at Cuba.

Jakowski N. and E. Paasch (1984) Ann. Geophys. 2 501

Report on the Observations of the Total Electron Content of the Ionosphere in Neustrelitz GDR from 1976 to 1980.

Joachim M. (1966) Nature 210 289

Study of Correlation of the Three Basic Indices of Ionospheric Propagation.

Johanson J. M., M. J. Buonsanto and J. A. Klobuchar (1978) Reference 3

The Variability of Ionospheric Time Delay.

Jones W. B. and R. M. Gallet (1962) Telecom. J. 29 129

The Representation of Diurnal and Geographic Variations of Ionospheric Data by Numerical Methods.

Kane R. P. (1975) J. Geophys. Res. 80 3091

Day–to–day Variability of Ionospheric Electron Content at Mid–Latitudes.

Kenrick G. W. and G. W. Pickard (1930) Proc. Inst. Elec. Eng. 18 649

Summary of Progress in the Study of Radio Wave Propagation Phenomena.

King J. W. and A. J. Slater (1973) Telecom. J. 40 766

Errors in Predicted Values of foF2 and hmF2 Compared to the Observed Day–to–day Variability.

Klobuchar J. A. (1982) National Telesystems Conference, Galveston, Texas, November, 1982

Ionospheric Corrections for the Single Frequency User of the Global Positioning System.

Klobuchar J. A. (1980) Proceedings of the Satellite Beacon Symposium, Warszawa, Poland, 1980

Present State of Ionospheric Time Delay Prediction.

Klobuchar J. A. (1978) AGARD LS-93 7-1
Ionospheric Effects on Satellite Navigation and Air Traffic Control Systems.

Klobuchar J. A. and J. M. Johanson (1977) AD A 048 117 AFGL-TR-77-0185
Correlation Distance of Mean Daytime Electron Content.

Klobuchar J. A. (1976) Proceedings of the Symposium on the Geophysical Use of Satellite Beacon Observations, Boston, Massachusetts, 1976
Review of Ionospheric Time Delay Limitations to Ranging Systems.

Klobuchar J. A. (1975) ADA 018 862 AFCRL-TR-75-0502
A First Order, Worldwide, Ionospheric, Time-Delay Algorithm.

Klobuchar J. A. (1973) AGARD AG-166 7
TEC from the Faraday Effect.

Klobuchar J. A. and H. E. Whitney (1965) Radio Sci. 1 1149
Mid-latitude Ionospheric Total Electron Content : Summer 1965.

Köhnlein W. (1978) Rev. Geophys. Spa. Phys. 16 341
Electron Density Models of the Ionosphere.

Lakshmi D. R., B. M. Reddy and R. S. Dabas (1988) J. Atmos. Terr. Phys. 50 207
On the Possible Uses of Recent EUV Data for Ionospheric Predictions.

Lambert M. and E. A. Cohen (1986) Rad. Sci. 21 347
Monitoring Ionospheric Irregularities in The Southern Auroral Region by Means of a Satellite Beacon.

Lame D. B. and G. H. Born (1982) J. Geophys. Res. 87 3175
Seasat Measurement System Evaluation : Achievements and Limitations.

Llewellyn S. K. and R. B. Bent (1973) AD A 772 733 AFCRL-TR-73-0657
Documentation and Description of the Bent Ionospheric Model.

Lorell J., E. Colquitt and R. J. Anderle (1982) J. Geophys. Res. 87 3207
Ionospheric Correction for SEASAT Altimeter Height Measurement.

Marconi G. (1902) Proc. Roy. Inst. 17 195
The Progress of Electric Space Telegraphy.

Marsh J. G. and T. V. Martin (1982) J. Geophys. Res. 87 3269
The Seasat Altimeter Mean Sea Surface Model.

McNamara L. F. (1984) Adv. Spa. Res. 4 25
Prediction of Total Electron Content Using the International Reference Ionosphere.

McNamara L. F. (1983) ADA 132 624 AFGL-TR-83-0092
The Conversion of Off-vertical Observations of Total Electron Content into Equivalent Vertical Incidence Values.

McNamara L. F. and P. J. Wilkinson (1984) Proceedings of the Solar-Terrestrial Predictions Workshop, Paris, France, 1984
A Cautionary Note on the Use of F2 Region Correlation Coefficients for Short-term Forecasting Purposes.

McNamara L. F. and P. J. Wilkinson (1983) J. Atmos. Terr. Phys. 45 169
Prediction of Total Electron Content Using the International Reference Ionosphere.

McNamara L. F. and D. H. Smith (1982) J. Atmos. Terr. Phys. 44 227
Total Electron Content of the Ionosphere at 31°S, 1967–1974.

Mendillo M. and J. A. Klobuchar (1975) J. Geophys. Res. 80 643
Investigations of the Ionospheric F Region Using Multistation Total Electron Content Observations.

Mendillo M. (1973) Planet. Spa. Sci. 21 349
A Study of the Relationship Between Geomagnetic Storms and Ionospheric Disturbances at Mid-latitudes.

Mendillo M. and J. A. Klobuchar (1973) AGARD AG–166 49
Low Elevation Angle Measurements of Total Electron Content Taken From Thule, Greenland.

Milsom J. D. (1984) Proceedings of the Solar–Terrestrial Predictions Workshop, Paris, France, 1984
Towards Improving a Short Term Ionospheric Forecasting Service.

Minakoshi H. and K. Sinno (1985) Proceedings of the 1985 International Symposium on Antennas and Propagation, Tokyo, Japan, 1985
Total Electron Content in the Asian Mid–latitude region and its Effect on Earth–Space Propagation.

Muggleton L. M. (1975) Telecom. J. 42 413
A Method of Predicting foE at Any Time or Place.

Mulkern F. A. (1976) ADA 029 348 AFGL–TR–76–0158
Comparison of the Predicted Means of Total Electron Content with Field Observations.

Nesterczuk G. (1981) NASA–CR–156811
Ionospheric Propagation Correction Modelling for Satellite Altimeters.

Nisbet J. S., O. F. Tyrnov, G. N. Zintchenko and W. J. Ross (1981) Rad. Sci. 16 127
Limits on the Accuracy of Correction of Trans–ionospheric Propagation Errors by Using Ionospheric Models Based on Solar and Magnetic Indices and Local Measurements.

Nisbet J. S. (1975) D. Reidel
Atmospheres of Earth and the Planets.

Ogawa T. and K. Ohbu (1986) J. Radio Res. Lab., Japan 33 87
Sudden Increases in Total Electron Content (SITECs) Induced by Solar Flares.

Papoulis A. (1965) McGraw Hill
Probability, Random Variables, and Stochastic Processes.

Paul M. P. (1982) NASA-CR-168852
Measurement of Total Electron Content of Mid-latitude Ionosphere and Protonosphere via Faraday Rotation and Group Delay Techniques Using Transmissions from Geostationary Satellites ATS3 and ATS6 – Final Report.

Pisacane V. L. (1984) NASA Conference Publication 2303 377
Satellite Techniques for Determining the Geopotential for Sea-surface Elevations.

Rajaram G., and R. G. Rastogi (1977) J. Atmos. Terr. Phys. 39 1175
Equatorial Electron Densities – Seasonal and Solar Cycle Changes.

Rapley C. G., H. D. Griffiths, V. A. Squire, J. G. Olliver, A. R. Birks, A. P. R. Cooper, A. M. Cowan, D. J. Drewery, M. R. Gorman, M. Guzkowska, S. Laxon, I. M. Mason, N. F. McIntyre, E. Novotny, R. Paterson, R. F. Scott and F. A. Street-Perrot (1985) ESA Report 5684/83/NL/BI
Applications and Scientific Uses of ERS-1 Radar Altimeter Data.

Rawer K. and D. Bilitza (1985) ESA CR 5375/83/D
Study of Ionospheric and Tropospheric Models.

Rawer K. (1983) Reference 4
25 Years of Beacon Satellite Measurements - Europe.

Rawer K., D. Bilitza and S. Ramakrishnan (1978) Rev. Geophys. Spa. Phys. 16 177
Goals and Status of the International Reference Ionosphere.

Rishbeth H. and O. K. Garriott (1969) Academic Press
Introduction to Ionospheric Physics.

Rishbeth H. (1967) Proc. I.E.E.E. 55 16
A Review of Ionospheric F Region Theory.

Royden H. N., D. W. Green and G. R. Walson (1980)
Proceedings of the Satellite Beacon Symposium, Warszawa, Poland, 1980
Use of Faraday-Rotation Data from Beacon Satellites to determine Ionospheric Corrections for Interplanetary Spacecraft Navigation.

Rush C. M., M. PoKempner, D. N. Anderson, J. Perry, F. G. Stewart and R. Reasoner (1984)
Rad. Sci. 19 1083 Maps of foF2 Derived from Observations and Theoretical Data.

Rush C. M., M. PoKempner, D. N. Anderson, F. G. Stewart and J. Perry (1983)
Rad. Sci. 18 95 Improving Ionospheric Maps Using Theoretically derived values of foF2.

Rush C. M. (1979) AGARD LS-99 4-1
Transionospheric Radio Propagation.

Rush C. M. (1976) Telecom. J. 43 544
An Ionospheric Observation Network for Use in Short-term Propagation Predictions.

Schatten K. H. and S. Sofia (1987) Geophys. Res. Lett. 14 632
Forecast of an Exceptionally Large Even-numbered Solar Cycle.

Shimazaki T. (1955) J. Rad. Res. Labs. Japan 2 85
World-wide Daily Variations in the Height of the Maximum Electron Density of the Ionospheric F2-layer.

Soicher H. (1985) AGARD CP-382 2.3-1
Variability of transionospheric Signal Time Delay at High-latitudes near Solar Minimum.

Soicher H. and F. J. Gorman (1982) AD-A113683
Total Electron Content Variations at Mid- and High-latitudes.

Soicher H. and F. J. Gorman (1985) Rad. Sci. 20 383
Seasonal and Day-to-day Variability of Total Electron Content at Mid-latitudes near Solar Maximum.

Soicher H., J. A. Klobuchar and P. H. Doherty (1984) Rad. Sci. 19 757
Spatial Variability of Total Electron Content in the Eastern Mediterranean Region.

Soicher H., Z. Houminer and A. Shuval (1982) Rad. Sci. 17 1623
Total Electron Content Structure in the Middle East.

Soicher H. (1978) IEEE Trans. Ant. Prop. AP-26 311
Spatial Correlation of Transionospheric Signal Time Delays.

Soicher H. (1977) IEEE Trans. Ant. Prop. AP-25 705
Ionospheric and Plasmaspheric Effects in Satellite Navigation Systems.

Szuszczewicz E. P., P. Rodriguez, M. Singh and S. Mango (1983) Radio Sci. 18 765
Ionospheric Irregularities and their Potential Impact on Synthetic Aperture Radars.

Tennent R. M. (1971) Oliver and Boyd
Science Data Book.

Titheridge J. E. (1972) Planet. Spa. Sci. 20 353
Determination of Ionospheric Electron Content from the Faraday Rotation of Geostationary Satellite Signals.

Tyagi T. R., H. Soicher, K. C. Yeh and A. Tauriainen (1982) J. Geophys. Res. 87 2525
The Electron Content and its Variations at Natal, Brazil.

Velten E. V. (1984)
Proceedings of the ESA Workshop on ERS–1 Data Products, Frascati, Italy, 1984
The ESA Remote Sensing Satellite System (ERS1).

Wakai N. and N. Matuura (1980) Acta Astronautica 7 999
Operation and Experimental Results of the Ionospheric Sounding Satellite–b.

Watson–Watt R. A. (1933) Nature 132 13
The Ionosphere.

Wilmes H., C. Reigber, W. Schäefer and P. Hartl (1987) Proceedings of the XIX General Assembly International Association of Geodesy, Vancouver, BC, Canada, 1987.
Precise Range and Range Rate Equipment, PRARE, on board ERS–1 Orbitography in Support to Radar Altimetry and Tool for Precise Geodetic Positioning.

Wolff R. S. (1985) Int. J. Sat. Com. 3 237

The Variability of the Ionospheric Total Electron Content and its Effect on Satellite Microwave Communications.

Yeh K. C. and V. H. Gonzales (1960) J. Geophys. Res. 65 3209

Note on the Geometry of the Earth Magnetic Field Useful to Faraday Effect Experiments.

Yip K. W., F. B. Winn, M. S. Reid and C. T. Stelzried (1975) Reference 2

Decimeter Modeling of Ionospheric Columnar Electron Content at S–band Frequencies.

Yunck T. P., W. G. Melbourne and C. L. Thornton (1985)

IEEE Trans. Geosci. Rem. Sens. 23 450

GPS–based Satellite Tracking System for Precise Positioning.